Principles of Hydrogen Catalysis in the Presence of Oxygen by a [NiFe] Hydrogenase from E. coli

Philip Wulff

St. John's College

Trinity Term 2014

A thesis submitted to the Board of the Faculty of Physical Sciences, for the degree of Doctor of Philosophy,

University of Oxford

Principles of Hydrogen Catalysis in the Presence of Oxygen by a [NiFe] Hydrogenase from E. coli

Philip Wulff, St. John's College, University of Oxford

A thesis submitted for the degree of DPhil, Trinity Term 2014

[NiFe] hydrogenases are metalloenzymes that act as highly efficient molecular electrocatalysts for the interconversion of protons and molecular hydrogen. Unlike any other known molecular electrocatalyst, the members of a subgroup of respiratory membrane-bound [NiFe] hydrogenases are able to maintain H_2 catalysis in the sustained presence of O_2. This O_2-tolerance depends on the ability to respond to oxidative inactivation by O_2 by exclusively forming rapidly reactivated active site states, thus implying a catalytic cycle in which O_2 acts as a competing substrate to H_2.

Using isotope ratio mass spectrometry it is proven that the O_2-tolerant *Escherichia coli* Hydrogenase 1 responds to O_2 attack by acting as a four-electron oxidoreductase, catalysing the reaction $2\ H_2 + O_2 \rightarrow 2\ H_2O$, equivalent to hydrogen combustion. Special features of the enzyme's electron relay system enable delivery of the required electrons. A small fraction of the H_2O produced arises from side reactions proceeding *via* reactive oxygen species, an unavoidable consequence of the presence of low-potential relay centres that release electrons from H_2 oxidation. While the ability to fully reduce O_2 to harmless H_2O at the active site to generate the rapidly reactivated state Ni-B, determines *if* a hydrogenase is O_2-tolerant, the ratio of oxidative inactivation to reductive reactivation rates determines *how* tolerant the enzyme is.

It is shown by protein film electrochemistry that the $(\alpha\beta)_2$ dimeric assembly of Hyd-1 plays an important role in O_2-tolerance by aiding reactivation of one catalytic unit through electron transfer from the other. The teamwork between two redundant partners implicates a new role for dimerisation and represents a new example of co-operativity in biology.

Finally, the non-natural amino acid p-azido-L-phenylalanine was synthesised and incorporated into Hyd-1, testing the possibility of introducing labels at specific sites.

Acknowledgements

First, I would like to thank Fraser Armstrong for the opportunity to carry out my research in his lab and for agreeing to supervise this work. I am grateful for all that he has taught me, especially through the writing of manuscripts. I would also like to use this opportunity to thank Alison Parkin, for her friendship, a great variety of help and advice during the early days of my work in the Armstrong group and her enormous commitment as senior post-doc to keeping the group running and in good spirits. I am also very grateful to Rhiannon Evans, who assumed much of the responsibility for keeping the group and lab in order when Alison moved on.

I thank Christopher Day for a refreshingly productive, straight-forward and enjoyable collaboration and my friends Adam Gammack and Andreas Bachmeier for helpful organic chemistry discussions; similarly, Frank Sargent has provided a wealth of biological information and insights throughout this work.

Looking back, I am acutely aware that my university education as a whole would probably not have been as fruitful without Manfred Gartemann, a truly remarkable high-school teacher who challenged and motivated me to continuously improve my work - an attitude that has served me well ever since.

Many wonderful friends have made my time at Oxford a unique, inspiring and joyful experience and I would like to especially thank Micha Lazarus, Thomas Owens, Jessica Fay, Jonah Rosenberg, Maeve Eason Hubbard, Navneet Vasistha, Benjamin Owens and Rahul Prabhakar for their enduring friendship.

My parents, Martina and Gerhard, and my brother Niklas have always been exceedingly generous in their love and support for me and I can only strive to follow their example.

Finally, I thank my wife Bonnie for countless discussions, suggestions and proof-reading, for her dedication and companionship - you are my life, my love and my greatest friend.

Collaborations and Contributions

The detection of $H_2{}^{18}O$ for Ch.2.2.1 and Ch.3.2.4 was carried out by isotope ratio mass spectrometry in collaboration with Christopher Day (Earth Sciences, University of Oxford), who established the protocol and operated the mass spectrometer (Chapter 5.2.2). Protein mass spectrometry of Hyd-1 (Ch.4.2.4) was carried out on a system managed by Lingzhi Gong (Central Mass Spectrometry Facility, Department of Chemistry, University of Oxford), who also developed the relevant method (Ch.5.12). I devised the experiments, prepared the samples and analysed the data for all mass spectrometry work.

The characterisation of dimeric and monomeric Hyd-1 by cyclic voltammetry (Fig.3.13) was devised, planned and analysed by me and carried out by the visiting student Claudia Bielak (Institute of Microbiology, Martin-Luther University Halle-Wittenberg) under my supervision.

The incorporation of p-azido-L-phenylalanine (AzF) into Hyd-1 builds on work, creating *hyaA* TAG stop codon variants, carried out by myself previously as part of my Master thesis ([1], RWTH Aachen University). The pEVOL vector with the aminoacyl-tRNA synthetase/tRNA pair for AzF was kindly provided by Peter Schultz (Scripps Research Institute).

The *E. coli* MC4100 and MG1655 strains with his-tagged Hyd-1 (hyaA-his), that were used in this thesis for expression and purification of Hyd-1, were constructed and provided by Frank Sargent (College of Life Sciences, University of Dundee) along with MC4100ΔTM and the respective purified protein Hyd-1ΔTM.

Purification of native Hyd-1 was performed by Elena Nomerotskaia, except for the experiments shown in Fig. 3.4.

Contents

List of Abbreviations

A_λ	absorbance at wavelength λ
aaRS	aminoacyl-tRNA synthetase
ABTS	2,2'-azino-bis(3-ethylbenzthiazoline-6-sulphonic acid)
ADH	alcohol dehydrogenase
Ampliflu Red	10-acetyl-3,7-dihydroxyphenoxazine
AOX	alternative oxidase
AzF	p-azido-L-phenylalanine
BisTris	bis(2-hydroxyethyl)-amino-tris(hydroxymethyl)-methane
BN PAGE	blue native polyacrylamide gel electrophoresis
BSA	bovine serum albumin
Ch.	chapter
CV	cyclic voltammetry
cyt *c*	cytochrome *c*
DDM	n-dodecyl-β-D-maltopyranoside
DFT	density functional theory
Dimer	dimer of heterodimers
DNA	deoxyribonucleic acid
DTSP	3,3'-dithiodipropionic acid di(N-hydroxysuccinimide ester)
E	potential
$E^{0'}$	formal potential of an electrode
EPR	electron paramagnetic resonance
Fig.	figure
FMN	flavin mononucleotide
GMP	guanosine monophosphate

HRP	horseradish peroxidase
hyaA	Hyd-1 small subunit
Hyd-1	*Escherichia coli* Hydrogenase-1
IMAC	immobilized metal ion affinity chromatography
IRMS	isotope ratio mass spectrometry
MBH	membrane-bound hydrogenase
Methylene-H_4MPT	methylene-tetrahydromethanopterin
MHB	mixed hydrogenase buffer
Monomer	monomer of heterodimers
MOPS	3-(N-morpholino)propanesulfonic acid
NAD^+/NADH	nicotinamide adenine dinucleotide
Ni-NTA	Ni-nitrilotriacetic acid
PAGE	polyacrylamide gel electrophoresis
PFE	protein film electrochemistry
PGE	pyrolytic graphite edge
PISA Software	proteins, interfaces, structures and assemblies - software
Resorufin	7-hydroxy-3H-phenoxazine-3-one
RNA	ribonucleic acid
SAM	self-assembled monolayer
SDS	sodium dodecyl sulfate
SEC	size exclusion chromatography
SLAP	standard light antarctic precipitation
Tab.	table
Tat	twin-arginine translocation
TBTA	tris-(benzyltriazolylmethyl)amine
TCEP	tris-(2-carboxyethyl)phosphine
Tris	tris-(hydroxymethyl)aminomethane
tRNA	transfer ribonucleic acid (here used as suppressor in aaRS pair)
VSMOW	vienna standard mean ocean water
WT	wild type

XO	xylenol orange
$\Delta G^{\ddagger}$	standard Gibbs free energy of activation
ΔTM	(Hyd-1) variant without trans-membrane helix
D. gigas	*Desulfovibrio gigas*
E. coli	*Escherichia coli*
ω	rotation rate

List of Figures

List of Tables

Chapter 1

General Introduction

1.1 Hydrogenases

Hydrogenases are the metalloenzymes that catalyse the interconversion of hydrogen and protons: $2H^+ + 2e^- \rightleftharpoons H_2$. For this reaction, the hydrogenases have proven to be extremely efficient, highly selective, molecular electrocatalysts with minimal activation energies (an electrocatalyst couples the chemical transformation in a catalysed redox 'half reaction' to electron transfer at an electrode) [2, 3]. Unlike surface electrocatalysts such as platinum or any *synthetic* molecular electrocatalysts discovered so far, a subset of hydrogenases is able to carry out H_2 catalysis in the sustained presence of O_2. The aim of this thesis is to elucidate the core principles that enable this O_2-tolerant H_2 catalysis in *Escherichia coli* Hydrogenase-1.

1.1.1 Active Site Structure

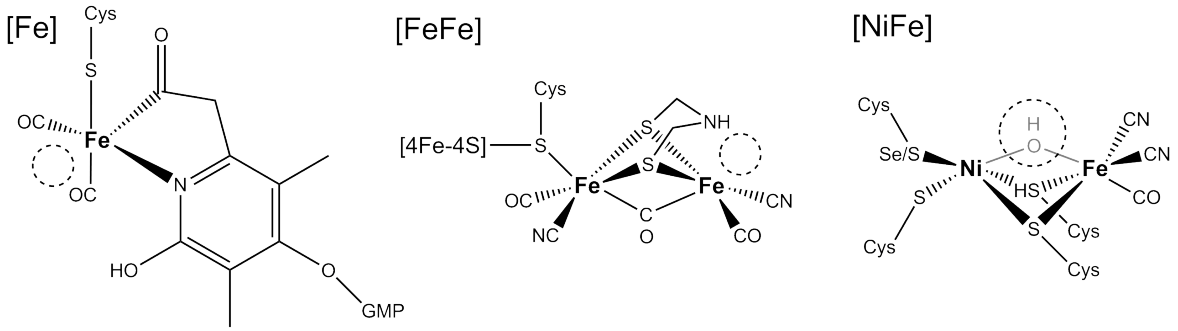

Figure 1.1 Hydrogenase Active Sites: Three principal hydrogenase active site configurations ([Fe], [FeFe] and [NiFe]) are known. Being a product of convergent evolution, they share a common motif of a low spin Fe(II) ligated by CO. The dashed circles indicate open sites for substrate binding. The [NiFe] active site is depicted with a briding -OH ligand (grey) occupying the binding site in the inactive Ni-B state. (GMP = guanosine monophosphate)

The known hydrogenases are commonly grouped into the three major classes [Fe], [FeFe] and [NiFe], according to their active site metal content [4]. These different classes of hydrogenase are an excellent example of convergent evolution, having evolved separately, sharing neither sequence similarity nor maturation proteins, yet catalysing the same reaction [4]. Intriguingly they do so using a common minimal active site motif. Referring to Figure 1.1, this minimal active site motif consists of a low spin Fe(II) ligated by CO (and effectively also CN^-, as the back-bonding properties of the 2-pyridinol ligand in [Fe] hydrogenase are considered to be functionally equivalent to CN^- [5, 6]). Both

CO and CN^- are biologically unique ligands and require special biosynthetic pathways and assembly. One such pathway, sourcing the CN^- from carbamoyl phosphate has been identified in *E. coli* [7]. The convergent evolution of this common motif in three instances and with such unusual ligands suggests an essential role for CO and CN^- in enabling effective hydrogen activation in complexes with the first row transition metals Fe and Ni, *e.g.* through π-acceptor properties [8].

In [Fe] hydrogenase one Fe is ligated by a pyridinol ligand and is thus part of the iron-guanylylpyridinol (FeGP) co-factor, while the substrate methenyl-H_4MPT^+, found in close proximity, is the hydride acceptor [5, 9, 10]. The active site of [FeFe] hydrogenases comprises the di-iron center and a directly attached [4Fe-4S] cluster, together forming what is known as the H-cluster. The bridgehead nitrogen atom depicted is thought to function in proton extraction and has been shown to be effective in model complexes [11, 12, 13]. In the [NiFe] hydrogenases substrate binding occurs at the Ni, while the Fe is spectroscopically observed to be redox inactive [14, 15]. The presence of the bridging hydroxide is dependent on the Ni oxidation state, see Ch. 1.1.3 and 1.1.4. A Ni-ligating cysteine is replaced by a selenocysteine in the subgroup of [NiFeSe] hydrogenases [16].

1.1.2 Protein Function and Structure

While the active sites of the known hydrogenase classes are highly conserved across species and physiological roles, the protein structures may vary greatly from organism to organism and with the individual function of the hydrogenases, *i.e.* its redox partner and location in the organism.

[Fe] Hydrogenases

The homodimeric [Fe] only hydrogenases are found in methanogenic archaea, along with [NiFe] hydrogenases. In cells grown under nickel limitation, a [Fe] hydrogenase can replace a ferredoxin-reducing [NiFe] hydrogenase; despite the fact that the $K_M(H_2)$ of [Fe] hydrogenases is 20 fold higher than that of the respective [NiFe] hydrogenase, these cells then exhibit a 40 times higher specific activity [17]. The [Fe] hydrogenases require their substrate methenyl-H_4MPT to catalyse the exchange of H^+ into H_2 [18].

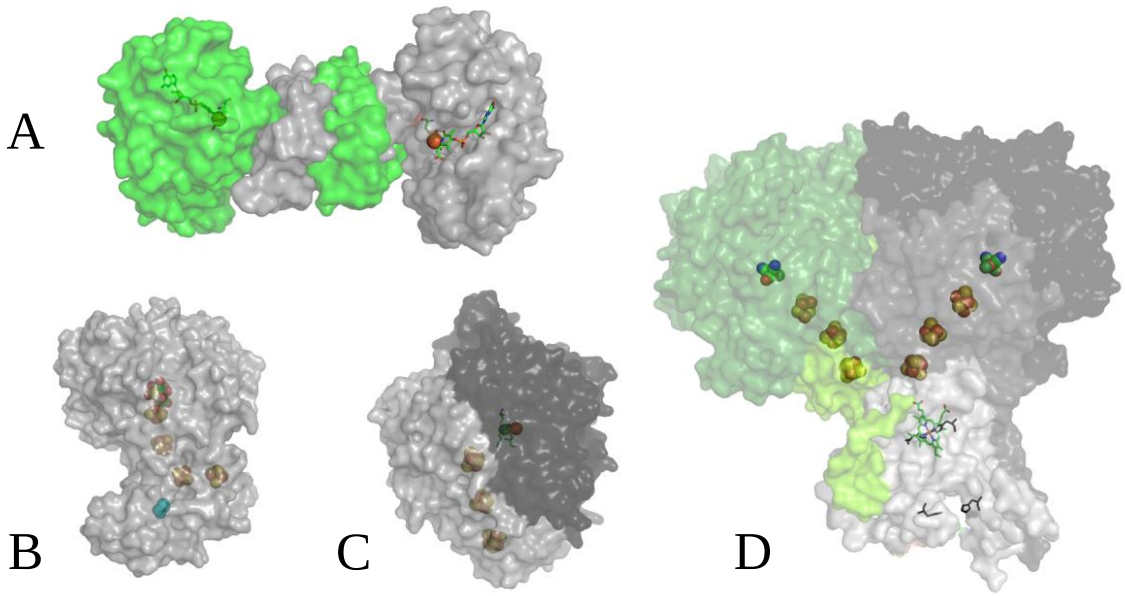

Figure 1.2 Hydrogenase Crystal Structures: A) [Fe] hydrogenase *Methanocaldococcus jannaschii* (PDB: 3DAG) **B)** [FeFe] hydrogenase *Clostridium pasteurianum* (PDB: 1FEH) **C)** [NiFe] hydrogenase *Desulfovibrio fructosovorans* (PDB: 1FRF) **D)** [NiFe] hydrogenase *E. coli* (PDB: 4GD3). Illustrations were created using Pymol.

[FeFe] Hydrogenases

The [FeFe] hydrogenases are found in anaerobic prokaryotes, *e.g. clostridia* and sulfate-reducing bacteria, as well as in lower eukaryotes. [FeFe] hydrogenases are in fact the only kind of hydrogenase found in eukaryotes and are exclusively located in cell organelles, *i.e.* hydrogenosomes and chloroplasts [4]. [FeFe] hydrogenases are bi-directional, usually utilised in hydrogen evolution, and have high turn-over rates on the order of 6000-9000 s^{-1} [19]. Electrons are delivered *via* ferredoxins and the simplest [FeFe] hydrogenases, found in green algae, are monomeric and contain only the H-cluster and no further FeS clusters or other relay centers [19]. The clostridial [FeFe] hydrogenases are also monomeric, but contain a varying number of additional FeS clusters and an intrinsic ferredoxin-like domain [11]. A crystal structure of *Clostridium pasteurianum* (CpI) hydrogenase is shown in Figure 1.2B. Multisubunit [FeFe] hydrogenases, such as the NADH-dependent hydrogenases in the thermophilic bacterium *Thermotoga maritima* [20], are also known but are structurally insufficiently characterised to date.

[NiFe] Hydrogenases

The [NiFe] hydrogenases are abundant among the prokaryotes (and archaea) and fulfil a plethora of roles. [NiFe] hydrogenases are multisubunit enzymes in which a main subunit, housing the buried [NiFe] active site, is attached to at least one smaller subunit, containing electron relay centers, thus forming a common heterodimeric assembly (Fig. 1.2C). Through phylogenetic analysis, Vignais and Billoud found that the evolution of [NiFe] hydrogenases could be understood by grouping them into four sub-classes (I-IV), according to the development of physiological function [4].

I) Membrane-bound respiratory H_2-uptake hydrogenases carry out hydrogen oxidation linked to quinone reduction. The final electron acceptors can vary, depending on the organism and environmental conditions; examples are fumarate, CO_2, SO_4^{2-} and NO_3^- in anaerobic respiration or O_2 in aerobic respiration (see Chapter 1.3). Uptake hydrogenases are attached to the periplasmic side of the (inner) membrane and connected to the quinone pool through cytochromes (see Figure 1.2D). *E. coli* Hyd-1, together with other hydrogenases such as *R. eutropha* and *H. marinus* MBH, belongs to the subgroup of O_2-tolerant membrane-bound respiratory hydrogenases; their special properties are discussed in detail in Chapters 1.1.4, 2 and 3.

II) Cytoplasmic [NiFe] H_2 uptake and sensory hydrogenases are not respiratory and lack a translocation signal peptide. The uptake hydrogenases in this group have been implicated in N_2 and CO_2 fixation [21, 22]. The H_2 sensory hydrogenases, such as *R. eutropha* RH [23], exhibit very low turn-over rates, regulate the expression of uptake hydrogenases depending on the availability of H_2, and have also been found to be relatively insensitive to oxygen. Study of this ability has led to consideration of restricted O_2 access through gas channels as a contributing factor in O_2-tolerance [24] (Ch.1.1.4). No crystal structures are available yet, but it is known that, like the uptake hydrogenases, the regulatory hydrogenases consist of at least one large [NiFe] subunit and a smaller FeS cluster-containing subunit. Two [2Fe-2S] clusters and a putative [4Fe-3S-3O] cluster have been proposed [25]. While it is not clear how these clusters

are involved in signal processing, or maybe even O_2 insensitivity, the first step in the H_2-sensing signal cascade crucially depends on the presence of a multimeric assembly of two large and two small subunits; this assembly is necessary for complex formation with a histidine protein kinase [25].

III) The third group comprises the bidirectional heteromultimeric cytoplasmic hydrogenases, in which the heterodimeric hydrogenase module is connected to further subunits that bind soluble co-factors; examples are NAD or the flavin derivative F_{420} (8-hydroxy-5-deazaflavin). A relatively well understood representative is the soluble NAD^+-dependent hydrogenase (SH) from *R. eutropha*, though no crystal structure is available. The enzyme is termed bidirectional as it can carry out NAD^+ reduction or NADH fuelled H_2 evolution. Through this function the SH has been shown to operate as an electron valve during the transition from aerobic to anaerobic growth of *R. eutropha* cultures [26]. The NADH dehydrogenase subunit, homologous to the NADH oxidising hydrophilic core subunits of respiratory Complex I, contains Fe-S, FMN and NAD(P) binding sites [27, 28].

IV) The H_2-evolving, energy conserving, membrane-associated hydrogenases reduce protons at low potential to dispel reducing equivalents derived from oxidation of organic C_1 molecules, *i.e.* formate and CO. An example from *E. coli* is Hyd-3, which is part of the formate hydrogenlyase complex (FHL). The complex consists of five to six subunits with sequence homology to Complex I [29]. Oxidation of formate to CO_2, H^+ and electrons is carried out by the formate dehydrogenase subunit, utilising molybdopterin guanine dinucleotide as cofactor. The FeS clusters in the smaller subunits relay electrons from formate oxidation to the large [NiFe] active site subunit where H^+ reduction to H_2 takes place. Indeed, almost all H_2 in *E. coli* is produced in this way [30]. The complex is associated with the membrane through interaction with membrane-integral subunits but is not anchored into the membrane itself [31].

1.1.3 Hydrogen Catalysis and [NiFe] Active Site States

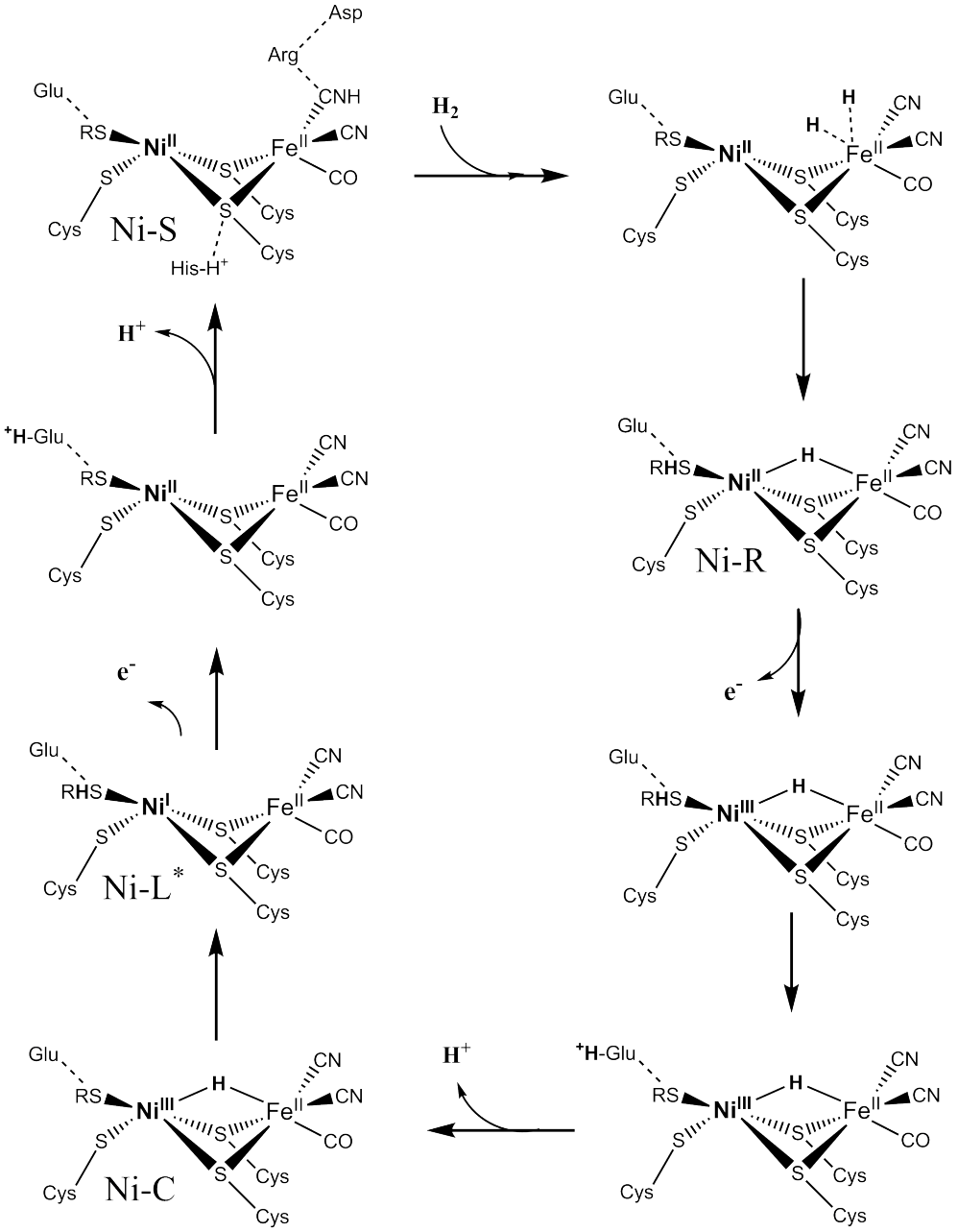

Figure 1.3 Mechanism of the Catalytic Hydrogen Oxidation Cycle of [NiFe]-hydrogenases, as proposed by Siegbahn *et al.* [32]. While the proposed proton acceptor Glu is shown through-out, the other amino acid residues thought to be important are only shown in the first structure for simplicity.

The active site of [NiFe] hydrogenases can be found in a number of different spectroscopically identifiable states, most of which are part of the hydrogen catalytic cycle while others are aerobic or anaerobic oxidation products. The full catalytic H_2 cycle has not been solved definitively, especially with regard to unstable intermediate states. Figure 1.3 shows a plausible H_2 oxidation cycle, devised by Siegbahn and co-workers

and based on density function theory (DFT) calculations [32]. The involvement of the specific amino acid residues shown is not certain.

The transition between the different active site states of [NiFe] hydrogenases is potential dependent, as shown in Fig.1.4. The states are defined by the active site Ni, while the Fe has been found to stay in a low-spin Fe(II) state, as determined by EPR, ENDOR and Mössbauer spectroscopy [33, 34, 35]. The Ni(II) states are EPR silent, while Ni-C, and the oxidised states Ni-A and Ni-B most relevant to this thesis, are visible ($S = 1/2$) [36]. The unusual active site ligands CN^- and CO offer the possibility, through their stretch frequencies, to study interactions at the Fe by FT-IR.

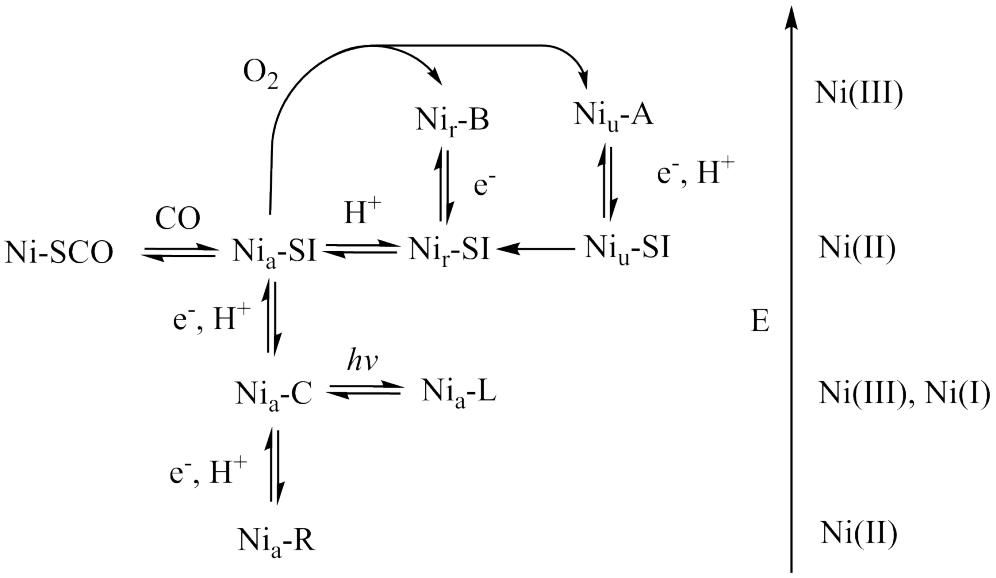

Figure 1.4 [NiFe] Hydrogenase Active Site States: Transitions are potential dependent as shown. Subscripts indicate enzyme: *a* available or active for hydrogen catalysis, *r* 'ready' for fast reactivation, *u* 'unready' for reactivation.

Ni-C, Ni-R and Ni_a-SI are undisputed catalytic intermediates and it is the latter state that is prone to potentially damaging O_2 attack. Reductive reactivation of Ni-A and Ni-B to Ni_a-SI proceeds *via* intermediate 'ready' and 'unready' Ni-SI states. Binding of the reversible inhibitor CO, the affinity for which varies greatly between different hydrogenases, can prevent reaction of Ni-S with O_2 [37]. The Ni-L state, included in the catalytic cycle as the Ni-C deprotonation product, can be formed reversibly at low temperatures by illumination [38]. The significance of the latter observation is still unclear and the occurrence of Ni-L as a catalytic state disputed, but recent studies on *E. coli* Hyd-1 suggest a low energy barrier and physiological relevance of this state [39].

Ni-A and Ni-B are generated either by reaction with O_2 or, at least in the case of Ni-B, can also simply be formed at very oxidising potentials (one recent study also suggests the possibility of anaerobic Ni-A formation) [40]. Both states are inactive for H_2 catalysis and have been shown to contain bridging ligands; in the case of Ni-B a hydroxide (as shown in Fig.1.1) and in the case of Ni-A possibly a peroxide [41, 14]. The Ni-B state is easily reduced to Ni-S (which can again partake in H_2 catalysis) and preferential formation of Ni-B over Ni-A is essential to oxygen tolerance, as discussed in Ch.1.1.4.

1.1.4 Oxygen Tolerance

The minimal active sites of hydrogenases contain low-spin Fe (II or I) coordinated by CO, CN^- and thiolate ligands (Ch.1.1.1), a combination expected to be unstable under aerobic conditions: indeed, most hydrogenases suffer long-term or permanent inactivation when exposed to even traces of O_2. It is therefore of special interest that certain [NiFe]-hydrogenases have evolved to sustain H_2 oxidation in the continued presence of O_2, without inactivation - this ability is termed O_2-tolerance.

Any useful definition of O_2-tolerance will require that an enzyme, in the sustained presence of substantial concentrations of O_2, must both maintain a significant level of catalytic activity and do so for a prolonged period of time.

To illustrate the different structural and mechanistic principles of O_2-tolerance, the hydrogenases may be helpfully divided into three groups with regard to their response to oxygen: (i) fragile ([FeFe]), (ii) stable (low potential [NiFe] and [NiFeSe]) and (iii) tolerant (high potential [NiFe], special FeS cluster, H_2 oxidation).

As a general rule, the stable and tolerant hydrogenases form oxidised states at the active site in response to oxygen attack, which (in principle) can be reactivated reductively; these states were introduced above in Ch.1.1.3 as deviations from hydrogen catalysis and are important for understanding the following remarks.

Fragile Hydrogenases

The [FeFe] hydrogenases are easily damaged by O_2 and H_2 oxidation activity is irreversibly lost by exposure to even low levels of O_2 [42]. Based on X-ray absorption experiments, the degradation reaction is proposed to proceed via initial O_2 binding to the distal iron of the active site (Fe_d) in the oxidised state (H_{ox}); this reaction generates reactive oxygen species, likely OOH and H_2O_2, which attack the Fe and cysteine ligands of the [4Fe4S] part of the H-cluster [43, 44]. As a result the cluster converts to a [3Fe4S] cluster, which, in analogy to the [4Fe4S] cluster in oxygen sensing FNR protein [45], would then degrade further.

The initial binding of O_2 is similar to the (much faster) binding of the reversible inhibitor CO. Indeed, exposure of active enzyme to CO first, preserving it in an inactive state, can prevent most, though not all, of the damage caused by subsequent O_2 exposure [46, 42]. In a similar fashion enzyme purified in inactive form (H_{ox}inact) remains largely structurally intact in the presence of oxygen [47]. Even under electron rich reducing conditions, when producing H_2, substantial activity loss can be observed within minutes in the presence of O_2 [48].

Stable Hydrogenases

Unlike the [FeFe] hydrogenases, the [NiFe] hydrogenases respond to O_2 attack by forming, to a certain degree, reversibly inactivated states from which activation can either be slow (then termed 'Unready' or Ni-A), or rapid ('Ready' or Ni-B).

In the inactive form, these enzymes are stable in the presence of O_2 for extended periods of time. At low potentials, [NiFe] hydrogenases are reported to be structurally stable in the presence of O_2 even when active, *i.e.* during H_2 production. For example, the [NiFeSe]-hydrogenase from *Desulfomicrobium baculatum*, containing a selenocysteine in place of a terminal cysteine ligand at the active site, retains significant reductive activity over several minutes of O_2 exposure at -0.45 V (vs. SHE). In addition, most of the enzyme activity can be regained upon removal of O_2 from the atmosphere,

demonstrating very little irreversible damage [49]. However, the extent of activity decrease is very responsive to the O_2 concentration, so that at only 1% O_2 more than half the activity is temporarily lost in the *D. baculatum* [NiFeSe]-hydrogenase.

It is further important to consider what fraction of reducing equivalents is channelled to H^+ reduction *vs.* to the competing O_2, the latter quickly becoming the dominant reaction: while the low potential, NAD^+-reducing, soluble hydrogenase (SH) from *Ralstonia eutropha* H16 retains some NADH fuelled H^+ reducing activity in O_2 atmospheres as high as 40%, the O_2 reduction rate ($1.6\,s^{-1}$) is then found to be 15-fold higher than the corresponding H_2 production rate ($0.11\,s^{-1}$) [50]. Substrate specificity is clearly a great challenge at very negative potentials.

The availability of electrons determines the relative distribution of 'Ready' and 'Unready' states formed in response to O_2 in such a way, that at more oxidising potentials a greater proportion of Ni-A is observed [51]. The equilibrium potential (see E_{switch} Ch.1.1.4) for conversion of inactive to active states varies between different enzymes, as do the reactivation rates [52]. In the low potential and H_2 producing [NiFe] hydrogenases, this conversion is found at relatively negative potentials, close to the H^+/H_2 equilibrium potential [53, 54]. These low potential hydrogenases are therefore not able to reactivate effectively under H_2 oxidising conditions and sustained catalysis is not possible. When the reactivation potential is more positive, accumulation of slowly reactivated Ni-A state eventually leads to effectively arrested activity [55]. Ensuring exclusive Ni-B formation and reactivation at high potential is therefore required for sustained H_2 oxidation (see tolerant hydrogenases below).

Tolerant Hydrogenases

Sustained and specific H_2 catalysis in the presence of O_2 at oxidising potentials is found in a subset of respiratory, membrane-bound [NiFe] hydrogenases, which couple H_2 oxidation to quinone reduction. The most studied examples are the membrane bound hydrogenase (MBH) from *Ralstonia eutropha* [56] and Hyd-1 from *E. coli* [57]. The key difference between tolerant and merely stable hydrogenases is the ability to strictly

avoid formation of 'Unready' active site states, such as Ni-A (Ch.1.1.3), which are taken out of the catalytic cycle for a long time, and to form only those that can be reactivated rapidly (Ni-B) [58, 59]. The following paragraphs explain the contributing factors to oxygen tolerance in more detail.

Gas Channels

Early models of oxygen tolerance, based on computational and crystallographic analysis of O_2-sensitive hydrogenases, involved gas channels acting as selective filters for the access of small molecules to the enzyme's active site and preventing oxygen attack in the first place [11]. While it could be shown that enlarging these proposed channels in a regulatory hydrogenase from *Rhodobacter capsulatus* decreased O_2-tolerance [60], a restriction of these channels could not be shown to have any positive effect on O_2-tolerance. It emerged that such channels could not explain the extent of O_2-tolerance observed in membrane bound [NiFe] hydrogenases and that formation of reactivateable states (at the [NiFe] active site) upon O_2 attack is a fingerprint of O_2-tolerance.

Substrate Affinity

The affinity of the active site for H_2, as apparent in low K_m values, had also been considered as playing a potential role in O_2-tolerance, *i.e.* Michaelis-complex formation might protect the active site from oxygen attack. This concept has since been ruled out as a defining factor of O_2-tolerance, since $K_m(H_2)$ and O_2-tolerance do not follow the same temperature dependence and because the $K_m(H_2)$ is not vastly different between O_2- tolerant and -sensitive enzymes [58]. A high H_2 affinity is likely helpful in catalysing H_2 oxidation in the presence of O_2, but it is by no means sufficient to confer O_2-tolerance. As discussed for the O_2-stable hydrogenases above, the greatest unsolved challenge for specific catalysis of H_2 over binding of O_2 exists at very negative potentials.

The Switch Potential E_{switch}

The apparent potential for reactivation of the inactive species Ni-B (as illustrated in Fig.1.8A) is commonly referred to as E_{switch}, the latter strictly being defined as the minimum of the first derivative of a (slow) scan from high to low potential, after (aerobic or anaerobic) Ni-B formation. As such it is a thermodynamic parameter of Ni-B interconversion and indeed has recently been shown to match the midpoint potential for Ni-B to Ni-SI conversion, as determined by EPR and FT-IR (potentiometric) titrations; the process also exhibits a one electron reduction step as expected for this reaction [61]. Since the reactivation *rate* is the crucial determinant in the electrochemical method, great care must be taken to conduct the experiment as close to equilibrium as possible, and therefore at a very low scan rate, when accurately measuring E_{switch}. Confusion on this issue has led some in the past to see E_{switch} as merely a kinetic parameter and as separate from E_{mid}(Ni-B) [62].

Since E_{switch} determines the potential at which inactive enzyme in the Ni-B state can be reactivated, it determines the available activity window, *i.e.* the potential range between the H^+/H_2 equilibrium potential (or onset potential, Ch.1.4.2) and E_{switch}, for a given enzyme.

The more negative of E_{switch} a chosen applied potential is situated, the faster reactivation of Ni-B will be. Accordingly O_2-tolerant hydrogenases are found to generally have a higher E_{switch} [52, 37] and a *Desulfovibrio fructosovorans* hydrogenase variant with faster reactivation exhibited enhanced O_2 tolerance [63].

Proximal FeS Cluster

The understanding of the ability of O_2-tolerant hydrogenases to avoid the formation of 'Unready' states has recently advanced significantly following the publication of the first crystal structures of O_2-tolerant hydrogenases [64, 65, 66] (Section 1.1.2). All known [NiFe] hydrogenases consist of large α subunits, containing the [NiFe] active site, and small β subunits, containing relays of iron sulphur clusters that connect the buried

active site to redox partners at the enzyme surface. It is this FeS cluster relay that differs significantly between O_2 -tolerant and -sensitive hydrogenases. Oxygen-tolerant hydrogenases contain a thus far unique [4Fe-3S] cluster proximal to the active site, ligated by two additional cysteines, as compared to the [4Fe-4S] cluster in O_2-sensitive hydrogenases (Fig.1.5). This special structure is be able to undergo two, instead of one, redox transitions at similar potential. Abstraction of the second electron yields an unusual Fe-N (peptide) bond in a reaction that is, locally at least, electroneutral [65, 66, 64, 56]. The presence of this special cluster is essential: removal of the supernumerary cysteines involved in the cluster rearrangement eliminates O_2-tolerance [57].

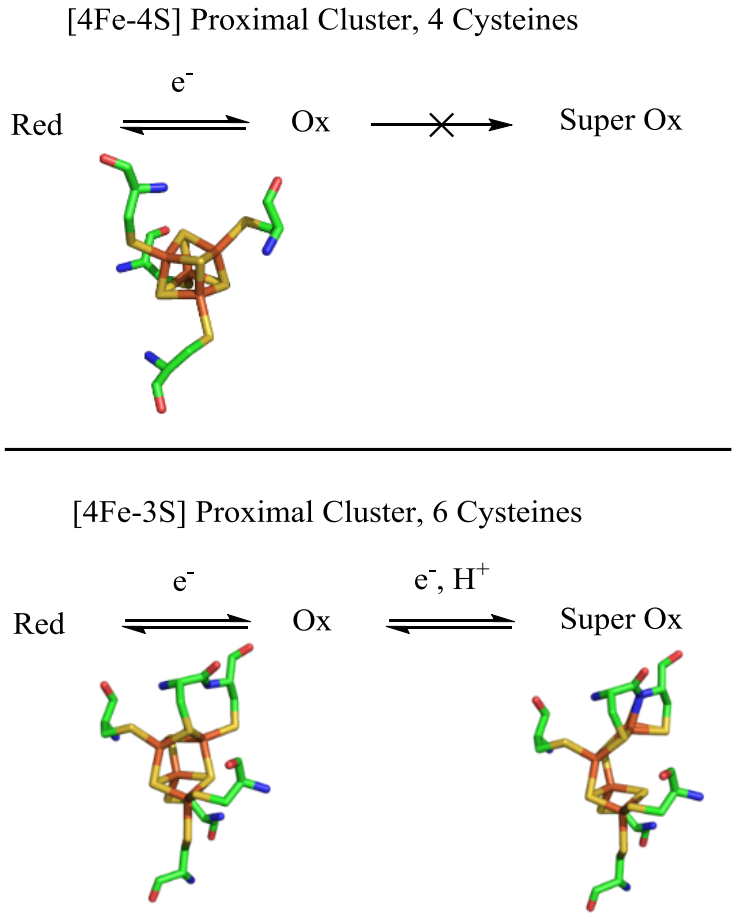

Figure 1.5 [NiFe] Hydrogenase Proximal Clusters: A [4Fe-4S] cluster ligated by four cysteines may undergo one electron transfer reaction without significant conformational change (top, [NiFe]-hydrogenase from *Desulfovibrio fructosovorans*, PDB: 1FRF). The special [4Fe-3S] cluster, found in membrane-bound O_2-tolerant hydrogenases, is ligated by six cysteines and able to undergo a second, proton coupled, electron transfer, which is accompanied by formation of a Fe-N(peptide) bond (bottom, *E. coli* Hyd-1 reduced and super oxidised, PDB: 3UQY and 3USC). The figure was created using PyMOL and reprinted with permission from reference [67] (Wulff *et al.*).

Medial FeS Cluster

The [3Fe-4S] medial cluster in class I [NiFe] hydrogenases has a higher reduction potential in O_2-tolerant hydrogenases (*e.g.* 190 ± 30 mV at pH 6 in *E. coli* Hyd-1 [39]) than in standard hydrogenases (*e.g.* -70 mV at pH 7 in *D. gigas* hydrogenase [68]). It is thought that a higher reduction potential increases availability of electrons near the active site, which can be rapidly supplied in the case of oxygen attack. To test this hypothesis, mutants with [4Fe-4S] medial clusters, which have much lower reduction potentials (*e.g.* -250 mV) than the native [3Fe-4S] clusters [69, 70], were created by changing a ligating proline to a cysteine, as found in class I [NiFeSe] hydrogenases. These mutants showed almost no change in hydrogen catalysis [70] and still exhibited significant tolerance to transient oxygen exposure, but were not able to sustain activity in the continued presence of oxygen [71].

1.2 *E. coli* Hyd-1 Expression

E. coli expresses three known hydrogenases, all of which are either integrated or bound to the inner membrane: Hyd-1 and Hyd-2 are generally viewed as H_2 oxidisers and both face the periplasm, while Hyd-3 produces H_2 (exclusively) from formate [72, 73]. The latter works in concert with the formate dehydrogenase (FDH), forming the membrane-anchored formate hydrogen lyase (FHL) complex, and faces the cytoplasm. Based on sequence similarity with FHL, a fourth putative Hydrogenase-4 has been identified but not isolated to date [74].

While Hyd-1 and Hyd-2 are both able to oxidise H_2, the actual physiological role of Hyd-1 is unknown and the expression patterns of the two enzymes vary significantly. Hyd-2 is expressed during exponential growth (with non-fermentable carbon sources), functions in anaerobic respiration and is responsible for recycling of the H_2 produced by Hyd-3 [75, 76, 77, 30]. Deletion of the *hyb* operon, coding for Hyd-2, eliminates the ability of *E. coli* to grow on H_2/fumarate medium [78].

Hyd-1, on the other hand, is expressed during growth on fermentable sugars, during the stationary phase of a batch culture and, like Hyd-2 though to a lesser degree, can also be found when the organism is grown on glycerol and fumarate [79, 80]. Transcription of Hyd-1 is induced by a shift from aerobic to anaerobic growth and as such is regulated by ArcA and AppY [80, 77, 81, 82]. The *hya* operon (Hyd-1) is up-regulated during carbon (and phosphate) starvation, a process which for Hyd-1 depends on the regulator σ^s which also governs the transition into stationary phase. The *cbdAB-appA* operon of the cytochrome *bd*-II is co-expressed with Hyd-1 under these conditions and also depends on the transcriptional activator AppY, suggesting a possible respiratory role in cooperation with Hyd-1 [83].

The maturation process of Hyd-1 is very complex, largely owing to the coordinated insertion of the unusual CN^- and CO ligands into the active site and their respective biosynthesis pathways [73, 7]. Insertion of nickel is the last step in active site assembly and serves as the signal for cleavage of a C-terminal peptide sequence on the large subunit; the subunit closes around the active site as a result [84]. As a periplasmic membrane protein Hyd-1, assembled and folded in the cytoplasm, requires translocation across the membrane; this is achieved *via* the twin-arginine translocation pathway, for which the Hyd-1 small subunit precursor protein carries a signal peptide at the extreme N-terminus [85]. The twin-arginine motif at the n-/h-region boundary of this signal peptide in HyaA is [T-R-R-S-F-L-K], where underlined letters indicate agreement with the general consensus twin-arginine motif within known Tat signal sequences.

To ensure the expression of functional enzyme, it is crucial that cofactor insertion into both subunits is complete and, since the signal peptide is only located on the small subunit, the heterodimer is formed before the protein is exported. This integrity check or 'proofreading' ability is likely carried out by chaperone molecules, and HyaE has been identified to play such a role for Hyd-1 [86]. The Tat signal sequence also plays a crucial role here: Replacement of the signal peptide on HybO (Hyd-2 small subunit) with a Tat signal from another *E. coli* protein allowed continued translocation of the small subunit, but mostly without attached HybC (large subunit) [87]. The result is a large amount

of dysfunctional protein. The realisation, that identification of the chaperones' cognate proteins is at least in part dependent on the Tat signal peptide, explains the high degree of variation found across all the different Tat sequences, while only some core motifs are kept constant: Individual 'proofreading' followed by universial (or collective) use of the translocation machinery (TatABC) can be encoded by the same signal. After successful transport across the membrane in a proton-motive-force-dependent process, the signal sequence is eventually cleaved off [85].

1.3 Respiration in *E. coli*

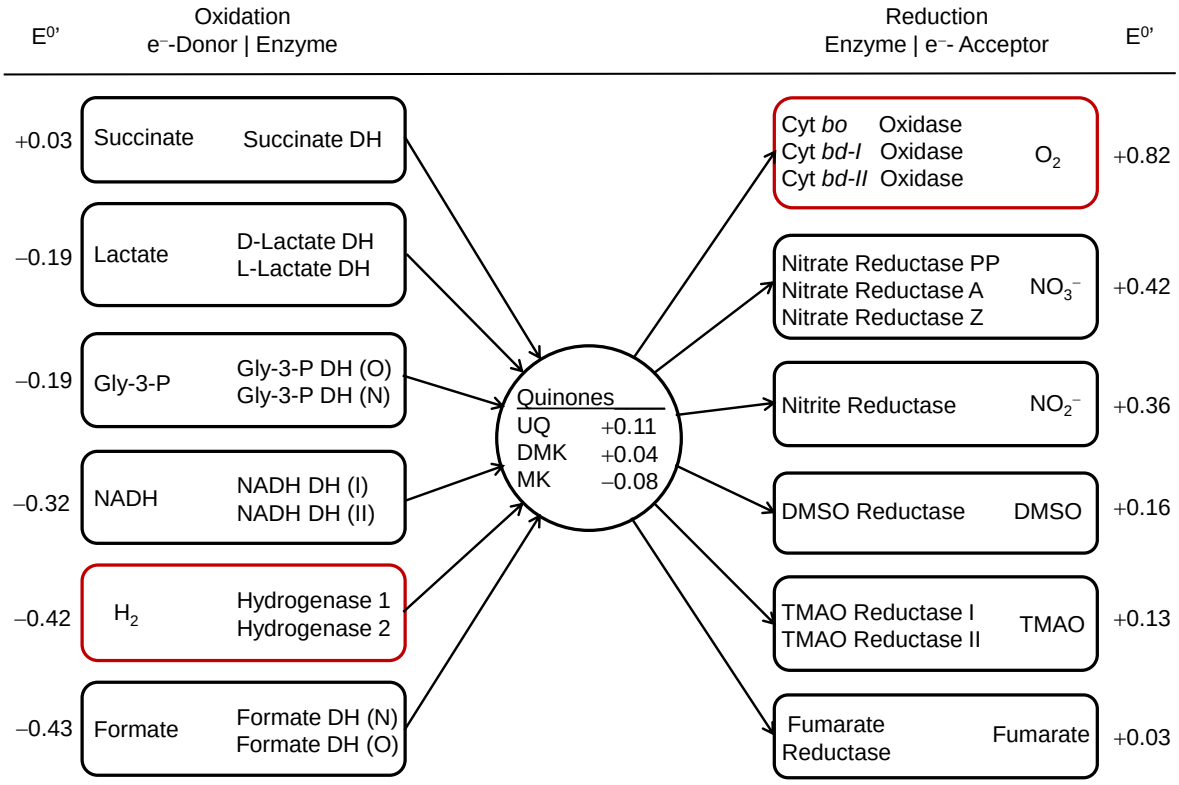

Figure 1.6 Respiration in *E. coli* with various substrates: The primary dehydrogenases are shown with their substrate molecules on the left. Electrons from the oxidation reaction are passed through the quinone pool in the membrane to terminal reductases and their respective electron acceptors [88]. $E^{0'}$= standard biological reduction potential for the respective redox couple (e.g. NAD^+/NADH) [89], DH = dehydrogenase, Cyt = cytochrome, UQ = ubiquinone, DMK = demethylmenaquinone, MK = menaquinone, DMSO = dimethyl sulfoxide, TMAO = trimethylamine N-oxide. The most relevant substrates (H_2 & O_2), for the purpose of this thesis, are highlighted in red.

Respiration in *E. coli* can be very complex and adaptive. As shown in Fig.1.6 several different electron donors and acceptors can be used and iso-enzymes exist for

most substrates [88]. In the (inner) membrane, a quinone 'pool' of varying composition connects the two ends of the electron transfer chain. Menaquinone (MK) and demethylmenaquinone (DMK) have relatively low midpoint potentials and are involved in anaerobic respiration, while ubiquinone, with a higher midpoint potential, is involved in aerobic and nitrate respiration [90]. The redox state of this quinone pool is linked to expression control of the involved respiratory proteins through the two component ArcAB system [91, 92].

Energy released by the oxidation of electron donors is conserved, *i.e.* made available for use by the organism, in the form of a proton electrochemical gradient (Δp), by coupling the electron flow along the respiratory chain towards the electron acceptors to proton translocation across the membrane. In general, protons may be translocated across the membrane either directly by active 'pumping', which is one of the mechanisms by which cytochrome *c* oxidase (an enzyme not present in *E. coli*) operates [93]; or indirectly by quinone/quinol cycling and redox loops. In such a redox loop, oxidation and reduction of the electron donors and acceptors (substrates), and/or quinones, on opposite sides of the membrane results in net proton transfer. Many respiratory enzymes employ membrane-intregral (di-*b*-heme) cytochromes to mediate such electron transfer with the quinone pool, which often allows the active site to be located on one side of the membrane and the quinone binding site on the other [94]. Both substrates relevant to this thesis (H_2 & O_2 highlighted in red in Fig.1.6) are processed by enzymes that interact with the quinone pool *via* *b*-type cytochromes. Complex I, on the other hand, (containing NADH dehydrogenase) oxidises NADH by reduction of flavin mononucleotide (FMN) and transfers electrons along its internal FeS cluster chain to the membrane interface where reduction of quinone activates (through an unknown mechanism) proton transfer by membrane integral proton pumping subunits [95, 96]. Superoxide (and H_2O_2) are also produced in the process, by reaction of O_2 with reduced FMN [97, 98]. *E. coli* expresses three different terminal cytochome oxidases for reduction of O_2: The cytochrome $bo_{(3)}$ oxidase operates under high O_2 levels and is a proton pump, while the cytochrome *bd* oxidases are both high affinity oxidases with a $K_m(O_2)$ in the range of 3-8 nM and at least *bd*-I contributes to Δp through substrate (O_2) reduction in the

cytoplasm [99, 100, 101, 102]. Microbial communities often live in environments where transition zones exist with a gradient of substrate concentrations; here fine-tuning of the respiration machinery can be hugely beneficial. The gastrointestinal tract of animals is a good example of such an environment, in which an O_2 gradient develops as diffusion from the surrounding tissue towards the lumen is exceeded by O_2 consumption [103]. In these transition zones, where H_2 is also present in *E. coli*'s native environment, microaerobic conditions exist under which the Cyt *bd* oxidases are able to operate [101, 104, 105, 103]. So, while expression of *E. coli* Hyd-1 is induced by a shift from aerobic to anaerobic growth (see Ch.1.2), not using an O_2-tolerant hydrogenase for respiration under such microaerobic conditions would appear to be quite the missed opportunity. The so called 'Knallgas bacteria', such as *Ralstonia eutropha*, are well known to carry out H_2/O_2 respiration [58].

1.4 Protein Film Electrochemistry

Protein film electrochemistry (PFE) is a technique in which (metallo) proteins are attached to an electrode in order to, either, study simple redox transitions as pioneered by Hill and Kuwana [106, 107] with cytochrome *c* or, indeed, catalysis in redox enzymes. The proteins can either be linked specifically,*e.g.* covalently, or can more commonly be simply adsorbed onto an electrode. Carbon electrodes are frequently used in the latter case and exposed functional groups, such as -COOH and -COH on the edge plane of pyrolytic graphite, are understood to aid this adsorption [108]. In either case, a 'film' of protein is formed on the electrode surface, the electron transfer to which is controlled directly by the applied potential (see Fig.1.7). The use of a rotating electrode allows for control of diffusion, and thus also avoidance of diffusion as a rate limiting step in catalytic investigations.

Prior to the development of PFE, electrochemical protein studies required protein solutions of very high concentrations; they also required mediator molecules to 'shuttle' electrons between the proteins and the electrode, with the implication that diffusion

would also invariably limit electron transfer. The use of mediators also restricted the potential sensed by the proteins to the redox potential of whatever mediator, or mix thereof, was used.

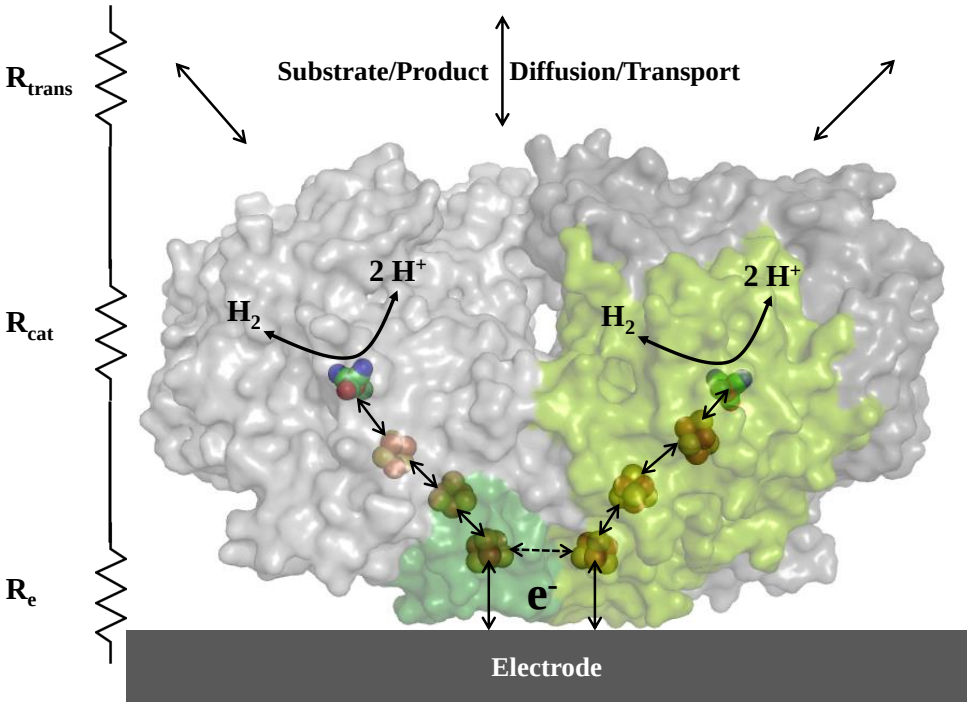

Figure 1.7 Schematic Representation of Protein Film Electrochemistry: The protein (here *E. coli* Hyd-1 (PDB:3UQY)) is adsorbed onto the electrode. The applied potential controls electron transfer to, and from, the protein and. In the case of an adsorbed *enzyme*, catalysis can be driven in this way, as shown for hydrogen interconversion. Rate, and therefore current, limiting steps are conceptualised as resistors: R_{trans} substrate and product transport to and from the electrode, R_{cat} catalytic turnover and internal electron transfer, R_e interfacial electron transfer between electrode surface and enzyme [109].

1.4.1 Electrochemical Basics

The following introductory deliberations and derivations are based on, and adapted from, the comprehensive text book by Bard and Faulkner [110] and will establish how electrochemical reactions at an electrode can be described at a basic level. In this regard, the most relevant questions to this thesis are how electrochemical reactions are defined at equilibrium and what happens when a certain potential is applied to drive a reaction (the so called driving force).

Reaction at Equilibrium

Consider a simple redox reaction at an electrode:

$$O + ne \underset{k_b}{\overset{k_f}{\rightleftharpoons}} R \tag{1.1}$$

The Nernst equation relates the bulk concentration of participating redox species and the electrode potential at equilibrium as

$$E = E^{0'} + \frac{RT}{nF} ln \frac{C_O^*}{C_R^*} \tag{1.2}$$

where C_O^* and C_R^* are the bulk concentrations of the oxidised and reduced form of the redox active species. In the special case of the hydrogen couple $2H^+/H_2$, the Nernst equation can be written as:

$$E = E^0 - \frac{2.303RT}{F} pH - \frac{RT}{2F} ln \left(\frac{pH_2}{p^0} \right) \tag{1.3}$$

Returning to Eq.1.1, the simple general reaction will proceed in the forward direction at a rate v_f, which must depend on the available concentration of O at the electrode surface. If the concentration of C at a distance x from the electrode at time t is $C_O(x,t)$, then $C_O(0,t)$ will be the surface concentration of of O. With the rate constant for the forward reaction k_f this yields

$$v_f = k_f C_O(0,t) = \frac{i_c}{nFA} \tag{1.4}$$

where i_c is the cathodic current originating from reduction at the rate v_f (F is the Faraday constant and A the electrode surface area). With the same considerations for the backward reaction v_b and the resulting anodic current i_a the net reaction is described by

$$v_{net} = v_f - v_b = k_f C_O(0,t) - k_b C_R(0,t) = \frac{i}{nFA} \tag{1.5}$$

or

$$i = i_c - i_a = nFA[k_f C_O(0,t) - k_b C_R(0,t)] \tag{1.6}$$

Current-Potential Characteristics

How does the reaction rate, and therefore the current i, change with potential? Consider again the same simple reaction, as a one electron process ($n = 1$) for simplicity.

$$O + ne \underset{k_b}{\overset{k_f}{\rightleftharpoons}} R \tag{1.1}$$

To begin with, the electrode shall be at a potential $E^{0'}$, so that the corresponding cathodic and anodic activation energies are $\Delta G^{\ddagger}_{0c}$ and $\Delta G^{\ddagger}_{0a}$. When the electrode potential is changed by ΔE, the (relative) energy of the electron on said electrode will change accordingly, by $-F\Delta E = -F(E - E^{0'})$. If, for example, ΔE is positive, *i.e.* the electrode becomes more oxidising, the barrier for oxidation $\Delta G^{\ddagger}_{a}$ will decrease. This decrease will depend on the transfer coefficient α (which ranges from 0 to 1 and is a representation of the shape of the intersection of the reaction coordinates of forward and backward reaction, see [110] p.97):

$$\Delta G_a^{\ddagger} = \Delta G_{0a}^{\ddagger} - (1-\alpha)F(E - E^{0'}) \tag{1.7}$$

and conversely:

$$\Delta G_c^{\ddagger} = \Delta G_{0c}^{\ddagger} + \alpha F(E - E^{0'}) \tag{1.8}$$

The rate constants for forward and backward reaction k_f and k_b will be assumed to be temperature dependent (Arrhenius):

$$k_f = A_f e^{-\Delta G_c^{\ddagger}/RT} \tag{1.9}$$

$$k_b = A_b e^{-\Delta G_a^{\ddagger}/RT} \tag{1.10}$$

Insertion of Eq.1.7 and 1.8 yields:

$$k_f = A_f e^{-\Delta G^{\ddagger}_{0c}/RT} e^{-\alpha f(E-E^{0'})} \tag{1.11}$$

$$k_b = A_b e^{-\Delta G^{\ddagger}_{0c}/RT} e^{(1-\alpha) f(E-E^{0'})} \tag{1.12}$$

where $f = F/RT$.

If the electrode interface is at equilibrium with a solution of equal bulk concentrations of the two redox species ($C^*_O = C^*_R$), then $E = E^{0'}$ and $k_f C^*_O = k_b C^*_R$. Accordingly, the forward and backward rate constants have the same value at equilibrium ($k_f = k_b$), which is the standard rate constant k^0. At $E = E^{0'}$, equations 1.11 and 1.12 collapse to the potential-independent part, which thus also equals k_0. The rate constants k_f and k_b at any given potential can then be expressed more simply by:

$$k_f = k^0 e^{-\alpha f(E-E^{0'})} \tag{1.13}$$

$$k_b = k^0 e^{(1-\alpha) f(E-E^{0'})} \tag{1.14}$$

Insertion of k_f and k_b for any given potential into the general equation 1.6 for net current obtained above yields the current-potential characteristic:

$$i = FAk^0 \left[C_0(0,t) e^{-\alpha f(E-E^{0'})} - C_R(0,t) e^{(1-\alpha) f(E-E^{0'})} \right] \tag{1.15}$$

Current-Overpotential Characteristics

The relevant question to electrocatalysis is now how the net current changes with deviation from the equilibrium potential of a reaction, by application of an *overpotential* η. At equilibrium the net current is zero and eq 1.15 simplifies to

$$e^{f(E_{eq}-E^{0'})} = \frac{C^*_O}{C^*_R} \tag{1.16}$$

or

$$e^{-\alpha f(E_{eq}-E^{0'})} = \left(\frac{C_O^*}{C_R^*}\right)^{-\alpha} \tag{1.17}$$

Further, while the net current at equilibrium is zero, the forward and backward reaction will still contribute equal, but opposed, Faradaic currents i_c and i_a, the magnitude of which is the exchange current i_0:

$$i_0 = FAk^0 C_O^* e^{-\alpha f(E_{eq}-E^{0'})} \tag{1.18}$$

so that substitution of Eq.1.17 yields:

$$i_0 = FAk^0 C_O^{*(1-\alpha)} C_R^{*\alpha} \tag{1.19}$$

Division of the current-potential characteristic (Eq.1.15) by Eq.1.19 then yields the current-overpotential equation

$$i = i_0 \left[\frac{C_0(0,t)}{C_O^*} e^{-\alpha f\eta} - \frac{C_R(0,t)}{C_R^*} e^{(1-\alpha)f\eta}\right] \tag{1.20}$$

with the applied overpotential $\eta = E - E_{eq}$. Departure from the equilibrium potential E_{eq} causes a rapid rise in current, as the exponential terms dominate. With increasing overpotential the respective opposing current becomes negligible, *e.g.* at sufficiently negative potentials i effectively becomes i_c. However, at extreme overpotentials mass transfer limitations will restrict the reactant supply, causing the current to level off. Eventually the chemical step of a reaction will also become rate-limiting, resulting in a potential-independent current plateau. It is useful to note that, using such information, v_{max} and K_M can be determined for enzymatic catalysis in protein film electrochemistry.

If mass transfer limitations are effectively eliminated, because the electrode is either rapidly rotated or the solution is well stirred and the overpotentials are not too large,

Eq.1.20 simplifies to the so called *Butler-Volmer* equation

$$i = i_0 \left[e^{-\alpha f \eta} - e^{(1-\alpha) f \eta} \right] \tag{1.21}$$

and at small overpotentials (where $e^{\eta} \approx 1 + \eta$) to

$$i = -i_0 f \eta \tag{1.22}$$

In the absence of mass-transfer limitations, the overpotential applied to achieve a given current is solely reflective of the activation energy required to drive the reaction at the corresponding rate. It is apparent from Eq.1.21 that this overpotential for activation must be larger, the lower the exchange current. If, on the other hand, the kinetics of the reaction are facile instead of sluggish, the exchange current will be large and minimal overpotentials will be sufficient to achieve an immediate and steep current increase, when departing from the equilibrium potential.

Non-Faradaic Current

Two processes contribute to the currents observed in protein film electrochemistry experiments: Faradic currents originate from processes in which charge transfer occurs between the working electrode and the solution (as detailed further below). Non-Faradaic currents do not involve interfacial charge transfer, but instead stem from capacitance and changes in electrode potential.

Capacitance arises at the interface of working electrode and solution, as a so called electrical double layer is formed. Application of a positive charge to the electrode results in specific adsorption of anions as the inner (*Helmholtz*) layer, adjacent to which an outer layer is formed from solvated cations. As the applied potential is changed, these layers, and thus the capacitance, adjust and a corresponding current is recorded. If the potential is changed in a single step from one constant potential to another, *e.g.* in chronoamperometry, a current spike is observed that decays over time. If the potential is instead swept at a constant scan rate v, the current will at first rapidly increase as

an acceleration in scan rate from zero to v is registered. The resulting current will then eventually reach a value of vC_d, where C_d is the capacitance of the double layer.

Fardaic Current

The fardaic currents may as well be called the interesting currents, for the purpose of this thesis; they originate from charge transfer between the (working) electrode and solution or adsorbed molecules. In protein film electrochemistry there are two relevant origins of these currents. On the one hand, there are the so called non-turnover signals due to redox events in the protein and its co-factors. Since the number of redox-active sites (of the same potential) in a given protein film is low in absolute terms, the non-turnover signals usually generate only very small currents, and require very fast scan rates to be visible against the electrical background noise. In the case of an adsorbed electro-active redox *enzyme* on the other hand, enzyme turnover can generate catalytic currents with a very high signal-to-noise ratio. Potential control, through the electrode, then allows for highly detailed enzymatic assays of kinetic and thermodynamic parameters.

1.4.2 Features of Hyd-1 Cyclic Voltammetry

In cyclic voltammetry (CV) the potential is linearly swept from one potential E_i to another potential E_{ii} and back. Figure 1.8.A shows such an experiment, sweeping from low to high potential and back down. The grey line represents a CV obtained from a blank electrode where the observed currents originate from non-Faradaic processes (see above). In the CV of Hyd-1 (black line) the observed currents are dominated by Faradaic currents originating from catalytic turnover.

The shape of the Hyd-1 CV (Fig.1.8.A) exhibits a number of noteworthy features: i) With an increase in potential the current originating from H_2 oxidation increases. ii) At sufficiently high potentials the current levels off. iii) The CV does not steeply cut the zero current line. The Onset potential, where significant current is observed, is also well above the equilibrium potential (ca. -406 mV) for the $2H^+/H_2$ couple, under

the present conditions. All three points (i-iii) are in good agreement with established current-overpotential characteristics (see above) and betray a significant activation overpotential requirement for the enzyme, and thus sluggish kinetics and exchange currents; this aspect is discussed in more detail further below. iv) Finally, at high potential Hyd-1 begins to slowly inactivate and to form the oxidised inactive state Ni-B (see Fig.1.4). Since this process is slow, the visible effect on the voltammogram is scan rate dependent and hysteresis is frequently observed. At the beginning of the backward scan the driving force for oxidation is lowered while oxidation to Ni-B is still favourable; this results in a current decrease due to slower turnover and a smaller fraction of active enzyme. As the switch potential for Ni-B formation is passed (see. Ch.1.1.3 and 1.1.4), the oxidised enzyme rapidly reactivates and the current temporarily increases until the decrease in driving force dominates again.

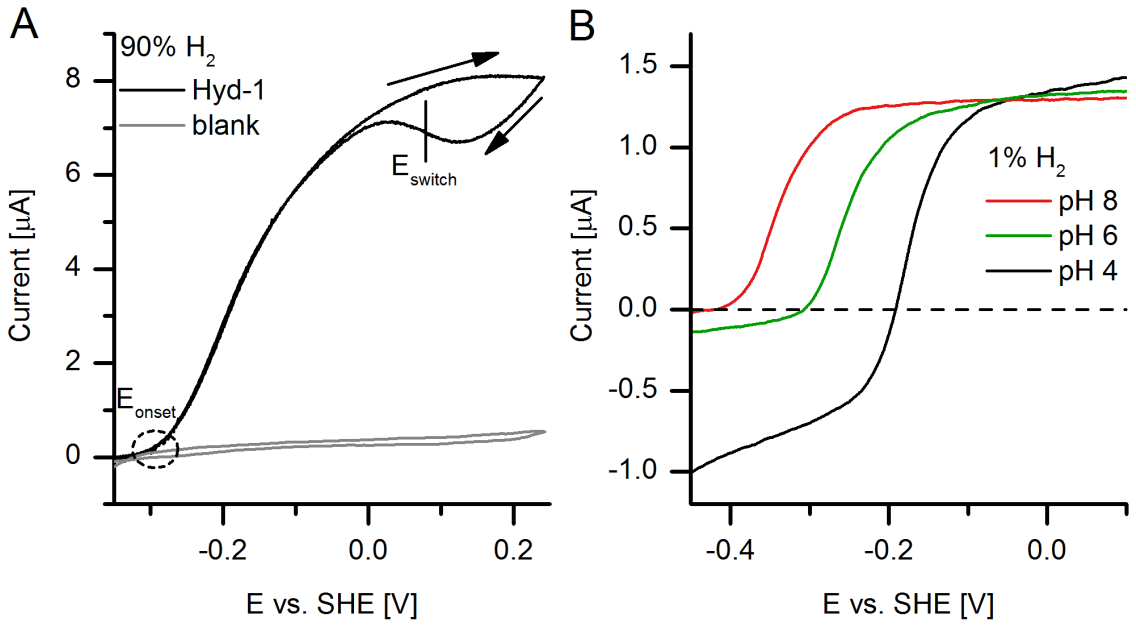

Figure 1.8 Cyclic Voltammetry of Hyd-1: A) Hyd-1 vs. blank PGE electrode at a scan rate of 1 mV/s under 90% H_2 at pH 7, 20 °C, 2000 rpm. Arrows indicate the direction of the scan. The apparent E_{switch}, potential of fastest reactivation from inactive enzyme (Ni-B), is indicated by a vertical line and the approximate onset potential, at which the catalytic current deviates significantly from the blank, is highlighted by a dashed circle. **B)** Hyd-1 averaged forward and backward scans at different pH under 1% H_2 at 10 mV/s, 37 °C, 2000 rpm. The data for the averaged scans was kindly provided by Dr. B. J. Murphy [111].

Murphy *et al.* found the overpotential requirement of Hyd-1 to change with pH and $\rho(H_2)$, *i.e.* the onset potential did not simply shift in unison with the $2H^+/H_2$ equilibrium potential [111]. On the one hand, the onset potential of Hyd-1 does not change at all over a 100-fold range of H_2 partial pressures, so that shifting the $2H^+/H_2$ equilibrium potential by ca. 30 mV through a 10-fold decrease in $\rho(H_2)$ has the effect of lowering the overpotential requirement by ca. 30 mV. A change in pH, on the other hand, does have a marked effect on onset potential, but the onset potential was found to decrease by ca. 20 mV less per pH unit than the equilibrium potential (at 100% H_2). Murphy realised that under both very low $\rho(H_2)$ and low pH the activation overpotential requirement for H_2 oxidation by Hyd-1 could be eliminated entirely, and reversible catalysis achieved. Figure 1.8.B shows this transition from overpotential requirement to fully reversible catalysis as the pH is shifted from pH 8 to 4 under 1% H_2. In contrast to *E.coli* Hyd-1 and other O_2-tolerant membrane-bound hydrogenases [112, 37, 113], such an overpotential requirement or change in bias has not been observed for O_2 sensitive [NiFe] hydrogenases.

The change in pH, or $\rho(H_2)$, does not determine the overpotential requirement through a specific effect on the enzyme. Instead, it is the resulting change in equilibrium potential relative to the potential at which the electrons either leave, or enter, the catalytic cycle [111], that determines the overpotential requirement; this site is called the catalytic control centre (ECC) of the hydrogenase [114]. The closer together the equilibrium and ECC potentials are, the smaller the bias and overpotential requirement become. The distal FeS cluster, at which interfacial electron transfer with the electrode or external redox partners (quinones *in vivo*) occurs, is a good candidate for the ECC.

Chapter 2

How a Respiratory [NiFe] Hydrogenase reacts with Oxygen

The essential findings presented in this chapter were selected for publication:

Wulff, P., Day, C. C., Sargent, F. & Armstrong, F. A. How oxygen reacts with oxygen-tolerant respiratory [NiFe]-hydrogenases. *Proceedings of the National Academy of Sciences* **111**, 6606–6611 (2014)

2.1 Introduction

2.1.1 Catalytic Model of Oxygen Tolerance

A detailed discussion of O_2-tolerance in hydrogenases in general, its enabling features and deliberations on different degrees of tolerance to O_2, can be found in Chapter 1.1.4. In short, it is of central importance that the enzyme is able to respond to O_2 attack at the active site by exclusively forming states which can be quickly reactivated under turn over conditions, while avoiding formation of damaging reactive species. The proven ability of Hyd-1 to do so continuously [71] gives rise to the notion of a catalytic O_2-tolerance mechanism, in which O_2 is effectively a competing substrate of the hydrogenase. The scheme in Figure 2.1 illustrates this concept.

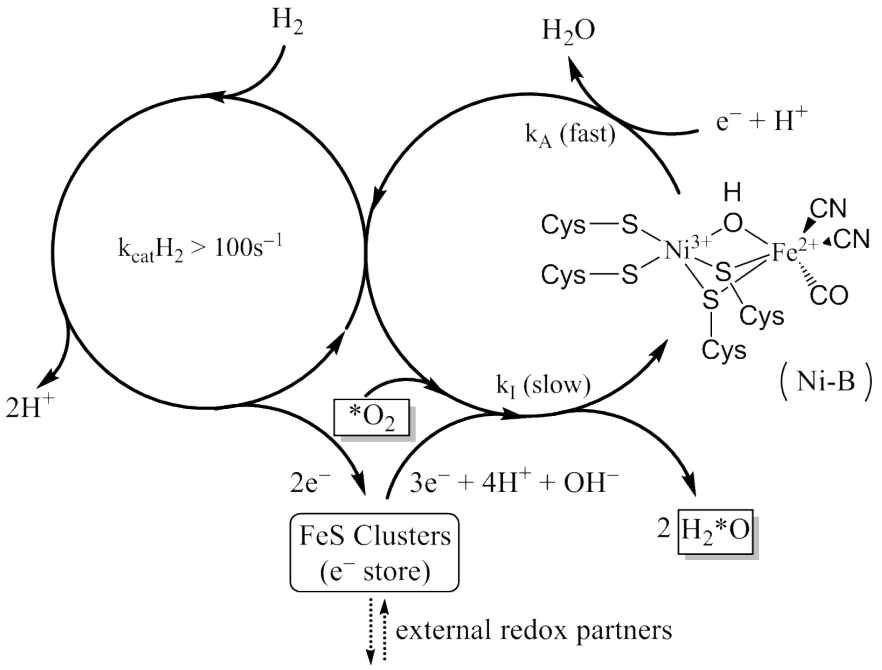

Figure 2.1 Simplified catalytic cycles of Hyd-1: Hydrogen oxidation proceeds at rates exceeding 100 s^{-1} (left) and feeds electrons into the relay system of FeS clusters, where they may be stored. Oxygen reduction to water (right), begins with O_2 attack at the active site to form exclusively Ni-B (k_I) and consumes electrons stored in the FeS relay in the process. The reactivation of Ni-B (k_A), to a state (probably Ni-SI) which might re-enter either catalytic cycle, is fast. The asterisk indicates the labelled $^{18}O_2$ introduced and measured in the following experiments. Reprinted with permission from reference [67] (Wulff *et al.*).

A fast H_2 oxidation cycle continously releases electrons which can be stored in the proximal and medial FeS clusters as well as passed on to external redox partners *via* the distal cluster. Upon O_2 attack, three stored electrons are provided by the proximal and medial clusters (Chapter 1.1.4), while the fourth electron necessary to fully reduce O_2 to harmless water can be derived from Ni oxidation (II→III). The stoichiometries are displayed in accordance with spectroscopic results showing that the bridging OH ligand in the Ni-B state originates from solvent, and not from O_2 [36]. This result is supported by the common observation that Ni-B can also be formed at oxidising potentials under anaerobic conditions (see 1.1). The role of the OH ligand might therefore be in stabilising the Ni(III) species.

Reactivation of Ni-B (k_A) is fast and leads to a state that may participate in either catalytic cycle. This state is likely Ni-SI (see Ch.1.1.3) though this has not been proven conclusively. The electron required for Ni-B reactivation could come either from the distal cluster itself or *via* the distal cluster from the conjoined heterodimer (see Chapter 3). This chapter seeks to the test the validity of the described catalytic model and answer the question: *What is the chemical reaction that forms the basis of oxygen tolerance in hydrogen catalysis?*

For any discussion of how and where O_2 might react with a hydrogenase, it is helpful to take a look at the enzyme's structure. Figure 2.2 shows *E. coli* Hyd-1 with highlighted possible reaction sites. The distal cluster, relatively close to the enzyme surface and accepting electrons from H_2 oxidation at the active site, is a likely site of reaction with O_2. An outer-sphere electron transfer could result in release of O_2^- or, if a second electron can transfer very rapidly from the opposite distal cluster, eventually H_2O_2. A reduced *b*-type haem in the attached cytochrome might undergo a similar reaction. Instead of the catalytic cycle proposed in Fig.2.1, the active site might instead be able to avoid Ni-A formation by somehow effectively releasing partially reduced oxygen species, *e.g.* H_2O_2.

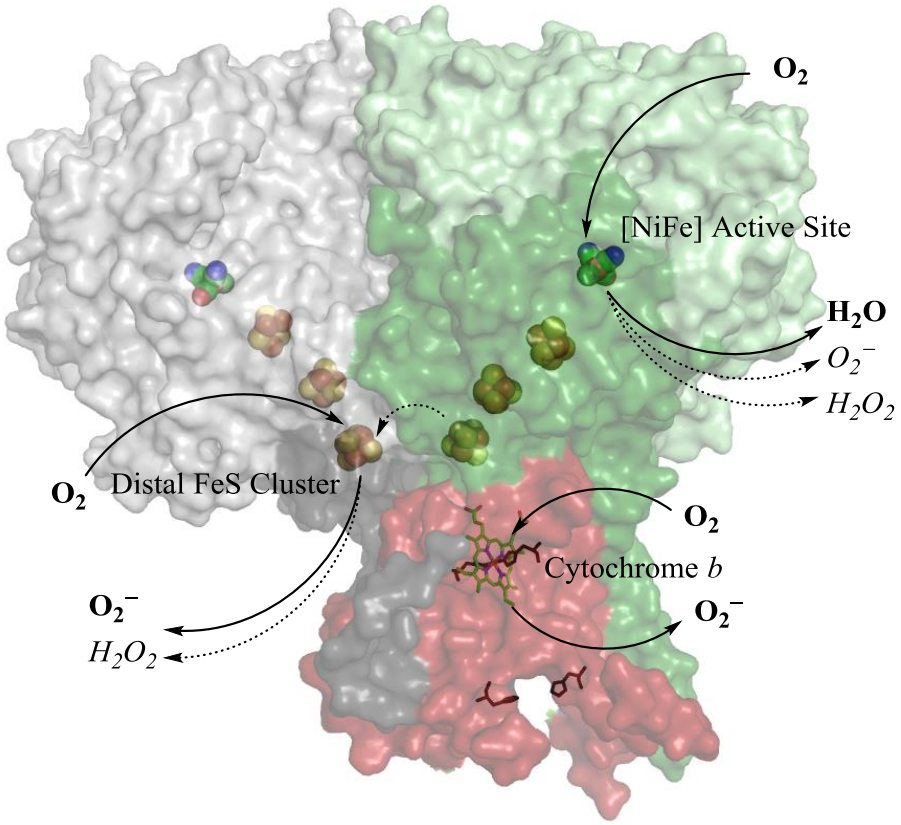

Figure 2.2 Possible Reactions of Hyd-1 with O_2: Sites likely to react with O_2 are depicted with the expected products. The large subunits containing the [NiFe] active site are shown in light green & grey, the small subunits with the FeS clusters in dark green & grey and the cognate cytochrome *b* in red (PDB: 4GD3). The labile nature of both the cyt *b* and the haem itself are evident from the missing second cytochrome and the vacant lower haem binding site (the ligating histidines are highlighted in black). In addition to the reactions shown, formation of H_2O_2 at the proximal cluster (with two available electrons), though buried, cannot be ruled out completely. Hydrogen peroxide production might also proceed indirectly *via* an O_2^- intermediate at the haem group. Reprinted with permission from reference [67] (Wulff *et al.*).

2.1.2 Oxidases

An implicit prediction of the model presented in Fig.2.1 is that O_2-tolerant [NiFe] hydrogenases are high-fidelity four-electron oxidases (Fig. 2.1), yet this has never been established directly by a method that analyses reaction products. Four-electron oxidases catalyse the reduction of O_2 to water, notable examples being cytochrome *c* oxidase and the blue Cu oxidases. These well-established enzymes are very efficient catalysts: cytochrome *c* oxidase must deliver high rates of O_2 reduction by cytochrome *c*, using much of the energy released to pump protons [93], whereas fungal blue Cu oxidases reduce O_2 to water at sufficiently high potentials to generate organic (phenolic) radicals [115].

Another, more unusual example is the alternative oxidase (AOX), a di-iron enzyme present in many plants, among them the carrion flowers of the aroid family with such pungent representatives as *Amorphophallus titanum*, and in parasites, including *Trypanosoma brucei*, the protozoan causing sleeping sickness [116]. The membrane-bound AOX, which like Hyd-1 is a dimer, diverts electrons from the respiratory chain by oxidising ubiquinol to reduce oxygen to water without proton pumping [116, 117, 118, 119], which is highly energy inefficient. Hence, the main role of alternative oxidases is thought to be the production of heat.

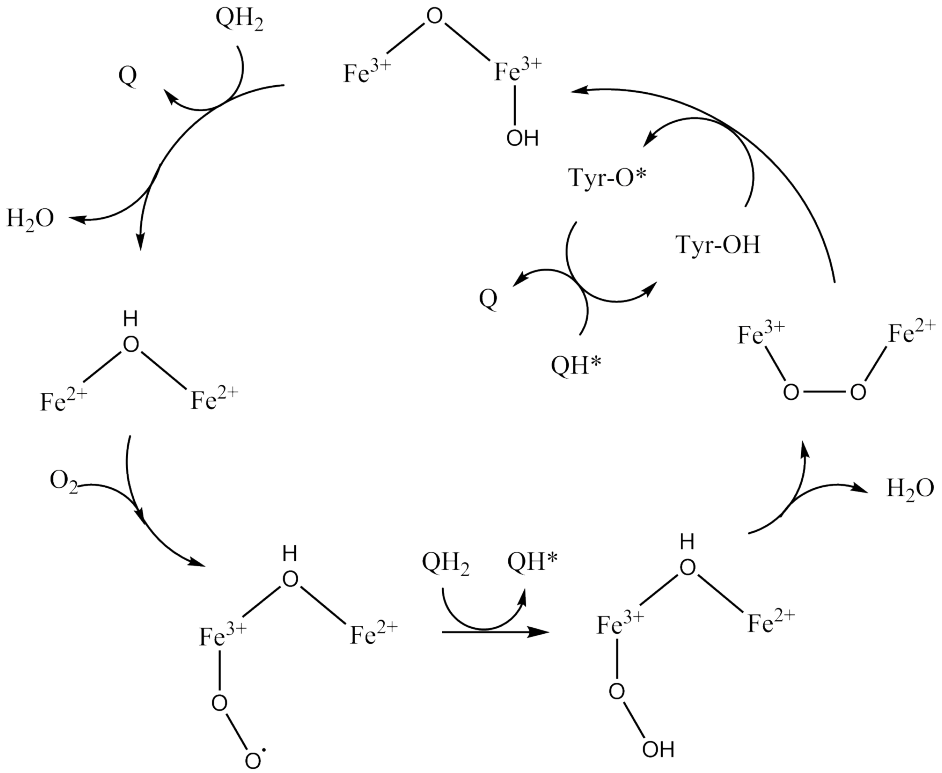

Figure 2.3 Alternative Oxidase Reaction Mechanism,
as proposed by *Moore et al.* [116]: Beginning on the left, O_2 binds to the diferrous center, resulting in Fe oxidation and formation of a superoxo species. Following rapid further reduction and proton transfer from a bound ubiquinol and subsequent rearrangement, one H_2O is released to form a peroxodiiron state. A nearby tryosine is proposed to then donate an electron and a proton to form an oxodiiron resting state. The tyrosine can be regenerated from the previously formed radical, ubisemiquinone. A final ubiquinol oxidation step completes the catalytic cycle with release of a second H_2O molecule.

For comparison with hydrogenases (Chapter 1.1), the alternative oxidase and its most recently proposed catalytic model (Fig. 2.3, [116]) are instructive for several reasons: Like the hydrogenases, the AOX has a dimetallic, Fe-containing active site buried deep within the protein body in a hydrophobic environment [118]. In addition,

the AOX reaction mechanism would be predicted to be relatively simple, since it is not complicated by the proton translocation found in many other oxidases. Unlike in hydrogenases, the Fe atoms of AOX are not ligated by cysteines, CN^- and CO 1.1; instead the active site Fe atoms are ligated by four conserved glutamate residues, two of which perform a bridging function. Two conserved histidines are also found in close proximity [116, 118]. Whereas hydrogenases rely on an FeS cluster relay, in the alternative oxidase electrons are provided directly *via* quinones. The proposed mechanism involves formation of a radical at the [FeFe] active site, which in the case of [FeFe] hydrogenases leads to irreversible active site degradation, especially of the affiliated [4Fe-4S] cluster (Chapter 1.1.4). The direct use of quinones as electron carriers would help to avoid this problem of irreversible degradation in the alternative oxidase. In [NiFe] hydrogenases the proximal [4Fe-3S] cluster is positioned in a separate subunit at a distance of 11.7 Å from the active site. Interestingly, a bridging hydroxide ligand is found in both hydrogenase and alternative oxidase structures and is crucially involved in the proposed reaction mechanisms. The hydroxide bridge appears to play a dynamic stabilising function in both cases; in contrast to the permanent amino acid ligands, it is released at some stage in the catalytic cycle and is later rebound. The current AOX model implies that the hydroxide originates from molecular oxygen and not from solvent, although it should be noted that this assumption is not based on experimental evidence.

Of special interest in the context of *E. coli* Hyd-1 and its O_2-tolerance is also the cytochrome *bd*-II oxidase of *E. coli*, which is co-expressed with Hyd-1 in stationary phase and under carbon- and phosphate-starved conditions [83]. As a high affinity oxidase (cyt *bd* oxidases having a K_m in the nM range) it functions as a terminal oxidase to allow respiration under oxygen-limited, or micro-aerobic conditions [103]. Does Hyd-1 have a similar four-electron oxidase capability to this co-expressed, purpose built oxidase and if so what are the implications?

2.1.3 Experimental Design

Two principal approaches were undertaken to determine the products and intermediates of Hyd-1 reacting exclusively with H_2 and O_2 in aqueous solution (Fig 2.4):
1) Measurement of the time-dependent formation of $H_2{}^{18}O$ from $H_2/{}^{18}O_2$ gas mixtures using isotope ratio mass spectrometry (IRMS) [120]. For the detection of $H_2{}^{18}O$ this technique utilises equilibration of aqueous samples under a CO_2 atmosphere, *i.e.* the equilibrium $CO_2 + H_2{}^{18}O \rightleftharpoons H_2CO_2{}^{18}O \rightleftharpoons CO^{18}O + H_2O$ creates ^{18}O-enriched CO_2 gas as a measurement proxy (see Methods 5.2).
2) Colorimetric determination of the formation and decay of reactive oxygen species O_2^- and H_2O_2, also in a time-dependent manner.

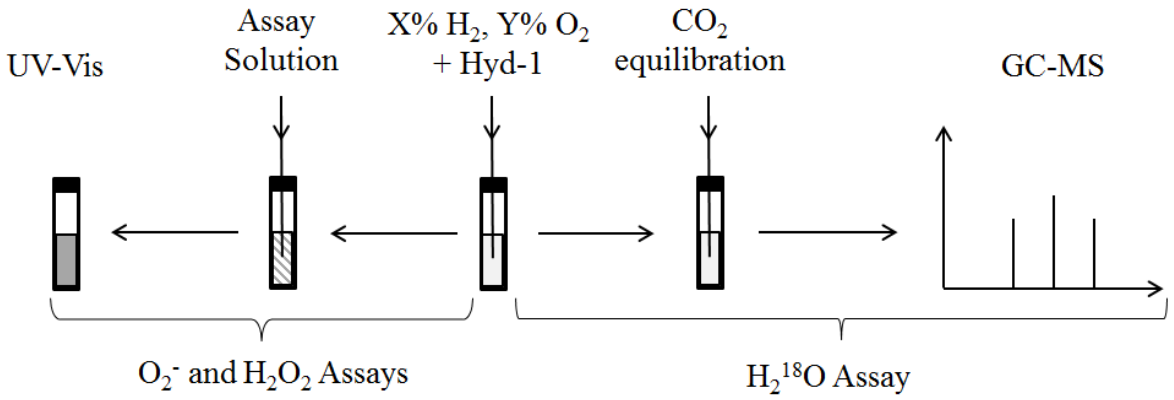

Figure 2.4 Experimental Design: Hyd-1 samples in aqueous buffer at pH 7 were incubated under a mixed H_2/O_2 atmosphere (see. Ch.5.2 and Fig.5.3 for more detail). Unlabeled $^{(16)}O_2$-exposed samples were added to assay solutions containing either Griess reagent (for O_2^-), or Ampliflu Red and the UV-vis absorption changes were used, with appropriate calibrations, to measure the production of O_2^- and H_2O_2. To determine H_2O production, $^{18}O_2$-exposed samples were equilibrated with CO_2, which was subsequently subjected to GC-mass spectrometry to detect changes in the $^{18}O/^{16}O$ ratio.

H_2O_2 was detected spectroscopically by addition of sample solution, after a defined reaction time, to an assay solution containing 10-Acetyl-3,7-(dihydroxy-phenoxazine) (Ampliflu Red), which in the presence of H_2O_2 is irreversibly converted into the fluorescent dye 7-Hydroxy-3H-phenoxazine-3-one (Resorufin) by Horse Radish Peroxidase (HRP). This assay has been used in the past to monitor H_2O_2-evolving side reactions simultaneous with the principal redox reaction of an enzyme [97]. In establishing the experiments presented in this chapter it was observed however, that Hyd-1 reduces

Resorufin, a quinone, in the presence of H_2. The reduced Resorufin then creates reactive oxygen species, including H_2O_2, via reaction with O_2 [121]. It was therefore only possible to take endpoint, rather than concurrent, H_2O_2 measurements after having stopped the reaction by purging the sample solution with Argon (Ch. 5).

Detection of $O_2{}^-$ is inherently more complicated due to its short lifetime and potential cross reactivity of assay components. A common $O_2{}^-$ assay employs cytochrome *c* as a spectroscopically detectable high fidelity scavenger [97]. Since Hyd-1 reduces cytochrome *c* at catalytic rates (Ch. 2.2.4), the hydroxylamine assay developed by Elstner et al. [122] was employed instead; it relies on hydroxylamine reacting with scavenged $O_2{}^-$ to form NO_2^-, which can be detected *via* UV-spectroscopy using the Griess reagent. Hydroxylamine is reported neither to impede hydrogenase activity [123] nor to react with H_2O_2 to produce nitrite [124]. Both observations were verified prior to carrying out the experiments described here.

2.2 Results

An overview of the products measured for the reaction of O_2 and H_2 with Hyd-1 is presented in Figure 2.5. Each product is discussed in detail in the subsections below.

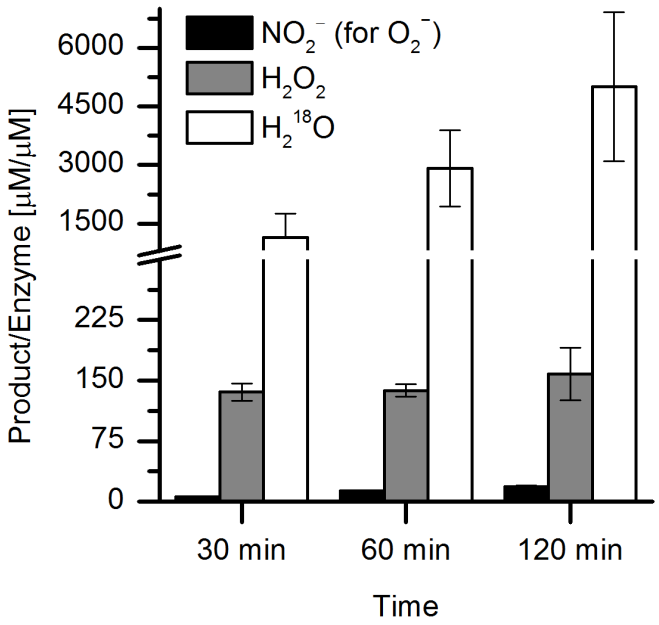

Figure 2.5 Overview of Oxygen Reduction Products: The measured reduction products are shown on a µM(Product) per µM(Hyd-1) basis after 30, 60 and 120 min reaction time under 90% H_2 and 10% O_2 in mixed hydrogenase buffer at pH 7.0, 20 °C. Error bars represent the standard deviation of three independent measurements. Note that the nitrite error bars are too small to be visible on this scale.

2.2.1 Water Formation

Exposure of Hyd-1 in aqueous buffer to 90% H_2 and 10% $^{18}O_2$ resulted in large yields of $H_2{}^{18}O$, as shown in Fig. 2.5. The amount of additional detected $H_2{}^{18}O$, as compared to enzyme-free or $^{(16)}O_2$-exposed samples, accumulated robustly over time from ca. 1148 ± 642 µM per µM Hyd-1 after 30 min to 5003 ± 1911 µM per µM Hyd-1 after 120 min. Measurements were taken over a wide range of incubation times to establish a rate of reductive $H_2{}^{18}O$ formation (Fig. 2.6). Fitting the wild-type data with a straight line through the origin yields a slope representing a $H_2{}^{18}O$ turnover rate of approx. 0.65 µM($H_2{}^{18}O$) µM(Hyd-1)$^{-1}$ s^{-1}. The error of the mass spectrometry measurements for each individual experiment was very low at 4.8 to 17.8 µM $H_2{}^{18}O$. Thus the significant scatter of data points is credited to disagreeably difficult and delicate manual sample

handling. It can further be seen from Fig. 2.6 that the rate of $H_2{}^{18}O$ formation is at least twice as high under 10% $^{18}O_2$ as it is under 5% $^{18}O_2$, based on the limited data available for 5% $^{18}O_2$ after 3 and 4 h of incubation. It is highly important to note at this stage, that 10% O_2 does not cause inactivation over a period of at least 4 h, *i.e.* the enzyme activity is maintained at a constant level throughout (*sustained activity*).

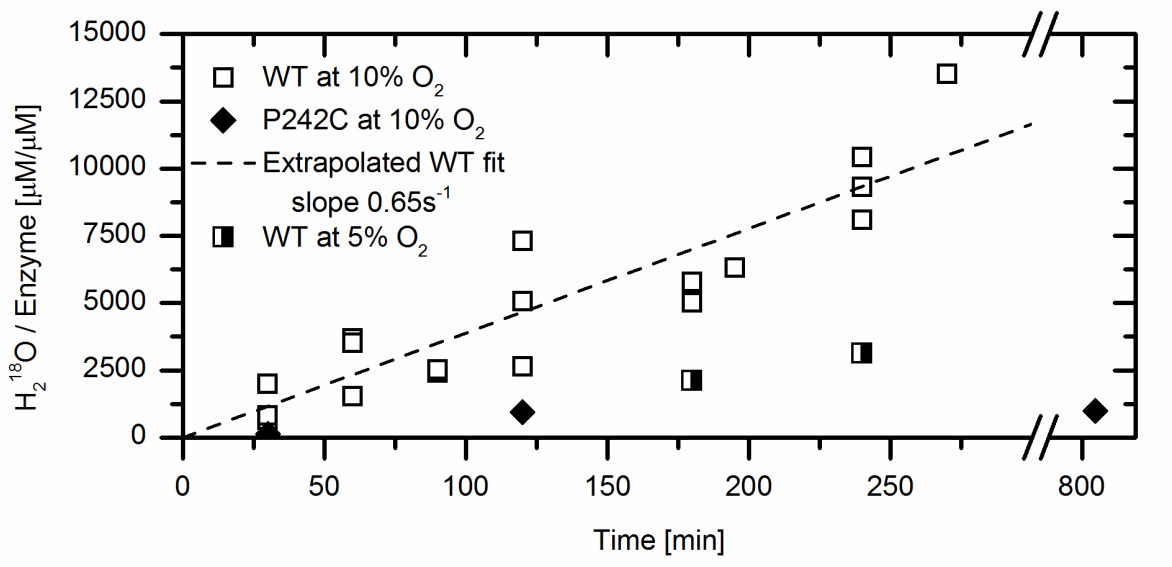

Figure 2.6 The Rate of H_2O Formation by WT Hyd-1 and an O_2-sensitive variant: The amount of $H_2{}^{18}O$ formed, relative to enzyme-free (blank) controls, is plotted over time. The concentrations measured by mass spectrometry in µM($H_2{}^{18}O$) were divided by the enzyme concentration employed, in µM(Hyd-1). Wild type enzyme (empty squares) and P242C variant (black diamonds) were incubated in 90% H_2 and 10% $^{18}O_2$ atmosphere, while a set of further WT samples (half squares) were incubated in 5% $^{18}O_2$ atmosphere with 95% H_2, for comparison. The slope of the extrapolated linear fit (dashed line) to the 10% $^{18}O_2$ wild type data yields an approximate $H_2{}^{18}O$ formation rate of 0.65 s^{-1}. Common conditions: mixed hydrogenase buffer at pH 7.0 and 20 °C.

In addition to these experiments carried out on native enzyme, a variant with a substitution in the small subunit (P242C) was studied for comparison. In this variant the medial [3Fe-4S] cluster is converted to a [4Fe-4S] cluster with lower redox potential. While high rates of H_2 oxidation and resistance to short term O_2 exposure are maintained [70], electrochemical experiments have shown that H_2 oxidation is severely impared in the sustained presence of O_2 [71]. Importantly, the P242C variant shows decreased $H_2{}^{18}O$ production after 30 min as compared to WT and no measurable increase in $H_2{}^{18}O$ from 120 min to over 800 min.

2.2.2 Hydrogen Peroxide Formation

Hydrogen peroxide was assayed with endpoint measurements via the Ampliflu Red to Resorufin conversion, as described in Chapters 2.1.3 and 5. Incubation of Hyd-1 in aqueous solution in the presence of 90% H_2 and 10% O_2 yielded low levels of H_2O_2; a typical concentration being ca. 22 µM H_2O_2 for 0.15 µM Hyd-1. The amount thus detected was independent of reaction time: Fig. 2.5 shows a H_2O_2/Hyd-1 ratio of 135.7 ± 10.9 µM(H_2O_2) per µM(Hyd-1) after 30 min with similar values of 137.7 ± 7.6 and 158.4 ± 32.5 µM(H_2O_2) per µM(Hyd-1) after 60 and 120 min respectively. In control experiments without O_2, no H_2O_2 was detected.

To investigate why the H_2O_2 levels were independent of time, Hyd-1 was incubated with known starting concentrations of H_2O_2 under 1 atm H_2 (and no O_2). The H_2O_2 concentration was seen to fall over time, with higher rates observed for higher initial H_2O_2 concentrations (Fig. 2.7(A)). In the absence of enzyme, using only the reaction buffer, a much smaller but still significant decrease in H_2O_2 concentrations was observed. At low enzyme concentrations (e.g. 0.15 µM, as in Fig. 2.7(A)) the component of H_2O_2 decomposition due to the presence of enzyme is comparable in extent to that in plain buffer. Fig. 2.7(B) illustrates the effect of different enzyme concentrations on H_2O_2 levels after 30 min of incubation time; here in the presence of only 4.2% O_2 and employing the Xylenol Orange based assay (see chapter 5). A 2.3 fold increase in enzyme concentration yields an almost 4 fold increase in the measured peroxide concentration. It was found that the non enzyme-dependent decomposition could be reduced significantly by sealing freshly cleaned reaction vials under a flow of nitrogen, presumably preventing airborne contamination. Neither the enzyme-dependent nor the -independent decomposition activity, as assayed via Ampliflu Red, was suppressed by the addition of 100 µM Deferoxamine, which complexes free Fe that might participate in a Fenton reaction (data not shown).

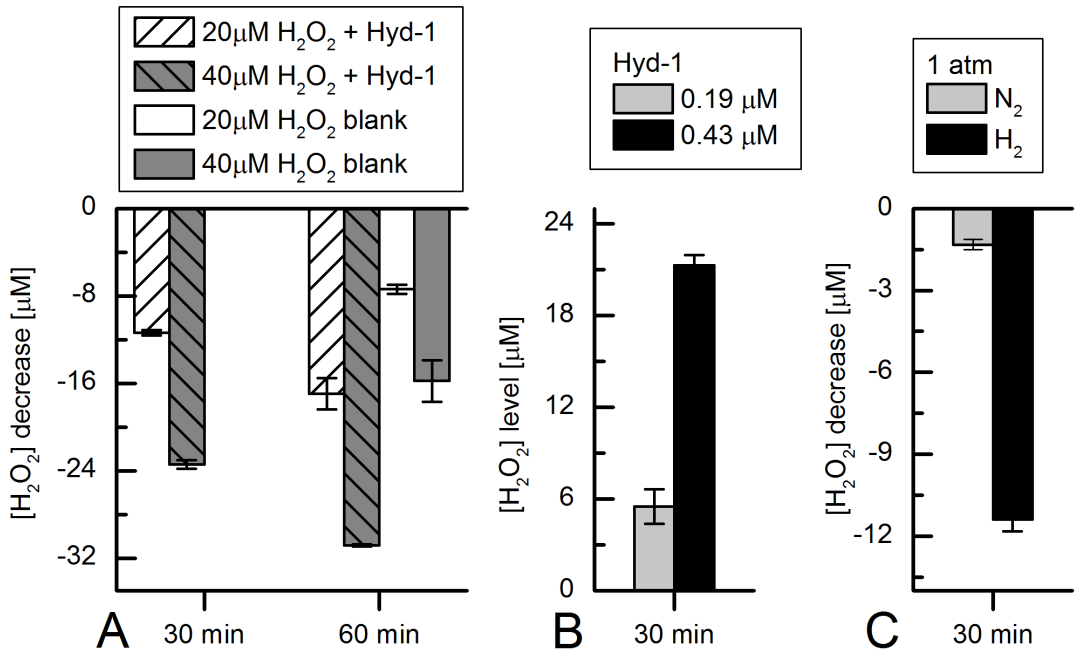

Figure 2.7 Decomposition and Steady State Concentrations of H_2O_2:
(A) Decomposition: Solutions containing 20 and 40 µM H_2O_2 were incubated with and without 0.15 µM Hyd-1 for 30 and 60 min; 1 atm H_2, no O_2.
(B) Enzyme Dependence: Steady state H_2O_2 concentration after 30 min incubation under 80% H_2 and 20% air (ca. 4.2% O_2) of samples containing 0.19 and 0.42 µM Hyd-1.
(C) Peroxidase Activity: Decrease in H_2O_2 concentration from 27 µM after 30 min in the presence of 1 atm N_2 or H_2; 0.225 µM Hyd-1, with background (enzyme-free) decomposition subtracted.
Common conditions: mixed hydrogenase buffer at pH 7.0 and 20 °C; error bars represent standard deviations of at least three independent experiments.

The peroxide decomposition activity was further investigated in the presence and absence of H_2 as shown in Fig. 2.7(C). The use of an N_2 or H_2 atmosphere had no discernible effect on buffer-dependent decomposition. The results shown here were achieved using very clean reaction vials sealed under a flow of nitrogen as mentioned above and described in chapter 5. In the presence of 0.225 µM Hyd-1 under 1 atm N_2 there is essentially no decrease in H_2O_2 concentration, compared to the low background level. The combination of 0.225 µM Hyd-1 and 1 atm H_2 however, yields an additional H_2O_2 decomposition of 10 µM after 30 min (from a starting concentration of 27 µM). This establishes *E. coli* Hyd-1 as a H_2-dependent peroxidase.

The apparent rate constant for peroxide decomposition was calculated, dividing the change in concentration after 30 min (Fig. 2.7(A)) by the initial H_2O_2 concentration (20 or 40 µM); this yields an average value of 3.2 ± 0.1 x 10^{-4} µM$(H_2O_2)^{-1}$ s^{-1}, including

background contributions, for 0.15 µM Hyd-1 under the same experimental conditions as the peroxide detection experiments (Fig. 2.5).

The observation that H_2O_2 remains at an approximately constant concentration over time (Fig. 2.5) under a mixed H_2/O_2 atmosphere, but decreases distinctly in the absence of O_2, demonstrates that H_2O_2 is kept at a steady state. Using the steady state concentration measured in these experiments (approx. 22 µM) and the apparent rate constant determined above for the same amount of enzyme (0.15 µM), the total H_2O_2 decomposition rate [*i.e.* 3.2 x 10^{-4} µM$(H_2O_2)^{-1}$ s^{-1} x 22 µM(H_2O_2)] is estimated as 0.007 s^{-1}. At steady state this decomposition rate must be equal to the H_2O_2 evolution rate. Thus, the rate constant for H_2O_2 formation is $k_{cat}(H_2O_2)$ = 0.007 s^{-1} / 0.15 µM(Hyd-1) = 0.047 µM(Hyd-1)$^{-1}$ s^{-1}.

In addition to this unexpected peroxidase activity, Hyd-1 displays a remarkable stability in the presence of significant concentrations of the bleach H_2O_2, which might generally be expected to damage biological molecules. Following initial experiments such as those described above, Hyd-1 was subjected to much larger concentrations of up to 1 mM H_2O_2. Figure 2.8 shows protein film electrochemistry (PFE) experiments (see chapter 5) examining the influence of H_2O_2 on Hyd-1 H_2 oxidation activity and stability. While a Hyd-1 film on a rotating disk electrode remained approximately stable in 1mM H_2O_2 over 3 h, reversible inactivation at high potential was observed (Fig. 2.8A). This inactivation could be mitigated by bubbling the solution continuously with H_2, *i.e.* removing O_2 originating from H_2O_2 decomposition (Fig. 2.8B). Indeed, high-potential inactivation resumed when bubbling was arrested. Figure 2.8C highlights the similarity of reversible high-potential inactivation originating from O_2 supplied in the headspace and O_2 originating from H_2O_2 in solution. It is concluded that H_2O_2 itself does not react extensively, if at all, with Hyd-1 to compete with or to arrest H_2 oxidation. Therefore, at least externally supplied, H_2O_2 does not detrimentally react with the active site, nor does it appear to react by any other irreversible pathway resulting in permanent damage to the enzyme, especially under the low peroxide concentrations of the solution-based O_2 reduction experiments.

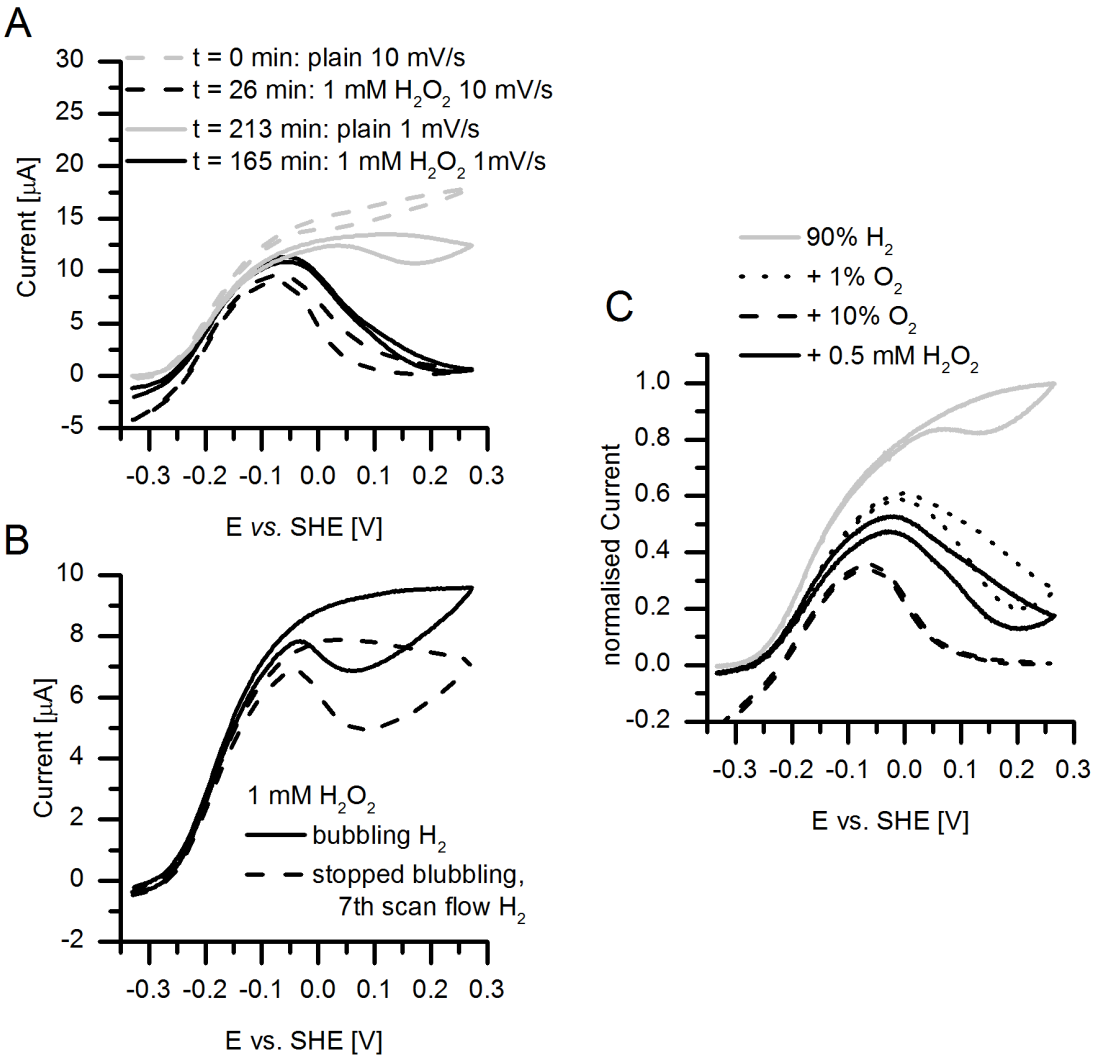

Figure 2.8 Cyclic Voltammetry of Hyd-1 in the presence of H_2O_2:
(A) Stability of Hyd-1: Active enzyme film was first assayed in plain buffer (t = 0 min, 10 mV/s, grey dashed line). The electrode (with active enzyme) was then transferred to buffer containing 1mM H_2O_2 (t = 26 min, 10 mV s^{-1}, black dashed line and t = 165 min, 1 mV s^{-1}, black solid line). Final transfer back to plain buffer (t = 213 min, 1 mV s^{-1}, grey solid line) established a comparable activity level.
(B) Origin of Inactivation: Flow of H_2 was guided either through the buffer solution (bubbling, solid black line) containing 1 mM H_2O_2 or through the headspace (dashed black line) as per standard procedure. Scans were recorded just before and seven scans after bubbling was stopped.
(C) Influence of O_2 and H_2O_2 on inactivation: Hyd-1 under a flow of 90% H_2 (grey solid line) through the headspace was subjected to either 1% O_2 (black dotted line), 10% O_2 (black dashed line) or 0.5 mM H_2O_2 (black solid line), with Ar serving as carrier gas.
Other conditions: mixed buffer pH 7, 20 °C, ω = 2000 rpm, enzyme activated at -0.527 V for >600 s. A) 1 atm H_2; B) 1 atm H_2, 10 mV s^{-1}; C) 1 mV s^{-1}.

2.2.3 Superoxide Formation

The amount of NO_2^- detected as a proxy of O_2^- rose from 5.8 ± 0.9 µM after 30 min to 18.7 ± 1.6 µM(NO_2^-) per µM(Hyd-1) after 120 min (Fig. 2.5). From these results a rate constant $k_{cat}(NO_2^-)$ of 3.2 ± 0.4 x 10^{-3} s^{-1} is calculated. The quantity of scavanged NO_2^- also scaled approximately linearly with enzyme concentration, so that in separate experiments similar values of 7.6 ± 1.1 and 7.4 ± 2.1 µM(NO_2^-) per µM(Hyd-1) were obtained for 0.15 and 0.45 µM(Hyd-1) respectively, after ca. 30 min of reaction.

The low, and reproducibly scaling, micro-molar concentrations measured seem to give, at first sight, the impression of at least qualitatively reliable O_2^- detection. This is likely the reason that this assay is frequently used; quick searches on *Web of Knowledge* and *Google Scholar* yield dozens to hundreds of papers, applications and citations. However, a more thorough foray into the literature, including the original publications by Elstner *et al.*, written in German and never made available in digital form [124, 125], reveals a great deal of uncertainty about the underlying reaction of this hydroxylamine-based assay [126]. Presumably these papers, although often cited, are seldom read. As a result different authors adopt disparate O_2^-/NO_2^- ratios. For example, a ratio of 2.0 is attributed to Elstner *et al.* [122] by Kono [127] (cited over 600 times) in a reaction that includes release of one equivalent of H_2O_2. Schneider and Schlegel, among other authors, simply assume that *"The amounts of nitrite are considered to represent the amounts of superoxide radicals."* [123], implying a ratio of 1.0. With these disagreements in mind, and conservatively adopting the stoichiometric ratio of 1.3 O_2^-/NO_2^-, the rate constant $k_{cat}(NO_2^-)$ of 3.2 ± 0.4 x 10^{-3} s^{-1} is converted to an apparent O_2^- production rate of 4.1 ± 0.6 x 10^{-3} µM(O_2^-) µM(Hyd-1)$^{-1}$ s^{-1}.

As an indirect measurement of the amount of the H_2O_2 that might derive from any O_2^- initally formed, H_2O_2 levels were measured in the presence and absence of hydroxylamine. Incubation of 0.225 µM Hyd-1 in the presence of 90% H_2 and 10% O_2 at 20 °C and pH 7, resulted in 18.5 ± 1.2 and 26.4 ± 1.6 µM(H_2O_2) in the presence and absence of hydroxylamine respectively, representing a 7.9 µM or 30% decrease due to O_2^--scavenging by hydroxylamine.

2.2.4 Cytochrome *c* Reduction

The rate of cytochrome *c* (cyt *c*) reduction was measured initially as an assay for superoxide production (Method, Ch.5.2.5). Cytochrome *c*, partially acetylated to minimize interaction with enzymes, has indeed been used successfully to this end in studies of such complex redox systems as NADH:ubiquinone oxidoreductase (complex I) [97]. It was found however that Hyd-1 reduces cytochrome *c* directly and at catalytic rates when provided with H_2, even in the absence of any O_2. An apparent rate constant of ca. 53 s^{-1} for transfer of electrons from Hyd-1 to acetylated cyt *c* was calculated, which is unexpected given the only slightly higher rate of 58 s^{-1} obtained for non-acetylated cyt *c*. These results confirm and highlight the proficiency of Hyd-1 outside its physiological context in confering electrons derived from H_2 over long distances even to *non-cognate* bulky macromolecules.

2.2.5 Hydrogen Oxidation

The H_2 oxidation activity of Hyd-1 in solution, with small molecules as electron acceptors, was assayed spectroscopically using benzyl viologen, as described previously by Lukey et al. [37]. In H_2-saturated buffer an initial turnover frequency for H_2 oxidation $k_{ox}(H_2)$ of ca. 125 H_2 s^{-1} was observed at pH 7.0 and 20 °C. For comparison: Lukey and co-workers found rates of approximately 100 H_2 s^{-1} for their Hyd-1 preparations.

2.3 Discussion

According to the most recent models, the O_2-tolerance of [NiFe] hydrogenases (Ch. 1.1.4 and 2.1.1) is dependent upon the ability of the hydrogenase to supply four electrons and protons to the active site in quick succession when O_2 attacks, fully reducing O_2 to benign water in the process. Oxygen would simply suppress H_2 oxidation activity at some new equilibrium but trapped, potentially damaging, intermediate oxygen species are avoided. The active site is, however, not the only electron-rich site where O_2 might be reduced (see Fig. 2.2). The high rates of H_2-dependent cyt *c* reduction displayed by Hyd-1 underscore the availability of electrons for remote outer-sphere 1-e^- transfer reactions. As a consequence outside an ideal model, it would be unrealistic to expect to detect exclusively H_2O, and no O_2^- or H_2O_2 when Hyd-1 is exposed to a mixture of H_2 and O_2. In general, production and release of reactive oxygen species is both unavoidable and well documented in enzymes which have low-potential, accessible redox centres, such as mitochondrial complexes I and II [128, 28]. The important task is therefore to carefully compare the amounts of detected products with each other, but also the calculated rates with rates measured and predicted from electrochemical experiments.

The rate of $H_2{}^{18}O$ formation established here to be 0.65 µM(H_2O) µM(Hyd-1)$^{-1}$ s^{-1}, and to be approximately constant over more than 4 h, translates into an $^{18}O_2$ reduction, or removal, rate of 0.325 µM(O_2) µM(Hyd-1)$^{-1}$ s^{-1} under 10% O_2. Hydrogen peroxide, in contrast, is maintained at a low steady state level where production from O_2 and decomposition are equal, such that $k_{cat}(H_2O_2) = 0.047$ µM(Hyd-1)$^{-1}$ s^{-1}. From this it is obvious that, however the H_2O_2 is formed, its maximum rate is 6-7 times lower than the rate of $H_2{}^{18}O$ formation from $^{18}O_2$, confirming that a direct 4 e^- pathway is the dominant O_2-reduction reaction. The apparent rate constant for this direct reduction pathway to H_2O is 0.325 - 0.047 = 0.28 s^{-1}. Direct reduction of O_2 to H_2O requires a distinct site that is able to deliver four electrons and protons in a concerted manner. Given that the peroxidase activity was shown to be much slower in comparison, we can conclude that 86% of O_2 is indeed reduced directly to H_2O at the [NiFe] active site.

The contribution of O_2^- to H_2O_2 generation was determined to be between ca. 9% and 30% using the hydroxylamine assay. This fraction might indeed be higher, since the mechanism and efficency of this assay are rather poorly understood [126] and the rate of disproportionation of O_2^- into H_2O and H_2O_2 at 6 x 10^5 M^{-1} s^{-1} (pH 7) is rapid [129]. At the observed micro molar concentrations most or of even all of the H_2O_2 could thus derive from O_2^-, if the latter is not otherwise scavenged.

Generation of H_2O_2 by a route other than *via* O_2^- requires one of the following two conditions. First, O_2 could undergo two successive and sufficiently rapid one-electron reactions so that O_2^- exists only as an intermediate which, before it can escape, is reduced further. Looking at the structure of Hyd-1 (Fig. 2.2) the space between the two adjacent distal clusters of the dimer is identified as a possible location for this reaction. Second, O_2 might react at a site inherently capable of transferring two electrons simultaneously. This could occur at the [NiFe] active site, in which case the formed H_2O_2 would have to be released harmlessly. Other candidate sites are the proximal [4Fe-3S] cluster or a site in the cytochrome *b* subunit resulting from disruption of the haem-binding site and involving Fe(IV) as an intermediate. Indeed, the slow peroxidase activity discovered for Hyd-1 might too derive from a reaction with a labile haem-*b* site with axial ligand disruption. Such a reaction is well documented as so-called microperoxidase activity in cytochrome *c* samples [130].

To determine the amount of co-purified or associated cyt *b* [131], the Hyd-1 stock solutions used in the presented experiments were assayed *via* UV-vis spectroscopy and the ratio of haem *b* to Hyd-1 (dimer of heterodimers) was found to be approx. 1.65; assuming two haems per cytochrome that would translate to 0.82 Cyt-*b* per dimer of heterodimers (see Ch. 3.2.3 and Ch.5.5 method).

Establishing that H_2O is in fact the main product of O_2-attack on Hyd-1 in the presence of H_2 is important but not sufficient to investigate the mechanism of O_2-tolerance and to assess whether the proposed model is plausible. A crucial task is the comparison of reaction rates predicted from the model, and rates obtained from independent

electrochemical experiments, with the rates obtained here for direct reduction of $^{18}O_2$ to $H_2{}^{18}O$ (0.28 s^{-1}).

Cracknell, Evans and co-workers established in earlier experiments, that suppression of H_2-oxidation activity by O_2 (k_I, see Fig. 2.1) depends on O_2 concentration but not on potential [58, 71]. The rate of reactivation of Ni-B (k_A), however, increases exponentially as the potential is lowered [58, 71]. Considering the high levels of H_2 in the $^{18}O_2$ experiment (Fig. 2.6) and assuming that the solution potential experienced by the active site is effectively set by the rapid interconversion of H_2 and H^+ (and thus could be as low as -0.4 V), the rate of reactivation is predicted to exceed 100 s^{-1} at 20 °C [71]. Thus, k_A should not determine the overall catalytic rate of O_2 reduction to H_2O as the rate of inactivation (k_I) is much lower: Evans *et al.* measured the initial change in current due to O_2 introduction and found a reaction rate of 0.45 s^{-1} for Hyd-1 (under 10% O_2 and at 30 °C) [71]. In a related respiratory hydrogenase (MBH of *Ralstonia eutropha*) Cracknell *et al.* found inactivation rates of 0.19 s^{-1} and 0.31 s^{-1} (under 25 % O_2) at 20 °C and 30 °C respectively. Noting the temperature difference, the above rates are matched closely by the rate of 0.28 s^{-1} obtained here for direct $^{18}O_2$ reduction to $H_2{}^{18}O$ at 20 °C. The agreement between these values is convincing evidence that both types of experiment measure the same process.

Further evidence is provided by the experiments on the Hyd-1 P242C variant. Figure 2.9A highlights the importance of exclusive Ni-B ('Ready' state) formation in response to O_2 exposure. It is apparent that the native enzyme attains a steady state of inactivation (r_I) and reactivation (r_A) at a given O_2 concentration, so that the fraction f of active enzyme may be expressed as [71]:

$$f = \frac{r_A}{r_A + r_I} \tag{2.1}$$

The P242C mutant, which forms a mixture of easily reactivated Ni-B and other states that reactivate slowly, continuously loses activity, soon approaching zero [71]. Figure 2.9B showcases the rate of H_2O production by native and mutant enzyme,

with the activity of Hyd-1 P242C similarly diminishing nearly to zero over time. The comparison of these two experiments implies that the ability of an enzyme to form exclusive Ni-B is not just involved in but crucial to both O_2-tolerance, as defined by sustained H_2-oxidation in the presence of O_2, and to catalytic O_2 reduction to harmless water.

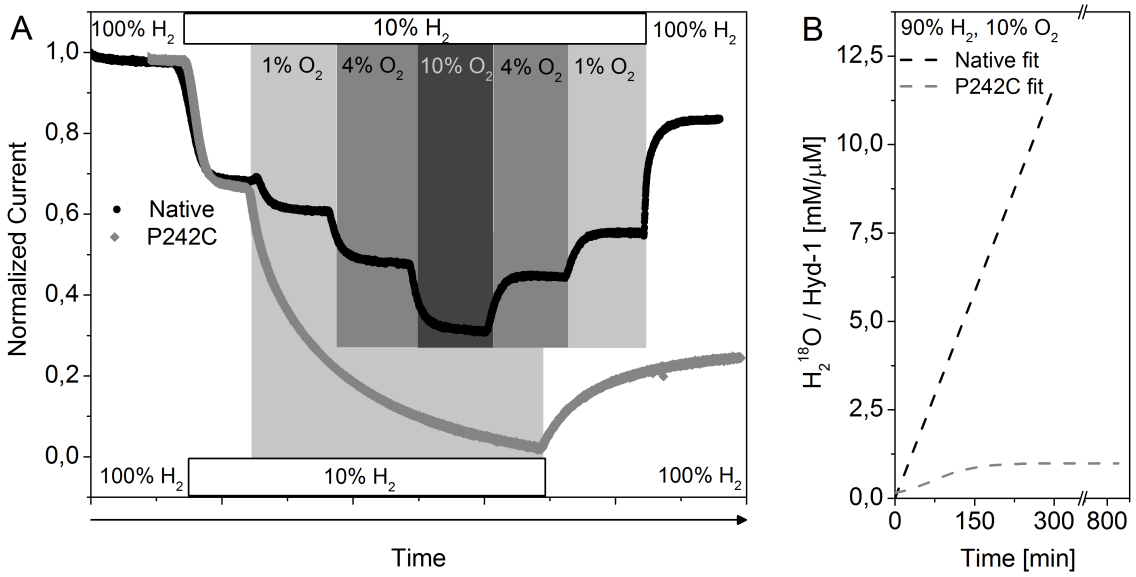

Figure 2.9 Hyd-1 WT and P242C Response to O_2:
(A) Chronoamperometry of Hyd-1 on a rotating PGE electrode. The hydrogen oxidation current is normalised to starting activity. The enzyme films were exposed to the indicated O_2 atmospheres in the presence of 10% H_2 while a potential of 0 V vs. SHE was applied. The experiments were carried out by Dr. R. M. Evans [71] and the data kindly provided for reproduction in this comparison figure.
(B) Water production from 90% H_2 and 10% O_2 by native and P242C Hyd-1

Before the completion of this chapter Lauterbach *et al.* published a study measuring the products of O_2 reaction with a related enzyme; the soluble (cytoplasmic) NAD^+-reducing hydrogenase (SH) from *Ralstonia eutropha* [50]. (For an introduction to this enzyme and a discussion of its tolerance to O_2 see Chapter 1.1.4). The aim of the study was, as in this thesis, to explore the products and mechanism of O_2 tolerance. At this point it is prudent to dicuss their findings as well as the differences between both surveys. While the structure of SH is unresolved, it is known that SH contains labile flavin mononucleotide (FMN) and is composed of both a hydrogenase and a NADH dehydrogenase module [53, 132]. Thus the SH has even more potential sites for O_2 attack than Hyd-1 and it is harder to ascribe a given product to a specific site and reaction. With this in mind, Lauterbach and co-workers found that, overall,

H_2O was produced at equivalent rates to H_2O_2. In contrast to Hyd-1, only a short 5 - 7 min linear phase of O_2 reduction to H_2O was observed, with activity ceasing completely after 20 min. At least half of the H_2O produced could be attributed to O_2 reaction at the diaphorase subunit, whereas all of the H_2O_2 was produced by the hydrogenase module. Although the authors discussed H_2O_2 decomposition to water as a major pathway, this pathway was not investigated, so that the interconnections of O_2 reduction pathways in SH remain unresolved. As a result it is not possible to connect an observed product, *e.g.* H_2O, to a specific origin or reaction. Since there are also no comparable rates from other experiments under similar [O_2] conditions, these results cannot be related to predictions from O_2-tolerance models. The necessary experiment, to determine tolerance to O_2 in SH and to obtain the corresponding rates, would be to evaluate O_2-based inactivation electrochemically under reactivating conditions, *i.e.* potentials between the H_2/H^+ equilibrium potential (E_{eq}) and E_{switch}, as established by Cracknell, Evans and co-workers for Hyd-1 [58, 71].

Returning to the discussion of *E. coli*, we can now consider the implications of O_2 tolerance for the organism. Hyd-1, in its biological context, is anchored to the perisplamic side of the inner membrane together with its cognate cytochrome *b*. Through the associated cyt *b*, Hyd-1 passes electrons from H_2 oxidation to the cytoplasmic side of the membrane for reduction of menaquinone or, under microaerobic conditions, preferentially ubiquinone [79, 133, 134]. The destiny of the resulting quinol is not firmly established, but the available evidence suggests that a co-expressed high-affinity cytochrome *bd*-II oxidase is the most likely recipient (Ch.1.2) [83]. In this short respiratory electron transport chain between H_2 and O_2 the two enzymes will contribute to the generation of a trans-membrane electrochemical gradient. In the case of O_2-attack at the Hyd-1 active site, the electron flow is temporarily reversed and reduction of O_2 to H_2O now takes place at the hydrogenase instead of the oxidase active site. The result is a *short circuit* rescue mechanism, disposing of O_2 through combustion. Given the high cost of complex enzymes and the potential disruption to metabolism, avoiding damage to the active site in this way is energetically essential for the bacterium.

As implicated by the experimental results and illustrated by the above analogy, *E. coli* Hydrogenase-1 can also be classified as a high-fidelity four-electron hydrogen-oxygen oxidoreductase. This not only introduces the novel subgroup EC 1.12.3 [(Oxidoreductase).(H_2 as donor).(O_2 as acceptor)] but it also extends the general group EC 1.X.3, which already includes the Fe and Co containing oxidases discussed in Chapter 2.1.2, to include Ni as an active element. While the catalytic rates of oxidase activity in Hyd-1 are just one order of magnitue slower than those measured for the di-iron Alternative Oxidase (> 5 s^{-1}) [135], the rates observed in many Cu containing oxidases, *e.g.* Cytochrome *c* oxidase (ca. 100 s^{-1}) [93, 136] or blue Cu oxidases (ca. 10 to 300 s^{-1}) [137, 138, 139], are much higher.

The 'new' enzymatic O_2-activating role for Ni has interesting implications. Copper, only soluble in oxidising environments, was available to biology much later in earth's history than Ni or Fe [140, 141]. The [NiFe]-hydrogenases are considered to be among the most ancient enzymes [142]. Hydrogen released from rock formations in aqueous environments, by oxidation of Fe(II) minerals, from hydrothermal vents and volcanic sites was accessible to organisms from the very beginning of life and thus long before O_2 levels began to rise [141]. It is intriguing to think how a slow rise in molecular oxygen concentrations, *e.g.* from $<$ 10 ppm 2.5 billion years ago to 1000 ppm 1.5 billion years ago [141], would have enabled and driven hydrogenase evolution. At first, tolerance to transient exposure would have simply averted irreversible poisoning and avoided the energetic cost of damaged enzyme. Later, at concentrations where O_2 becomes a viable substrate for respiration, the ability to sustain H_2 oxidation in a respiratory chain with high-affinity iron-containing (cytochrome *bd*) oxidases, would have delivered a truly productive competitive advantage.

2.4 Conclusion

This chapter has established that the respiratory [NiFe] hydrogenase Hyd-1 from *E. coli* is a four-electron hydrogen|oxygen oxidoreductase. As such it catalyses the reaction $2\ H_2 + O_2 \rightarrow 2\ H_2O$, which is equivalent to classic hydrogen combustion, though in a ping-pong-like mechanism. This activity is maintained over a prolonged period of time in the sustained presence of O_2 without permanent or accumulative inactivation of the enzyme. Under 90% H_2 and 10% O_2 at least 86% of H_2O produced by Hyd-1 can be assigned to a direct four-electron pathway occurring at the [NiFe] active site. The remaining 14% of H_2O detected is seen to arise from much slower side reactions, through H_2O_2 or O_2^- pathways. In a complex redox system with low-potential relay centres, fed with a steady supply of electrons, side reactions are unavoidable. It was therefore of great importance to experimentally resolve the interconnected pathways of reactive oxygen species formation and decomposition, especially of H_2O_2, in order to identify side reactions and to be able to account for the origin of the H_2O produced.

The use of isotope ratio mass spectrometry to characterise the oxidase activity in Hyd-1, in which H_2O is the definitive principal product of O_2 reaction with Hyd-1, is strong evidence in support of the catalytic O_2-tolerance model; this is further supported by the fact that the determined catalytic rates closely match those predicted from the model as well as independent electrochemical measurements of sustained activity in the presence of O_2. This suggests that both methods measure the same process. Finally, experiments with the O_2-sensitive Hyd-1 variant P242C establish that both O_2-tolerance and catalytic H_2O production crucially depend on exclusive formation of the rapidly reactivated Ni-B state as an intermediate.

When considered together with previous work, it is thus possible to conclude that catalytic direct four-electron reduction of O_2 to H_2O at the active site, with essential supply of stored electrons from the proximal and medial FeS clusters, is indeed the chemical basis of O_2-tolerance in respiratory [NiFe] hydrogenases, as exemplified by *E. coli* Hyd-1.

Chapter 3

Hyd-1 Quaternary Structure and its Impact on Electron Transfer and O_2-Tolerance

3.1 Introduction

3.1.1 Queries arising from the Hyd-1 Crystal Structure

The crystal structures of 'standard' (strongly O_2-inhibited) [NiFe] hydrogenases, such as the *D. fructosovorans* hydrogenase (Fig. 1.2C), have been known for many years, but only recently have the structures of O_2-tolerant hydrogenases of the subgroup of membrane-bound respiratory [NiFe]-hydrogenases, isolated from *Hydrogenovibrio marinus*, *Ralstonia eutropha H16*, *Escherichia coli* and *Salmonella enterica*, been resolved [65, 56, 64, 143]. These new structures not only led to the discovery of the novel [4Fe-3S] cluster, which is essential in bestowing O_2-tolerance as discussed in Ch.1.1.4 and Ch.2, but they also show an interesting quaternary organisation.

The crystal structure of *E. coli* Hyd-1 shows an $(\alpha\beta)_2$ dimer of heterodimers with a C2 symmetry, in contrast to the monomer of heterodimers found in standard hydrogenase crystal structures (see Fig. 1.2 C and D and inset in Fig.3.1) [64]. *In vivo*, the cognate cytochromes of Hyd-1 are integrated into the membrane [79, 133], and isolation of a stable complex in solution is expected to be difficult. Indeed, the first crystal structure obtained for Hyd-1 did not include its cognate cytochrome *b* [64]. A subsequent effort with the Hyd-1 variant P242C (the one actually depicted in Fig. 3.1) however, included one cytochrome attached to one of the small subunits [131]. While the helical membrane anchor of this small subunit runs smoothly along the cytochrome's flank, the membrane anchor of the other small subunit wraps around the cytochrome in a disorderly fashion. One might suspect this second membrane anchor to act in an accidentally stabilising manner after the loss of its own cytochrome.

Perhaps the most intriguing observation is the fact that the distance between the two distal clusters in Hyd-1 is only 12.2 Å. In a survey of electron transfer proteins, Page and co-workers calculated a distance of up to 14 Å to be generally short enough to allow electron transfer of sufficient speed between an enzyme's redox centres as not to impose a limit on the rate of catalysis [144]. At this point it should be noted, that

the latter finding has led to a rather widespread conception in the field that there exists a 14 Å cut-off distance for electron transfer; this is of course inaccurate at best. Nonetheless, comparison of the inter distal cluster distance to the distances between the other iron sulfur clusters in Hyd-1 (ca. 12.2 Å *vs.* 7.7 and 10.6 Å, Fig.3.1), strongly suggests that electron exchange between the two distal clusters should not only be possible but that it might occur readily and routinely.

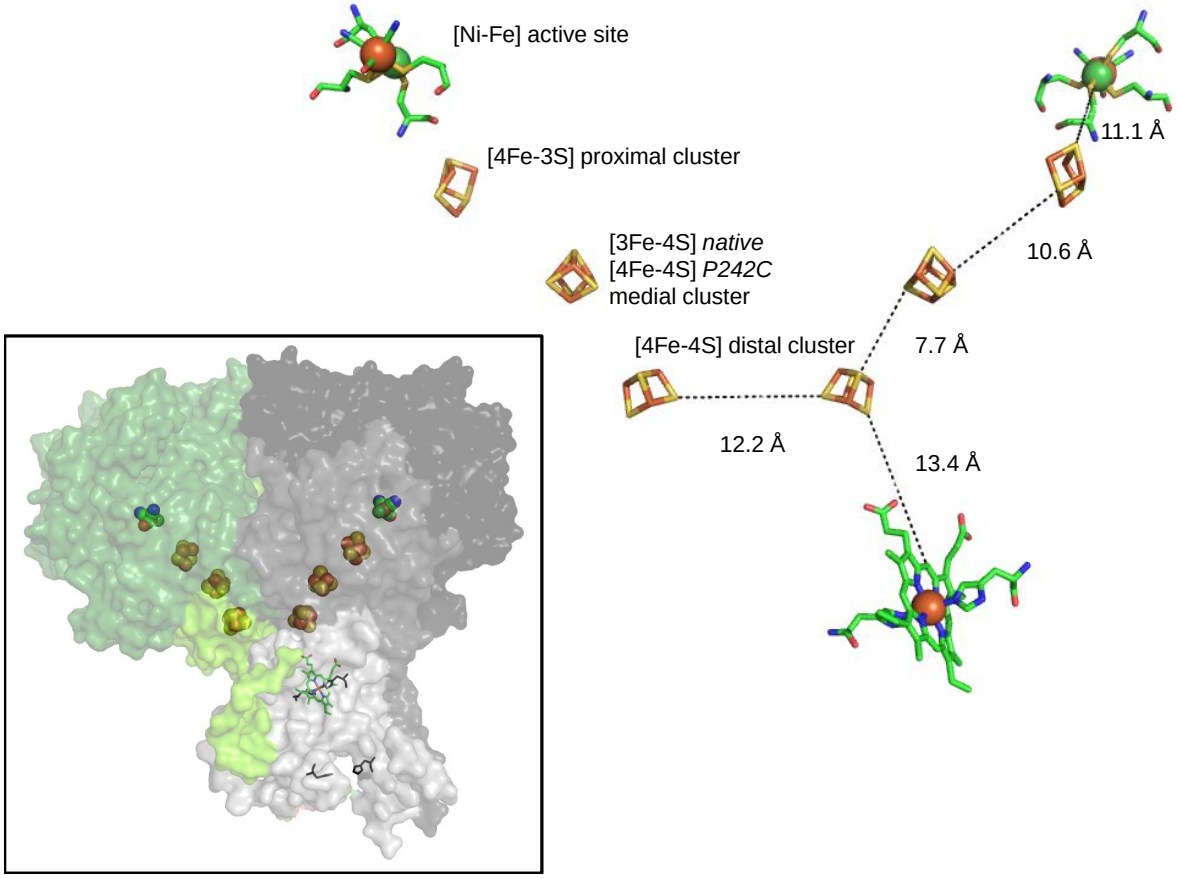

Figure 3.1 *E. coli* Hydrogenase 1 Crystal Structure and Redox Centres: The Hyd-1 structure shown here is of the P242C variant in which the medial cluster is converted to a lower potential [4Fe-4S] cluster from the native [3Fe-4S] cluster (PDB: 4GD3). **(Inset)** Overall structure consisting of an $(\alpha\beta)_2$ motif displayed in surface representation with highlighted redox centres. The two halves of the dimer of heterodimers (Dimer) are shown in green and grey with darker to lighter shades representing the respective large, small (and cytochrome) subunit. **(Main)** [NiFe] active site, iron sulphur clusters and intact *b*-type haem labeled with edge-to-edge electron transfer distances.

Shomura and co-workers, having solved the similarly heterotetrameric structure of the membrane-bound hydrogenase (MBH) from *H. marinus*, ruled out the possibility that dimerisation might be an artefact of crystallisation (crystal packing) on the basis (of the arguably insufficient evidence) that the contact between heteromers adds up to 11% of the total surface area of the protein and that the subunits have precisely

matching orientations; the latter pointing towards purposeful joint alignment on the cell membrane [65]. Using a different approach, the PISA (Proteins, Interfaces, Structures and Assemblies) software aims to evaluate oligomer formation and protein interfaces by calculating the binding energy and entropy of dissociation of the proteins in question, calibrated against known macromolecular complexes [145].

Table 3.1 shows an assessment of the oligomeric assembly of all known [NiFe] hydrogenase structures, evaluated with Pymol and PISA software, based on the relevant PDB files. All the O_2-tolerant hydrogenases resolved so far, marked with an asterisk in the table, are membrane-bound *in vivo* and all but the *R. eutropha* MBH show dimers of heterodimers $(\alpha\beta)_2$ in the crystal structure. Frielingsdorf and co-workers did, however, show that the latter could be isolated in a trimeric $(\alpha\beta\gamma)_3$ supercomplex, including cytochrome *b*, as identified by static light scattering [146]. For the O_2-tolerant hydrogenases the approximated free energy of assembly dissociation (ΔG^{diss}) within the heterodimer is twice as large as the corresponding inter-heterodimer value (60 *vs.* 30 kcal/mol), and appears to be slightly higher than in the standard hydrogenases. The *A. vinosum* hydrogenase is the only standard hydrogenase found to crystallise as a dimer, albeit with only half the calculated ΔG^{diss}. The distance between the two distal iron sulphur clusters, around 12.5 Å in the O_2-tolerant enzymes, is a little higher in the *A. vinosum* hydrogenase, at 14 Å, but should still allow for electron transfer; this will be considered further in the discussion (Ch. 3.3).

In the context of *E. coli* Hyd-1, it is worth considering that Wait and co-workers carried out an enzymatic membrane-less fuel cell experiment, with a Hyd-1 covered electrode as H_2-oxidising anode and bilirubin oxidase at the cathode, in which they observed that an oxidatively inactivated Hyd-1 electrode could be revived by connecting a second anode with active Hyd-1 [147]. This effect, in which hydrogenases from one electrode provide electrons to reactivate hydrogenases from the Ni-B state on the other electrode, was likened to jump-starting a car with a flat battery. Inspired by this concept, Volbeda and co-workers suggested that the proximity of the distal clusters in Hyd-1 might enable a similar jump-start reactivation of Ni-B to operate between the two halves of the enzyme [64].

Table 3.1 Oligomeric assembly of all known [NiFe] hydrogenase structures Based on crystal structure visual assessment and PISA (Proteins, Interfaces, Structures and Assemblies) software calculations [145], the oligomeric assembly of large subunit (α) and small subunit (β) is presented along with PISA estimates of the free energy of assembly dissociation (ΔG^{diss}) in kcal/mol of large and small subunit within one heteromer (α:β) and between two heteromers (αβ):(αβ), where applicable. The proximity (edge-to-edge) of adjoining distal iron sulphur clusters was measured with the Pymol software. Organisms and enzyme PDB codes: *Escherichia coli* (3UQY), *Hydrogenovibrio marinus* (3AYY), *Salmonella enterica* (4C3O), *Ralstonia eutropha* (3RGW), *Allochromatium vinosum* (3MYR), *Desulfovibrio fructosovorans* (1FRF), *Desulfovibrio gigas* (1FRV), *Desulfovibrio desulfuricans* (1E3D),*Desulfovibrio vulgaris* (1WUL), *Desulfovibrio vulgaris* Hildenborough (2WPN), *Desulfomicrobium baculatum* (4KN9). *oxygen tolerant enzyme; †described as trimeric $(\alpha\beta\gamma)_3$, including cytochromes, by Frielingsdorf *et al.* [146] in gel filtration experiments but not in the crystal structure; ‡[NiFeSe] hydrogenase

Organism (Hydrogenase)	**Assembly**	**ΔG^{diss} [kcal/mol]**		**Distal Cluster Proximity**
		α:β	**(αβ):(αβ)**	
E. coli Hyd-1*	$(\alpha\beta)_2$	60	32	12.2 Å
H. marinus MBH*	$(\alpha\beta)_2$	64	27	12.6 Å
S. enterica Hyd-5*	$(\alpha\beta)_2$	62	32	12.7 Å
R. eutropha MBH*	$(\alpha\beta)^{\dagger}$	57	–	–
A. vinosum Hyd	$(\alpha\beta)_2$	53	16	14.0 Å
D. fructosovorans Hyd	$(\alpha\beta)$	53	–	–
D. gigas Hyd	$(\alpha\beta)$	54	–	–
D. desulfuricans Hyd	$(\alpha\beta)$	51	–	–
D. vulgaris Hyd	$(\alpha\beta)$	57	–	–
D. baculatum Hyd‡	$(\alpha\beta)$	53	–	–
D. vulgaris H Hyd‡	$(\alpha\beta)$	30	–	–

When Sawers and Boxer first isolated *E. coli* Hyd-1 in 1986 they estimated the total molecular mass of Hyd-1 to be 200 (± 20) kDa, a size in agreement with a multimeric assembly, as now observed in the crystal structure (though the iron content, calculated for the enzyme on the basis of this mass, was about 50% too low) [79]. Without more detailed structural information there was little inspiration to be translated into further meaningful inquiry. The revelation of the Hyd-1 dimer of heterodimers quaternary structure now raises the following questions: What is the oligomeric state of Hyd-1 in the samples used in current and past research? What is the dominant, stable form and is this form catalytically and physiologically relevant? Is it possible to isolate distinct dimers and monomers of heterodimers to test for cooperation? If so, and if there is cooperation, does working with a partner help the enzyme in dealing with oxygen. If O_2-tolerance is indeed affected, which part of the mechanism is affected?

3.1.2 Protein Oligomerisation in Biology

It is very common for proteins to form dimeric or otherwise multimeric complexes [148], since *"All proteins require physical interaction with other proteins in order to perform their functions."* [149]. While the majority of proteins form homomers, interactions with other proteins, in particular in the case of enzymes, often come in the form of at least transient or indeed obligate heteromers [149]. The purpose of protein oligomerisation is no straight-forward question and a variety of explanations and observed functions exist.

In the simplest case, dimerisation is beneficial for the development of novel protein functions. Changes at protein interfaces, evolving more easily than protein folds, facilitate the development of metal-binding and active sites, enabled by amino acid residues from two or more subunits. The underlying oligomerisation is usually homomeric, as found in the prominent example of the HIV protease, and the carbon monoxide dehydrogenase discussed below [149, 150].

Modulation of an existing function of the constituent monomers is probably the most well-known outcome of protein oligomerisation, with the prominent example of cooperativity in the oxygen-carrier protein hemoglobin. In enzymes, activity modulation can be either fine-tuned as in classic allostery, in which binding of an effector molecule affects conformational changes to adjust activity to a new level, or extend as far as a binary on-off switch between dimeric and monomeric forms, as observed for the triose phosphate isomerase [151, 152]. In a similar fashion, whole signalling pathways and regulatory networks may depend on dimerisation events. Many G-protein-coupled receptors, ubiquitous cell-surface signal receivers, require a dimerisation event to take place, either before or after agonist binding, for successful signal transduction [153, 154]. Gene expression, in which transcription requires assembly of multimeric complexes at specific DNA regions, is an example where oligomeric assembly is not only essential to the main function but also affords an added layer of complexity, allowing for subtle regulation through varied complex composition [155].

Membrane-bound proteins are especially inclined to the formation of larger complexes, even whole functionally organised membrane domains, driven by crowding and protein geometry, often without the need for special interactions. In this context it is of interest that structural membrane domains of different fluidity are found to be important in facilitating diffusion in crowded areas [156]. As such, a possible arrangement of respiratory hydrogenases into even larger structured assemblies *in vivo* could play a role in orchestrating quinol supply. On a smaller scale, integral membrane proteins form channels and pores, *e.g.* (homo-) tetrameric K^+ channels and aquaporins, for transport of substrate across the membrane [157, 158].

When oligomerisation turns into polymerisation, as in the many structural proteins, such as collagen and tubulin, complex formation serves to kill two birds with one stone: dynamically adjustable size and economy in use of the coding DNA [148].

A final potential benefit of dimerisation is increased stability. However, while theoretical arguments, more internal interactions and less solvent-exposed surface area, seem intuitively convincing, evidence to this effect is to date mostly anecdotal and oligomerisation is found to play only a very minor role in heat adaptation, where it might be expected to benefit most [149, 159].

Returning to electron exchange across separate subunits, the carbon monoxide dehydrogenase 1 (CODH1) from *Rhodospirillum rubrum*, an enzyme that carries out reversible oxidation of CO to CO_2, is a most interesting case of dimerisation (Fig.3.2). The enzyme contains five iron sulphur clusters arranged in a V-shape, so that the two [Ni-3Fe4S] active sites, known as 'C' clusters, are found at one end each. From here electrons are passed *via* the two [4Fe4S] 'B' clusters to the one [4Fe4S] 'D' cluster [160]. The latter is shared between the two subunits which contribute two ligating cysteines each, representing a good example of functionality arising at the interface as discussed above. Though fanciful, one cannot help thinking of a V-twin engine. Curiously, the two subunits overlap in such a way that the 'B' cluster adjacent to the active site is actually part of the other monomer (see Fig.3.2). Thus, electrons pass from the active site of one monomer *via* an iron sulphur cluster in the other monomer to a shared cluster

before leaving the enzyme. It is not known what the purpose of this arrangement is and it would probably be impossible to test by trying to separate the subunits, both because of the high dissociation energy and the expected instability and activity loss of the resulting product.

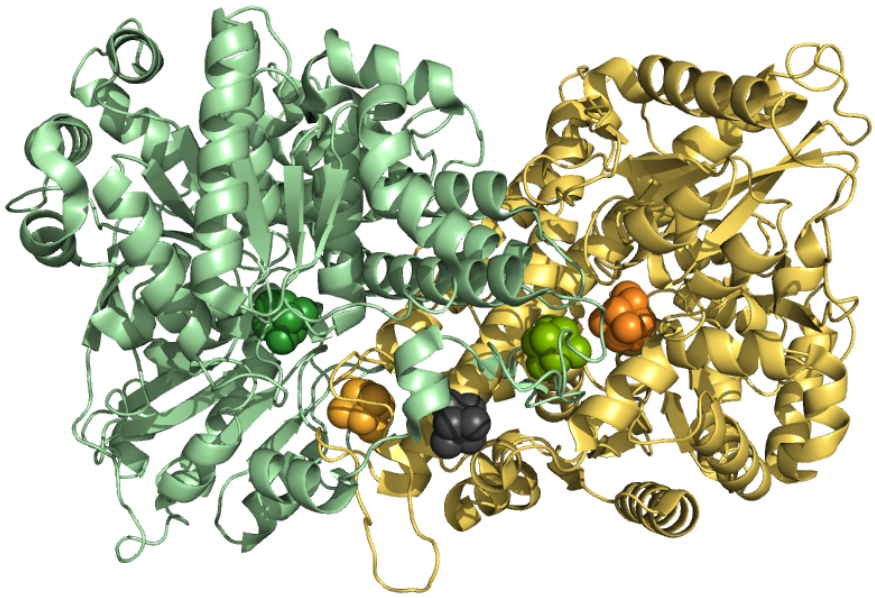

Figure 3.2 Crystal Structure of Carbon Monoxide Dehydrogenase 1: The quaternary structure is that of a homodimer. The protein backbone is shown in cartoon representation with one subunit in pale green and the other in yellow. The iron sulphur clusters, separated from their nearest neighbours by between 10 and 11 Å, are shown in sphere representation in the colour theme of the ligating subunit and in grey in case of the central shared cluster. The active sites, the [Ni-3Fe4S] 'C' clusters [160], are positioned at the end of the 'V'-shaped cluster arrangement in slightly darker shades. (*Rhodospirillum rubrum*, PISA: ΔG^{diss} ca. 50 kcal/mol [145], PDB: 1JQK, PyMOL)

In *E. coli* Hyd-1 there is a much better chance of separating the oligomeric assembly into the functional heterodimers, as observed in the *Desulfovibrio* hydrogenase structures, to investigate whether any kind of additional function or form of cooperativity is afforded by the arrangement.

On a final note, it should not be omitted that the [Fe]-only hydrogenases can also be found in a dimeric (2α) state in which there is overlap between subunits (Fig.1.2A.), but unlike in CODH there is no sharing or swapping of ligands, cofactors or electron transfer clusters.

3.2 Results

The following experiments will first assess whether and how distinct *E. coli* 'Dimer' (dimer of heterodimers) and 'Monomer' (monomer of heterodimers) species of Hyd-1 may be isolated. To this end Ch.3.2.1 and Ch. 3.2.2 look at the enzyme's purification and separation, while Ch.3.2.3 addresses the composition of isolated fractions. Once this prerequisite work has been dealt with, Ch.3.2.4, 3.2.5 and 3.2.6 introduce experiments suitable to identifying, or indeed ruling out, any catalytic characteristics, such as differences in overpotential for H_2 oxidation or response to O_2 exposure, that might be affected by the enzyme's quaternary structure.

In an effort to increase readability and simplicity, this chapter adopts a terminology in which 'Dimer' and 'Monomer' are short for 'dimer of heterodimers' and 'monomer of heterodimers', implying a composition of two large subunits (2×64.6 kDa), two small subunits (2×36.8 kDa) and potentially cytochrome *b* (at 27.6 kDa) for the 'Dimer' and only one subunit each for the 'Monomer'. This assumption is verified by SDS PAGE and UV-vis experiments as shown further below (Ch.3.2.3).

3.2.1 Dissecting the Hyd-1 Purification

In a first attempt to evaluate the sample composition and oligomeric state of purified Hyd-1, samples were taken at every stage in a 'standard' Hyd-1 Ni-NTA purification protocol, *i.e.* the protocol used for almost all Hyd-1 preparations for the Armstrong and Fontecilla-Camps groups and the resulting host of publications (see Ch.5.8 for the protocol and Tab.3.2 below for sample description).

The early stages of the purification protocol yield the cloudy samples S1 and S2, containing floating solids and bound protein, which were not used further. All other samples were analysed by native polyacrylamide gel electrophoresis (PAGE) as shown in Figure 3.3. In native, non denaturing, gel electrophoresis Hyd-1 bands would be expected to be visible at 101 kDa (large subunit 64.6 kDa plus small subunit 36.8 kDa) or multiples thereof. Attached *b*-type cytochromes (at 27.6 kDa) would shift this accordingly.

Table 3.2 Description of samples taken at various stages throughout Hyd-1 purification

Sample	Protein [mg/mL]	Solution Description
S1	NA	lysed cell solution
S2	NA	solid cell membranes
S3	7.7	homogenised membranes
S4	7.4	solubilised membranes
S5	7.6	solubilised membrane proteins
S6	6.7	Ni-NTA column flow-through
S7	1.3	Ni-NTA column wash
S8	0.8	Ni-NTA column eluted peaks (Hyd-1)
S9	nil	buffer exchange flow-through
S10	17.4	concentrated Hyd-1
S11	8.2	desalted Hyd-1

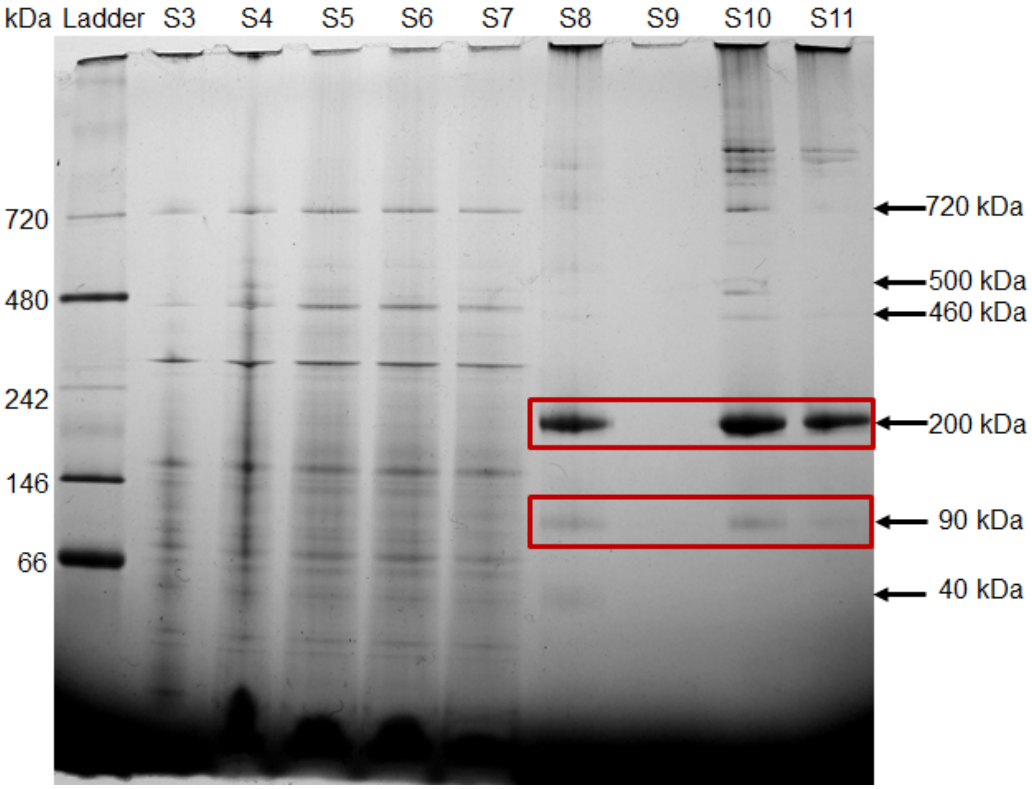

Figure 3.3 Native PAGE of samples taken at different stages of Hyd-1 Purification: The analysed samples S3-S11 are described in table 3.2. A pre-cast 4-16% BisTris gel was run for approx. 130 min at 150 V (see Ch.5.10 for details) and 1.4 µL of each sample were applied to the indicated lanes. Putative Dimer and Monomer bands are highlighted in red.

Considerable aggregate, probably membrane debris, is found in samples S3 and S4 (homogenised and solubilised membranes), with all other bands matching those of the membrane proteins found in the supernatant after centrifugation (S5). These detergent-solubilised membrane proteins are loaded onto a Ni-NTA affinity column. Both the column flow-through and column wash samples (S6 and S7) do not differ visibly from sample S5, indicating that Hyd-1 expressed from the chromosome at native levels makes up only a small fraction of total membrane protein. After elution from the affinity column (S8) the most prominent band is found at around 200 kDa with a fainter band around 90 kDa. A small band around 40 kDa and a set of distinct bands of larger proteins or complexes (ca. 460, 500, 720, <800 kDa) are just visible. Especially noticeable is a large amount of non-mobile fraction or aggregate at the top of the lane. This pattern is repeated in samples S10, with stronger large complex bands, and S11, after concentration and desalting respectively. Not surprisingly, the small protein band is lost in the concentration step, as the spin concentrator filter has a 50 kDa cut-off.

During the purification stage on the Ni-NTA affinity column, two overlapping elution peaks are observed under 'standard protocol' conditions, with a Buffer C (750 mM Imidazole) gradient of 100% over 27 min at a flow rate of 1.5 mL/min. These two peaks are commonly pooled. Figure 3.4A shows this elution profile of Hyd-1 from a Ni-NTA column with the absorbance recorded over the elution volume; A_{420} probing both iron sulphur clusters and *b*-type haems, A_{280} probing protein content *via* tryptophan and tyrosine [161]. By 'stretching' the elution gradient (to 100% Buffer C over 50 min at 1.0 mL/min), a total of five distinct peaks or fractions, marked F1-F5, are revealed (Fig.3.4B). While both A_{280} peaks in Fig.3.4A have coinciding absorbance at 420 nm, indicative of high cytochrome levels, only fraction F5 in Figure 3.4B has a prominent (and broad) A_{420} peak.

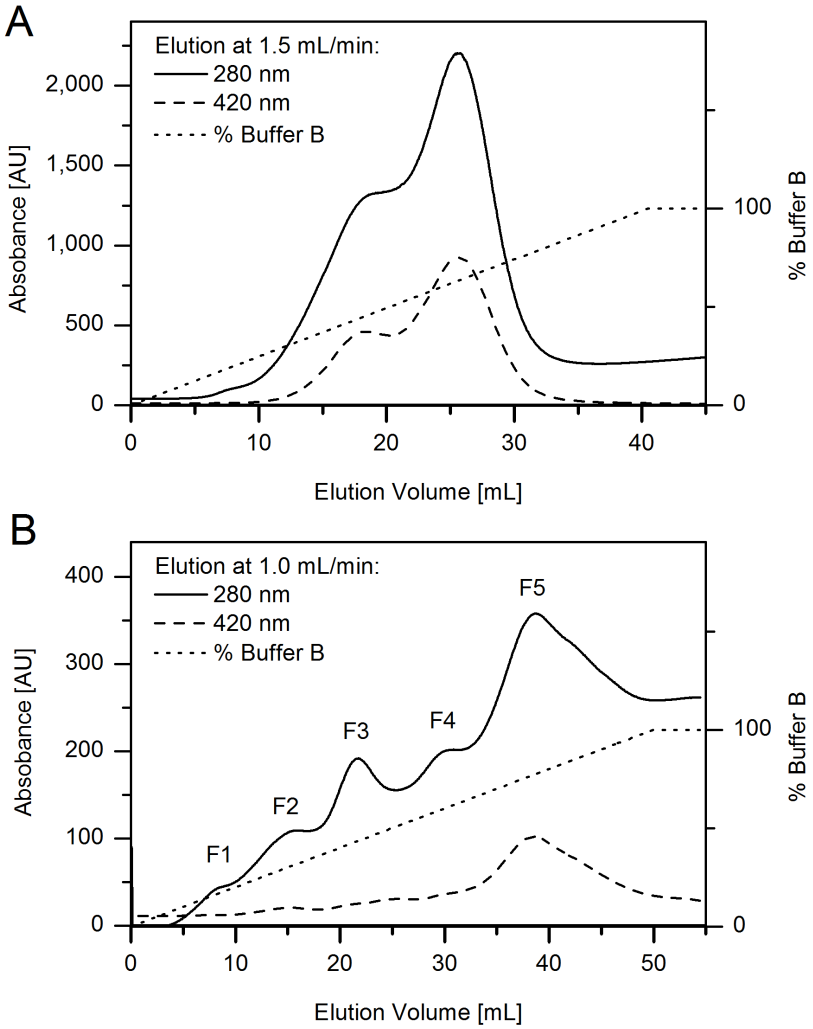

Figure 3.4 Hyd-1 Ni-NTA Affinity Chromatography: Hydrogenase was isolated from solubilised membrane fractions using a HisTrap column and an Äkta Purifier System as described in detail in Ch.5.8.3. In the presented experiments the elution gradient was varied as follows: **(A)** 40 to 750 mM imidazole over 27 min at a flow rate of 1.5 mL/min. **(B)** 40 to 750 mM imidazole over 50 min at 1.0 mL/min. Separately collected fractions are labelled F1-F5. The buffers contain 0.02% Triton X-100.

The isolated fractions F1 to F5 were evaluated by Native and SDS PAGE, as shown in Figure 3.5. Fraction F1 is very dilute and bands are only visible on the SDS PAGE gel (Fig.3.5.B). The bands standing out here are the same low molecular weight bands found in F2 and F3 but not F4 and F5. Fraction F2 is rich in proteins of various sizes, and although Hyd-1 candidates are among them (*e.g.* 200 kDa, Fig.3.5.A), Hyd-1 is far from being the dominant protein in this sample. Fraction F2 is thus precisely the kind of fraction that needs to be identified and discarded when using an elution gradient to obtain pure product. It is therefore of concern that F3, which looks to be part of the first peak in the 'standard' procedure, contains most of the same impurities.

Compared to fractions F1-F4, F5 contains a much greater proportion of non-mobile aggregate, presumably of Hyd-1, visible at the top of the lane. This higher aggregate portion in the late-elution peak might be the result of higher avidity (due to a larger number of histidines from His-tags). All described fractions are compared to a sample of pooled peaks, from a separate purification with a (standard) gradient, which had been exposed to a nitrogen atmosphere at room temperature in a glove box for a week. This 'pooled' sample does indeed contain most of the large molecular weight impurities found in fractions F2 and F3, as discussed above. Like in the similarly pooled samples S8, S10 and S11 (see Tab.3.2), but unlike in the fractions F4 and F5, a band is seen at ca. 100 kDa (Fig.3.5.A). In the following, the occurrence of this putative monomer band is investigated further with the goal of isolating it for catalytic experiments.

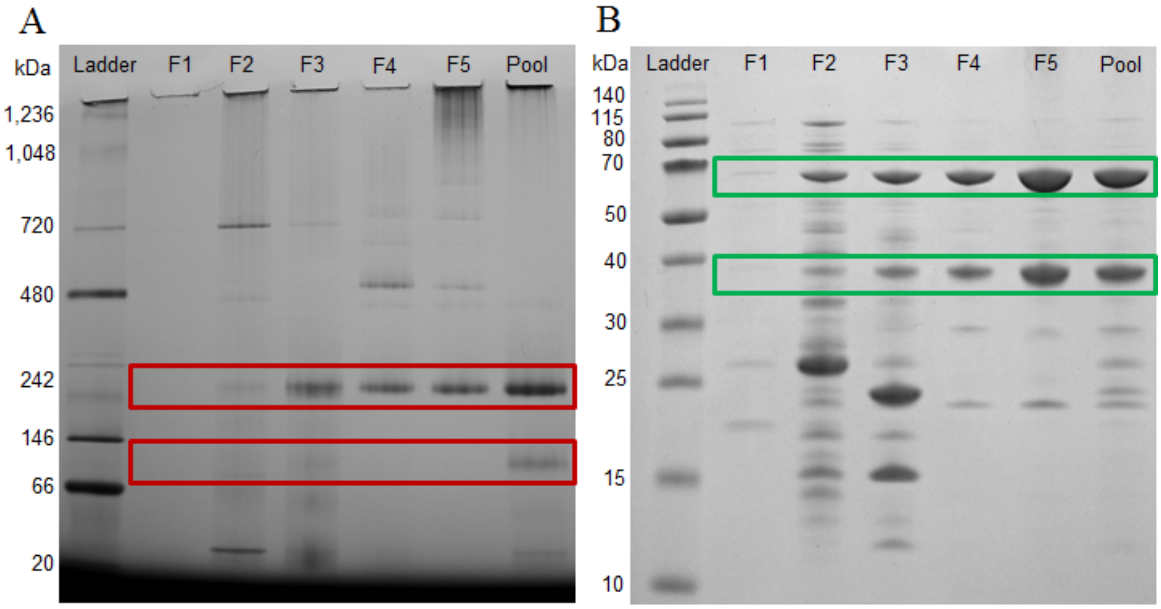

Figure 3.5 Hyd-1 Ni-NTA Purification Gel Electrophoresis: Fractions F1 to F5 from elution with a gradient of 40 to 750 mM imidazole over 50 min at 1.0 mL/min, see Fig.3.4B, are compared to a pooled sample, combining the two large peaks, from a fast elution procedure, such as shown in Fig.3.4A. The latter sample, though previously frozen, was exposed to room temperature in an O_2-free glove box for a week prior to the experiment. **A) Native PAGE** A pre-cast 4-16% BisTris gel was run for approx. 130 min at 150 V with ca. 2-4 µL of protein sample per lane (NativeMark ladder, see Ch.5.10 for details). Putative Dimer (ca. 200 kDa) and Monomer (ca. 100 kDa) bands are highlighted in red. **B) SDS PAGE** A pre-cast 4-12% BisTris gel was run for approx. 50 min at 200 V with ca. 3 µL of protein sample per lane (PageRuler ladder, see Ch.5.10 for details). Hyd-1 large (64.6 kDa) and small (36.8 kDa) subunit bands are highlighted in green.

3.2.2 Separation of Oligomeric States by Size Exclusion Chromatography

To assess the oligomeric composition of isolated Hyd-1 samples further, size exclusion chromatography (SEC) was performed with running buffers of various detergent (and salt) compositions. In general terms, it was found that, in detergent-free running buffer, Hyd-1 forms exclusively large, yet soluble, aggregates that are found to elute in the void volume (V_0 around 8 mL). An increase in detergent concentration (*e.g.* 0.00%, 0.02% and 0.05% Triton X-100) resulted in progressively smaller aggregate peaks and a number of peaks at lower molecular weight, which will be discussed below. Increasing salt concentrations have the opposite effect (NaCl above 150 mM aiding aggregation), which is not surprising for a membrane associated enzyme. The amount of detergent that could be employed was, however, quite limited, since precipitation of detergent at 4 °C was a constant problem throughout all of the experiments undertaken.

The SEC columns were calibrated with Sigma Aldrich's MWGF1000 kit of protein standards. Since the elution volume corresponding to a certain molecular weight depended significantly on the detergent used, and changed even more drastically with each column repacking, the column was recalibrated for each detergent and after every repacking of the column. In addition, alcohol dehydrogenase (ADH) protein standard (150 kDa) was frequently used between sample runs as a helpful guide in evaluating and estimating sample peak positions and confirming column integrity. After purification by Ni-NTA chromatography, concentrated Hyd-1 is stored in 'Buffer C' consisting of 20 mM Tris, 350 mM NaCl, 0.02% Triton. Aliquots of 100 µL of this solution were exchanged into running buffer with the relevant detergents (detailed below) using spin concentrators, and then applied to the SEC column.

Figure 3.6 shows Hyd-1 separation results with the detergent n-Dodecyl-β-D-maltopyranoside (DDM). Four distinct peaks, P1 to P4, are observed in size exclusion chromatography: P1 at the void volume constitutes the soluble aggregate mentioned above and its presence is in accordance with aggregates observed in Native PAGE experiments (Figs. 3.3 and 3.5). At around 430 kDa, P2 probably relates to the larger complexes (around 500 kDa) observed in Native Page, especially in fractions F4 and F5 (Fig. 3.5). Peaks 3 and 4, either side of the 150 kDa marker protein, are assigned as approx. 205 and 95 kDa and are thus putative Dimer and Monomer fractions. The peaks were collected and concentrated using spin concentrators.

Cyclic voltammetry (CV) was used to test each peak for hydrogenase activity. Concentrated aliquots of each peak were applied to a rotating pyrolytic graphite edge (PGE) electrode and briefly activated at low potential (while this did not ensure full activation, the chosen time period of 30 s was the same for every enzyme film). As shown in Figure 3.6, every peak yielded active hydrogenase film, though with significant differences both in the maximum current and voltammogram shape. Generally, the maximum current of an enzyme film would be expected to depend on the amount of applied enzyme. However, here P3 and P4 yield much larger currents than might be expected in comparison to P2 (which had the highest protein content). With regard to the shape of the voltammograms, the Dimer (P2) shows much less dispersion (residual current increase at high potential, see Ch.3.2.5 and [162]) than the other samples. A more regular enzyme orientation within the film, with more favourable interfacial electron transfer, is the most obvious explanation.

Unfortunately, regular precipitation of the protein sample when using DDM caused excessive column blockage and collapse for unknown reasons, excluding DDM from further use despite the promising initial results.

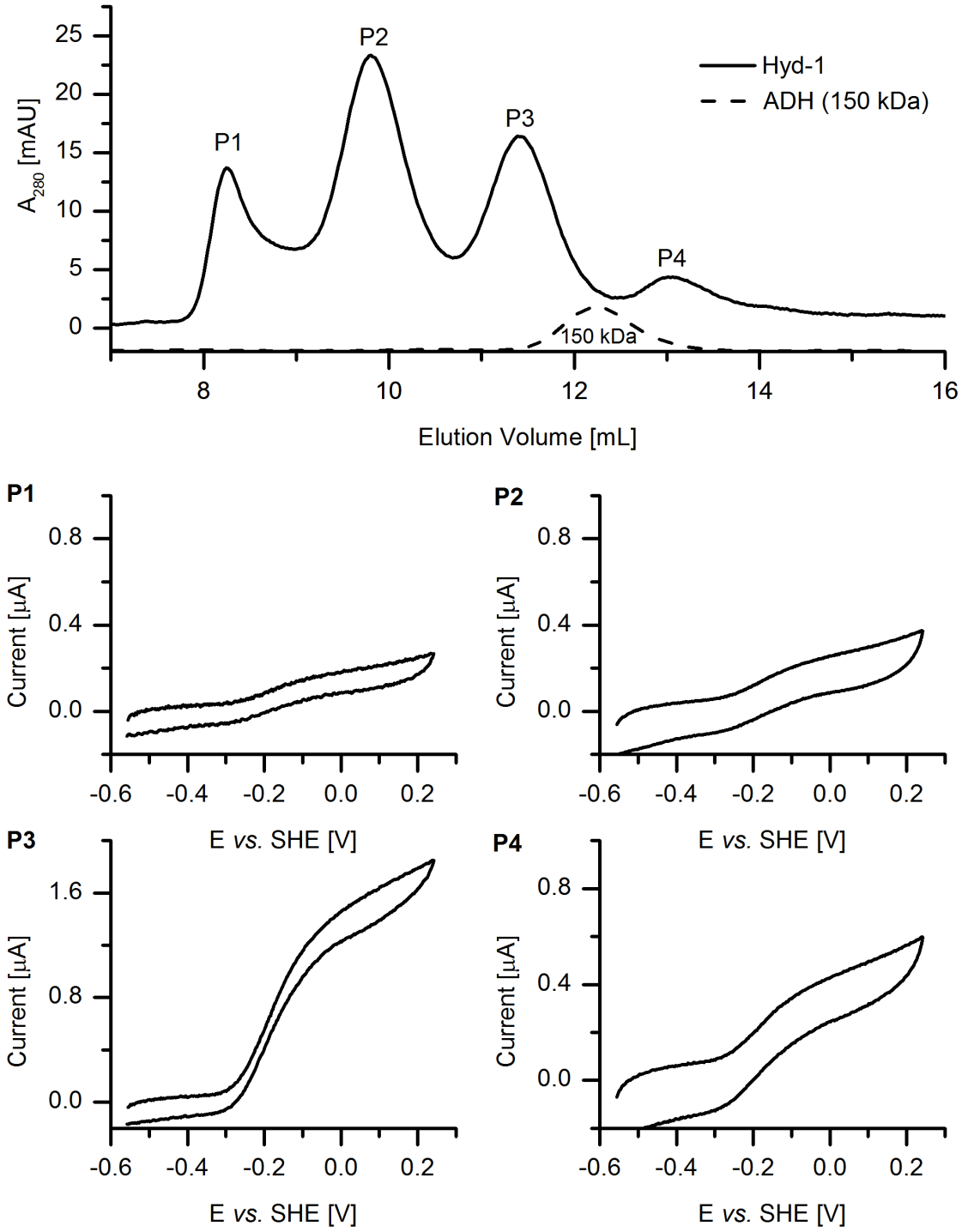

Figure 3.6 Hyd-1 Size Exclusion Chromatography with DDM (Top): Separation of Hyd-1 (pooled fractions) with 0.02 % n-Dodecyl-β-D-maltopyranoside (DDM). The absorbance (A_{280}) is shown over the elution volume, with the elution peak of standard protein ADH (150 kDa) provided for reference. The four peaks (P1-P4) correspond to the void volume (V_0) and approximately 430, 205 and 95 kDa respectively. Conditions: flow at 0.15 mL/min, Superdex 200 HR column (10/30), pH 7, 50 mM Sodium Phosphate, 100 mM NaCl, 4 ℃. The enzyme loaded onto the column was first purified via Ni-NTA affinity chromatography.
Hyd-1 Cyclic Voltametry (Bottom): Concentrated aliquots of the isolated peaks (P1-P4) were applied to a rotating pyrolytic graphite edge electrode (PGE) and subjected to cyclic voltammetry after brief activation at -0.56 V vs. SHE for 30 s. Conditions: 10 mV/s, 30 ℃, 100% H_2, 1000 rpm, MHB pH 6.0

Figure 3.7A shows Hyd-1 oligomer separation in buffer containing 0.02% Triton X-100. A large, well-defined peak at 12 mL and a much smaller peak at 13.5 mL, corresponding to ca. 220 and 110 kDa respectively, can be identified. These peaks are putatively assigned as Dimer and Monomer. The 430 kDa peak found with DDM (Fig. 3.6) is notably absent in this experiment. Significant absorbance due to iron sulphur clusters and haem groups (A_{420}) is found for both the aggregate and the Dimer peaks. The inset (Fig.3.7.A) shows an SEC experiment of the collected Dimer fraction after 5 days of storage at 4 ℃. The majority of the protein fraction elutes at the same volume (12 mL), indicating that the collected dimeric assembly is sufficiently stable to be used in experiments investigating its distinct properties. However, the reproducibility of the oligomer separation experiment with Triton X-100 (major panel Fig.3.7.A) was poor, especially with regard to the presence of the Monomer peak. The following experiments seek to explore and remedy this problem.

Like many other enzymes, Hyd-1 can be conveniently frozen and stored in liquid nitrogen, and this is considered routine practice with this enzyme. While freezing of Hyd-1 is not known to cause any noticeable changes to overall sample activity, subtle differences related to freezing are observed in SEC experiments. For illustrative purposes, Fig. 3.7B shows two extreme examples observed for Triton X-100-based separation. A sample frozen in liquid N_2 immediately following purification and thawed immediately before the SEC experiment (denoted N_2 Dewar) is compared to a sample stored in a -80 ℃ freezer. This latter sample is the result of a sample originally stored in a liquid nitrogen dewar and then thawed, split into smaller aliquots, refrozen and stored at -80 ℃ for convenient and frequent access to small amounts of enzyme, as needed for electrochemical experiments.

The ‘dewar’ sample exhibits the same ca. 400 kDa peak found in the DDM experiment (Fig.3.6); the sample for the DMM experiment was also stored in a dewar prior to use. However, no Monomer peak is found with Triton X-100. In contrast, for the ‘freezer’ sample the ca. 400 kDa peak is absent, while a small Monomer peak can be found.

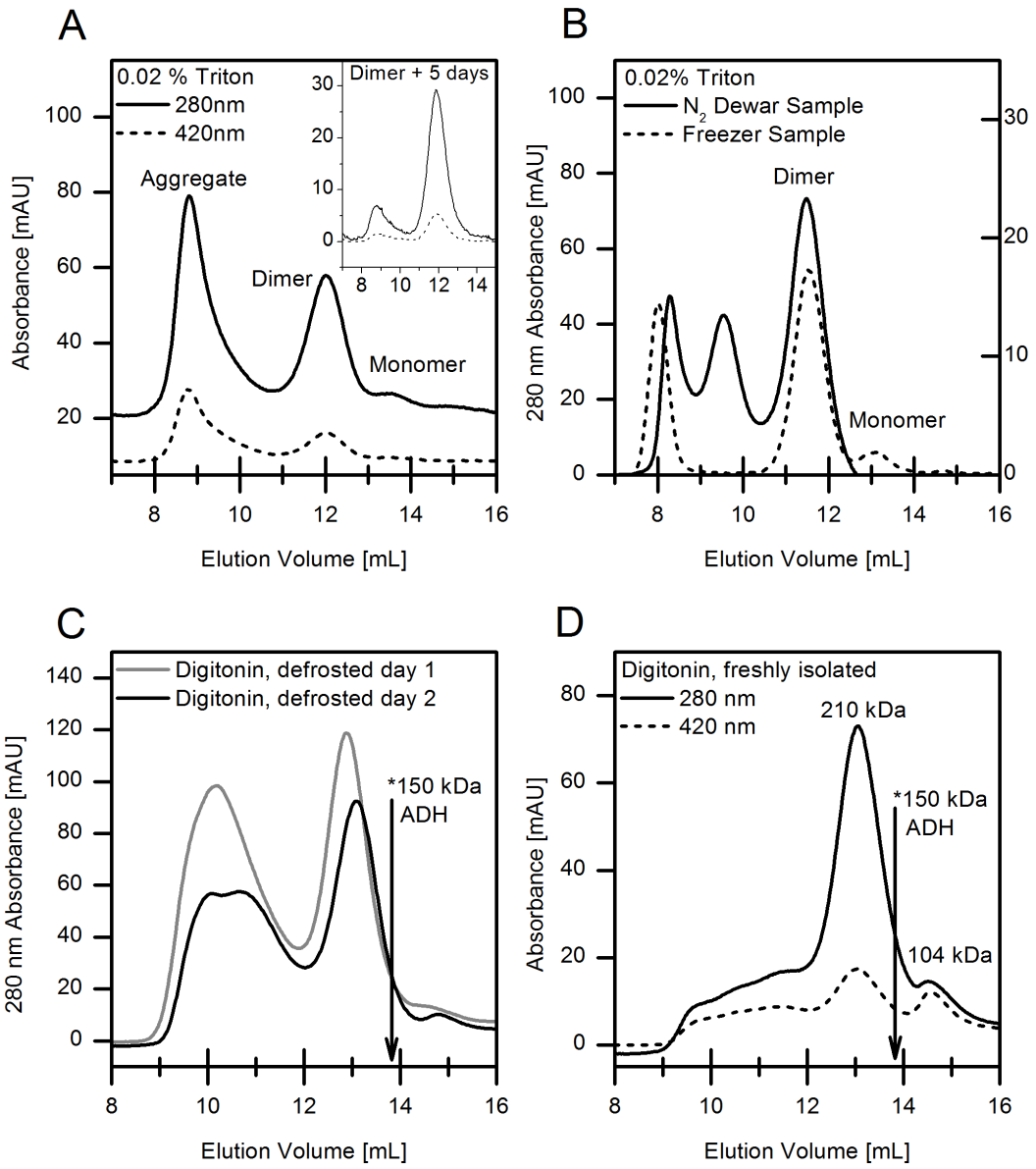

Figure 3.7 Hyd-1 Size Exclusion Chromatography with Triton X-100 and Digitonin: All samples shown were first purified by Ni-NTA affinity chromatography. The absorbance, at 420 and/or 280 nm, is shown over the elution volume with a flow rate of 0.15 mL/min. The arrow and asterisk (*) mark the peak position of 150 kDa Alcohol Dehydrogenase (ADH) protein standard in the respective experiment.
A) Separation of Hyd-1 with Triton X-100, exchanged from Ni-NTA purification buffer (20 mM Tris, 350 mM NaCl, 0.02% Triton; see Methods 5.8) into running buffer prior to the experiment. The peak centred around 12 mL was isolated and stored at 4 °C for 5 days before being subjected to chromatography again, as shown in the inset.
B) Separation of defrosted Hyd-1 samples from the liquid nitrogen dewar and a -80 °C freezer, with Triton X-100.
C) Defrosted, as-isolated, Hyd-1 samples were treated with addition of Digitonin to a final concentration of ca. 1% (wt/vol) for 2 h prior to application to the SEC column. The running buffer contained 0.007% Digitonin. Experiments No. 1 and 2 represent samples of the same defrosted aliquot, run on consecutive days.
D) Freshly isolated Hyd-1 was incubated for 2 h with ca. 1% Digitonin before chromatographic separation in running buffer containing 0.007% Digitonin. The indicated peak molecular weight was calculated from a full calibration (Methods 5.4).
Other conditions: flow at 0.15 mL/min, Superdex 200 HR column (10/30), pH 7, 50 mM Sodium Phosphate, 100 mM NaCl, 4 °C. The column was repacked between experiments A, B and C.

Unfortunately, reproducibility remains poor (not shown): across repeats the peaks vary drastically in size and separation, so that frequently no Monomer can be isolated at all. Accordingly, Triton X-100 was eventually replaced by Digitonin (see below).

Frielingsdorf and co-workers reported that the detergent Digitonin allows purification of *R. eutropha* membrane-bound hydrogenase (MBH) in a fragile multimeric complex with its native cytochrome b_{562}, while none of the other twenty detergents tested, including Triton X-100, were able to dissolve the MBH away from the bacterial membrane without destabilising the delicate complex [146]. Thus, Digitonin presented itself as a promising candidate for isolating the somewhat elusive monomeric *E. coli* Hyd-1.

Figure 3.7C shows the difference in oligomeric composition of aliquots of the same defrosted Hyd-1 sample run on the day of defrosting (1) and the following day (2). The samples were pre-incubated in buffer containing ca. 1% (wt/vol) Digitonin to enhance separation, while the concentration of Digitonin in the running buffer was only 0.007% to minimise detergent precipitation. For reference, the position of the 150 kDa ADH peak is indicated by an arrow. On day one, a broad aggregate peak is found next to a clear Dimer peak and a barely visible Monomer peak. On the second day, a widening of the aggregate peak into an overlapping double peak is observed, indicating decomposition of the complex aggregate. Furthermore, a small but distinct and comparatively well-separated monomer peak is found. In the context of these findings it is of interest that the sample showing a band around 100 kDa in the Native PAGE gel (Fig.3.5, 'pooled') was defrosted a week before the electrophoresis experiment.

Freshly isolated, and thus not frozen, Hyd-1 samples, again pre-incubated in concentrated Digitonin buffer, contain much less aggregate and the Dimer peak is dominant (Fig. 3.7.C). The molecular weights of the protein peaks identified as 'Dimer' and 'Monomer', calculated relative to a full calibration (see Methods 5.4), are 210 kDa and 104 kDa respectively. Particularly notable is the presence of two distinct A_{420} peaks pairing with the A_{280} Dimer and Monomer peaks.

Overall, the use of freshly-isolated Hyd-1 and Digitonin proved not only to allow the clearest, most reliable separation of distinct Dimer and Monomer fractions, but also produced the least 'waste' in the form of aggregate; while isolated aggregate fractions were observed to be initially stable and soluble, substantial precipitation of enzyme is observed over time. Obtaining sufficient quantities of Monomer remains the chief challenge for a rigorous characterisation of the Monomer fraction, since only the second half of each Monomer peak can be used: The first half slightly overlaps with the much larger Dimer peak and thus has to be discarded in order to avoid isolating a heterogeneous sample. In this context it should be noted that applying very concentrated samples to the gel filtration column, in an effort to reduce the number of purifications required to accumulate enough enzyme for subsequent experiments, tends to be futile since loading of concentrated samples reduces the peak separation.

3.2.3 Composition of Isolated Fractions (SDS-PAGE)

To evaluate the subunit composition of the aggregate and putative Dimer and Monomer peaks, isolated from Triton X-100 and Digitonin SEC experiments (Fig. 3.7 B and D), denaturing electrophoresis was carried out (SDS-PAGE gel, Fig. 3.8). All applied samples show characteristic large (64.6 kDa) and small (36.8 kDa) subunit bands just below the 70 and 40 kDa marker bands, demonstrating that the Monomer and Dimer fractions (at ca. 110 and 220 kDa total mass) are structurally intact and indeed consist of at least one and two assemblies, respectively, of a large and small subunit each. Some of the lanes are slightly overloaded (widening of the large subunit band), which is somewhat unavoidable in the search for fainter bands. The observation of fainter small subunit bands relative to the large subunit bands in these SEC-separated fractions is consistent with observations from non-separated samples (Fig. 3.5). While the overloading prevents a truly reliable quantitative comparison of band density, the Triton X-100 aggregate does appear to have a particularly low proportion of small subunit.

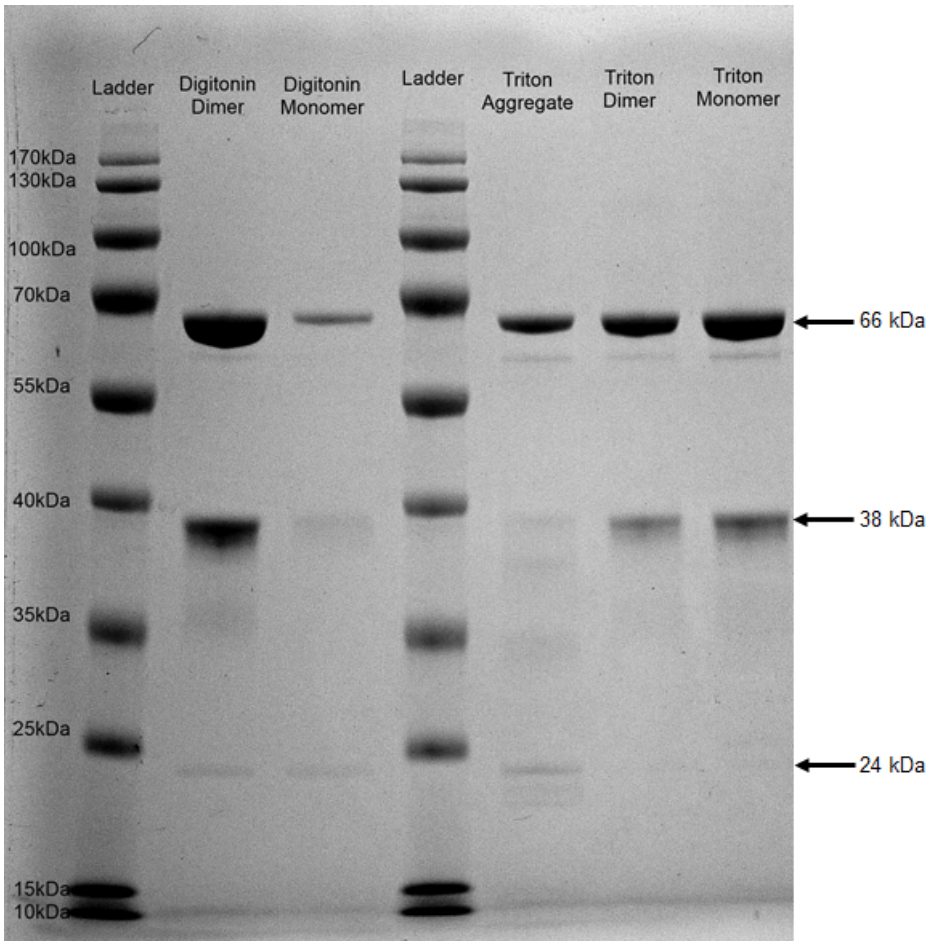

Figure 3.8 SDS-PAGE of Isolated Oligomeric Hyd-1 Fractions: Enzyme fractions isolated with the detergents Digitonin and Triton X-100, as shown in Fig.3.7, were analysed with denaturing gel electrophoresis. A pre-cast 4-12% BisTris gel was run for approx. 50 min at 200 V with ca. 4 µL of protein sample per lane (PageRuler ladder, see Ch.5.10 for details).

In addition, the aggregate sample and both Digitonin Dimer and Monomer samples also contain a clear band just below 25 kDa. Hydrophobic membrane-bound and especially membrane-integral proteins are found to interact with atypical quantities of detergent (including SDS), resulting in migration rates through the polyacrylamide gel varying by as much as -10% to +30%, relative to reference proteins of identical size [163]. This 24 kDa band is therefore a candidate for the 27.6 kDa cytochrome *b* found in the Hyd-1 crystal structure (Fig. 3.1).

Sargent and co-workers have created a Hyd-1 variant (ΔTM) in which the trans-membrane helix, thought to anchor the protein to the membrane and seen to bind the cytochrome in the crystal structure (Fig.3.1), is deleted by truncation after Arginine 266 - save a His-tag for affinity purification. This variant, which was created so that the

enzyme would be found in the periplasm and as such would be more easily purified, is isolated without the cytochrome. In the work presented here, it serves as a convenient negative control in assessing whether any cytochrome is attached to purified native Hyd-1 enzyme.

Fig.3.9 shows a native PAGE gel of native and ΔTM Hyd-1. The main band is around 200 kDa for both WT and ΔTM, indicating that, in the absence of the trans-membrane region, ΔTM Hyd-1 still exists preferentially as a Dimer. The ΔTM band is ca. 19 kDa smaller than the native Hyd-1 band, while the deleted trans-membrane α-helix of 36 amino acids only has a calculated size of approx. 3.4 kDa. The difference in molecular weight between native and ΔTM enzyme is therefore sufficiently large that, allowing for the the same considerations regarding migration of hydrophobic proteins as mentioned above, binding of one fewer cytochrome (MW 27.6 kDa) is the most likely explanation. The complete absence of bound cytochrome in the ΔTM sample is shown in Fig.3.10.A. The impurities found in the ΔTM sample (in native PAGE) are those found in early Ni-NTA column elution fractions, as shown in Ch.3.2.1.

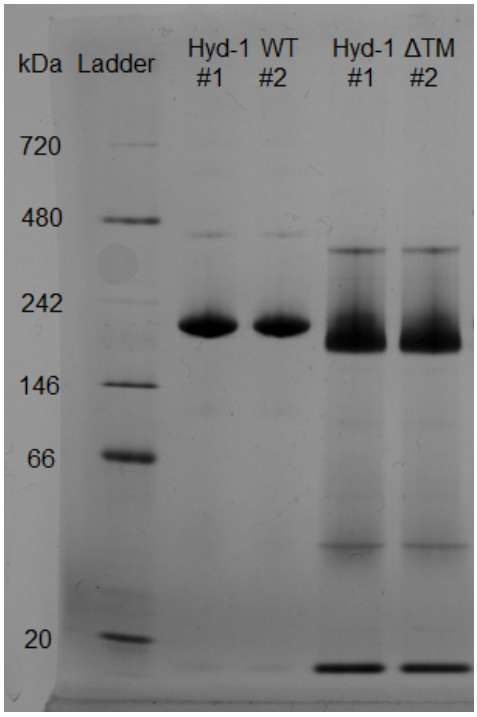

Figure 3.9 Native PAGE of Hyd-1 WT and ΔTM: A pre-cast 4-16% BisTris gel was run for approx. 130 min at 150 V with 3.5 µL of protein sample per lane (NativeMark ladder, see Ch.5.10 for details).

The presence of cytochrome *b* that is functionally attached to Hyd-1, *i.e.* that can interact through electron transfer with Hyd-1, can be detected by reduction of the *b*-type haems through Hyd-1 catalytic turnover in the presence of H_2 and subsequent oxidation in air. In this manner, a reduced minus oxidised absorbance spectrum (ΔA) is obtained for the WT enzyme, in which characteristic *b*-type haem Soret (429 nm), α (561 nm) and β (531 nm) bands can be identified [146, 131]. A similarly obtained spectrum for the ΔTM variant does not contain these features, which confirms the observed loss of cytochrome in the native PAGE experiment.

Figure 3.10A shows the reduced minus oxidised spectrum for as-isolated Hyd-1 WT and ΔTM. From the intensity of the 561 nm peak, the cytochrome *b* to Hyd-1 Dimer ratio can be calculated as described in Ch.5.5. Assuming the presence of two haems per cytochrome, a value of 0.74 cyt-*b* per Hyd-1 Dimer is found, a value which is slightly lower but near to those of around 0.82 obtained for the samples in Ch.2.3. A ratio of 1.64 cytochromes per Dimer is calculated on the basis of only one haem per cytochrome, considering the vacant second ligation site found in the crystal structure, Fig.2.2. *Vice versa*, assuming one cytochrome per Dimer as observed in the crystal structure, a ratio of 1.52 haems per dimer is obtained in good agreement with one stable and one labile haem binding site in isolated Hyd-1.Together with the gel electrophoresis results these calculations lend support to a Dimer structure with one cytochrome in as-isolated Hyd-1 solutions. In these as-isolated solutions, much of the enzyme presumably exists in soluble aggregates, based on the results in Ch.3.2.2.

Figure 3.10B shows the difference spectrum for Hyd-1 Dimer and Monomer separated by size exclusion chromatography using Digitonin or Triton X-100. The trace for Hyd-1 Dimer separated by Triton X-100 exhibits only a weak Soret band and no clear α- or β-bands. Dimer separated by Digitonin, however, displays all three bands and even the Monomershows a clearly visible 561 nm peak. The latter observation suggests that using Digitonin when solubilising the cell membranes and at every subsequent purification step, it might be possible to isolate Hyd-1 with two attached cytochromes in its assumed native state.

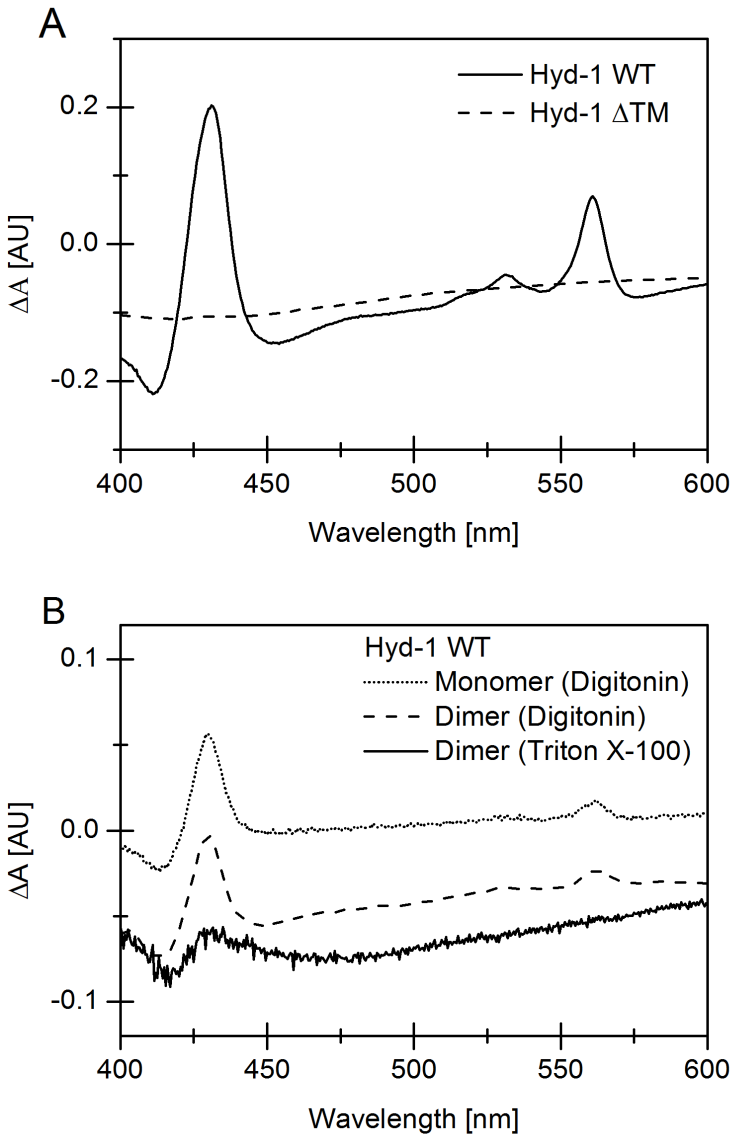

Figure 3.10 Reduced-Oxidised Cytochrome Spectrum: Characteristic *b*-type haem Soret (429 nm), α (561 nm) and β (531 nm) bands. **(A)** Hyd-1 WT, as-isolated sample, compared to the Hyd-1ΔTM variant without trans-membrane helix and cytochrome. Sample protein concentrations adjusted to 1.0 mg mL^{-1}.**(B)** Dimeric and Monomeric Hyd-1 WT, separated with Digitonin or Triton X-100. Common conditions: pH 7, 50 mM sodium phosphate, 100 mM NaCl, 0.01% detergent, room temperature. Samples were reduced by H_2 and oxidised by air.

3.2.4 Reactivation and Oxygen Reduction in Solution

Hydrogen oxidation by hydrogenases in solution is easily measured by monitoring the increase in absorbance at 604 nm (A_{604}) due to enzymatic reduction of benzyl viologen in the presence of H_2 [37]. When using enzyme samples that have previously been exposed to air, and have thus been inactivated, a so-called lag phase, without a change in A_{604}, is commonly observed at the beginning of the assay. This lag phase is caused both by the fact that enzyme reactivation is significantly slower than H_2 oxidation and by the fact that the reductive activation of hydrogenases by reduced viologens acts to oxidise the viologen. As part of the efforts to determine whether electron transfer between the two distal clusters in the macro-dimeric Hyd-1 assembly contributes to O_2-tolerance, the lag phases of Dimer and Monomer samples were compared.

Initial hydrogen oxidation assays revealed that Dimer samples were twice as active as Monomer samples, based on protein concentrations as determined by Bradford assay (*i.e.* specific activity ca. 323 µmol min^{-1} mg^{-1} for the Dimer and ca. 160 µmol min^{-1} mg^{-1} for the Monomer). It should be noted however, that the Bradford assay is very susceptible to, and easily biased by, the presence of detergents [161], which were instrumental in sample preparation, storage and use. Reagent binding might also be significantly affected by the level of protein aggregation (and the type of assembly). Determination of the protein concentration by UV-vis spectroscopy (A_{280}) yielded rates of turnover that were more similar for the two species. To make different measurements comparable in light of this uncertainty, the amount of enzyme used in the eventual solution-based reactivation assays was adjusted to yield samples of equal final activity and not apparent protein concentration.

Figure 3.11.A shows a typical result of the lag phase experiment, for which the Dimer and Monomer samples were exposed to air for several hours prior to the assay. Immediately following injection into H_2-saturated benzyl viologen buffer, the absorbance at 604 nm was recorded over time, as shown on the left. The eventual rate of viologen reduction in the samples was adjusted to be as similar as possible; in this case approx.

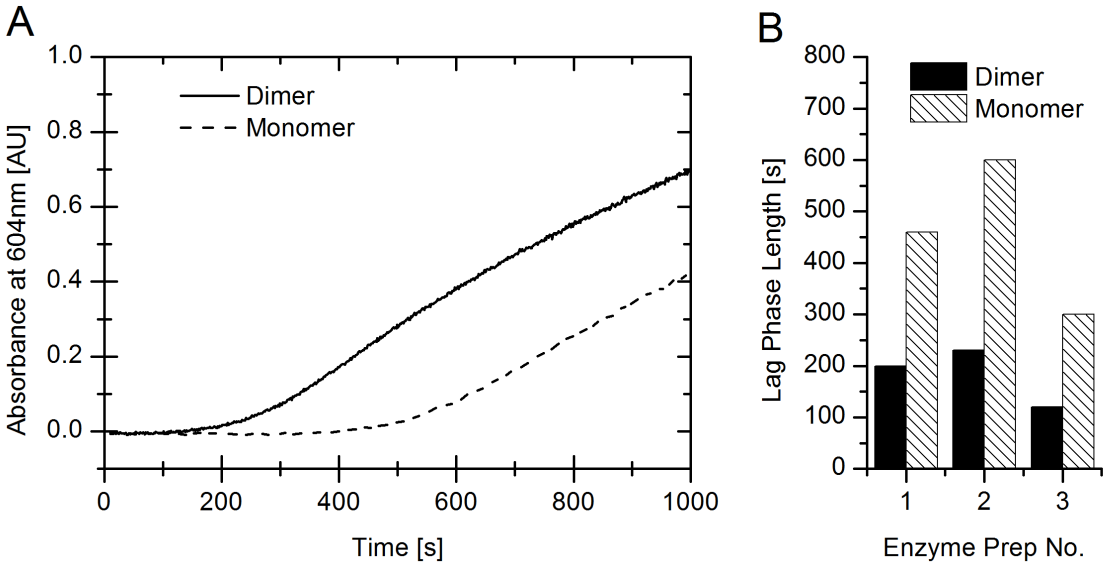

Figure 3.11 Benzyl Viologen Reduction Lag Phase Assay:
A) BV reduction followed over time by absorbance at 604 nm for Hyd-1 Dimer and Monomer solutions. Conditions: H_2-saturated buffer, pH 7, 50 mM sodium phosphate, 100 mM NaCl, 0.01% Digitonin, room temperature.
B) Comparison of the length of the lag phase for three separate experiments with enzyme from three separate preparations. The time-point of the end of the lag phase was determined by eye.

5.9 µM s^{-1} for the Dimer and 6.7 µM s^{-1} for the Monomer solution. Under these conditions the lag phases are seen to differ greatly between Monomer and Dimer. Fig. 3.11.B compares the lag phases of three sets of experiments, carried out using enzyme from three separate enzyme preparations. While both overall activity and the length of the lag phase vary between different Hyd-1 preparations, the qualitative difference between Dimer and Monomer for every individual prep is clear and consistent: the lag phase of the Monomer is slightly more than twice as long as that of the Dimer.

Oxygen-18 reduction experiments for Dimer and Monomer samples were carried out using isotope ratio mass spectrometry to detect the amount of $H_2{}^{18}O$ formed, in the same way as for samples in Ch.2. The very limited amount of Monomer available due to the low yield of the preparation posed a problem for determining the protein concentration by Bradford assay (in addition to the problems discussed above), if enough enzyme was to be kept for the actual experiment; these problems were bypassed in the following way: First, the concentration of Dimer samples was determined by Bradford assay. Then, the absorbance at 280 nm (A_{280}) was recorded by UV-vis spectroscopy

for these samples, allowing us to calculate a molar extinction coefficient so that the concentration of Monomer samples could be determined by UV-vis spectroscopy. Here, as in the previous chapter, the concentration of enzyme is expressed with reference to the functional Monomer containing one active site and having a mass of 101 kDa.

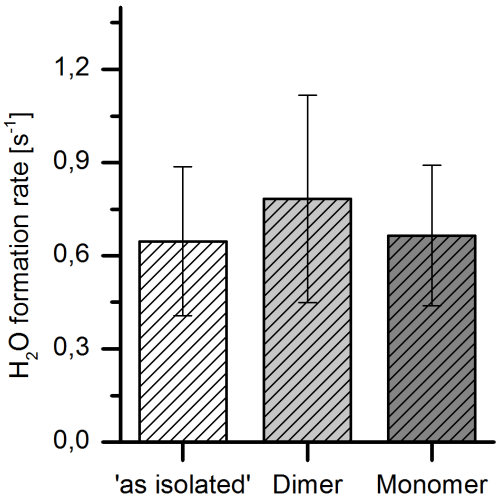

Figure 3.12 Rate of H_2O Formation by Hyd-1 Dimer and Monomer: The rate of water formation in µM $H_2{}^{18}O$ per µM Hyd-1, against blank controls, is given for 'as isolated' Hyd-1, Dimer and Monomer. The error bars show the standard deviation across eighteen, three and three measurements respectively. The concentration of $H_2{}^{18}O$ was measured by isotope ratio mass spectrometry as described in Ch.2. The experiments were conducted under an atmosphere of 90% H_2 and 10% $^{18}O_2$ in mixed hydrogenase buffer at pH 7.0 and 20 ℃.

Figure 3.12 provides the results obtained from eighteen data points in Ch.2.2.1 ('as isolated') where an $H_2{}^{18}O$ formation rate of 0.65 s^{-1} was obtained; this is compared with rates obtained as the average between three data points from samples incubated for approx. 4, 10 and 14 h for Dimer (0.78 s^{-1}) and Monomer (0.67 s^{-1}). The long incubation times were necessary to accumulate enough product for mass spectrometry measurements, given solutions with Hyd-1 concentrations as low as 0.06 μM.

3.2.5 Cyclic Voltammetry of Hyd-1 Dimer and Monomer

In order to evaluate any differences between Hyd-1 Dimer and Monomer in more detail, and as a function of potential, cyclic voltammetry was performed on enzyme 'films', grown using the two different fractions, with a rotating pyrolytic graphite edge (PGE) electrode (see methods Ch.5.1). This also allows for a reliable assessment of whether monomeric Hyd-1 is in fact fully functional with regard to H_2 oxidation or if, for example, different kinetics or a significantly altered overpotential requirement exist. For an introduction to overpotential, Butler-Volmer behaviour and the features of a Hyd-1 cyclic voltammogram, required knowledge for to the following paragraphs, see Ch. 1.4.

Figure 3.13.A shows the averaged forward and backward scan of a H_2 oxidation CV experiment with Hyd-1 Monomer and Dimer. The Dimer film yields significantly larger catalytic current than the Monomer; an approximate four fold difference being typical, whether the film was obtained through application of more or equally concentrated Dimer solution relative to the Monomer. Only in experiments with very dilute Monomer samples (a symptom of very low Monomer yields in early isolation experiments) were larger differences in total current observed. From the plot in Fig. 3.13.A it might appear at first sight that the Monomer displays a significantly increased overpotential requirement and more sluggish (onset) kinetics, *i.e.* current increase with applied overpotential, compared to the Dimer. The difficulty here lies with the already mentioned considerable difference in scale, *i.e.* total current. A small deviation from the zero current line for the Monomer plot is almost invisible to the eye on the scale of the Dimer trace.

It is within the context of the Monomer trace itself that the onset potential must be assessed; yet it still needs to be compared to the Dimer. For this and similar purposes cyclic voltammetry traces of greatly different currents are frequently resized or normalised so that they may be overlaid for this comparison, as can be found throughout the literature. Normalisation inherently results in significant stretching and compressing and herein lie a great many pitfalls, as illustrated blow. In the presented experiment,

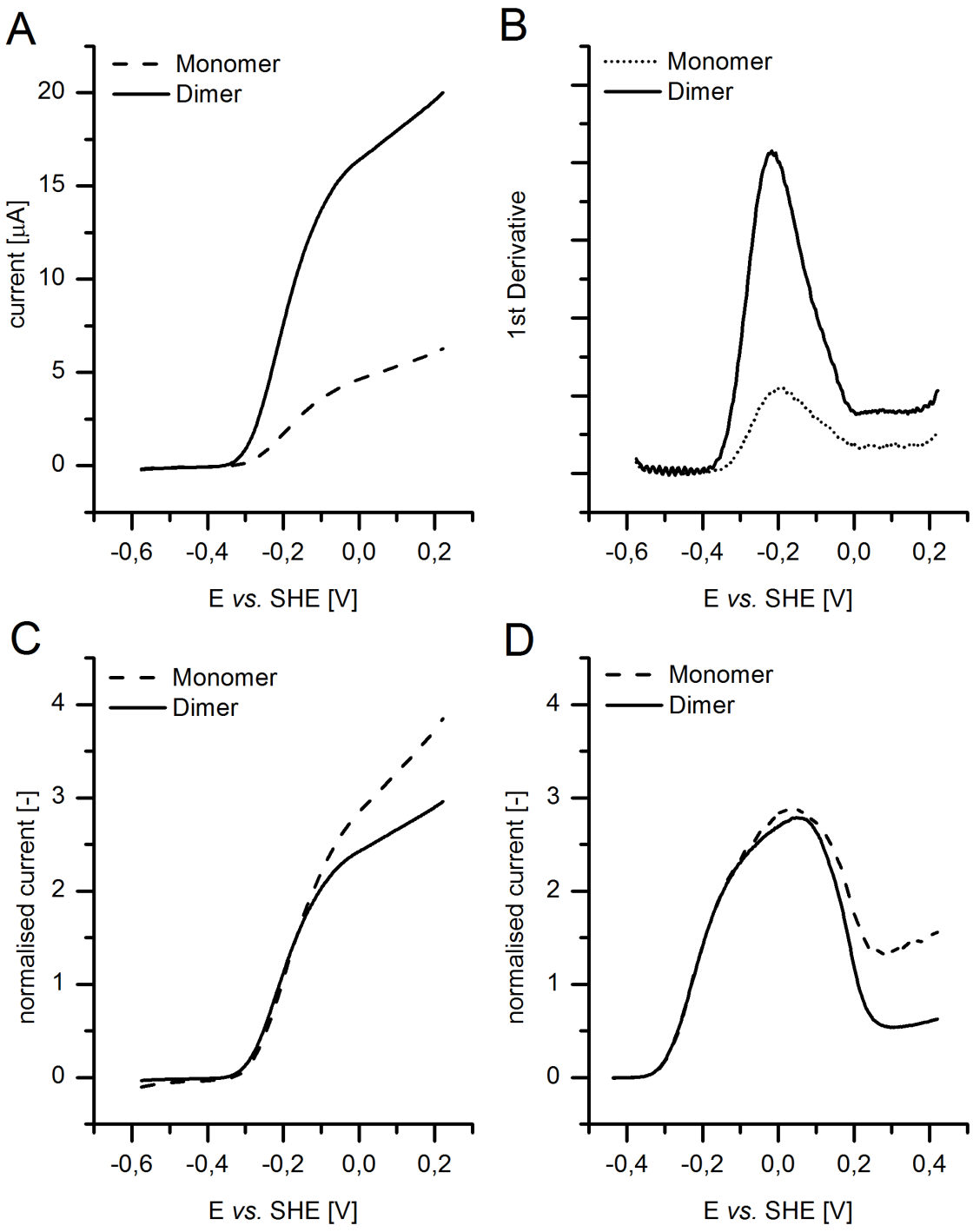

Figure 3.13 Hyd-1 Dimer and Monomer Cyclic Voltammetry: A) Averaged forward and backward scans (1 mV/s) of Dimer and Monomer films on a rotating PGE electrode. **B)** First derivative of the averaged cyclic voltammograms. **C)** CVs from panel A normalised to the current at the potential of the maxium derivative. **D)** Reverse scans of Dimer and Monomer films, slowly swept from 0.42 V to -0.44 V vs. SHE at 0.1 mV/s, to monitor reactivation of anaerobically inactivated oxidised states. The CVs are normalised to the current at the potential of maximum derivative. Common Conditions: 100% H_2, pH 6.5 mixed hydrogenase buffer, 30 °C, 3000 rpm.

simple normalisation to the maximum current, probably the most frequently used method in the field, would represent such a problem. In the specific case presented in Fig.3.13.A, the maximum current lies outside the potential region in which the current increase depends exponentially, and solely, on an increase in driving force, *i.e.* applied overpotential (Ch.1.4.1), and thus in a region where the very quality in question is not observable. The problem of distorting a CV might be described more generally as follows, for a normalisation potential E_N and its corresponding current I_N:

The lower the potential E_X (for $E_X \leq E_N$) at which the current $I_X \geq I_N$ or I_X closely approaches I_N, the steeper the slope will appear; regardless of the reason why there is little or indeed no further increase in I between E_X and E_N.

Factors that cause a cyclic voltammetry trace to 'level off' with (increasing) potential include a limiting chemical step, high potential inactivation or indeed substrate limitation. A simple thought experiment will serve to illustrate the result of incorrect normalisation in the latter case. Consider a cyclic voltammetry H_2 oxidation experiment of a Hyd-1 film with individual scans at increasing rotation rates, when substrate supply is limiting. Each successive scan will have a higher maximum current and will importantly reach this limited current at a higher potential. Normalisation at a potential where all scans have reached the limited current will now result in a graph with an extremely steep slope for the CV at the lowest rotation rate and a much more shallow slope for the high rotation rate CV; suggesting more sluggish electron transfer and a relative overpotential requirement in the latter case. Neither is obviously the case!

To avoid the problems discussed above, Fig. 3.13.B compares the first derivative (slope) of the Monomer and Dimer voltammograms (before normalisation). In the absence of mass-transfer effects, using a rotating electrode, the change in current with applied potential depends upon the activation energy and exchange currents, and thus in the latter case upon the kinetics of the reaction. These are parameters that are useful in comparing the catalytic properties of Hyd-1 in its different oligomeric states. The potentials of maximum current change are indeed very similar for the Monomer and Dimer, at approx. -203 mV and -212 mV vs. SHE respectively. Normalising the voltammograms to the currents at these potentials gives Fig.3.13.C.

As the close overlay of the graphs in Fig.3.13.C shows, H_2 oxidation activity by both oligomeric forms of Hyd-1 shows a nearly identical response to an increase in driving force at low potentials. Both have the same onset potential of approx. -335 mV vs. SHE. This value should be treated with care, since the onset potential is notoriously difficult to define accurately, as the current does not sharply cross the zero current line when an overpotential requirement exists. With the H_2/H^+ equilibrium potential E_{eq} at -391 mV vs. SHE, this overpotential is thus ca. 56 mV for both oligomeric forms. At higher potential however, the two voltammograms diverge significantly. Three factors principally affect the catalytic current of Hyd-1 at high potentials: 1) At sufficiently high currents, substrate limitation through mass transfer restrictions applies. Under identical conditions, limitations due to mass transfer will be more apparent with the Dimer film, which shows a larger current than the Monomer film. To minimise this effect, a 100% H_2 atmosphere was chosen along with an electrode rotation speed of 3000 rpm; further increases in rotation rate did not result in a visible increase in total current. 2) A variation in enzyme orientation on the electrode surface leads to a 'dispersion' effect, wherein kinetics of interfacial electron transfer differ between different enzyme molecules [162]. For some of these molecules, electron transfer to and from the electrode has to take place across a wider gap, so that higher (over-)potentials are required to drive electron transfer and catalysis for these enzymes. 3) Finally, a slow oxidative transition of the active site into the inactive Ni-B state renders a certain proportion of enzyme inactive, depending on the proximity to the switch potential E_{switch}; this fraction is a factor of both time and potential.

One way to look at formation and reactivation of inactive Ni-B states is to poise an active Hyd-1 film at high potential and then to sweep down to low potential at a very low scan rate, *e.g.* 0.1 mV/s. Such an experiment is shown in Fig. 3.13.D. The data are normalised in the same way as those in panel C, and it is noticeable that in this experiment the traces overlay perfectly at low potential. Again the two voltammograms differ at high potential. The fraction of monomeric enzyme that has inactivated is lower, while the apparent switch potential E_{switch} (point of steepest reactivation) appears unchanged.

In summary, the differences between Monomer and Dimer CVs, besides the fact that Monomer films generally give lower total current, are found at high potential and show characteristics of electron transfer dispersion, while the catalytically important current-overpotential response remains unchanged. The inactivation potential, though not the extent, is also unchanged. These results are addressed further in the discussion (Ch.3.4), with a focus on high potential inactivation and possible reasons for the dispersion effect.

3.2.6 Steady State Activity in the Presence of O_2

The true hallmark of oxygen tolerance in a hydrogen catalyst is continued activity in the presence of oxygen. As shown in Ch. 2, Hyd-1 achieves this through reduction of oxygen to water. If oxygen is introduced into a Hyd-1 chronoamperometry experiment at a given potential, the hydrogen oxidation activity will settle at a new steady state level, depending on the rates of inactivation r_I to and reactivation r_A from Ni-B (while Ni-A is avoided, see Ch.1.1.3, Ch.1.1.4, Ch.2 and *Evans et al.* [71]):

$$f = \frac{r_A}{r_A + r_I} \tag{2.1}$$

where f is the fraction of active enzyme, measured as the H_2 oxidation current relative to the current in the absence of O_2.

The chronoamperometry experiments shown in Fig.3.14 explore whether the oligomeric state of Hyd-1 has any impact on the steady state activity in the presence of O_2. The experiment was conducted at +10 mV vs. SHE, a potential negative enough to void anaerobic Ni-B formation and to lie within a potential region in which Monomer and Dimer films show only very small scan rate dependent differences (Fig.3.13.D). The potential is chosen to be sufficiently positive that the potential dependent reactivation rate is not too fast, ensuring that reversible inactivation by oxygen will have a significant and visible effect. As shown in Fig.3.14.A, H_2 oxidation under 100% H_2 is allowed to stabilise for 400 s, providing the reference current by which the individual experiments

are normalised. A certain concentration of O_2 is then introduced into the gas stream and the falling current is allowed to stabilise to a new steady state level, before O_2 is excluded from the gas stream once more. Note that recovery of the 'pre-O_2' current cannot be instantaneous, since flushing the remaining O_2 out of solution requires some time.

Panels B-D in Fig.3.14 show the results of the H_2/O_2 steady-state experiment described above for both Monomer and Dimer at different O_2 concentrations in the gas stream. Both Dimer and Monomer films achieve a new steady state upon introduction of 2.2% and 4.3% O_2, but the Monomer appears not to be able to sustain significant H_2 oxidation at +10 mV vs. SHE in the presence of 10.0% O_2. The fraction of remaining activity decreases with increasing O_2 concentration, as predicted. When the oxygen gas flow is stopped, activity is rapidly recovered, underlining the reversibility of the process.

The most important observation, however, is that the new steady state currents are consistently much lower for the Monomer than for the Dimer. The interpretation of this crucial finding is discussed at length below, in Ch.3.3.3.

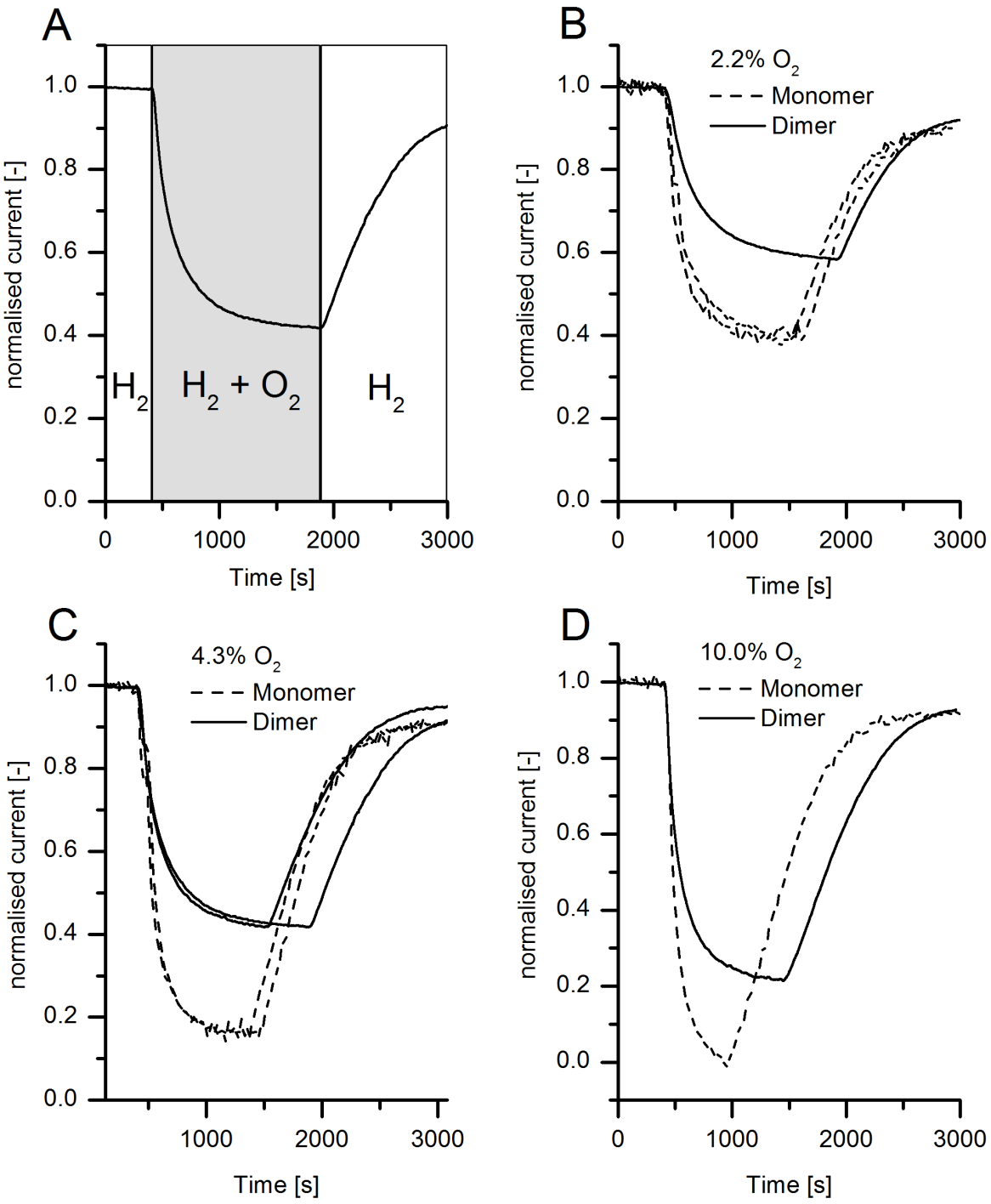

Figure 3.14 *E. coli* Hydrogenase 1 Monomer and Dimer H_2/O_2 steady-state Chronoamperometry: The H_2 oxidation current of Hyd-1 Dimer and Monomer films at +10 mV vs. SHE in an H_2 atmosphere was evaluated over time as shown in **A)** The current is normalised to the stable current under 100% H_2. After 400 seconds O_2 is added to the gas stream and removed again once the current has settled at a new stable level. The tested compositions of the mixed O_2/H_2 atmospheres were: **B)** 2.2% O_2, 97.8% H_2, **C)** 4.3% O_2, 95.7% H_2 and **D)** 10.0% O_2, 90.0% H_2. Prior to the experiment the protein films on rotating PGE electrodes were activated at -0.55 V vs. SHE and allowed to stabilise. Common conditions: pH 7.0 mixed hydrogenase buffer, 25 °C, 2500 rpm.

3.3 Discussion

3.3.1 Isolation of Hyd-1 Dimer and Monomer

Close inspection of the different stages of Hyd-1 Ni-NTA purification reveals a number of protein impurities that are collected along with Hyd-1 in the current protocol. By spreading out the elution gradient over time, it would be possible to reduce this problem and achieve the full potential of purification by gradient elution from an affinity matrix. The imidazole gradient is also seen to separate, to an extent, different oligomeric states of the protein: larger oligomeric assemblies of protein identified as Hyd-1 elute later. This observation is most easily explained by an additive effect of histidine binding (avidity). Crystallisation of such larger aggregates would only be expected if they were indeed highly ordered, which in turn is only likely to be the case if they are purposefully arranged this way *in vivo* as well. However, an accidental observation (poorly sealing lids of vials resulting in enhanced evaporation of electrochemical samples over-night) supports the idea that the Dimer is the biologically relevant state: pure Dimer fractions were found to spontaneously form small crystals, while aggregate and Monomer fractions did not.

The size exclusion chromatography experiments to separate oligomeric states of Hyd-1 were arduous and frequently only qualitatively reproducible at best, owing to the host of influencing fators: detergent type and concentration complicated by precipitation restrictions, enzyme concentration, sample freezing and variation between bacterial growth batches. The single fully consistent observation is the persistent presence and stability of Hyd-1 Dimer. The only apparent exception occurs in the total absence of detergent when the enzyme aggregates visibly, which is wholly unsurprising for a membrane bound-protein. These results further support the dimer of heterodimers as the biological unit.

Digitonin eventually proved the most successful detergent in reproducibly isolating monomeric Hyd-1 by size exclusion chromatography, while the somewhat promising

DDM ruled itself out to all but the most motivated column re-packers by virtue of constant precipitation. Operation of a gel filtration system at room temperature might offer a solution to this. Higher temperatures would increase detergent solubility and reduce such precipitation issues for all detergents, allowing higher concentrations and potentially making the use of DDM an actual possibility, but also presumably improving the separation by Digitonin. The solvent-dependent ($\alpha\beta$):($\alpha\beta$) dissociation energy of 31.8 kcal/mol (see, Tab.3.1) of Hyd-1 is rather substantial. While this value is an overestimate, since the calculation does not account for the presence of detergent, low temperatures are still a significant impediment; this explains the relative success of incubating samples in detergent at room temperature prior to application to the gel filtration column (Ch.3.2.2). For future efforts of isolating monomeric Hyd-1, it might be useful to test elevated temperatures as high as 50 °C, if conditions can be found under which α:β dissociation remains unfavourable.

An implication of the success of pre-treatment at higher temperatures (Ch.3.2.2) is further that Monomers don't easily reassemble and that therefore Hyd-1 oligomers don't exist in a dynamic equilibrium; a conclusion supported by the observation that isolated Dimer fraction largely remains in the inital oligomeric state for days (Fig. 3.7.A). The influence of enzyme concentration on the obtained states, lower concentrations being more favourable for isolation of small oligomers, seems to contradict this conclusion at first; instead it is simply a result of better resolution of size exclusion chromatography at lower loading quantities (Ch.3.2.2).

The composition of isolated Hyd-1 oligomer samples was evaluated primarily by gel electrophoresis. Dimer and Monomer as well as larger aggregate fractions were found to consist of both small and large subunits of 36.8 kDa and 64.6 kDa in size, respectively. The ca. 210 kDa and 104 kDa oligomers are thus confidently assigned as Dimer and Monomer (of heterodimers). The presence of the cognate cytochrome *b*, only recently resolved in complex with Hyd-1, was more difficult to assess. The combination of native PAGE experiments with a non complex-forming variant (ΔTM) compared to wild type, and UV-vis measurements of haem *b* concentrations, indicate

a ratio of slightly under one two-haem-containing cytochrome per Hyd-1 Dimer, in accordance with the crystal structure. But does the cytochrome remain attached to the carbon electrode in electrochemical experiments and, if so, does it have an impact? As this question has already been addressed for the closely related membrane-bound hydrogenase (MBH) from *Ralstonia eutropha* with great experimental complexity, no specific efforts were made to this end in the present chapter. The study by Sezer *et al.* on the effect of cognate cytochrome *b* on the catalytic and electron transfer properties of the MBH [164] is, however, instructive. Alkylthiol functionalised electrodes were needed to enable favourable immobilisation of the cytochrome attached to the MBH. While the researchers were able to confirm binding of the cytochrome together with the main hydrogenase subunits to this specially prepared electrode, no significant difference in electron transfer or catalysis was discernible between these protein films and those containing only hydrogenase. In light of these results it appears very unlikely that cytochrome *b* would have any significant effect on the properties of Hyd-1 in electrochemical experiments, even if it were to attach to the electrode, and no previous Hyd-1 electrochemical data has given any indication that there might be.

3.3.2 Cyclic Voltammetry, Overpotential and Dispersion

As found in Ch.3.2.5, the overpotential requirement of ca. +56 mV (at pH 6.5, 100% H_2 and 30 °C) and the current response to increasing potential around the onset potential are the same for both Monomer and Dimer. Overpotential requirements for 'as-isolated' Hyd-1 were previously reported as ca. +50 mV under 10% H_2 (pH 6.0, 30 °C) by Lukey *et al.* [37], or in a more detailed study by Murphy and co-workers as + 54 mV and +82 mV at pH 6.0 and pH 7.0 respectively (100% H_2, 37 °C) [111]. The values determined for the pure oligomeric fractions in this chapter agree well with these earlier measurements and are if anything slightly below predicted values, since the overpotential requirement decreases with decreasing H_2 partial pressure and pH (see Ch.1.4.2).

Differences in the cyclic voltammetry traces recorded for the different oligomeric states are most prominent at high potential, where the Monomer shows a persistent increase in current with increasing potential, whereas for the Dimer the current increase due to further increase in potential above approx. -50 mV vs. SHE is less pronounced. (Fig.3.13.C). The cause of this effect is dispersion (of electron transfer rates), which is thought to originate from a variation of enzyme orientation on the electrode [162]: For a fraction of enzyme the distance over which electron transfer must occur is increased, with the implication that electron transfer does not occur at significant rates unless a large additional driving force is applied. It is therefore unsurprising that protein films of different oligomeric composition display differences in the 'dispersion' of electron transfer kinetics, as well as the total current density (Fig.3.6.P1-P4). Looking specifically at the increase in dispersion of the Monomer relative to the Dimer, the (newly) solvent-exposed area in the Monomer (*i.e.* the interface area in the Dimer) offers a range of new interactions and orientations with the electrode surface that could help explain the difference.

The residual current increase due to 'dispersion' occurs in the same potential region as oxidative inactivation to the Ni-B state and can therefore explain the apparent lesser extent of inactivation observed on a slow reverse scan for the Monomer (Fig.3.13.D). Importantly, the switch potential for Ni-B formation is unchanged, which indicates that there is no thermodynamic change in this transition between important active site states. The unchanged switch potential, in conjunction with the unchanged overpotential, supports the idea that the Hyd-1 Monomer is essentially intact and fully functional.

3.3.3 An Extended Model for the Reaction of Hyd-1 with O_2

Solution H_2 oxidation assays, starting from aerobically inactivated enzyme, gave a convincing indication of an oxygen-tolerance-related difference between Hyd-1 Monomer and Dimer: the Monomer displays a lag phase more than twice as long as the Dimer (Chapter 3.2.4). While the CV experiments described above rule out that damage to the enzyme, *e.g.* a disrupted or exposed distal cluster, causes this discrepancy, the difference in lag phase on its own leaves meaningful questions unanswered. Does the dimeric organisation help in ensuring exclusive formation of rapidly reactivated Ni-B and does the Monomer thus produce a certain ratio of less easily reactivated states, such as Ni-A? Alternatively, does the dimeric organisation affect the rates of reactivation of inactive states? Can a result similar to the difference in lag phase be reproduced in a more controlled environment, where uncertainty over enzyme concentration is not important? Chronoamperometry experiments, in which Hyd-1 attains a steady state of simultaneous substrate (H_2) and competing inhibitor (O_2) turnover, can answer these questions.

The fact that both Dimer and Monomer attain a steady state activity of H_2 oxidation in the presence of O_2 (Ch.3.2.6, Fig.3.14) shows that the ability to exclusively form Ni-B (and no Ni-A) and to effectively reduce O_2 are unaffected by the oligomeric state of the enzyme, since formation of even a small fraction of Ni-A leads to a persistent decline in oxidation current. The observation that under 10% O_2 the Monomer activity essentially drops to zero does not contradict the previous statement, as it is not caused by a slow gradual accumulation of 'Unready' states. Activity is recovered rapidly and instantly in all cases once the oxygen flow is stopped - demonstrating reversibility and constant reactivation even at approximately zero net remaining activity. The chief result of this chapter is that the relative steady state activity is significantly diminished for the Monomer compared to the Dimer. Further analysis of these steady-state levels holds the key to developing a plausible mechanistic explanation of the effects of dimerisation.

For the following discussion it will be useful to retrace the reasoning behind Eq.2.1, which predicts the fraction f of active enzyme at steady state, measured as the H_2 oxidation current relative to the current in the absence of O_2 [71]:

$$f = \frac{r_A}{r_A + r_I} \tag{2.1}$$

The basis is the simplification of the complex reaction of Hyd-1 with O_2 (as described in Ch.2 and Fig.2.1) to

$$A + O_2 \xrightarrow{k_I} B + 2\,H_2O \xrightarrow{k_A} A \tag{3.1}$$

where A is active enzyme (not to be confused with Ni-A). Inactive enzyme in the Ni-B state (Ni^{3+}-OH) is represented by B. Protons and electrons are omitted for simplification. It should be highlighted that $[O_2]$ is held constant in this instance by the experimental setup. With the total amount of enzyme E

$$E = A + B = 1 \tag{3.2}$$

and

$$\frac{d[B]}{dt} = 0 = k_I[A][O_2] - k_a[B] \tag{3.3}$$

we obtain the relative steady-state activity:

$$f = \frac{A}{E} = \frac{k_A}{k_A + k_I[O_2]} \tag{3.4}$$

Thus, a fit to the fraction of active Dimer at a given O_2 concentration is obtained as shown in Fig.3.15.A, using a ratio of apparent reactivation to inactivation rate constants of $C_D = k_A/k_I = 40$ (at +10 mV). For the Monomer, however, no fit can be found with any combination of rate constants; the best effort is represented by $C_M = k_A/k_I = 15$ where the reactivation rate is 38% that of the Dimer.

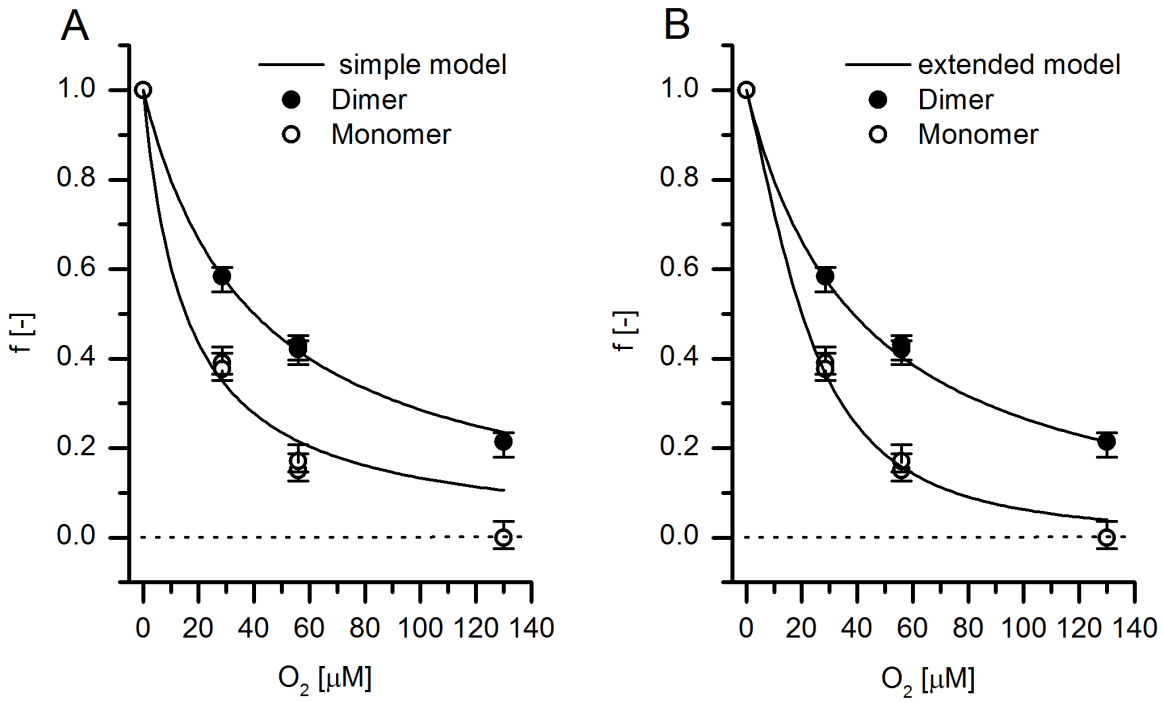

Figure 3.15 Steady State Activity of Hyd-1 Dimer and Monomer, relative to initial activity, depending on O_2 concentration. The respective values are obtained from the chronoamperometry experiments shown in Fig.3.14.B-D. Error bars represent estimated uncertainty based on film loss, residual slope and electrical noise contributions. The zero current line is drawn as a dotted black line for reference. **A)** Solid lines represent the fit to the *simple model* of O_2 catalysis by Hyd-1 in the presence of H_2 according to Eq.3.4, as explained in the main text. Fit parameters: $k_A/k_I = 40$ (Dimer) and $k_A/k_I = 15$ (Monomer) **B)** Solid lines represent the fit to the *extended model* (Eq.3.6) based on oligomeric assembly, oxidative side reactions and electron transfer (see below). Fit parameters: $k_A/k_I = 0.112/0.0028 = 40$ for Dimer and Monomer and $K_C = 1000$ (Dimer) and $K_C = 20$ (Monomer).

Having so far worked only with the ratio C, the individual rate constants shall also briefly be discussed. While they cannot be obtained directly from the presented experiments, previous experiments with Hyd-1 provide a guideline as to what values would be expected. In the previous chapter (Ch.2.3) a rate constant of $k_I = 0.002\ (\mu M\, O_2)^{-1} s^{-1}$ was determined at 20 °C while Evans *et al.* found $k_I = 0.0038\ (\mu M\, O_2)^{-1} s^{-1}$ at 30 °C. Using an Arrhenius plot, the rate constant for inactivation at 25 °C is estimated as $k_I = 0.0028\ (\mu M\, O_2)^{-1} s^{-1}$ through interpolation. With $C_D = k_A/k_I = 40$ (see above) the rate constant for reactivation is deduced to be $k_A = 0.112\ s^{-1}$ for the presented fit to the Dimer data. Since the reactivation rate is very fast at low potentials, it is not directly measurable under experimental conditions chosen to allow significant H_2 oxidation activity at high O_2 concentrations; a problem addressed previously by Evans *et al.* [71] by extrapolation from data obtained at both higher potential and lower

temperature to the desired conditions with the help of Arrhenius plots. Using the same process, rate constants of $k_A = 0.136\ (\mu M\, O_2)^{-1} s^{-1}$ and $k_A = 0.186\ (\mu M\, O_2)^{-1} s^{-1}$ are calculated for +10 mV vs. SHE and 25 °C from two separate data sets provided by Evans ([71], see Appendix A.2 for an example); the discrepancy between these two values illustrates the uncertainty and deviations introduced by double extrapolation. Nonetheless, these calculations show that the fit to the Dimer steady state data is achieved with rate constants that agree reasonably well with predicted values.

Referring back to Fig.3.15.A, a noticeable quality of the unsatisfying Monomer fit is that with increasing O_2 concentration the deviation from the model increases (towards smaller active fraction). In fact, this might also be the case for the Dimer in a much diminished fashion, but the data are insufficient to be certain. The steady state levels recorded for Hyd-1 (WT) by Evans *et al.* for a larger number of O_2 concentrations are helpful here as well: a fit is produced using $k_I = 0.0038 (\mu M\, O_2)^{-1} s^{-1}$ and $k_A = 0.245 s^{-1}$, as shown in Fig.3.16 as a solid line ($k_A = 0.212\, s^{-1}$ and $k_A = 0.343\, s^{-1}$ are predicted by extrapolation to 0 V and 30 °C, using the same two data sets from Evans mentioned above). The same trend of increasing deviation from the model with increasing O_2 concentration, that is found for the Monomer, is observed in a less pronounced way for the WT.

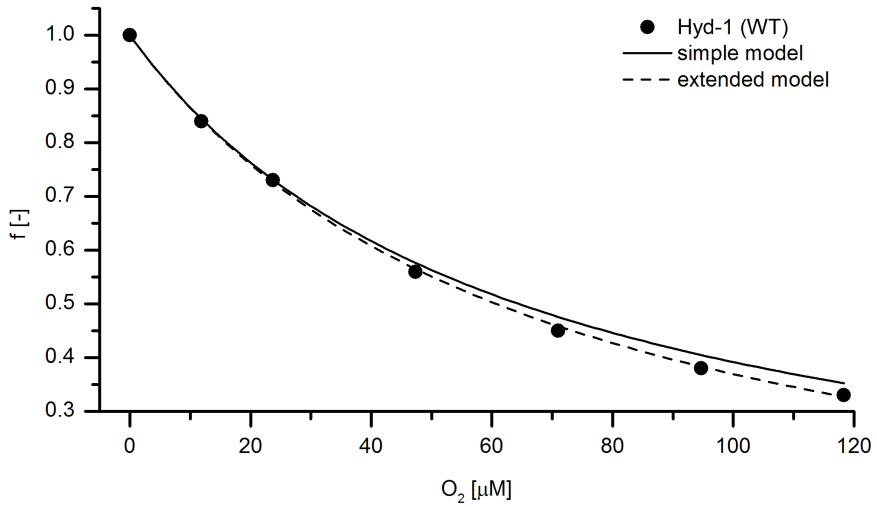

Figure 3.16 Steady State Activity of as-isolated Hyd-1 (WT), as measured by chronoamperometry by Evans *et al.* [71] at 0 V vs. SHE, 30 °C and pH 6.0. The solid line represents a fit to the *simple model* (Eq.3.4) and the dashed line represents a fit to the *extended model* (Eq.3.6, with $K_C = 1000$), using the rate constants $k_A/k_I = 0.245/0.038$ (discussed in the main text) in both cases.

The model of the reaction of Hyd-1 with O_2 will now be extended to include: (a) the observation that the active Monomer fraction decreases more strongly than the active Dimer fraction with an increase in O_2 concentration, (b) the observation that a relatively small but significant superoxide/peroxide producing side reaction is observed for Hyd-1 in the presence of O_2 as shown in Ch.2 and (c) the likelihood that the two partners in a Dimer might be able to share electrons *via* the distal clusters. These considerations yield the new reaction scheme shown in Fig.3.17.

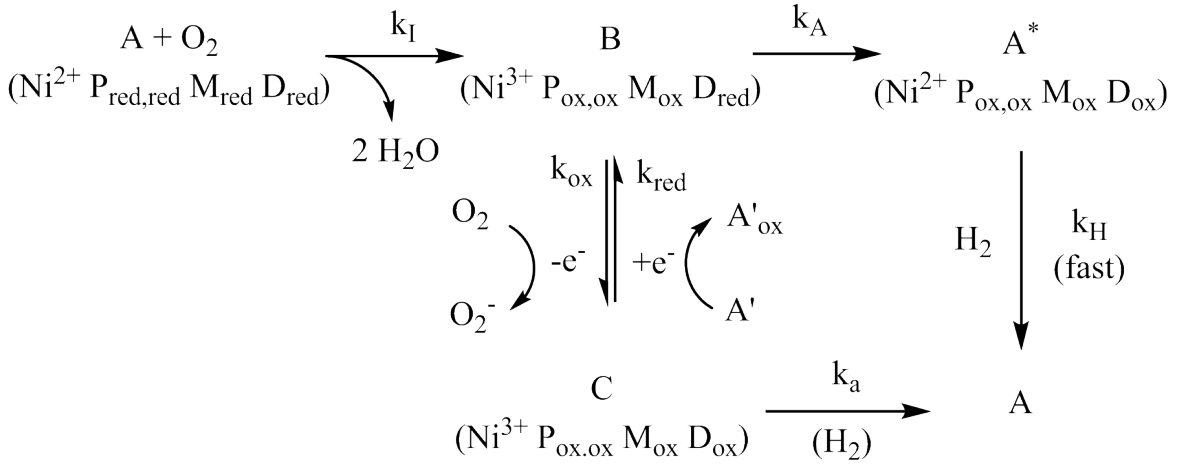

Figure 3.17 Extended Oxygen Reaction Model: The initial reaction of active enzyme A with O_2 yields B through the release of H_2O at the expense of four electrons. The enzyme's proximal P, medial M and distal D clusters are assigned as either reduced or oxidised (red/ox). The proximal cluster can undergo two redox transitions as detailed in Fig.1.5. Inactive enzyme B can be reactivated *via* a fast reaction k_A and an intermediate state A^* (see main text). Oxidation of B to C, due to an outer-sphere reaction with O_2 resulting in O_2^- formation (*e.g.* at the distal cluster), k_{ox} is reversible and the back reaction k_{red} is fast if an active partner enzyme A' can supply an electron to the distal cluster (k_{DD}) or slower if the electron has to be supplied from the electrode to the distal cluster k_{ED} (*i.e.* $k_{DD} >> k_{ED}$). Slow reactivation through hydrogen binding to Ni-B can also recover A from C.

The first stage of the reaction is as before Ni-B formation through O_2 reduction for which four electrons are needed to release two molecules of water, as established and described in detail in the previous chapter (Ch.2). Two electrons are delivered from the proximal FeS cluster P, one from the medial cluster M and one from oxidation of the active site Ni. Since the proton pathways are still unresolved, protons are omitted in this scheme which also aids simplicity. The Ni-B state is thus described as B (Ni^{3+} $P_{ox,ox}$ M_{ox} D_{red}). Formation of a Michaelis complex $A : O_2$ in the initial reaction of active enzyme with O_2 was also considered but eventually discarded, as a fit to the data

simply required a very large K_m value to impose the same linearity as in the simpler model. Correspondingly, Evans *et al.* measured the initial rate of O_2 reaction with active Hyd-1 and found it to increase linearly with O_2 concentration [71].

Enzyme inactive for H_2 catalysis (B) may now be reactivated rapidly by reduction of the active site Ni back to Ni^{2+} (k_A) by an electron from the distal cluster D. This new state of the enzyme A^* can now re-enter the catalytic H_2 cycle through binding of H_2 and subsequent turnover [165]. Binding of H_2 to the active site in the Ni^{2+} state to re-establish A is assumed to occur on a time scale closer to that of the rapid reactions of H_2 catalysis than the relatively slower O_2 turnover, and is thus considered to be effectively instantaneous for the purpose of this discussion. Following two or more rapid H_2 turnovers, active enzyme A may enter another cycle of the slower O_2 catalysis.

Inactive enzyme B may react in an alternative manner: The electron required for Ni reduction could be lost to O_2 from a reduced site, *e.g.* the distal cluster itself, in an outer-sphere side reaction, as discussed in Ch.2. The result of this reaction is a fully oxidised enzyme C. Oxidation of the distal cluster in this manner would be quasi reversible if another source of electrons were available; in the Dimer this would be the partner hydrogenase A' which could rapidly supply electrons with a rate constant k_{DD} from one distal cluster to the other. Another source of electrons could be an external redox partner which provides a driving force for H_2 oxidation, as in this special case the electrode for which a rate constant k_{ED} is assigned. At oxidising potentials this reverse electron transfer would likely be unfavourable (the distal cluster potential is unknown). In addition, the electron would have to tunnel over a longer distance from the electrode to the distal cluster than between the distal clusters, so that $k_{DD} >> k_{ED}$.

As far as the availability of an electron at the distal cluster (*i.e.* its redox state), prior to oxidising side reactions, is concerned, this would be governed by the supply of electrons from H_2 oxidation and by the applied electrode potential. At sufficiently high and increasing potentials an increasing proportion of distal clusters would be oxidised and unable to supply electrons, regardless of side reactions. Accordingly, [NiFe]-hydrogenases are more susceptible to oxygen close to the Ni-B equilibrium potential

because of both lower initial electron availability and the slower resupply of electrons for reactivation. In this context it is important to consider that, while Hyd-1 adsorption to the electrode will result in the individual distal clusters of Monomer and Dimer being on average in the same redox state (as set by the electrode potential), the Dimer will be more likely to have *at least one* reduced distal cluster.

Another possible pathway for reactivation is the very slow reaction k_a of fully oxidised enzyme C with H_2 to activate the enzyme and re-enter the catalytic H_2 cycle, as observed in solution without external electron donors. If distal cluster reduction in the Dimer is very fast, the slow rate constant k_a should be largely irrelevant for the Dimer so that the overall rate of (Dimer) reactivation v_A from B to A can be simplified by analogy to a reversible inhibition [151] depending on $[O_2]$ with an apparent inhibition constant K_C proportional to k_{red}/k_{ox}:

$$v_A = \frac{k_A}{1 + \frac{[O_2]}{K_C}} \tag{3.5}$$

Incorporation of v_A in place of k_A in Eq.3.4 yields the fraction of active enzyme for the new extended model:

$$f = \frac{A}{E} = \frac{k_A \left(1 + \frac{[O_2]}{K_C}\right)^{-1}}{k_A \left(1 + \frac{[O_2]}{K_C}\right)^{-1} + k_I[O_2]} \tag{3.6}$$

Indeed, incorporation of this idea into the model (with $K_C = 1000$) yields an even better fit to the data at high O_2 concentration, both for the Dimer (see Fig.3.15.B.) and for as-isolated enzyme in the Evans study (dashed line in Fig.3.16).

The large value for K_C implies that distal cluster reduction *via* the distal to distal route is very fast compared to k_{ox}, so that the oxidising side reaction has a very small effect which only becomes discernible at high O_2 concentrations (where coinciding oxidation of both distal clusters in a Dimer also becomes more probable). The apparent rate constant found for H_2O_2 formation in the previous chapter (Ch.2.3), divided by the O_2 concentration to yield $k(H_2O_2) = 0.00034\ (\mu M\, O_2)^{-1} s^{-1}$, may serve as an approximation of k_{ox} (assuming O_2^- disproportionation to H_2O_2). At this point it

should be noted that the O_2 concentration close to the electrode is likely to be lower than that in the bulk of the solution.

According to the model, in the Monomer oxidation of the distal cluster of enzyme in the Ni-B state leaves only the slower k_{ED} contribution to k_{red} and a much lower value for the constant K_C is expected. The slowest pathway for reactivation k_a might also play a small role under these circumstances; however, this would simply appear the same as a very slow distal cluster reduction k_{red} followed by fast reactivation k_A. In agreement with these considerations, a good fit to the Monomer data is obtained using the new extended model with $K_C = 20$ as shown in Fig.3.15.B.

The potential dependence of the observed k_A [58, 71] is consistent with the effect of electrode potential on distal cluster oxidation state and reverse supply of electrons k_{ED} for reactivation, as discussed above. The O_2 side reaction simply further diminishes electron availability for reactivation at any given potential. Accordingly, when there is no oxidising driving force, the side reaction is the only aspect negatively affecting turnover; *i.e.* the primary catalytic $^{18}O_2$ reduction to $H_2{}^{18}O$ at the active site (*via* the direct four electron pathway) is hindered by the side reaction, which was shown to be ca. 15% as fast as the primary reaction (Ch.2.3). Indeed, $H_2{}^{18}O$ mass spectrometry experiments found the $H_2{}^{18}O$ formation rate for the Monomer to be approx. 15% lower than for the Dimer (Fig.3.12); this would imply a rate constant k_a of the same order of magnitude as k_{ox}. However, because of the large deviations found in the Dimer/Monomer mass spectrometry experiment (representative of the low accuracy of the assay for reasons discussed in Ch.2.2.1 and Ch.3.2.4), this result should be treated with care. Nonetheless, the isotope ratio mass spectrometry experiment supports the notion that the observed differences in O_2 tolerance between Dimer and Monomer do not originate from separate pathways for primary O_2 attack (k_I).

The excellent fit of the new extended model to the data for both Dimer and Monomer (Fig.3.15.B) is a strong argument for its validity. Sharing of electrons between distal clusters for delivery to the active site, as described by the extended model, also covers the results of the lag phase solution assay. Ni-B reactivation at one catalytic site results

in very fast, and on the time scale in question effectively immediate, reactivation of the partner site. As a result only half of all active sites need to be reactivated *via* the slow pathway k_a, explaining the observed ca. two fold difference in lag phase between Dimer and Monomer (Fig.3.11).

3.3.4 Relation to other Hydrogenases

As shown in Tab.3.1, most other O_2-tolerant ([NiFe]-) hydrogenases with a known structure are also found as dimers, with very similar distances between adjacent distal clusters and similar dissociation energies. In this context the *R. eutropha* MBH is especially interesting, as it is not found to crystallise as a multimer; yet gel filtration and light scattering experiments show that it can be isolated as a trimeric assembly [146]. This Trimer might not be as favourable for crystallisation or as stable as for example the Hyd-1 Dimer but, in line with the new model presented here, would be expected to exhibit an even greater tolerance towards oxygen than the respective Monomer and possibly the Hyd-1 Dimer; provided that the distal clusters are in sufficiently close proximity. In order to be able to carry out the required steady state study, the MBH Trimer needs to be active and stable on an electrode. While the state of MBH on (PGE) electrodes was all but uncertain in the past, Radu and co-workers have recently managed to immobilise the trimeric complex, even complete with the cytochrome subunit [166] on a gold electrode. Immobilisation was achieved utilising cholesterol-based anchor molecules in tethered bilayer lipid membranes supported by spacer molecules on the electrode. The purpose of Radu's study was to observe the H_2-ubiquinone oxidoreduction by MBH in an imitated biological environment using the membrane integral quinone pool, the redox state of which can be controlled by the electrode potential [166]. While the authors claimed to observe enhanced O_2-tolerance, they unfortunately neither directly compared their results with simply adsorbed monomeric MBH nor did they carry out steady state experiments in the continued presence of O_2. Especially the latter experiment would not only support the claim of the paper, but also be of value for this discussion. Radu and co-workers did, however, find that Ni-B could be reactivated in the Trimer while the membrane ubiquinone pool was 'almost' fully oxidised [166]. In conjunction with

the common observation that anaerobic inactivation of [NiFe]-hydrogenases at high potential is faster at low H_2 concentrations (see *e.g.* [113, 52, 167]), and thus fast at slower turnover and electron flow through the distal cluster, Radu's new observation does support the idea of electron transfer between $\alpha\beta$ complexes for the benefit of reactivation.

In light of the results discussed in this chapter, it is intriguing that the hydrogenase from *A. vinosum*, which is usually considered to be O_2-sensitive, also crystallises as a Dimer (Tab.3.1), albeit as one with larger cluster separation and smaller binding energy. This apparent exception to the rule should, however, not be dismissed too hastily. Electron exchange between partner enzymes could also operate in O_2-sensitive hydrogenases that are at least structurally stable to attack by oxygen, and help to reactivate Ni-B. Dimerisation might thus help with H_2 catalysis during transient or extremely low O_2 exposure.

The purple sulfur bacterium *A. vinosum* is usually considered to be an anoxygenic phototroph, but is also able to grow chemotrophically at low oxygen concentrations [168]. Dincturk and co-workers showed that under such conditions the activity of a *Bd* quinol oxidase protects nitrogenase against inhibition by O_2. It is possible that under similar conditions a dimeric and otherwise O_2-intolerant but structurally stable hydrogenase might just be resilient enough to allow residual H_2 catalysis and give a competitive advantage. Full, sustained O_2-tolerance is, however, not possible, as indicated by the finding that the aerobically obtained crystal structure of the *A. vinosum* hydrogenase is found to over 90% in an inactive state assigned as Ni-A [14].

3.4 Conclusion

All Hyd-1 crystal structures solved in the past showed an $(\alpha\beta)_2$ dimeric species. It was thus proposed that this should not only be the form occurring *in vivo*, but that this assembly might also enable electron transfer between redundant subunits, which might serve a function in O_2-tolerance.

In this chapter it is demonstrated that it is possible to separate distinct oligomeric states of *E. coli* Hyd-1. Specifically, an $(\alpha\beta)_2$ dimer of heterodimers and an $(\alpha\beta)$ monomer of heterodimers were isolated. The Dimer is very stable, easy to isolate and is the favoured species at increasing detergent concentrations where larger aggregate fractions are broken down. Pure fractions of Dimer also form the most active and highly ordered protein films on electrodes and appear to be favourable for crystallisation.

Cyclic voltammetry experiments showed that both the Dimer and Monomer are functionally intact, as evidenced by the detection of no additional overpotential requirement for hydrogen oxidation (Ch.3.3.2). Important differences were, however, found in response to inactivation by O_2, as detailed below.

Fully aerobically inactivated Monomer samples took twice as long to reactivate as the relevant Dimer samples in H_2 oxidation solution assays (Ch.3.2.4). This observation lends strong support to the notion that dimerisation plays a role in reactivation from O_2 attack.

The proverbial litmus test of O_2-tolerance is the ability to maintain activity at a steady state in the sustained presence of O_2. In such chronoamperometry experiments the Monomer is found to generally maintain only a much smaller fraction of activity than the Dimer. The Monomer is disproportionately affected by increasing O_2 concentration.

A new extended model of O_2-tolerance offers a likely explanation for the observed differences between Hyd-1 Dimer and Monomer (Ch.3.3.3). The model starts with the four-electron reduction of O_2 to H_2O, forming the inactive 'Ready' state Ni-B, as confirmed in the previous chapter (Ch.2). Reactivation of Ni-B is fast if a further

electron can be supplied rapidly. However, if this electron is lost to O_2 in an outer-sphere reaction (accounting for the side reaction products identified in Ch.2), reactivation will be hindered. In the Dimer, electron transfer between the distal clusters would be able to compensate for this loss, as well as increase electron availability at more oxidising potentials (see Discussion Ch.3.3.3 for details). A fit of the extended model to the measured levels of steady state activity at different O_2 concentrations yields a very good agreement for both Dimer and Monomer.

Regardless of the details of the mechanism, it is clear that the $(\alpha\beta)_2$ dimeric assembly plays an important role in O_2-tolerance through the ability to transfer electrons between redundant halves of the Dimer (*via* adjacent distal clusters) to aid reactivation of an inactivated partner - Teamwork pays off! The findings in this chapter thus implicate both a new example of cooperativity in biology and a new role for dimerisation - very different from the known examples described in the introduction to this chapter (Ch.3.1.2).

Chapter 4

Incorporation of Azido Phenylalanine into Hyd-1

4.1 Introduction

The ability to incorporate non-natural amino acids, with functional groups and physical properties not found in nature, offers unique opportunities for the study of structure-function relationships in proteins. In addition to fluorescent or photo-reactive molecules [169, 170], amino acids with novel metal-binding sites or unusual reactive groups can be utilised [171, 172] and potentially enhance enzyme performance or even add entirely new functionality.

For most applications it is desirable or even necessary to introduce the non-natural amino acid at a specific site. Co-translational incorporation is the most universally applicable solution to this problem. A proven method for such co-translation incorporation utilises a stop condon (here TAG), re-purposed to be recognised by a newly introduced, modified aminoacyl-tRNA synthetase/tRNA pair (aaRS/tRNA, see Ch.4.1.2): a host of synthetic amino acids have been incorporated into proteins in bacteria, yeasts and even mammalian cells in this way [173, 174, 175].

Here, the amino acid p-azido-L-phenylalanine (AzF) was chosen for incorporation into *E.coli* Hyd-1. In contrast to the natural amino acids, AzF can undergo a specific cycloaddition with alkynes (Ch.4.1.3); this reaction might be utilised to immobilise the enzyme covalently in a specific orientation or to attach (spin) labels for spectroscopy experiments.

4.1.1 Site and Approach of AzF Incorporation into Hyd-1

TAG stop codons were previously introduced into the *hyaA* gene for the small subunit of *E. coli* (*Ec*) Hyd-1 in two locations [1], as shown in Fig.4.1. In the absence of a Hyd-1 crystal structure at the time, the choice of these sites was based on the crystal structure of, and sequence alignment with, the related *D. fructosovorans* (*Df*) [NiFe] hydrogenase. The two hydrogenases share 32.4% sequence identity, as determined using the EMBOSS Needle algorithm.

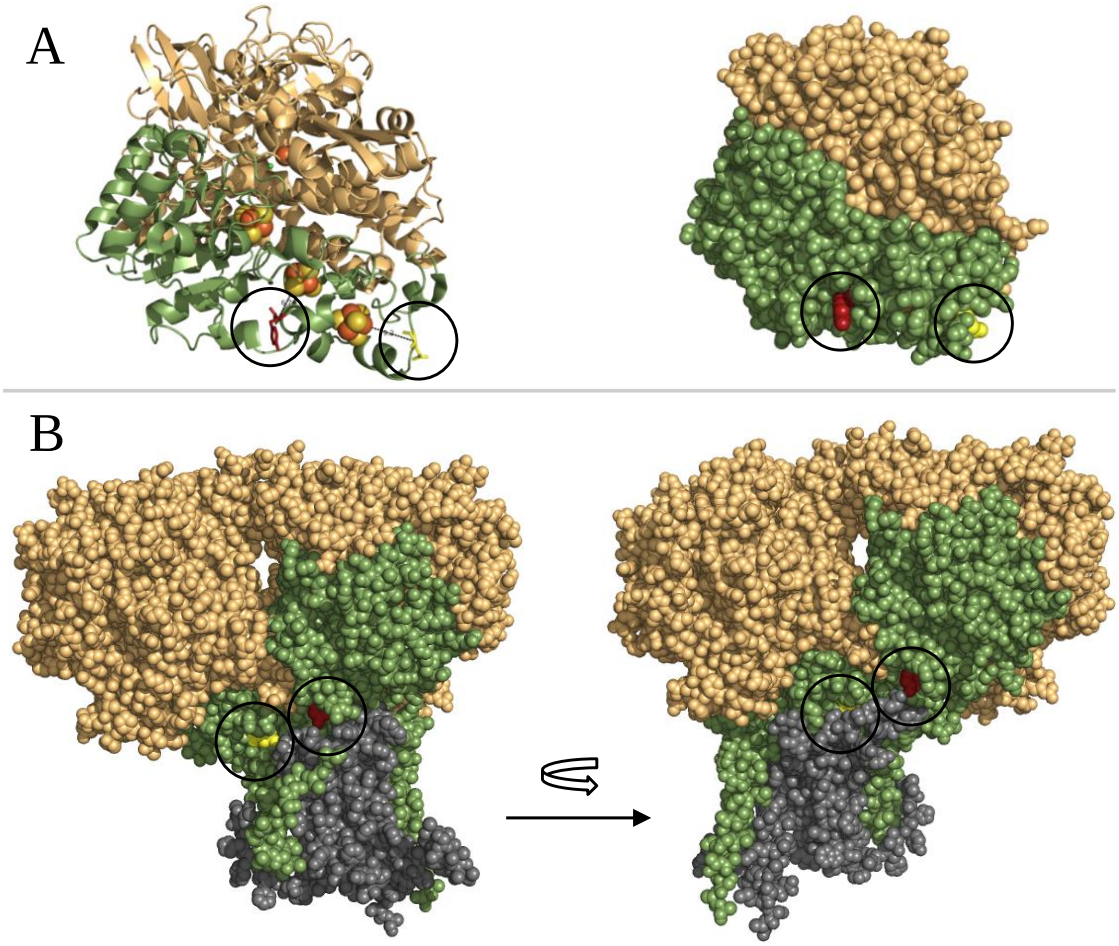

Figure 4.1 Location of Mutations mapped onto *Df* Hyd and *Ec* Hyd-1: The location of the amino acid corresponding to the TAG mutation is shown in red for the site in proximity to the medial FeS cluster, and in yellow for the site in proximity to the distal FeS cluster. The large subunits are shown in beige, small subunits in green and cognate cytochrome *b* in grey. **A**) Cartoon and spheres representation of the *D. fructosovorans* [NiFe] hydrogenase crystal structure (PDB: 1FRF). **B**) Spheres representation of the *E. coli* Hyd-1 crystal structure, shown from both 'front' and 'back' (PDB: 4G3D). Figure created using PyMOL.

As seen on in Fig.4.1.A, one site (shown in red) was chosen in close proximity to the medial cluster. The amino acid in question is a tyrosine (corresponding to Y227

in HyaA), so that incorporation of AzF in its place would results in exchange of only one functional group (-OH) on the protein surface by another ($-N_3$), minimising the possible structural impact. On the genetic level only one base change is required in *hyaA* (TAT814TAG). In the following, this near medial cluster variant will be called Hyd-1 Y227AzF. The other modified site in the small subunit (GAG733TAG or E200AzF), was chosen close to the distal FeS cluster. Since it was suspected that E200 could be partially occluded by the trans-membrane helix of Hyd-1, Y227AzF was selected for all the experiments shown in this chapter.

The crystal structure of *E. coli* Hyd-1 was only published later [64]. As shown in Fig.4.1.B, multimeric assembly in the form of a dimer of heterodimers $(\alpha\beta)_2$ has profound implications for the local environment of the mutant sites. The distal site on one small subunit is very close to the medial site on the other. Moreover, the distal site on the hydrogenase carrying the cognate cytochrome *b* is completely buried. The results in Ch.3.2.3 show that this assembly, with one attached cytochrome, is likely to be the dominant species of isolated Hyd-1 in solution. The medial site Y227 is located in a recess in proximity to the dimer interface, instead of the very exposed position found in the *Df* hydrogenase.

The aaRS/tRNA pair (see Ch.4.1.2), required for co-translational incorporation of AzF in response to the TAG stop codon, was kindly provided by Peter Schultz (Scripps Research Institute). It is expressed from the pEVOL vector (see Appendix A.2), which was developed by Young and co-workers to enhance the yield of mutant protein in *E. coli*, by placing one copy of the *aaRS* gene under an (arabinose) inducible promoter and another copy under the control of a constitutive promoter [176]. The *E.coli* MC4100 strains previously used for his-tagged Hyd-1 expression carry the $araD^-$ mutation, which renders arabinose toxic to the cells [177]. As a consequence, growth of these cells was strongly inhibited in the presence of arabinose for *aaRS* induction and the TAG mutations had to be repeated in *E. coli* MG1655, into which the HyaA his-tag was introduced by Frank Sargent (University of Dundee). Azido-L-phenylalanine itself was synthesised for incorporation as described in Ch.4.2.1 and Ch.5.6.

4.1.2 An aaRS and tRNA pair for Non-Natural Amino Acids

The approach for incorporation of non-natural amino acids used in this thesis, developed by Schultz and co-workers, re-purposes a rarely used stop codon in *E. coli* (the so called 'amber' codon TAG) to code for the new amino acid (AzF); this involves recognition of the TAG codon by a unique tRNA and specific attachment of the synthetic amino acid to the tRNA by an aminoacyl-tRNA synthetase (aaRS) [173]. The new aaRS/tRNA pair with the desired codon and amino acid specificity was created by Chin and co-workers through directed evolution from an orthogonal tyrosyl-RS/$tRNA^{Tyr}_{CUA}$ pair from the archaea *Methanocaldococcus jannaschii* [178]; this orthogonal aaRS does not aminoacylate *E. coli* tRNA, while the archaeal tRNA is not aminoacylated by any endogenous aaRS. The directed evolution procedure to change the specificity of tyrosyl-tRNA synthetase and $tRNA^{Tyr}_{CUA}$ to AzF and TAG involved several cycles of positive and negative selection, performed on libraries of randomly modified recognition sites [178].

Finally, it is noteworthy that recent advances in the field have made it possible to incorporate several non-natural amino acids simultaneously. Neumann and co-workers synthetically evolved an orthogonal ribosome that recognises quadruplets, thus adding to the pool of available codons [179]. Following a different strategy, Isaacs and co-workers demonstrated the genome-wide removal of a redundant codon, freeing it up to be exclusively reassigned to a new amino acid [180].

4.1.3 Azide-Alkyne Cycloaddition

Unlike any of the natural amino acids, p-azido-L-phenylalanine is able to specifically react with alkynes in the Huisgen cycloaddition [181]. While the uncatalysed reaction requires elevated temperatures, catalysis by Cu(I) enables the reaction to proceed at physiological conditions [182]. The catalytically active Cu(I) is commonly generated from $Cu(II)SO_4$ by use of a reducing agent such as sodium ascorbate.

Polydentate nitrogen donors, *e.g* tris-triazolyl amines, were found to greatly enhance the reaction rate. Hein *et al.* proposed that these molecules support the Cu-catalysed azide-alkyne cycloaddition (CuAAC) through a combination of strong and weak donor ligands, binding and stabilising Cu(I) sufficiently to prevent the formation of unreactive polymeric complexes, while leaving the coordination sphere of the σ-acetylide Cu center accessible to the azide. Figure 4.2 shows the CuAAC for a phenyl azide (representing the azido-phenylalanine used in this chapter) with the stabilised reactive intermediate proposed by Hein and Fokin, which includes a dinuclear Cu(I) acetylide, as suggested by kinetic and computational studies [183].

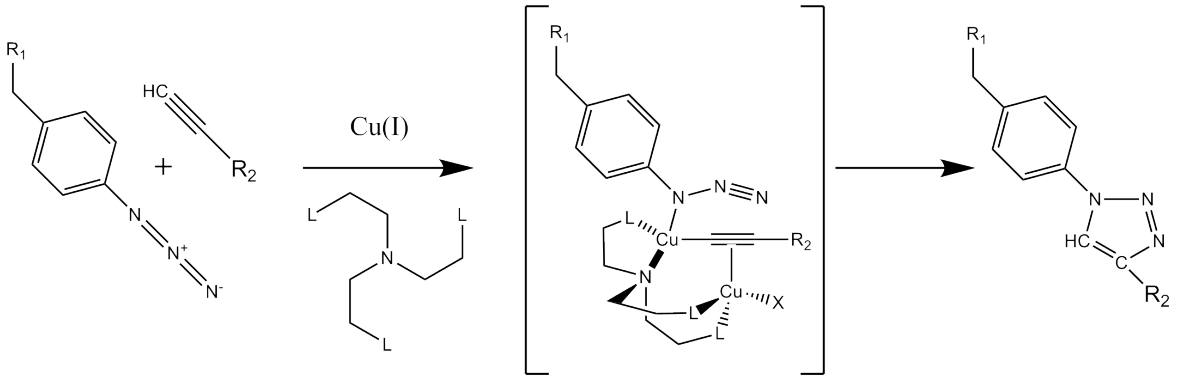

Figure 4.2 Copper-catalysed azide-alkyne cycloaddition (CuAAC) shown for a phenyl azide and including the tris-triazolyl amine stabilised intermediate reactive complex, as proposed by Hein and Fokin [183]. The reaction product is a triazole.

Modification of *in vivo* generated azide-containing protein by CuAAC was successfully demonstrated by Deiters and co-workers at room temperature in phosphate buffer (pH 8.0), using tris-(2-carboxyethyl)phosphine (TCEP) as the reducing agent and tris-(benzyltriazolylmethyl)amine (TBTA) as the ligand. The latter is itself synthesised through an azide-alkyne cycloaddition from tripropargylamine and benzyl azide [184].

Another way to aktivate alkynes for the cycloaddition reaction is by making use of cyclic alkynes with significant ring strain. In cyclooctyne the deformation of the triple bond angle accounts for as much as 18 kJ/mol of ring strain, a destabilisation of the ground state that results in much increased reaction rates in comparison to unstrained alkynes [185]. Use of such strained alkynes for Cu-free azide-alkyne cycloaddition was

demonstrated for living systems by Agard *et al.*, a reaction that requires no further auxiliary reagents [186]. The reaction with a simple cyclooctyne is, however, still relatively slow compared to the Cu-catalysed reaction. The recent addition of further aromatic rings to further increase ring strain, along with functional groups to enhance solubility in aqueous solvents, as made the Cu-free cycloaddition more widely applicable [187, 188].

Both the Cu-catalysed and Cu-free AAC fall within the so called 'click reactions'. 'Click chemistry' is a description of a set of reactions that join molecules with high specificity, efficiency and, usually, speed in a modular fashion through a large driving force [189]. Sharpless and co-workers defined click reactions with the following requirements: modularity, high selectivity and yield, readily available substrates, inoffensive by-products and benign solvents. Especially the latter two requirements mean that click chemistry can often be carried out in biological systems.

4.2 Results

4.2.1 Synthesis of p-Azido-L-Phenylalanine

The synthesis of p-azido-L-phenylalanine (AzF) was designed based on work published by Schwyzer and Cavieziel [190] and Liu and Tor [191], with slight adjustments to the relevant procedures. The synthesis route is outlined in Fig.4.3, while the detailed final procedure can be found in the methods chapter (Ch.5.6).

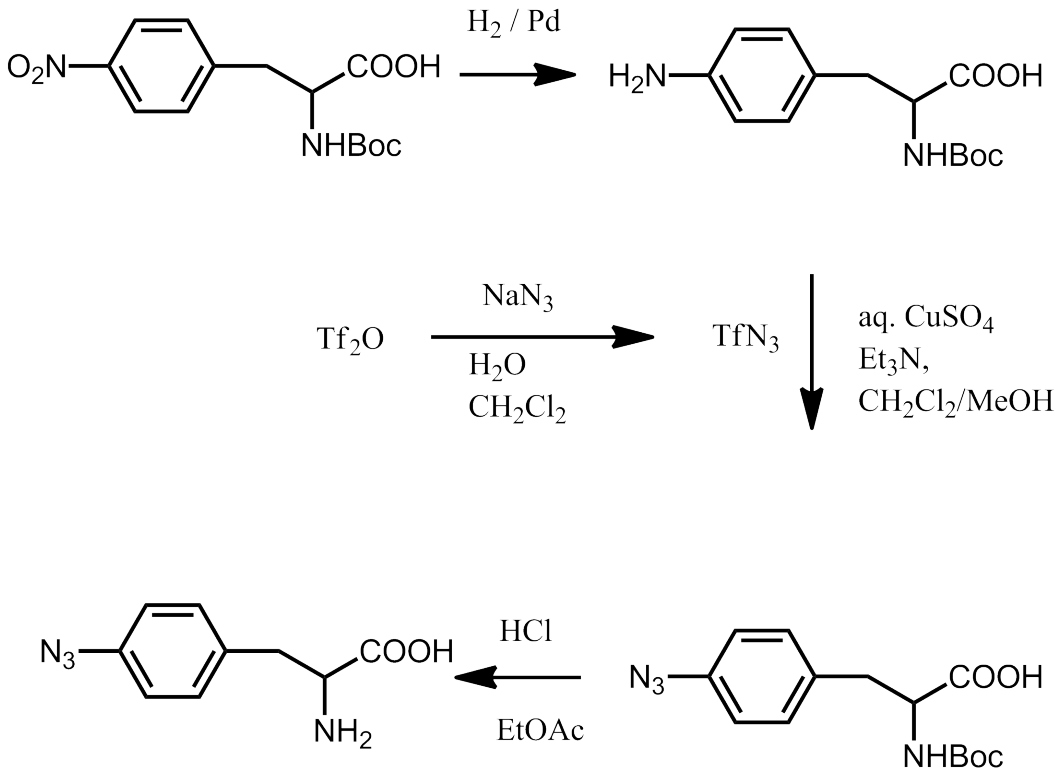

Figure 4.3 AzF Synthesis Overview:
N-(tert-butoxycarbonyl)-4-nitro-L-phenylalanine is hydrogenated over a palladium catalyst to yield the corresponding amine. Trifyl azide is produced from triflic anhydride (TfO_2) and sodium azide and used for Cu-catalysed diazo transfer to the phenylalanine. Removal of the protecting Boc group by HCl yields the final product p-azido-L-phenylalanine.

The starting material, tert-butoxycarbonyl (Boc) protected nitro-L-phenylalanine, was hydrogenated in a reaction catalysed by palladium on activated carbon to yield the corresponding amine. Conversion into the azide was achieved by Cu^{2+} catalysed diazo transfer from triflyl azide. Full substrate conversion at these steps was monitored by following the shift of the ^1H NMR peaks of the aromatic protons. Mass spectrometry was also employed to verify the intermediate products and to follow the removal of the

protecting Boc group. Figure 4.4.A shows the azido phenylalanine before deprotection, with an expected exact mass of 306.13 Da and its MALDI TOF ES$^-$ spectrum with deprotonated product peaks at 305.13 and 611.26 m/z. After removal of the Boc group (100.06 Da) the final product is expected to have a mass of 206.08 Da and indeed the mayor peak is found at 205.09 m/z in the ES$^-$ spectrum (Fig.4.4.B). The spectrum was recorded before the final washing steps.

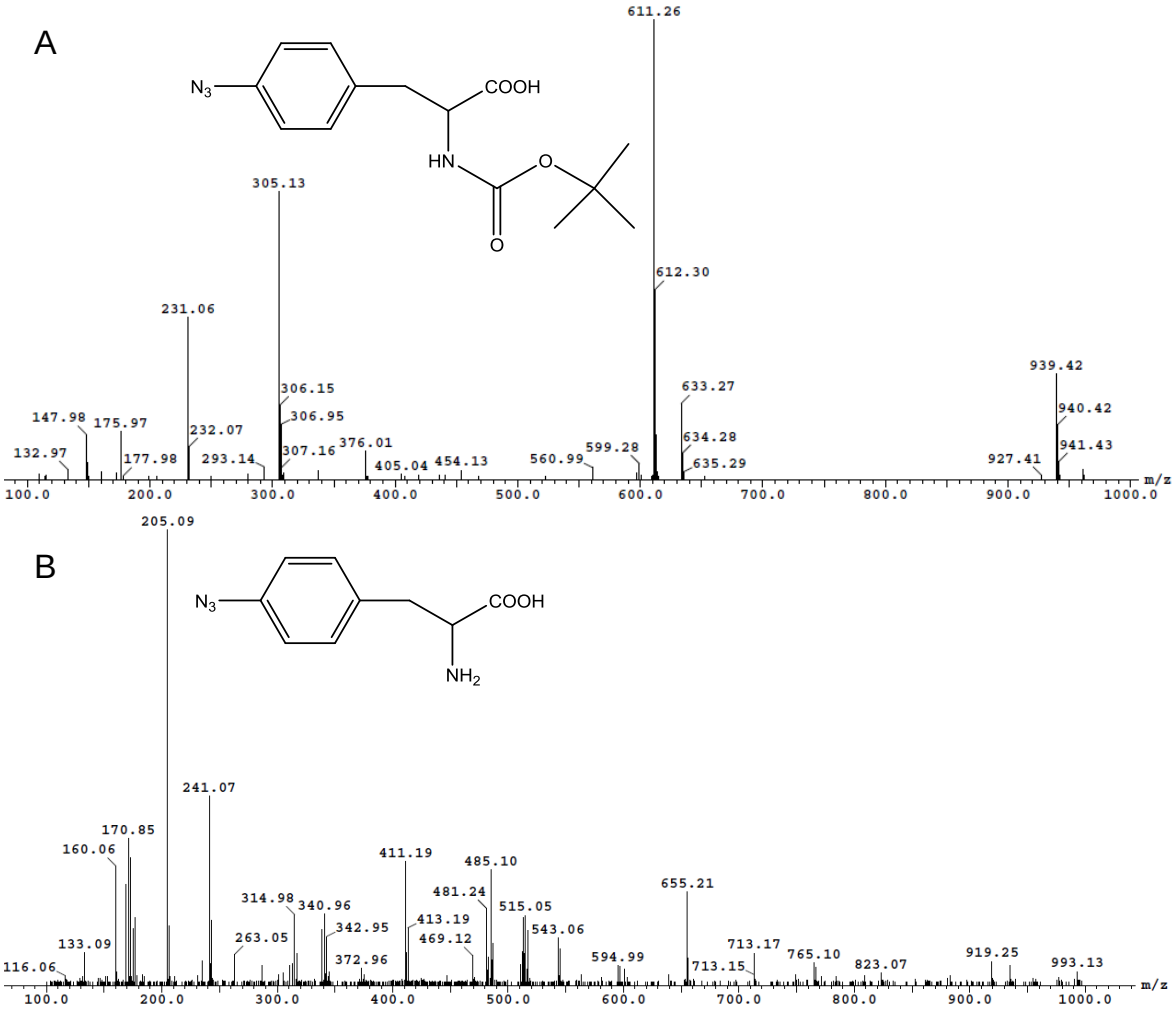

Figure 4.4 ESI TOF Mass Spectrometry of AzF in negative electrospray ionisation mode: **A)** The intermediate product containing the tert-butoxycarbonyl protecting group with a total exact mass of 306.13 Da. The corresponding deprotonated peak is found at 305.13 m/z. **B)** The final product after removal of the 100.06 Da Boc group. For an exact mass of 206.08 Da the deprotonated peak is found at 205.09 m/z.

The overall yield (mol/mol) of the synthesis route from (Boc-nitro) to (p-azido)-L-phenylalanine varied between 80 and 85% (from batch to batch) and an ^{1}H NMR spectrum was recorded for the final product. Using the table of NMR chemical shifts of common laboratory solvent compiled by Gottlieb *et al.* [192], mayor solvent peaks (4.88 ppm H_2O in CD_3OD and 3.30 ppm residual protonated CD_3OD) and minor impurity peaks (ethyl acetate and diethyl ether from product washing steps) can be accounted for. The p-azido-L-phenylalanine peaks are assigned as follows:
^{1}H NMR (300 MHz, Methanol-d_4) δ[ppm] 7.38 - 7.26 (m, 2H, **4, 6**), 7.13 - 7.01 (m, 2H, **1, 3**), 4.22 (dd, J = 7.7, 5.5 Hz, 1H, **8**), 3.29 - 3.06 (m, 2H, **7**).

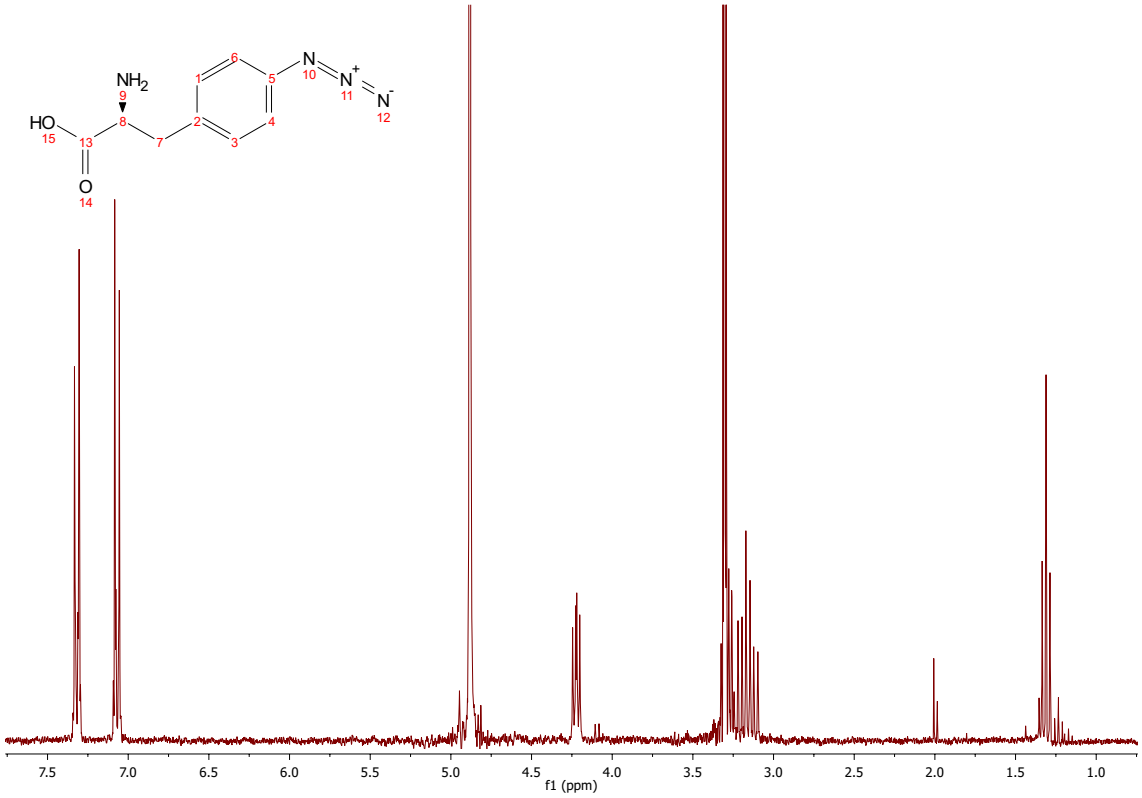

Figure 4.5 ^{1}H NMR 300MHz Spectrum of p-azido-L-phenylalanine: After deprotection the product precipitate was washed with ethyl acetate and diethyl ether and subjected to NMR analysis in CD_3OD using a Varian Hg-300 spectrometer and evaluated with the MestReNova software.

4.2.2 Hyd-1 AzF Expression and Purification

For expression of Hyd-1 Y227AzF the corresponding *E. coli* strain was transformed with the arabinose-inducible pEVOL vector containing the genes for the unnatural aaRS/tRNA pair as well as a chloramphenicol acetyltransferase marker. Expression and purification of enzyme was carried out as described in detail in Ch.5.8, in batches of 2-10 L. Before inoculation, the presence of the pEVOL plasmid was verified by isolating it from an aliquot of starter culture (miniprep) and visualising the plasmid *via* DNA gel electrophoresis.

As mentioned above (Ch.4.1.1) the *E. coli* MC4100 strain usually used for Hyd-1 expression had to be replaced by the MG1655 strain, carrying the same mutations, to avoid drastically repressed growth due to arabinose toxicity. Yet, under Hyd-1 AzF expression with the pEVOL plasmid even this strain showed a much decreased growth rate and final cell density. The selection pressure through chloramphenicol and especially the detrimental effect of the suppressed native TAG stop codons elsewhere in the *E. coli* genome are the obvious causes of such reduced growth [176]. Other studies have been able to compensate for the resulting low yield per culture volume by over-expression of the (simple) target protein from a second plasmid [193]. For Hyd-1, construction of an over-expression plasmid has not been achieved to date, so that it is expressed from the (modified) genome at native levels. As a consequence, the gene is also under native regulation and the anaerobic late growth stage requirement for Hyd-1 expression (Ch.1.2) hinders well timed induction of AzF incorporation. However, the presence of the second (constitutive) promoter on the pEVOL vector (see Appendix A.4) is expected to mitigate this complication. Indeed, after only a few attempts with varied induction time points, a protocol (Ch.5.8) was found that yielded sufficient quantities of purified enzyme for electrochemical and labelling experiments.

4.2.3 Hyd-1 AzF Electrochemistry

Purified Hyd-1 Y227AzF was tested for activity in a standard cyclic voltammetry experiment on a rotating PGE electrode, as shown in Fig.4.6.A. The enzyme is found to be active and the CV shape fully consistent with native enzyme (Fig.1.4.2.A), confirming that the amino acid exchange in proximity to, but not right at, the medial cluster has no deleterious catalytic effect.

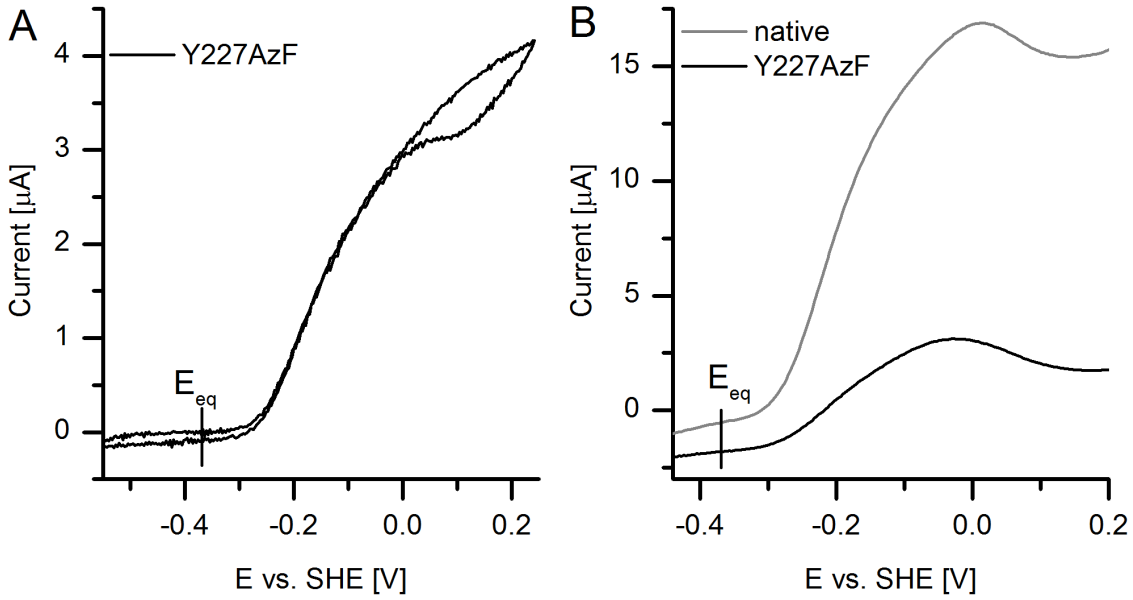

Figure 4.6 Hyd-1 Y227AzF Cyclic Voltammetry:
A) Adsorbed at a rotating PGE electrode (100% H_2, pH 6, 37 °C, 10 mV/s, ω = 2000 rpm). **B)** Averaged forward and backward scans of Hyd-1 on a stationary alkyne-modified gold electrode: Hyd-1 Y227AzF (black line) was incubated on the electrode in the presence of click reagents, native Hyd-1 (grey line) in the absence of click reagents. (100% H_2 at 1000 ccm, pH 6, 37 °C, 10 mV/s, stirred solution). The $2H^+/H_2$ equilibrium potential is marked by a vertical line in both panels.

A gold electrode (Au layer on a silica wafer substrate, see Ch.5.1.2) was functionalised with an alkyne monolayer as depicted in Fig.4.7, to test whether site-specific immobilisation *via* the azide residue could be achieved. The modified electrode was then incubated with click reaction reagents ($CuSO_4$, TCEP, TBTA, phosphate buffer pH 8.0, see Ch.5.13) in the presence of Hyd-1 Y227AzF. Native Hyd-1 was applied to a modified electrode as a negative control. Cyclic voltammetry was then performed on the electrodes, as shown in Fig.4.6.B. It is apparent, that both native and Y227AzF Hyd-1 form active protein films on the alkyne functionalised electrode surface. It should

be noted that varying current offsets were observed with the Au electrodes and that the electrode size, and thus the observed currents, varied significantly as a result of uneven wafer cutting.

Since native enzyme readily adsorbes onto the alkyne layer, specific immobilisation is not possible, nor is it clear at this stage whether the Y227AzF variant successfully forms a triazole.

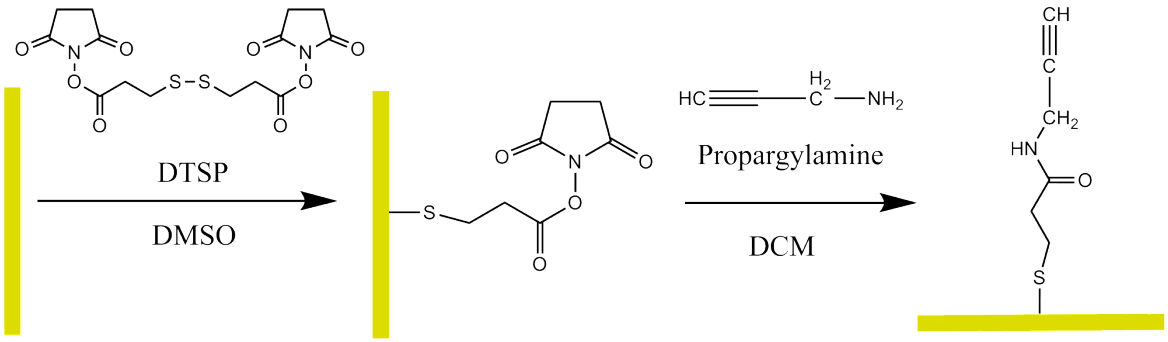

Figure 4.7 Assembly of an Alkyne Monolayer on a Gold Electrode: The Au surface is first treated with 3,3'-dithiodipropionic acid di(N-hydroxysuccinimide ester) in dimethyl sulfoxide, the product of which then reacts further with propargylamine in dichloromethane. See Ch.5.1.2 for the protcol.

4.2.4 Hyd-1 Mass Spectrometry

Protein mass spectrometry of Hyd-1 was carried out as described in Ch. 5.12. The Hyd-1 samples were prepared by exchanging Hyd-1 into ammonium acetate buffer (50 mM, pH 7.4), using a 3 kDa centrifugal filter. Exemplary results of liquid chromatography electrospray ionisation mass spectrometry (LC-ESI-MS), performed in positive ionisation mode on Hyd-1 (native and Y227AzF), are shown in Fig.4.8. Panel A shows the LC elution profile for both native and Y227AzF Hyd-1, and the peaks corresponding to large and small subunit are marked LS and SS respectively. All the recorded mass spectrometry protein fragment peaks (m/z) contributing to an LC peak (here SS) are summed up, using the MassLynx Software package (Micromass, Waters); this yields the data subset shown in Fig.4.8.B which is processed with the the MaxEntI plugin (maximum entropy I algorithm) to calculate the average isotopic (uncharged) mass of the protein (Fig.4.8.C).

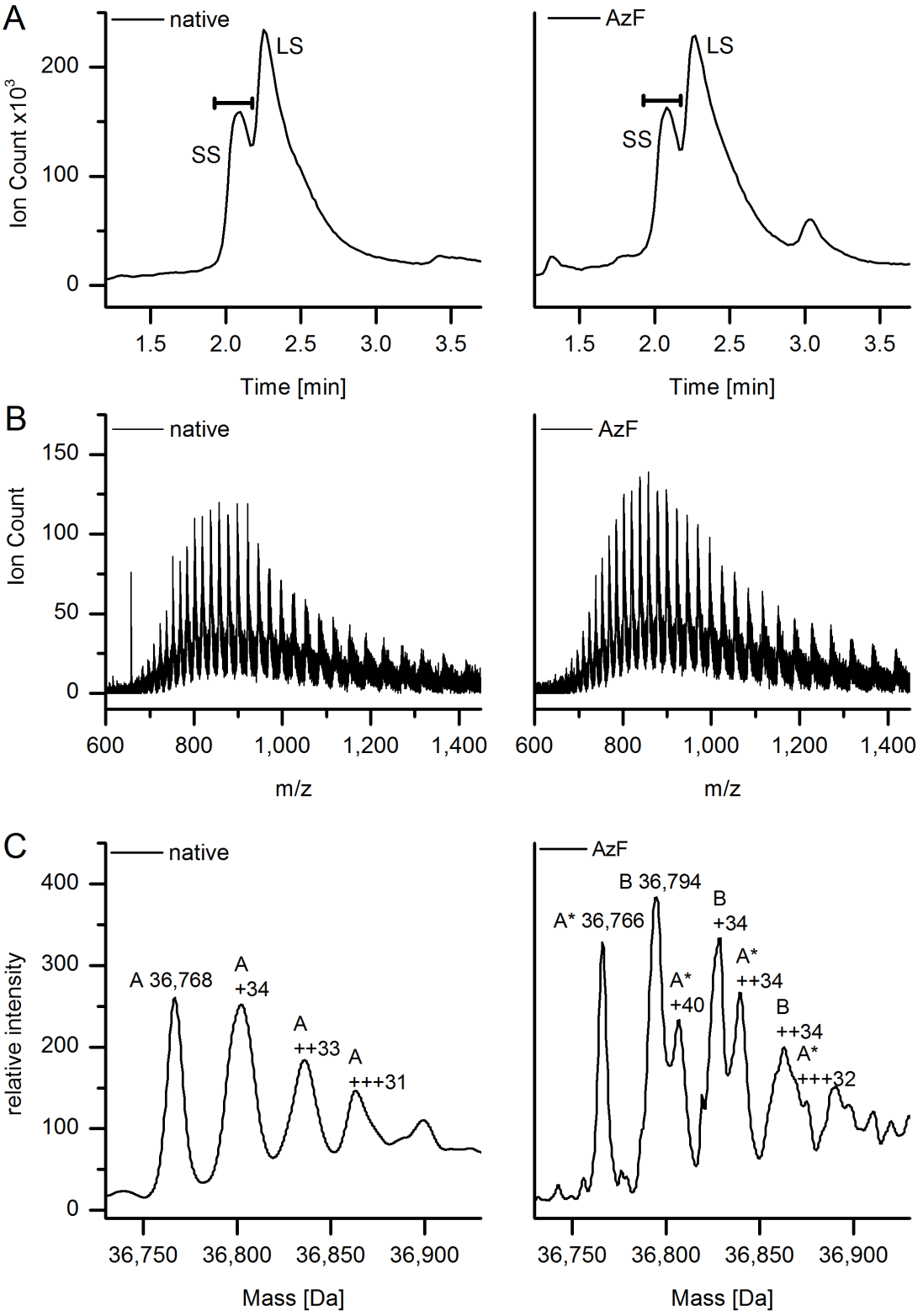

Figure 4.8 LC-ESI$^+$ Mass Spectrometry of Hyd-1: Results for native Hyd-1 are shown on the left and those for the Y227AzF variant on the right (ionisation mode: positive). **A)** Liquid chromatography (reversed phase) elution profile. Large and small subunit peaks (LS and SS) are marked accordingly and the summing-up process of mass spectrometry peaks for panel B is illustrated by a double blunt-ended arrow. **B)** Sum of m/z protein fragment peaks recorded for the small subunit. Processing of this data subset with the MaxEntI algorithm (0.5 Da/Channel resolution, 0.4 Da peak width at half height) yields the bottom panel. **C)** Individual whole subunit peaks are labelled with a letter and the calculated average mass (Da). Adduct peaks are marked with sequential weight additions in Da to the respective main species.

Since the calculated average mass peaks are much broader than the more precisely defined, directly measured m/z values, the accuracy of absolute mass estimated from these peaks will be subject to a certain variation, which is estimated here as ca. ±2 Da. The expected small subunit (SS) monoisotopic mass was calculated with the BioLynx plugin (MassLynx software) from the amino acid sequence, giving the following results with the indicated functional group on the phenyl residue at position 227: native (-OH) 36,767.8 Da, AzF (-N_3) 36,792.8 Da and (-N) 36,764.8 Da.

For the native enzyme (Fig.4.8.C, left) the first average mass peak at 36,767 ±2 Da is assigned as the unmodified small subunit (designated A). A series of peaks correlating to sequential mass increases of ca. 32 ±2 Da relative to A are assigned as adducts (where $A + 34 + 33 \equiv A + +33$). These +32 Da adducts are assigned as sulphur adducts resulting from addition of inorganic sulphur to cysteine residues, a reaction that has been observed in mass spectrometry of FeS cluster containing proteins before [194].

The Hyd-1 Y227AzF variant presents a more complex spectrum (Fig.4.8.C). The first peak at 36,766 ±2 Da could either correspond to native enzyme with an unmodified tyrosine (-OH) or to a nitrene stabilised as a phenyl amine (-NH_2). Decomposition of phenyl azides *via* nitrenes is observed at temperatures as low as 140-170 ℃ [195**?**], and is thus a feasible reaction given the desolvation temperature of 250 ℃ in this experiment (see Ch.5.12). This first peak is tentatively assigned A^*. The second peak is unlikely to be an adduct peak of A^*, as it has a higher intensity. At 36,794 ±2 Da the second peak also matches the intact azide (-N_3) and is thus designated as a distinct species B. The remaining peaks are assigned as alternating sulphur adducts of A^* and B, except for the first A^* adduct which is a better match for K^+ addition. The electrophilic nature of a nitrile might favour such binding.

A brief analysis of the (unmodified) FeS cluster-free large subunit can be found in the appendix (A.5); it shows only one sulphur adduct peak, probably originating from the active site bridging ligands (Ch.1.1.1).

4.2.5 Hyd-1 AzF Labelling

To increase the mass difference between native and variant enzyme for unambiguous identification by mass spectrometry, but also to establish if an incorporated azide could react as part of the protein in the specific azide-alkyne cycloaddition (Ch.4.1.3), labelling experiments were carried out both with and without Cu(I) as a catalyst.

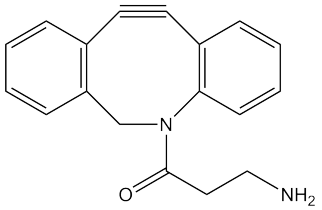

Figure 4.9 Structure of Dibenzocyclooctyne-amine (DBCOA)

Copper-free cycloaddition, developed more recently than the Cu-catalysed reaction and experimentally simpler, was undertaken with dibenzocyclooctyne-amine (DBCOA, from Sigma-Aldrich) as the label. While the amine residue, and the nitrogen atom in the ring structure, of DBCOA (Fig.4.9) are supposed to aid hydrophilicity [188], it was necessary to add a small volume of EtOH to DBCOA prior to addition to the reaction solution (30 mM phosphate buffer, pH 8.5) to achieve dissolution. After incubation of Hyd-1 with DBCOA for 3 to 4 hours, both native and AzF Hyd-1 appeared undamaged by eye, but precipitated unavoidably when concentrated and exchanged into ammonium acetate buffer for mass spectrometry (for unknown reasons). As this sample precipitation prevented confirmation of azide labelling with DBCOA by LC-ESI MS, use of a highly sensitive dye (adding a second analysis option) appeared favourable.

The alkyne cyanine dye (ACD, from Sigma-Aldrich) shown in Fig.4.10 was used for labelling in a Cu-catalysed reaction. The method employed, adapted from work published by Deiters *et al.* [193], had to be adjusted to a lower phosphate buffer concentration (33 mM instead of 100 mM). Use of the published concentrations led to formation of large quantities of light-blue precipitate (presumably Cu phosphate), even in the absence of dye and enzyme; this precipitate, in turn, led to precipitation of enzyme as well. The use of ACD was limited to concentrations of approx. 60 µM by the low solubility in water.

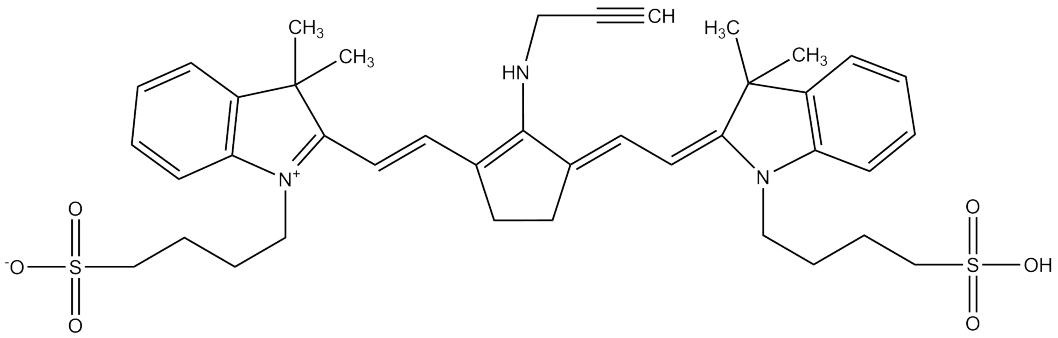

Figure 4.10 Structure of Alkyne Cyanine Dye 718 (ACD)

In aqueous buffer ACD was found to undergo an irreversible colour change from blue to lavender and finally to light pink. The rate of this colour change was increased by exposure to light, *e.g.* recording of a UV-vis spectrum or (less so) simple ambient light. These colour changes were also affected by the pH of the solution, *i.e.* a high pH stabilised the original blue colour of the solution. Fig.4.11 shows the changes in the UV-vis spectrum of ACD with varying pH in aqueous buffer. The complex spectrum contains mayor peaks at 349, 510, 623 and 740 nm. As the pH decreases, the peaks at 623 and 740 nm decrease strongly, while the peaks at 349 and 510 nm increase. The changes are irreversible and the peaks at 349 and 510 nm are retained after incubation in aqueous solution for many days.

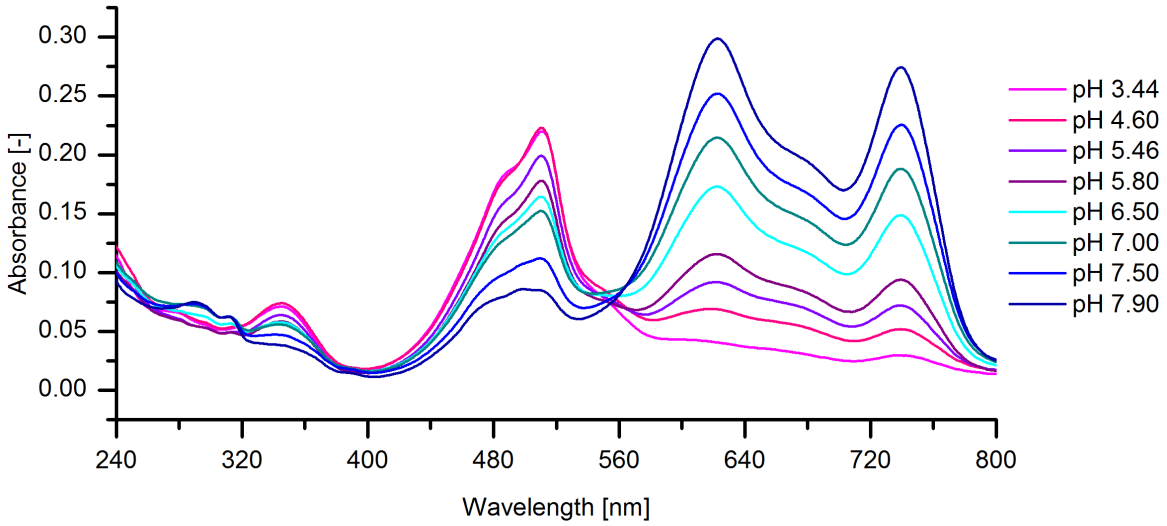

Figure 4.11 UV-vis Spectrum of ACD in aqueous buffer with varying pH: In freshly prepared solutions mayor peaks are found at 349, 510, 623 and 740 nm. With decreasing pH the colour shifts from blue to light pink (50 mM phosphate buffer, room temperature).

The reaction of ACD with Hyd-1 was carried out over 8 to 9 hours at pH 8.0 as described in Ch.5.13, with $CuSO_4$, TCEP as the reducing agent (Cu(II)→Cu(I)) and TBTA as ligand (Ch.4.1.3). After the reaction, exchange of the products into ammonium acetate buffer for mass spectrometry was attempted. Unfortunately, the enzyme precipitated on the centrifugal filter membrane, as with DBCOA above, along with significant quantities of the dye. The same precipitation was observed when phosphate or mixed hydrogenase buffer (MHB) were used, instead of ammonium acetate, to simply remove excess dye. After various tests, DNA extraction columns (QIAquick®, QIAGEN) were identified as a way of separating most of the dissolved dye from Hyd-1 without precipitating the enzyme. The samples obtained this way were clear to the eye, but still not exchangeable into ammonium acetate without precipitation of enzyme; they did, however, allow for a comparison of native and Y227AzF Hyd-1 by UV-vis spectroscopy. Figure 4.12.A shows the resulting UV-vis spectrum of ACD solution with and without click reagents ($CuSO_4$, TCEP, TBTA) in the absence of enzyme.

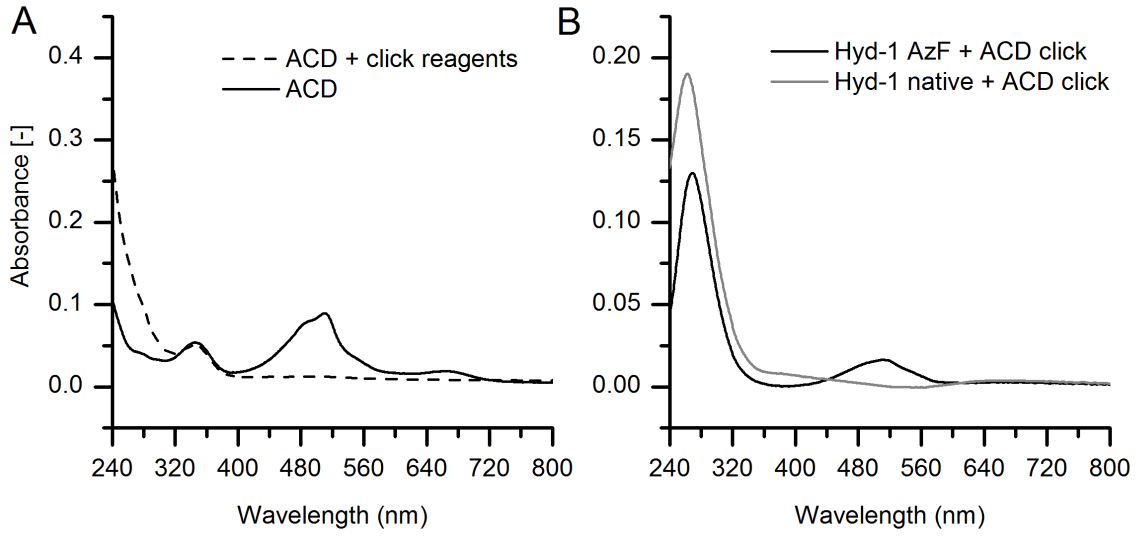

Figure 4.12 Labeling of Hyd-1 with ACD: A) UV-vis spectrum of ACD after ca. 8 h in reaction buffer with and without click reagents in the absence of enzyme. The spectrum was recorded against plain phosphate buffer as the blank. **B)** UV-vis spectrum of Hyd-1 and ACD after 8 h of click reaction. The spectrum is shown against ACD + click reagent as the blank (dashed line in panel A).

The peaks at 623 and 740 nm have almost completely disappeared in the plain ACD solution, while the solution with click reagents has also lost the 510 nm peak. In the latter case, a small amount of dark precipitate can be observed at the bottom of the reaction vial. If native Hyd-1 is exposed to ACD in the click reaction solution the same effect is observed, *i.e.* the 510 nm peak is also lost. In the presence of Hyd-1 Y227AzF, however, the UV-vis spectrum still shows a distinct 510 nm peak after the reaction. The availability of an azide for reaction with ACD appears to preserve some fraction of the dye in the state in which it shows absorbance at 510 nm (see Discussion, Ch.4.3).

Aliquots of 33 mM phosphate buffer at pH 8.0 (which represents the reaction conditions) and known concentrations of ACD, but no other reactants, were exposed to light and allowed to slowly loose all absorbance at high wavelength until they resembled the 'pink' ACD (solid line) in Fig.4.12.A. Using these samples, a calibration for absorbance at 510 nm (A_{510}) was carried out. This calibration allowed for the determination of the amount of 'pink' ACD retained in the labelling experiment (Fig.4.12). For the reagent-free ACD solution (panel A) a concentration of 5.52 µM 'pink' ACD is calculated (which means that ca. 55 µM ACD were removed by the DNA extraction column). In the presence of click reagents for labelling of Hyd-1 AzF (ca. 0.85 µM Hyd-1 in the presented experiment), a value of 0.59 µM 'pink' ACD is calculated. Assuming that the difference in absorbance (by ACD) between native and Y227AzF Hyd-1 reactions is due to successful reaction of ACD with the azide group in the latter case (see Discussion below), labelling of ca. 69% Y227AzF Hyd-1 is calculated.

4.3 Discussion

Synthesis of p-azido-L-phenylalanine was successful, but rather large amounts of the costly product are required to achieve 1 mM concentrations in the large culture volumes entailed by the genomic expression method of Hyd-1. In addition to the impact on growth conditions addressed in Ch.4.2.2, the yield of mutant protein relative to WT is not only generally lower, but also depends on the location of the site in the protein, for unknown reasons. In their work establishing the expression with the pEVOL vector, Young *et al.* found the relative yield to vary between 25-85% for different incorporation sites of AzF in (over-expressed) green fluorescent protein (GFP) [176]. Despite such negative impact on yield, a sufficient amount of Hyd-1 could be isolated here for further experiments.

Since the TAG codon, in conjunction with the pEVOL vector coding for AzF, was introduced before the His-tag of Hyd-1 (see Appendix A.3), only intact hydrogenase with incorporation of an amino acid in response to the stop codon should be purified by the Ni-NTA column. There is, however, also the problem of background incorporation of endogenous amino acids instead of, or in addition to, AzF. While the aaRS was evolved to avoid such unwanted reactions and no background products are found in minimal media, complex media tend to present more of a challenge. A particular problem of specificity is presented by the strutural similarity of AzF to phenylalanine and tyrosine. Young *et al.* found ca. 14% tyrosine and putative p-aminophenylalanine incorporation into the TAG codon site in (over-expressed) myoglobin in rich media, as determined by mass spectrometry [176]. Such background incorporation would therefore also be expected in Hyd-1 (cells were grown in complex medium) and is another explanation for the presence of the putative small subunit 36,766 ±2 Da peak found in LC-ESI$^+$-MS of Hyd-1 Y227AzF, see Fig.4.8 (in addition to the decomposition of the azide in response to elevated desolvation temperatures, see Ch.4.2.4). Young and co-workers propose a metabolic conversion of azido-phenylalanine as the source of amino-phenylalanine; while this is a reasonable possibility, the sources the authors provide to back up the argument are unfortunately not concerned with metabolic processes involving AzF, but

with laser and Hg-Xe arc lamp induced photolysis of phenyl azide *in vitro* at 254 nm [196, 197]. The tyrosine (227) to azido-phenylalanine exchange seemed like an elegant solution with minimal disruption, when designing a variant with a novel functional group in proximity to the medial cluster of Hyd-1. In hindsight, considering the native background incorporation and mass spectrometry discussion above, a different site would have helped greatly in creating a more easily distinguishable variant enzyme.

Previous azide-alkyne cycloaddition reactions with proteins used much simpler and smaller molecules. For example, Debets and van Dongen used the single subunit horseradish peroxidase (HRP, ca. 43 kDa) and DsRed (ca. 26 kDa), which were functionalised by diazotransfer after purification [188, 198]. Deiters and co-workers modified the single subunit superoxide dismutase (SOD, 16 kDa) co-translationally with AzF, and had the advantage of being able to over-express the enzyme from a plasmid [193].

The revelation of the sheltered, yet not hidden, location of the Y227AzF site in the actual Hyd-1 dimeric structure (Fig.4.1) suggested that specific and oriented immobilisation might be impossible to achieve. In addition, it was found that an alkyne layer is also an excellent substrate for native Hyd-1 (Ch.4.2.3). Finally, Krishnan and Armstrong developed a three dimensional nano structured carbon electrode that allowed an order of magnitude enhancement of native Hyd-1-based fuel cell electrodes; it also made the requirement for specific immobilisation obsolete by providing several possible electron transfer interfaces to the enzyme molecules [199]. As a consequence of these three factors, specific immobilisation was not further pursued. The recessed Y227AzF position did not, however, clearly exclude labelling experiments with individual, soluble molecules.

Cu-free labelling of Hyd-1 Y227AzF with DBCOA could not be confirmed due to precipitation of enzyme after the reaction, during the sample preparation for mass spectrometry. The Cu-catalysed labelling reaction with the alkyne cyanine dye (ACD) was successful, but also experienced a number of complications. The pH- and light-dependent irreversible change in the dye's UV-vis spectrum (Fig.4.11) points to chemical

and structural changes involving the conjugated π systems. Since the blue and pink dye fragmentation patterns of the main peaks in mass spectrometry were found to be identical (see Appendix A.6), a slight structural rearrangement without a net change in mass must take place. A light-induced *trans-cis* rotation around a double bond connecting the rings is a candidate for this process, provided it can be trapped in a H^+-dependent, (irreversible) minor structural rearrangement that disrupts the π conjugation. Fig.4.13 shows the plausible product of such a reaction in which, upon excitation and *trans-cis* rotation, steric interactions between the substituents about the *cis* double bond are relieved by protonation, which is irreversible (see Fig.4.10 for comparison with 'original or blue' ACD).

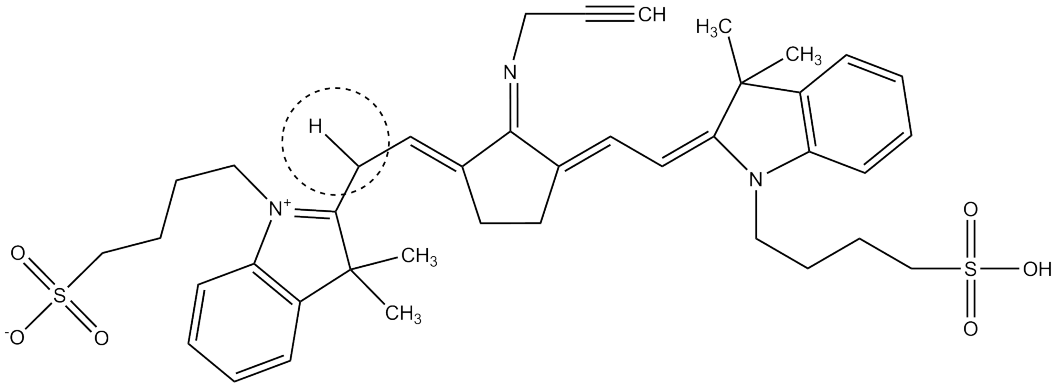

Figure 4.13 Plausible Structure of 'Pink' ACD: Steric interactions as a result of light-induced *trans-cis* rotation might be relieved by protonation at the indicated site, resulting in interrupted conjugation and a distinct change in absorbance, to yield 'pink' ACD.

In phosphate buffer, the alkyne cyanine dye effectively transforms into its pink form completely over the duration of the labeling reaction (Fig.4.12.A). The 510 nm absorbance peak is therefore still a good handle for measuring the presence and concentration of ACD, regardless of the exact nature of the process underlying the absorbance change. However, during the incubation of ACD with click reagents ($CuSO_4$, TCEP and TBTA) this 510 nm peak also disappears. What side reactions might be triggered by the click reagents? An obvious possibility is that Cu_2^+ (after reoxidation by oxygen) catalyses the oxidative Glaser coupling [200] with TBTA as the initiating base. This 'head-on' addition of the two triple bonds [201] would yield a di-alkyne. In the presence of azide (Y227AzF Hyd-1) the azide-alkyne click reaction would likely still be carried out preferentially (due to the Cu(I)-supplying reducing agent TCEP). However,

it is not clear why Glaser coupling should affect conjugation (and thus absorbance) on a different part of the molecule, while the azide-alkyne cycloaddition does not (Fig.4.12). A reaction that would affect the absorbance is an addition reaction to the conjugated π system of the dye. One such reaction might be the Diels-Alder cycloaddition, in which either the alkyne or another alkene group could act as dienophil. Since the Diels-Alder addition usually requires elevated temperatures, it is not expected to occur at significant rates in simple aqueous buffer; it is, however, aided by Lewis acids and catalysis by copper is well documented [202]. The difference in ACD absorbance between native and azide-bearing Hyd-1 (Fig.4.12) might then be explained by negative steric effects for addition reactions to ACD, once the dye is attached to the AzF site on the enzyme. The partially occluded environment of the modified site (Fig.4.1) might even be beneficial to the experiment in this instance, by enhancing the steric effect.

Finally, the labelling yield of Hyd-1 was only approx. 70 %, despite the fact that a vast excess of dye was used. This observation is in good agreement with the likely co-expression of tyrosine-containing native enzyme and the mass spectrometry experiments discussed above.

4.4 Conclusion

This chapter aimed to incorporate the non-natural amino acid p-azido-L-phenylalanine (AzF) into Hyd-1, in place of a tyrosine, close to the medial cluster in the small subunit (Y227AzF), using an evolved orthogonal aminoacyl-tRNA synthetase (aaRS)/t-RNA pair in the pEVOL vector.

Synthesis of AzF was successful, as verified by mass spectrometry and nuclear magnetic resonance spectroscopy. Expression and purification of Hyd-1 Y227AzF was hindered by the growth-diminishing side effects of the pEVOL system and low variant enzyme yield compared to WT, but a sufficient quantity of enzyme for further experiments could be purified. Hyd-1 Y227AzF was evaluated for catalytic activity by cyclic voltammetry and, as expected, showed the same activity as native enzyme.

Liquid chromatography electrospray mass spectrometry was performed, comparing native and Y227AzF Hyd-1. In both cases the spectrum of the small subunit contained sulphur adduct peaks, originating from addition of inorganic sulphur from the FeS clusters to ligating cysteines. These adduct peaks significantly complicated the mass spectrum. The principal small subunit peak of the native enzyme, containing tyrosine, was found as expected at 36,767 ±2 Da. For Y227AzF a principal peak was found at At 36,794 ±2 Da, as expected for AzF in place of tyrosine. Another major peak at 36,766 ±2 Da was, however, also identified and assigned to native enzyme and/or a phenyl nitrile decomposition product of AzF.

Labelling of Hyd-1 with small molecules also proved more complicated than expected. Due to precipitation of enzyme, mass spectrometry experiments could not be performed on these samples. The Cu-catalysed azide-alkyne cycloaddition of an alkyne cyanine dye (ACD) to Hyd-1 Y227AzF, though riddled with side reactions, was eventually successful. At ca. 70% yield this labelling reaction was incomplete, in agreement with unsuppressed background expression of native enzyme and the mass spectrometry results described above. The development an AzF aaRS optimised for expression in complex medium would likely improve purification and labelling yields, as might a different incorporation site. Alternatively, an amino acid bearing an alkyne functional group could be incorporated instead.

Chapter 5

Experimental Methods

5.1 Electrochemical Setup

All electrochemical experiments presented in this thesis were conducted with a three-electrode setup as represented in Fig.5.1. A potentiostat is used to apply a given voltage to the working electrode, relative to the reference electrode. The third electrode 'counters' current flow in the working electrode with a current of the same magnitude but in the opposite direction; this prevents significant current flow through the reference electrode, which would result in a change in electrode potential relative to solution and thus in an effective potential different from that initially intended [110]. The potentiostat used was an AUTOLAB PGSTAT(-101, -128N or -20) controlled by a computer running the NOVA v1.5 software (both EcoChemie).

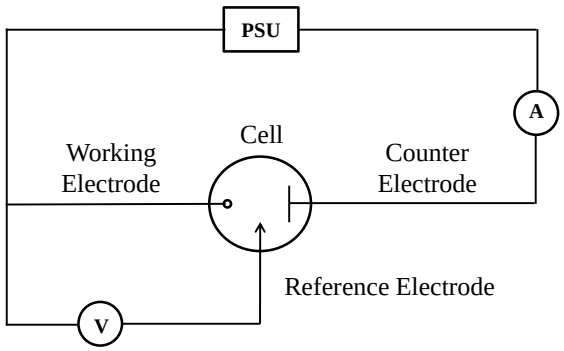

Figure 5.1 Three-Electrode Setup: A working electrode, reference electrode and counter electrode are connected to a potentiostat, which contains a power supply unit, a voltmeter and an ammeter.

The design of the electrochemical cell is shown in Fig.5.2. The working electrode, housed in the main compartment and connected to a rotator (EG&G), has a pyrolytic graphite edge (PGE) tip held in an epoxy resin. The solution-exposed 'edge' surface of this electrode has a diameter of approx. 2 mm. The main compartment contains the electrolyte solution, which was mixed hydrogenase buffer (100 mM NaCl, 15 mM MES, 15 mM HEPES, 15 mM TAPS, 15 mM CHAPS, 15 mM sodium acetate) for all experiments in this thesis. The counter electrode is also placed in the main compartment and consists of a Pt wire. The saturated calomel (SCE) reference electrode is housed in a semi-separate compartment in saturated aqueous NaCl solution, connected to the main cell via a Luggin capillary close to the working electrode. The gas stream through

the head space of the cell is adjusted with mass flow controllers (Sierra) to achieve (and hold constant) the desired atmospheric composition. The temperature of the water passed through the water jacket is controlled with a Neslab water circulator.

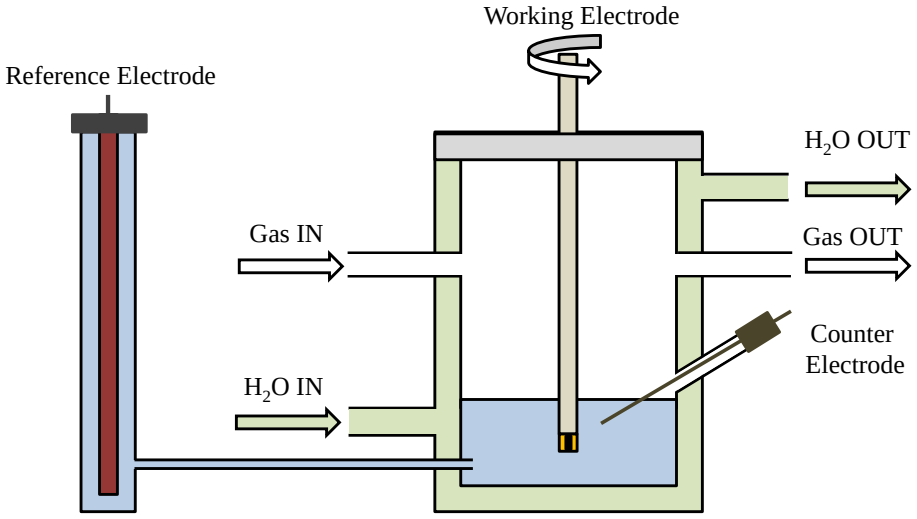

Figure 5.2 Electrochemical Cell: Representation of the glass cell setup used in all electrochemical experiments. The rotating, graphite working and the Pt counter electrode are housed in the main compartment; the reference electrode in a side arm connected through a Luggin capillary. Gas in- and outlets allow establishment of a defined and constant atmosphere in the head space. The temperature of the cell can be set by water circulating through the water jacket.

Prior to an experiment, the working electrode surface was polished with sand paper (P400 Tufbak Durite) and cotton wool to remove any contamination and previous enzyme films. The new hydrogenase film is then 'grown' by application of a small amount of enzyme (ca. 2-6 µL depending on concentration) to the polished surface, repeatedly pipetting up and down.

The applied potential vs. SCE is converted to the potential vs. SHE (standard hydrogen electrode) using

$$E_{SHE} = E_{SCE} + E_{corr} + E_{offset} \tag{5.1}$$

where $E_{corr} = 0.241V$ at 25 ℃ [110] and E_{offset} is the (varying) offset of the individual reference electrode, which is determined periodically.

5.1.1 Carbon Electrodes

The electrode casings consisted of a steel rod housed in Teflon (PTFE) with a screw thread at the top, through which the connection to the rotator is established. A cylindrical piece of pyrolytic graphite (ca. 10 mm long and 2 mm in diameter) was attached to the steel rod with conducting silver epoxy and held in place by a surrounding layer of non-conductive epoxy resin (both from RS Components). The only conductive surface exposed to the solution was thus the circular pyrolytic carbon edge plane.

5.1.2 Gold Electrodes

A thin gold layer was applied to silica wafers (100, Virginia Semiconductor) by vaccum deposition with a chromium support (by R. Jacobs, Surface Analysis Facility, University of Oxford). Individual electrodes with surface areas of ca. 1 to 2.5 cm^2 were cut out with a glass cutter. The gold surface was cleaned with Pirhana solution (ca. 3:1 ratio of H_2SO_4 (18 M) and H_2O_2 (30%)) for 15 minutes, followed by rinsing with EtOH and deionised H_2O, right before use.

Self-assembled monolayers (SAM) with alkyne functionality were created by incubating the cleaned electrode in 2 mg/mL DTSP in DMSO for 1.5 h, followed by incubation with progargylamine in EtOH (1% v/v) for 1h.

5.2 Measurement of Oxygen Reduction Products

All reactions of Hyd-1 with H_2 and O_2 or $^{18}O_2$ described below were carried out in mixed hydrogenase buffer (100 mM NaCl, 15 mM MES, 15 mM HEPES, 15 mM TAPS, 15 mM CHAPS, 15 mM sodium acetate) at pH 7.0 and 20 ℃.

5.2.1 Hyd-1 and $H_2/^{18}O_2$ Reaction Setup

Reactions of Hyd-1 with H_2 and $^{18}O_2$ were carried out in a glass vial with septa-covered inlets and a three-way tap and syringe for selective addition of sample and gases on one of the inlets (see Fig.5.3). This setup was housed inside an O_2-free (<10ppm) glove box (Belle Technologies). Hyd-1 at concentrations ranging from 0.1 to 1.0 µM were incubated in 1 mL mixed hydrogenase buffer at pH 7.0 and 20 ℃ for the indicated time periods, after flushing the reaction chamber with H_2 and addition of the appropriate amount of $^{18}O_2$ (99.9% Cambridge Isotopes) gas via the three-way tap and a syringe. After the reaction, the samples were stored at 4 ℃ in glass vials with minimal head space, until subjected to mass spectrometry.

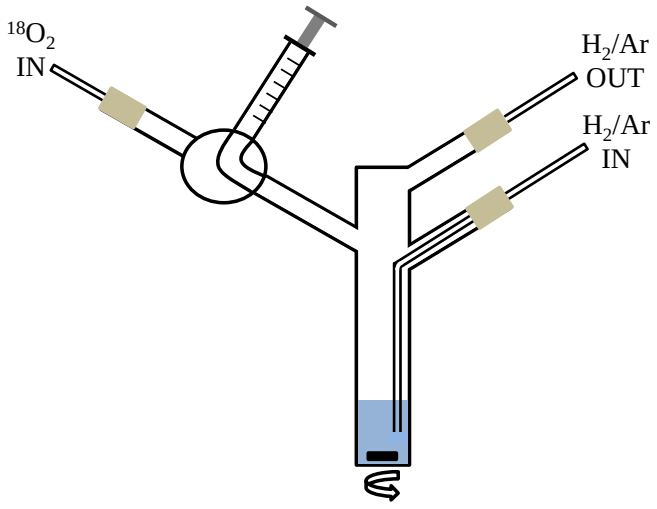

Figure 5.3 $^{18}O_2$ Reduction Setup: The main compartment, holding the enzyme in the reaction buffer, is stirred by a magnetic stir bar. Removable needles pierce the rubber septa at the outlets to allow or stop gas flow. H_2 is bubbled through the solution and head space prior to the experiment, to generate the required atmosphere. An adjustable volume of $^{18}O_2$ is added via a syringe and a three way tap. After the desired duration, the solution is briefly purged with pure Argon to stop the reaction.

5.2.2 Water Isotope Ratio Mass Spectrometry

Experimental samples were equilibration under a CO_2 atmosphere, utilising the reaction $CO_2 + H_2{}^{18}O \rightleftharpoons H_2CO_2{}^{18}O \rightleftharpoons CO^{18}O + H_2O$, which creates ^{18}O-enriched CO_2 gas as a measurement proxy. All solution oxygen isotope measurements were performed on a Delta V Advantage isotope mass spectrometer fitted with a Gas Bench II device, using the procedure described by Nelson [120]. The handling of the instrument was carried out by Dr. Christopher Day (Oxford Department of Earth Sciences). A two-point linear normalisation was carried out with Iso-Analytical Limited standards IA-RO52 = -19.64 ± 0.11‰ and IA-RO55 = 108.63 ± 0.33‰ relative to VSMOW2 (Vienna Standard Mean Ocean Water). External error and accuracy were evaluated through repeat measurements of Iso-Analytical standard IA-RO54, and the two-point normalised results ($\delta^{18}O_{H_2O} = 0.53 \pm 0.11$, $n = 21$) found within error of reference Iso-Analytical Limited laboratory results ($\delta^{18}O_{H_2O} = 0.56 \pm 0.23$, $n = 20$). Experimental results are expressed on the same normalised scale such that $\delta^{18}O$ of SLAP2 (Standard Light Antarctic Precipitation) reference water is -55.5‰. The measured $\delta^{18}O/^{16}O$ vs. VSMOW sample values were converted to µM $H_2{}^{18}O$ concentration increases relative to enzyme-free samples (blank reactions), assuming a concentration of 55.5 M H_2O in aqueous buffer and an isotopic ratio $^{18}O/^{16}O$ of VSMOW of 2005 ppm: a $\delta^{18}O$ increase (*i.e.* deviation of the $^{18}O/^{16}O$ ratio for the sample from the reference value) of 1‰ = 2 ppm = 111 µM $H_2{}^{18}O$. Results were validated by comparison with O_2-exposed (unlabelled) control reactions.

5.2.3 Hydrogen Peroxide Measurements

The required H_2/O_2 atmospheres for reaction with Hyd-1 were adjusted using mass flow controller (Sierra) and carried out in glass vials sealed with rubber septa. Following incubation for a certain time period (see Ch.2.2.2) the reaction solution was purged with Argon.

Ampliflu Red Assay

Three volumes of assay solution, containing 100 µM 10-acetyl-3,7-dihydroxyphenoxazine (Ampliflu Red) and 2.2 units/mL horseradish peroxidase (both from Sigma), were added to purged reaction solution. After 15 min the absorbance was measured at 571 nm (formation of Resorufin). Calibrations were carried out with H_2O_2 standards in the range of 2-40 µM.

Xylenol Orange Assay

Purged reaction solution was added to assay solution, containing 25 mM H_2SO_4, 100 mM Sorbitol, 125 µM Xylenol Orange and 250 µM Ammonium Fe(II) sulphate hexahydrate, following the method developed by Gay *et al.* [203]. Calibrations were carried out with 2-20 µM H_2O_2 standards. The absorbance change was measured at 560 nm. Catalase (0.1 mg/mL) controls were used, in calibration and enzyme sample measurements, to verify that the signal was due to H_2O_2.

5.2.4 Superoxide Assay

To estimate superoxide concentrations, 1 mM hydroxylamine (Sigma) was added to the reaction buffer described above (Ch.5.2), in the same setup as in the hydrogen peroxide experiments (Ch.5.2.3). Rapid reaction of hydroxylamine with superoxide yields nitrite. The reaction was stopped by flushing of the solution with Argon, and 300 µL sample were added to 300 µL assay solution (modified Griess reagent, Sigma); the latter turns pink in response to nitrite. The assay was calibrated against known nitrite concentrations (using $NaNO_2$, Fisher) at A_{540}.

5.2.5 Cytochrome *c* Assay

Reduction of cytochrome *c* in solution was observed by following the increase in absorbance at 550 nm with a Perkin Elmer UV/VIS/NIR Lamda 19 Spectrometer. H_2-saturated solutions of cytochrome *c* and partially acetylated cytochrome *c* (from equine heart, Sigma) at 0.6 mg/mL and 0.8 mg/mL in MHB (at pH 7.0, 20 ℃) respectively, were used with 0.12 µM Hyd-1 concentrations. Cytochrome *c* reduction rates were calculated from the initial absorbance increase using ε_{550nm}= 18 $mM^{-1}cm^{-1}$[97].

5.3 Benzyl Viologen Assay

The solution assay of hydrogen oxidation activity was carried out by following the 604 nm absorbance change of benzyl viologen (BV) due to reduction by Hyd-1 in H_2-saturated buffer (50 mM Tris/HCl, 100mM NaCl buffer, 25 mM benzyl viologen, pH 7.0 at 20 ℃). Initial absorbance increase rates were converted into catalytic rates using an absorbance coefficient for BV of ε_{604nm} = 9.82 $mM^{-1}cm^{-1}$.

5.4 Size Exclusion Chromatography

Separation of Hyd-1 oligomeric states was carried out using a Superdex 200 10/30HR column and an Äkta Purifier System (both GE Healthcare) in the cold room (ca. 4 ℃). Enzyme, purified as described below in Ch.1.2, was loaded onto the column in diluted (1:2 to 1:10) 100 µL aliquots per run. The running buffer (50 mM sodium phosphate, 100 mM NaCl) was supplemented with different detergents, as detailed in each experiment (see Ch.3.2.2). Best separation was achieved with a flow rate of 0.15 mL/min and fractions were automatically collected in 0.3 mL aliquots. The column was calibrated against a set of standard proteins (MWGF1000 kit, Sigma Aldrich) as shown in Fig.5.4. The three fold calibration was only carried out for the initial peak size calculation. To assign peaks after later column re-packings, only one simple calibration was carried out each time.

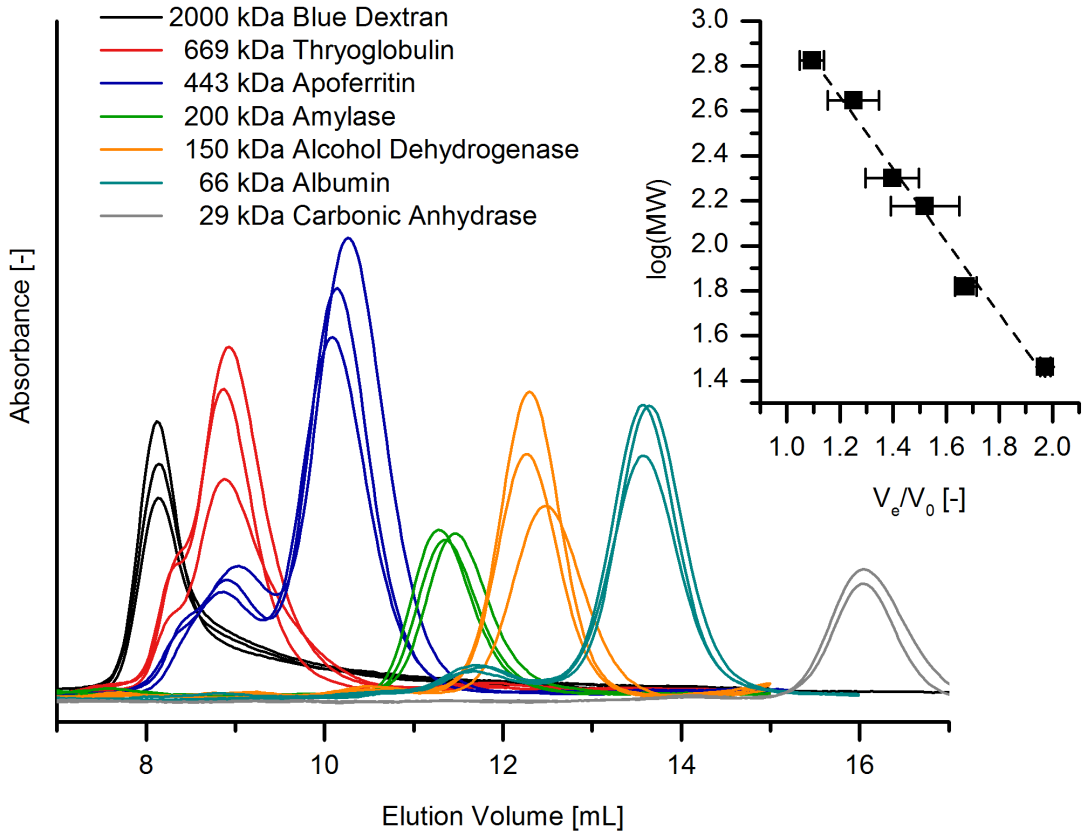

Figure 5.4 Size Exclusion Chromatography Calibration: shown for running buffer with 0.02% Triton X100 and at a flow rate of 0.15 mL/min. Each standard protein was applied separately and the resulting peak positions were averaged for the semi-logarithmic plot shown in the inset. For this purpose, the elution volume V_e of each protein is calculated relative to the void volume V_0, as defined by the average dextran peak position. The error bars indicate the standard deviation of the averaged protein peaks plus the standard deviation of the dextran peaks. The dashed trend line is used to calculate the molecular weight of unknown protein peaks.

5.5 Cytochrome *b* Assay

The cytochrome content of Hyd-1 samples is assessed through UV-vis measurements in the range of 400 to 600 nm. First, the hydrogenase sample is reduced under 100% H_2 for at least three hours, before recording of the reduced spectrum. Subsequent oxidation by air is complete within half an hour, if the sample is frequently shaken. Subtraction of the two spectra yields a difference spectrum, in which characteristic *b*-type haem Soret (429 nm), α (561 nm) and β (531 nm) bands can be identified [146, 131]. Using the 561 nm peak height, relative to the local base line, the haem and cytochrome content and the ratio relative to hydrogenase enzyme can be estimated, based on a *b*-type haem extinction coefficient of $\varepsilon_{(\text{haem-}b)} = 22\ \text{mM}^{-1}\ \text{cm}^{-1}$ [204].

In the following, the experiment from Ch.3.2.3, Fig.3.10A with Hyd-1 WT is used as an example. In this experiment, the total protein concentration in solution was adjusted to 1.0 mg mL^{-1}, as determined by Bradford assay. The relevant moceluar weights of the proteins involved are: Cyt-*b* 27.6 kDa, Hyd-1 small 36.8 kDa and large 64.6 kDa subunit.

Concentration of *b*-type haem:

$$\begin{aligned} \frac{\Delta \text{A} \times \text{path length}}{\epsilon_{(\text{haem-}b)}} &= [\text{haem-}b] \\ \frac{0.145 \times 1.0\, cm}{22\, mM^{-1}\, cm^{-1}} &= 6.59\, \mu M \end{aligned} \tag{5.2}$$

Assuming one haem per cytochrome, *i.e.* $[Cyt-b] = [haem-b] = 6.59\, \mu M$

Concentration of Hyd-1 Dimer $[(\alpha\beta)_2]$:

$$\begin{aligned} \frac{(\text{total Protein}) - (\text{MW(Cyt-}b) \times [Cyt-b])}{MW(\alpha\beta)_2} &= [(\alpha\beta)_2] \\ \frac{1.0\, mg\, mL^{-1} - 0.182\, mg\, mL^{-1}}{202.8 \times 10^3\, g\, mol^{-1}} &= 4.03\, \mu M \end{aligned} \tag{5.3}$$

Radio of Cyt-*b* to Hyd-1 Dimer:

$$\frac{[Cyt-b]}{[(\alpha\beta)_2]} = \frac{6.59\, \mu M}{4.03\, \mu M} = 1.64 \tag{5.4}$$

Assuming two haems per cytochrome, *i.e.* $[Cyt-b] = \frac{1}{2} \times [haem-b] = 3.30\, \mu M$

Assuming two haems per cytochrome, *i.e.* $[Cyt-b] = \frac{1}{2} \times [haem-b] = 3.30\, \mu M$

Concentration of Hyd-1 Dimer $[(\alpha\beta)_2]$:

$$\begin{aligned} \frac{(\text{total Protein}) - (\text{MW(Cyt-}b) \times [Cyt-b])}{MW(\alpha\beta)_2} &= [(\alpha\beta)_2] \\ \frac{1.0\, mg\, mL^{-1} - 0.091\, mg\, mL^{-1}}{202.8 \times 10^3\, g\, mol^{-1}} &= 4.48\, \mu M \end{aligned} \tag{5.5}$$

Radio of Cyt-*b* to Hyd-1 Dimer:

$$\frac{[Cyt-b]}{[(\alpha\beta)_2]} = \frac{3.30\, \mu M}{4.48\, \mu M} = 0.74 \tag{5.6}$$

Assuming one cytochrome per Hyd-1 Dimer, *i.e.* $(\alpha\beta)_2\gamma$

Concentration of Hyd-1 Dimer $[(\alpha\beta)_2\gamma]$:

$$[(\alpha\beta)_2\gamma] = \frac{\text{(total Protein)}}{\text{MW}(\alpha\beta)_2\gamma} = \frac{1.0\, mg\, mL^{-1}}{230.5 \times 10^3\, g\, mol^{-1}} = 4.34\, \mu M \tag{5.7}$$

Ratio of haem-*b* to Hyd-1 Dimer:

$$\frac{[haem - b]}{[(\alpha\beta)_2\gamma]} = \frac{6.59\, \mu M}{4.34\, \mu M} = 1.52 \tag{5.8}$$

resulting in a haem site occupancy of $1.52/2 = 0.76$.

Assuming two cytochromes per Hyd-1 Dimer, *i.e.* $(\alpha\beta\gamma)_2$

Concentration of Hyd-1 Dimer $[(\alpha\beta\gamma)_2]$:

$$[(\alpha\beta\gamma)_2] = \frac{\text{(total Protein)}}{\text{MW}(\alpha\beta\gamma)_2} = \frac{1.0\, mg\, mL^{-1}}{258.0 \times 10^3\, g\, mol^{-1}} = 3.88\, \mu M \tag{5.9}$$

Ratio of haem-*b* to Hyd-1 Dimer:

$$\frac{[haem - b]}{[(\alpha\beta\gamma)_2]} = \frac{6.59\, \mu M}{3.88\, \mu M} = 1.70 \tag{5.10}$$

resulting in a haem site occupancy of $1.70/4 = 0.425$.

5.6 p-Azido-L-Phenylalanine Synthesis

The synthesis of p-azido-L-phenylalanine from N-boc-4-nitro-L-phenylalanine was based on procedures published by Schwyzer and Caviezel (hydrogenation and deprotection) and Liu and Tor (TfN_3 preparation and azide conversion) with a few adjustments, which are highlighted where appropriate. The individual amounts of the employed reagents for the procedure, as given here, are calculated for 11.8 mmol N-boc-4-nitro phenylalanine as starting material: At a final yield of 80 to 85%, just slightly over 9 mmol of p-azido phenylalanine can be obtained (1 mM concentrations were used in *e.g.* 5 to 9 L enzyme expression experiments, see Ch.5.8.2). The mass spectrometry and NMR spectra for the synthesis product are shown in Ch.4.2.1.

5.6.1 Hydrogenation

11.8 mmol (3.66 g) of N-boc-4-nitro phenylalanine (MW 310.12, Alfa Aesar) and 200 mg palladium on activated carbon (10% Pd, Acros Organics) were dissolved in 88.5 mL EtOH (in deviation from Schwyzer's method, where MeOH and glacial acetic acid were used). Hydrogenation was carried out by stirring the solution on an ice bath for 4 h, employing a hydrogen-filled balloon (100% High Purity Hydrogen, BOC) to supply the atmosphere. The carbon particles were removed by filtration through a celite (Sigma) column, while ensuring the powder did not dry out. The EtOH was removed from the orange brown hydrogenation product by roti-evaporation.

5.6.2 Trifluoromethanesulfonyl azide (TfN_3) Preparation

A solution of 13.8 g sodium azide (NaN_3, MW 65.01, Sigma) in 31.4 mL H_2O and 11.8 mL dichloromethane (CH_2Cl_2) was cooled to ca. 0 ℃ in an ice bath. To the stirred solution 10 g of Tf_2O (MW 282.14, $d = 1.677$ g/mL, $> 99\%$ trifluoromethanesulfonic anhydride or triflic anhydride, Aldrich) was added drop wise and the reaction allowed to proceed for 2 h. The organic phase was separated, and the aqueous phase extracted multiple times with small amounts of CH_2Cl_2 (total ca. 8 mL). The combined organic phases were washed with saturated aqueous $NaHCO_3$ (40 mL) and used immediately.

5.6.3 Azide Conversion

The hydrogenated substrate was added to 7.86 mL CH_2Cl_2 followed by 4.91 mL Et_3N and 94.3 mg $CuSO_4$ in 1.97 mL H_2O. In slight deviation from the more general procedure for conversion of aromatic amines into azides published by Liu and Tor [191], the substrate only dissolved once Et_3N was added. The freshly-prepared TfN_3 product was added to the dissolved substrate solution and the mixture brought to homogeneity by addition of ca. 8 mL MeOH. The reaction was stirred at room temperature for two and a half hours. The mixture was then poured into saturated aqueous $NaHCO_3$ (118 mL) and extracted three times with 118 mL CH_2Cl_2. The combined organic phases were washed with brine and dried over anhydrous $MgSO_4$, filtered and concentrated by roti-evaporation, leaving a dark brown residue.

5.6.4 Deprotection

Removal of the protecting tert-butoxycarbonyl group was achieved by treatment of the substrate with an excess of 1.5 M HCl in 130.5 mL ethyl acetate in an ice bath, under vigorous stirring for approx. half an hour. The precipitate was separated by filtration and the flow-through treated by further addition of HCl. Finally, the accumulated precipitate was thoroughly washed with ethyl acetate and diethyl ether to yield a silvery white product.

5.7 *E. coli* Transformation with pEVOL

E.coli MG1655 Hyd-1 Y227AzF was made competent by treatment with RbCl, and the pEVOL vector introduced by heat shock transformation, using the following protocol:

- Inoculate 5 mL of LB medium from single colony
- Grow over night at 37 ℃ while shaking
- Dilute over-night culture 1:500 (use 100 µL in 50 mL)
- Grow at 37 ℃ until an OD_{600} of approx. 0.4 is reached
- Cool the culture on ice for 30 min
- Centrifuge cells at 3750 rpm (GS-6R, Beckman) for 10 min at 4 ℃
- Remove supernatant and carefully re-suspend cells in 30 mL TFB I buffer
- Incubate cells on ice for 15 min
- Centrifuge cells at 3750 rpm (GS-6R, Beckman) for 10 min at 4 ℃
- Remove supernatant and carefully re-suspend in 2 mL TFB II buffer
- Incubate cells on ice for 15 min and divide into 100 µL aliquots
- Store RbCl competent cells at -80 ℃ if necessary
- Preheat LB broth to 42 ℃
- Thaw 100 µL competent aliquots in Eppendorf tubes on ice
- Add ca. 1 µL of pEVOL vector to 100 µL competent cells
- Mix and incubate on ice for 30 min
- Heat-pulse the tubes in a 42 ℃ water bath for 30 s
- Incubate the tubes on ice for 2 min
- Add 0.9 mL LB medium (preheated to 42 ℃) and incubate the tubes at 37 ℃ for 1 h while shaking
- Plate 50 µL of the transformation mixture on LB agar plates containing 30 µg/mL chloramphenicol
- Incubate at 37 ℃ over night

Table 5.1 Aqueous Buffers TFB I (pH 5.8) and TFB II (pH 6.5)

TFB I Buffer		TFB II Buffer	
Compound	**Concentration**	**Compound**	**Concentration**
KOAc	30 mM	MOPS	10 mM
RbCl	100 mM	RbCl	10mM
$CaCl_2$	10 mM	$CaCl_2$	75mM
glycerol	15% v/v	glycerol	15% v/v
$MnCl_2$	50 mM		
$[Co(NH_3)_6]Cl_3$	3 mM		

5.8 Expression and Purification of *E. coli* Hyd-1

Detergents are an important agent in isolating membrane-bound or associated proteins. In order to avoid confusion about detergent choice later in the chapter, the following shall be briefly mentioned. Even though the detergent Triton X-100 was utilised in the first isolation of *E. coli* Hyd-1 by Sawers and co-workers in 1985/86 [76, 79], n-Dodecyl-β-D-maltopyranoside (DDM) was adopted by the Sargent and Armstrong groups in the initial purification of his-tagged Hyd-1, in the hope of affording better solubilisation, higher yield and purity. However, because of only moderate success in this regard, the pricier DDM was subsequently re-substituted with Triton X-100.

Table 5.2 Aqueous Buffers used in Hyd-1 Purification

Name	Composition
Buffer 1	100 mM Tris, 50 mM NaCl, 1 mM EDTA, pH 7.5
Buffer 2	100 mM Tris, 350 mM NaCl, pH 7.5
Buffer A	60 mM imidazole, 20 mM Tris,
	350 mM NaCl, 0.02% Triton X100, pH 7.2
Buffer B	750 mM imidazole, 20 mM Tris,
	350 mM NaCl, 0.02% Triton X100, pH 7.2
Buffer C	0.02% glycerol, 20 mM Tris,
	350 mM NaCl, 0.02% Triton X100, pH 7.2

5.8.1 Expression of native Hyd-1

The expression and purification (by Ni-NTA affinity chromatography) of most of the *native* Hyd-1 used in this thesis was carried by Elena Nomerotskaia (except for the experiments shown in Fig.3.4). The His-tagged *E. coli* strains MC4100 HyaA-his and MG1655 HyaA-his (the latter before TAG incorporation) were supplied by Frank Sargent, University of Dundee.

Day 1:

Inoculation

- Media
  - 42 L of LB medium (25 g/L) (Sigma)
  - 420 mL of autoclaved 50 % glycerol solution
  - 168 g of sodium fumarate dissolved in 800 mL DI water, filter sterilize before inoculation
- Starter cultures *E. coli* MC4100 HyaA-his 5mL LB in falcon tube, 37 ℃, 6 h
- Inoculation: add glycerol and sodium fumarate solutions to LB media, top up bottles as much as possible and add starter culture
- Growing: 37 ℃ stationary incubator over night (ca. 16 h)

Day 2:

Harvest

- Spin: 5,000 rpm for 12 min, 4 ℃ (Avanti J-26 XP, Beckman)
- Make: re-suspension buffer (150 mL Buffer 1 + lysozyme + DNase I)
- Add 25 mL of re-suspension buffer to each 1 L centrifuge tube
- Incubate in shaker at room temperature for ca. 20 min
- Pass through french press (Constant Systems) three times at 20 kpsi
- Spin: 3,750 rpm (GS-6R, Beckman) for 30 min at 4 ℃ to remove unlysed cells
- Spin: 45,000 rpm (L8-70M, Beckman) for 60 min at 4 ℃ to precipitate membrane fraction, discard supernatant
- Homogenise membranes: add ca. 10 mL Buffer 2 to each tube and resuspend pellet by drawing up and down in plastic pipette. Combine all aliquots into a

small flask, bring volume up to 200 mL, stir in the cold room for at least 1 h

- Solubilise membranes: add 26 mL of Triton X100 solution to membrane suspension and stirr for 1 h in the cold room

Column

Subsequently purification via Ni-NTA affinity chromatography was performed as described below.

5.8.2 Expression of Hyd-1 with p-Azido-L-Phenylalanine

The procedure is a modification of the Hyd-1 standard preparation (above) and detailed for a 5 L growth experiment, using p-AzF at a 1 mM final concentration.

Day 1:

Inoculation

- Media
  - 5 L of LB medium
  - 50 ml of autoclaved 50 % glycerol solution
  - 125 mg chloramphenicol in 5 mL EtOH
  - 20 g of sodium fumarate and 1 g (L-) arabinose (final concentration in 5 L medium 0.02%) dissolved in 140 mL DI water, filter sterilize before inoculation
- Starter cultures MG1655 HyaA-his 814TAG plus pEVOL (check for plasmid with agarose gel) : 4x 15 ml LB in falcon tube, 37 ℃, 6 hours
- Inoculation: add glycerol, chloramphenicol and sodium fumarate solutions to LB media and add 1.5 mL of starter culture
- Growing: 37 ℃ stationary incubator for 8 hours
- To induce p-AzF incorporation via pEVOLvector add:
  - >5 mmol (1 g) p-AzF dissolved in water
  - 1 g (L-) arabinose in ca. 5mL water
- grow for another 8 hours

Day 2:

Harvest

- Spin: 3,200 rpm for 12 min, 4 ℃ (Avanti J-26 XP, Beckman)
- Make: re-suspension buffer (50 mL B-PER Reagent (Thermo Scientific)+ lysozyme + DNase I + one pellet of EDTA-free protease inhibitor)
- Re-suspend with a 5 mL pipette until homogeneous
- Incubate for 15 min at room temperature
- Spin: 30,000 rpm for 40 min at 4 ℃ (L8-70M, Beckman)
- Solubilise membranes by addition of 24 mL Buffer 2 and 3 mL of 30% Triton X100 and stirring for 2 h in the cold room

Column

Subsequently purification via Ni-NTA affinity chromatography was performed as described below.

5.8.3 Äkta Ni-NTA Affinity Purification

Isolate Hyd-1

- Add: DTT (1 mM) to Buffers A (300 mL) and B (150 mL)
- Attach HisTrap™ FF IMAC column (5 mL or 1 mL) to Äkta Purifier System (both GE Healthcare)
- Pump wash with Buffers A and B
- Wash column with Buffer A (2 mL/min, 50 mL)
- Spin: 45,000 rpm for 60 min at 4 ℃ (L8-70M, Beckman)
- Add DTT (1 mM) and imidazole (40 mM) to supernatant
- Load supernatant onto the column (1.5 mL/min)
- Wash the column with Buffer A (2 mL/min, 100 mL)
- Elute Hyd-1 using linear gradient (100% B in 27 min, 1.5 mL/min, 1 mL fractions, 50 mL total)
- Collect Hyd-1 containing fractions (use 420 nm absorbance as a guide)
- Pump wash with DI water

- Wash the column with DI water (4 mL/min, 25 mL)
- Pump wash with 20% ethanol
- Start cleaning the column with 20% ethanol (4 mL/min, 300 mL)

Concentrate and Exchange Buffer

- Add DTT (1 mM) to Buffer C (ca. 60 mL)
- Concentrate collected fractions with centrifugal filter (50kDa, Vivaspin 20, Sartorius) at 3,700 rpm (4 ℃, GS-6R, Beckman) to 0.5-1 mL
- Top up concentrator with Buffer C and repeat three times
- Aliquot enzyme into cryo vials and freeze in liquid nitrogen

5.9 Bradford Assay

Colourimetric (A_{595}) determination of protein concentrations was carried out with Bradford reagent (Sigma Aldrich) against a linear calibration of bovine serum albumin (BSA), in the range of 0 to 20 µM. Hydrogenase samples, purified as described in Ch.5.8, were usually diluted 100 to 1000 fold to obtain several data points.

5.10 Electrophoresis

The size of sample bands was was estimated in relation to known reference bands (marker or ladder): The migration distance of the reference bands along the gel was determined with a graphics software (Paint.net) to create a semi-logarithmic plot of size over migration distance as a calibration.

DNA Agarose Gel Electrophoresis

Agarose was added to hot TAE buffer (40 mM Tris, 40 mM acetic acid, 1 mM EDTA at pH 8.3) to create a 1% solution. Right before casting the gel (using Bio-Rad casings) SYBR Safe Stain® (Invitrogen) was added to the solution to a final concentration of approx. 0.007% (v/v). The 1kb DNA ladder from New England Biolabs was used as a reference standard, and all samples were prepared by addition of 6x DNA loading dye

(NEB). A voltage of 100 V was applied across the gel for 55-70 min to develop the gel in TAE buffer. Where necessary, the resulting bands were excised with a scalpel and the DNA extracted with an extraction kit (QIAquick®, QIAGEN).

SDS Polyacrylamide Gel Electrophoresis

Protein samples for denaturing electrophoresis were prepared by addition of 4x LDS sample buffer (Invitrogen) (total volume 10 µL) and heating for 10 min at 70 ℃. PageRuler® pre-stained protein ladder (Thermo Scientific) was used as a reference standard. The samples were loaded onto a NuPAGE® 4-12% Bis-Tris pre-cast gel (Invitrogen) and run at 200 V for ca. 50 min in MOPS running buffer (50 mM MOPS, 50 mM Tris base, 1 mM EDTA, 0.1% SDS, pH 7.7) using the XCell SureLock™ electrophoresis system (Life Technologies). Gels were developed by incubation in coomassie staining solution (0.25 % Coomassie Brilliant Blue, 50% Ethanol, 10% glacial acetic acid, deionised water) for ca. 10 min at around 50 to 60 ℃ and subsequent destaining until satisfactory (20 % Ethanol, 10% glacial acetic acid, deionised water).

Native Polyacrylamide Gel Electrophoresis

Protein samples for native electrophoresis were prepared by addition of sample buffer (Invitrogen, final concentration 50 mM BisTris, 6 N HCl, 50 mM NaCl, 10% w/v glycerol, 0.001% Ponceau S, pH 7.2). NativeMark™ Unstained Protein Standard (Invitrogen) was used as a reference. The Anode Buffer consisted simply of Running Buffer (50 mM BisTris, 50 mM Tricine, pH 6.8) while the Cathode Buffer included 20x Cathode Additive (0.4% Coomassie ® G-250). The gel (pre-cast 4-16% BisTris, Invitrogen) was run at 150 V for ca. 130 min, using the XCell SureLock™ electrophoresis system (Life Technologies). The gel was developed as follows: incubation in ca. 100 mL fixing solution (40% methanol, 10% acetic acid) for approx. 60 s in the microwave at ca. 700 W, followed by 15-20 min at room temperature on a gel shaker. Subsequently the gel was transfered to destaining solution (8% acetic acid) and incubated, first in the microwave for 60 s at 700 W and then at room temperature on the shaker until satisfactory.

5.11 Small Molecule NMR and Mass Spec

The OpenAccess Service of the Oxford Chemistry department was used for analysis of small molecules in Chapter 4. Samples were submitted to the auto-sampler at concentrations below 0.1 mg/mL in MeOH for liquid chromatography electro spray ionisation time-of-flight mass spectrometry (LC-ESI-TOF-MS, Waters LCT Premier or Agilent instrument). For nuclear magnetic resonance spectroscopy, samples were submitted at varying high concentrations in CD_3OD (1H NMR, Varian Hg-300 instrument). NMR results were analysed using the MestReNova software, while the mass spectra shown in chapter 4 were not processed further.

5.12 Protein Mass Spectrometry

Unfortunately the automated Protein MassSpec Service (Department of Chemistry, University of Oxford) proved unsuccessful in resolving the small subunit of Hyd-1 (for unknown reasons). The following manual method, established and managed by Dr. L. Gong (Central Mass Spectrometry Facility, Department of Chemistry, University of Oxford) was first successfully used by Dr. B.J. Murphy for *E. coli* Hyd-2 and finally also proved successful for Hyd-1 here.

Whole protein mass analysis was carried out by liquid chromatography electro spray ionisation mass spectrometry (LC-ESI-MS). Hyd-1 samples were prepared by buffer exchange into ammonium acetate (50 mM, pH 7.54) through repeated (8x) use of a centrifugal filter with a 3 kDa cut-off (Amicon Ultra, Millipore), concentrated and reduced in volume to ca. 10 µL. Samples were applied to the LC column (reverse phase, Waters nanoAcquity C4) in 5 µL aliquots and eluted over a 7 min 5 - 80% CH_3CN in H_2O gradient at a flow rate of 0.3 mL/min. Both phases contained 0.1% formic acid. The LC setup (Acquity UPLC, Waters) was directly inline with the ESI-TOF (time of flight) mass spectrometer (Micromass LCT Premier, Waters). The latter was operated *via* a computer running the MassLynx software (v 4.1, Micromass, Waters) with the settings shown in Tab.5.3. The same software was used to analyse the results (see Ch.4.2.4, Fig.4.8).

Table 5.3 Protein Mass Spec Settings

Parameter	Setting
Ionisation Mode	Positive
Data Mode	Continuum
Mass Range	510 - 3000 m/z
Source Temperature	120 °C
Desolvation Temperature	250 °C
Desolvation Gas Flow	550 L/h
Sample Cone Voltage	100 V
Cone Gas Flow	30 L/h
Capillary Voltage	3000 V
Tube Lens	186 V

5.13 Azide Labelling Reactions

Copper-free cycloaddition reactions were carried out with ca. 10 fold excess of dibenzocyclooctyne-amine (DBCOA, from Sigma Aldrich), relative to enzyme, in 30 mM phosphate buffer (pH 8.5) for three to four hours at room temperature [188]. DBCOA was pre-dissolved in a small volume of EtOH.

The Cu-catalysed cycloaddition reaction was carried out with 60 µM Alkyne Cyanine Dye 718 (ACD, from Sigma Aldrich) and ca. 0.5-3.0 µM Hyd-1 in 33 mM phosphate buffer (K_2HPO_4/KH_2PO_4) with 1 mM $CuSO_4$, 1 mM tris[(1-benzyl-1H-[1,2,3]triazol-4-yl)methyl]-amine (TBTA) and 2 mM tris-(carboxy ethyl) phosphine (TCEP) as reducing agent, in adaptation of the method described by Deiters and co-workers [193]. The pH was adjusted to pH 8.0 and the reagents incubated for eight to nine hours. After the reaction, the majority of the dye was removed from solution by passing the batch through a DNA extraction column (QIAquick®, QIAGEN), to which the dye was found to bind easily.

Appendix

A.1 Gas Concentration in Aqueous Solution

The concentration of gases in aqueous solution was calculated using the respective Henry coefficient k_H (see Tab.A.1) and the Van't Hoff equation, neglecting salt contributions:

$$[gas] = k_H \times exp\left(C\left[\frac{1}{T} - \frac{1}{T^{\ominus}}\right]\right) \tag{A.1}$$

with $T^{\ominus} = 298.15\ K$.

Table A.1 Henry constants of various gases

Gas	$\mathbf{k_H}$	**C**
H_2	7.8×10^{-4}	500
O_2	1.2×10^{-3}	1700
N_2	6.1×10^{-4}	1300
Ar	1.4×10^{-3}	1300
CO_2	9.5×10^{-4}	2400

A.2 Extrapolation of Ni-B Reactivation Rate

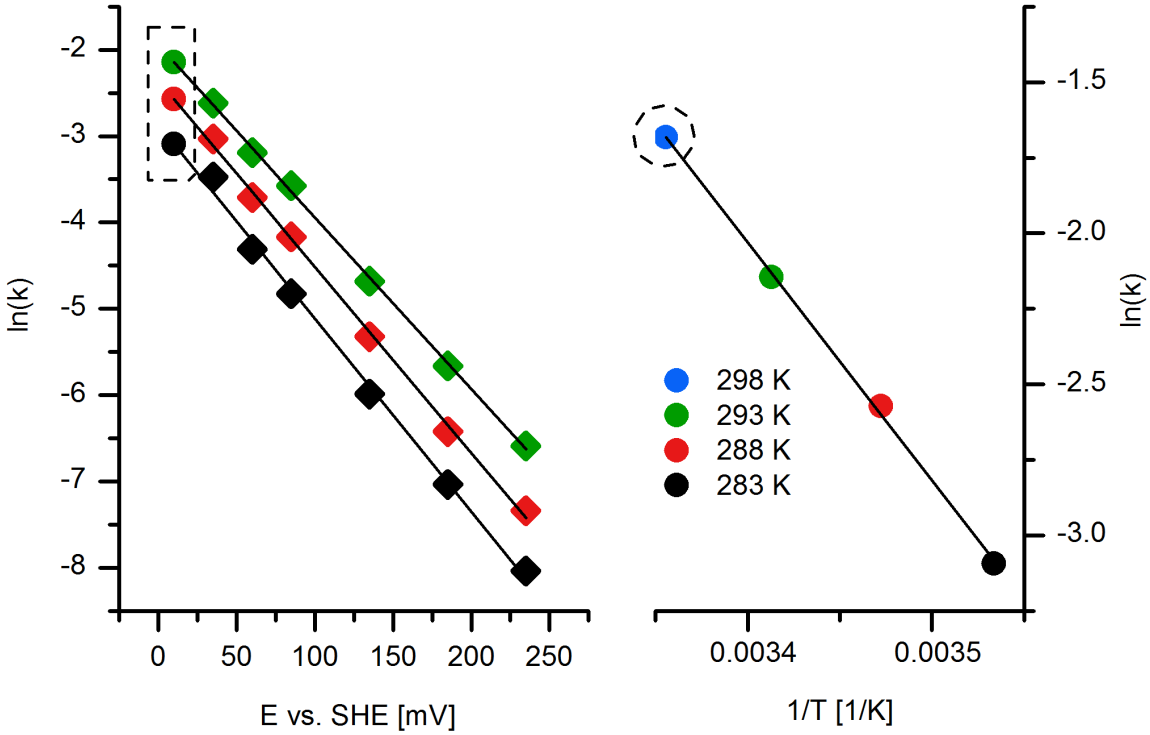

Figure A.1 Example Extrapolation of *E. coli* Hyd-1 Ni-B Reactivation Rate from a series of potentials to +10 mV at three different temperatures **(Left)**. The dashed box marks the extrapolated values, which are used in an Arrhenius plot **(Right)** to extrapolate to 25 °C. The example shown here uses one of the data sets provided by R.E. Evans (Evans *et al.* S11) [71].

A.3 *E. coli* MG1655 *hyaA*-his TAT814TAG

DNA Sequence without flanking regions. Native start and stop codons are marked in red, the his-tag in green and the TAG codon (introduced in place of TAT) in yellow.

```
   1 ATGAATAACG AGGAAACATT TTACCAGGCC ATGCGGCGTC AGGGCGTTAC CCGGCGCAGC
  61 TTTCTCAAAT ATTGTAGTCT GGCTGCCACG TCGCTGGGAT TAGGCGCGGG AATGGCACCA
 121 AAGATTGCCT GGGCGCTGGA GAACAAACCG CGCATTCCGG TGGTATGGAT CCACGGTCTG
 181 GAATGCACCT GCTGTACCGA ATCTTTTATC CGCTCCGCTC ACCCACTGGC GAAGGACGTC
 241 ATCCTTTCCC TGATTTCCCT CGATTACGAC GATACTTTGA TGGCTGCCGC CGGAACCCAG
 301 GCGGAAGAAG TCTTTGAAGA CATCATCACG CAATACAATG GCAAATATAT CCTCGCAGTA
 361 GAAGGTAATC CGCCGCTGGG CGAGCAGGGG ATGTTCTGTA TCAGCAGCGG TCGACCGTTT
 421 ATTGAGAAAC TCAAACGTGC CGCTGCCGGA GCCAGCGCGA TTATCGCCTG GGGAACCTGC
 481 GCGTCCTGGG GCTGCGTGCA GGCCGCGCGA CCCAATCCGA CGCAGGCAAC GCCTATCGAC
 541 AAAGTCATCA CCGACAAACC CATTATCAAA GTACCTGGCT GCCCGCCGAT CCCGGATGTG
 601 ATGAGCGCCA TCATTACTTA CATGGTGACC TTTGATCGCT TGCCAGATGT CGACAGAATG
 661 GGCCGTCCGC TGATGTTCTA TGGTCAGCGA ATCCACGATA AATGCTATCG CCGCGCCCAC
 721 TTCGACGCCG GAGAGTTCGT CCAGAGTTGG GATGATGACG CTGCCCGCAA AGGTTACTGC
 781 CTGTACAAAA TGGGCTGCAA AGGGCCTACC ACCTAGAACG CCTGTTCCTC CACACGCTGG
 841 AATGATGGCG TTTCTTTCCC AATCCAGTCT GGTCACGGCT GCCTGGGCTG TGCGGAAAAT
 901 GGTTTCTGGG ATCGCGGTTC GTTCTACAGC CGCGTGGTCG ATATTCCGCA AATGGGTACT
 961 CATTCCACCG CCGATACCGT CGGTTTAACC GCGCTTGGCG TGGTGGCAGC GGCTGTTGGT
1021 GTGCACGCAG TCGCCAGCGC CGTTGACCAG CGCAGACGTC ATAACCAGCA ACCTACAGAA
1081 ACCGAACATC AGCCAGGCAA TGAGGATAAA CAGGCAAGAT CTCATCACCA TCACCATCAC
1141 TAA
```

A.4 The aaRS/tRNA Vector pEVOL

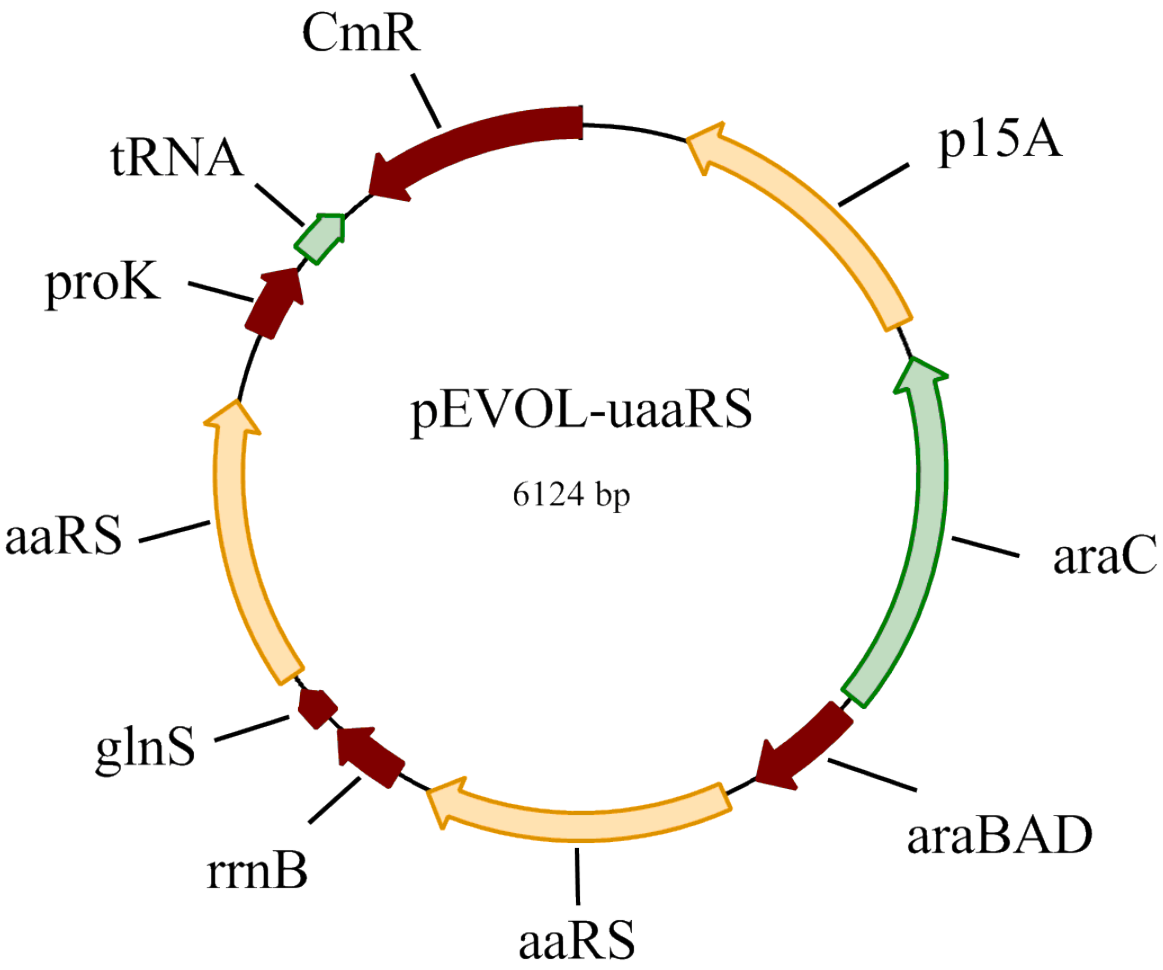

Figure A.2 The aaRS/tRNA Vector pEVOL: *aaRS* aminoacyl-tRNA synthetase, *araBAD* arabinose inducible promoter, *rrnB* terminator, *glnS* (glutaminyl-tRNA synthetase) constitutive promoter, *tRNA* transfer ribonucleic acid for TAG stop codon recognition, *proK* promoter, *CmR* chloramphenicol acetyltransferase (confers resistance), *p15A* origin of replication [176]

A.5 Hyd-1 Large Subunit Mass Spectrometry

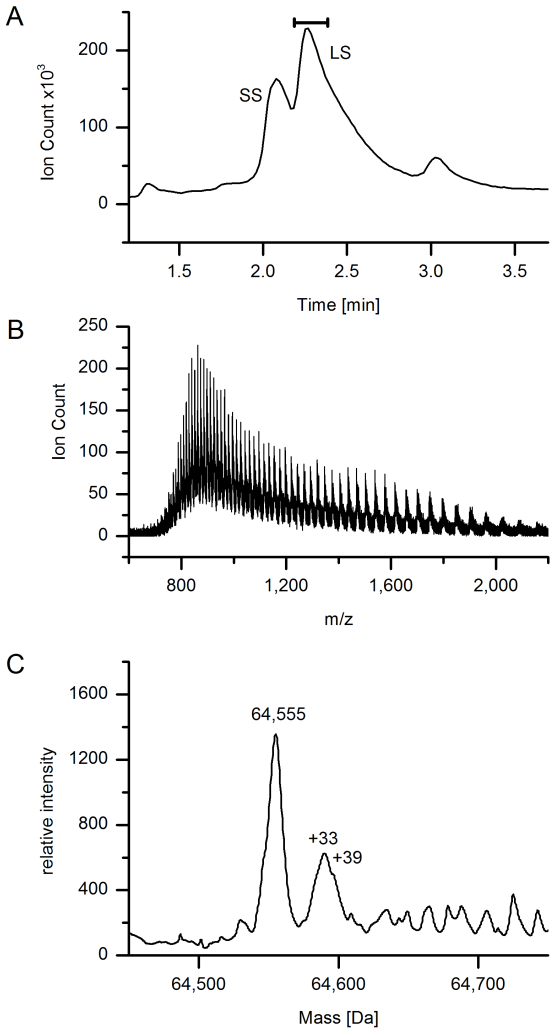

Figure A.3 LC-ESI$^+$ Mass Spectrometry of the Hyd-1 Large Subunit:
A) Liquid chromatography (reversed phase) elution profile. Large and small subunit peaks (LS and SS) are marked accordingly and the summing-up process of mass spectrometry peaks for panel B is illustrated by a double blunt-ended arrow. **B)** Sum of m/z protein fragment peaks recorded for the large subunit. Processing of this data subset with the MaxEntI algorithm (0.5 Da/Channel resolution, 0.4 Da peak width at half height) yields the bottom panel. **C)** The main peak is found at 64,555 kDa where 64,553 kDa are expected from the amino acid sequence. The broad adduct peak with +33 Da has a shoulder at +39 Da, matching sulphur and potassium respectively.

A.6 Alkyne Cyanine Dye Mass Spectrometry

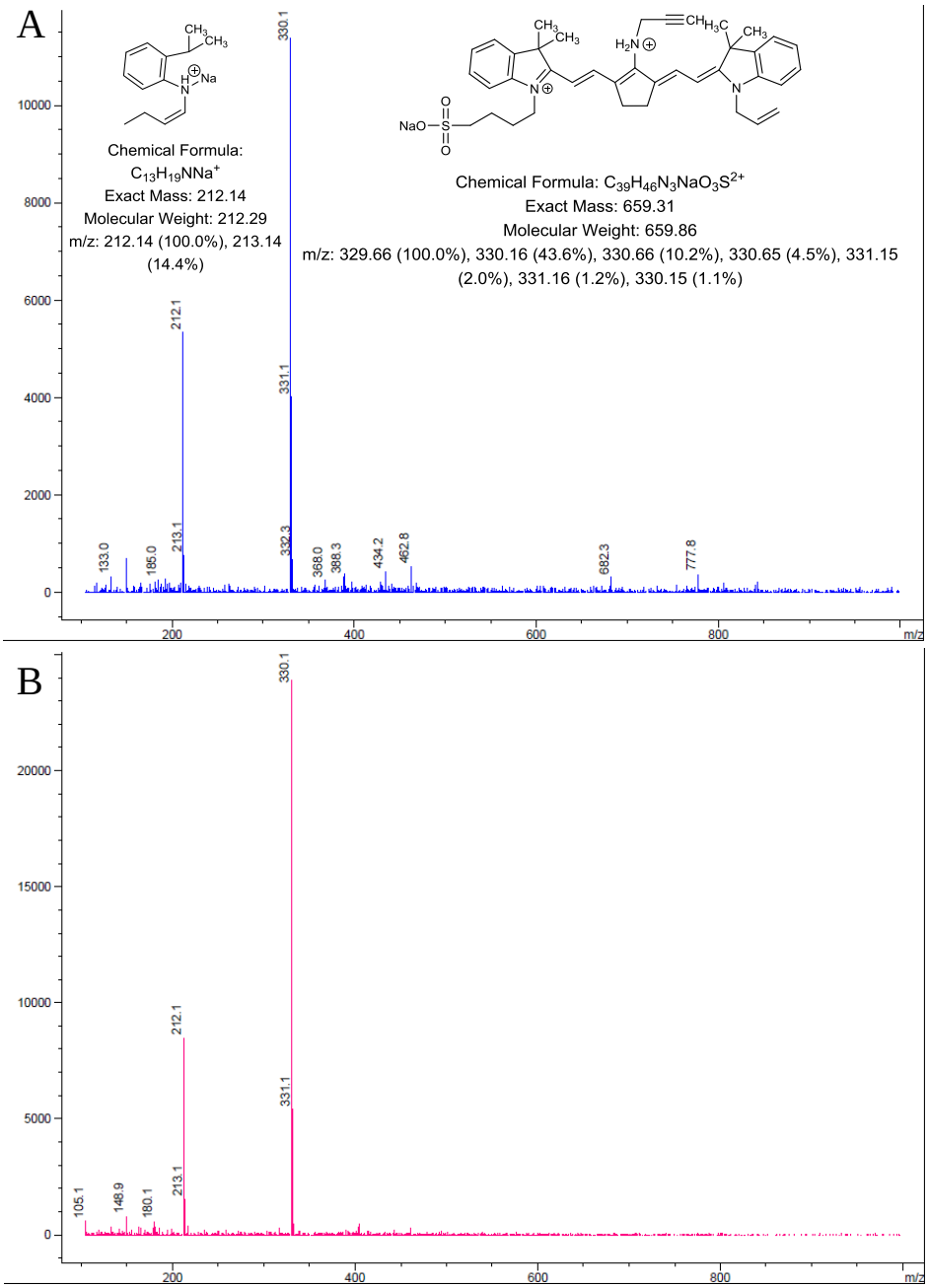

Figure A.4 Alkyne Cyanine Dye ESI$^+$-TOF Mass Spectrometry: Blue dye in MeOH without (**A**) and pink dye in H_2O after (**B**) exposure to light. Plausible fragmentation products, their mass distributions calculated by ChemBioDraw software (Perkin Elmer), are shown. Positive ionisation mode

Bibliography

[1] Wulff, P. *Characterisation and Immobilisation of Redox Enzymes on Interactive Surfaces* (RWTH Aachen University, Master Thesis, 2010).

[2] Armstrong, F. A. & Hirst, J. Reversibility and efficiency in electrocatalytic energy conversion and lessons from enzymes. *Proceedings of the National Academy of Sciences* **108**, 14049–14054 (2011).

[3] Savéant, J.-M. Molecular catalysis of electrochemical reactions - mechanistic aspects. *Chemical Reviews* **108**, 2348–2378 (2008).

[4] Vignais, P. M. & Billoud, B. Occurrence, classification, and biological function of hydrogenases: An overview. *Chemical Reviews* **107**, 4206–4272 (2007).

[5] Shima, S. *et al.* The crystal structure of [Fe]-hydrogenase reveals the geometry of the active site. *Science* **321**, 572–575 (2008).

[6] Thauer, R. K. Hydrogenases and the global H_2 cycle. *European Journal of Inorganic Chemistry* **2011**, 919–921 (2011).

[7] Lenz, O., Zebger, I., Hamann, J., Hildebrandt, P. & Friedrich, B. Carbamoylphosphate serves as the source of CN^-, but not of the intrinsic CO in the active site of the regulatory [NiFe]-hydrogenase from *Ralstonia eutropha*. *FEBS Letters* **581**, 3322–3326 (2007).

[8] Atkins, P., Overton, T., Rourke, J., Weller, M. & Armstrong, F. *Shriver and Atkins' Inorganic Chemistry* (Oxford University Press: Oxford, UK, 2010).

[9] Hiromoto, T. *et al.* The crystal structure of C176A mutated [Fe]-hydrogenase suggests an acyl-iron ligation in the active site iron complex. *FEBS Letters* **583**, 585–590 (2009).

[10] Thauer, R. K. *et al.* Hydrogenases from methanogenic archaea, nickel, a novel cofactor, and H_2 storage. *Annual Review of Biochemistry* **79**, 507–536 (2010).

[11] Fontecilla-Camps, J. C., Volbeda, A., Cavazza, C. & Nicolet, Y. Structure/function relationships of [NiFe]- and [FeFe]-hydrogenases. *Chemical Reviews* **107**, 4273–4303 (2007).

[12] Erdem, z. F. *et al.* A model of the [FeFe]-hydrogenase active site with a biologically relevant azadithiolate bridge: A spectroscopic and theoretical investigation. *Angewandte Chemie International Edition* **50**, 1439–1443 (2011).

[13] Helm, M., Stewart, M., Bullock, R., DuBois, M. & DuBois, D. A synthetic nickel electrocatalyst

with a turnover frequency above 100,000 s^{-1} for H_2 production. *Science* **333**, 863 (2011).

[14] Ogata, H., Kellers, P. & Lubitz, W. The crystal structure of the [NiFe]-hydrogenase from the photosynthetic bacterium allochromatium vinosum: Characterization of the oxidized enzyme (Ni-A state). *Journal of Molecular Biology* **402**, 428–444 (2010).

[15] Frey, M. Hydrogenases: Hydrogen-activating enzymes. *ChemBioChem* **3**, 153–160 (2002).

[16] Garcin, E. *et al.* The crystal structure of a reduced [NiFeSe]-hydrogenase provides an image of the activated catalytic center. *Structure* **7**, 557–566 (1999).

[17] Afting, C., Hochheimer, A. & Thauer, R. K. Function of H_2-forming methylenetetrahydromethanopterin dehydrogenase from methanobacterium thermoautotrophicum in coenzyme F420 reduction with H_2. *Archives of Microbiology* **169**, 206–210 (1998).

[18] Vogt, S., Lyon, E., Shima, S. & Thauer, R. The exchange activities of [Fe] hydrogenase (iron-sulfur-cluster-free hydrogenase) from methanogenic archaea in comparison with the exchange activities of [FeFe] and [NiFe] hydrogenases. *Journal of Biological Inorganic Chemistry* **13**, 97–106 (2008).

[19] Ghirardi, M. L., Dubini, A., Yu, J. & Maness, P.-C. Photobiological hydrogen-producing systems. *Chemical Society Reviews* **38**, 52–61 (2009).

[20] Verhagen, M. F. J. M., O'Rourke, T. & Adams, M. W. W. The hyperthermophilic bacterium, thermotoga maritima, contains an unusually complex iron-hydrogenase: amino acid sequence analyses versus biochemical characterization. *Biochimica et Biophysica Acta - Bioenergetics* **1412**, 212–229 (1999).

[21] Brugna-Guiral, M. *et al.* [NiFe] hydrogenases from the hyperthermophilic bacterium aquifex aeolicus: properties, function, and phylogenetics. *Extremophiles* **7**, 145–157 (2003).

[22] Appel, J. & Schulz, R. Hydrogen metabolism in organisms with oxygenic photosynthesis: hydrogenases as important regulatory devices for a proper redox poising? *Journal of Photochemistry and Photobiology B: Biology* **47**, 1–11 (1998).

[23] Buhrke, T., Lenz, O., Porthun, A. & Friedrich, B. The H_2-sensing complex of *Ralstonia eutropha*: interaction between a regulatory [NiFe] hydrogenase and a histidine protein kinase. *Molecular Microbiology* **51**, 1677–1689 (2004).

[24] Buhrke, T., Lenz, O., Krauss, N. & Friedrich, B. Oxygen tolerance of the H_2-sensing [NiFe] hydrogenase from *Ralstonia eutropha* H16 is based on limited access of oxygen to the active site. *Journal of Biological Chemistry* **280**, 23791–23796 (2005).

[25] Buhrke, T. *et al.* Reduction of unusual iron-sulfur clusters in the H_2-sensing regulatory [NiFe] hydrogenase from *Ralstonia eutropha* H16. *Journal of Biological Chemistry* **280**, 19488–19495 (2005).

[26] Kuhn, M., Steinbüchel, A. & Schlegel, H. G. Hydrogen evolution by strictly aerobic hydrogen bacteria under anaerobic conditions. *Journal of Bacteriology* **159**, 633–639 (1984).

[27] Vignais, P. M. & Colbeau, A. Molecular biology of microbial hydrogenases. *Current Issues in Molecular Biology* **6**, 159–188 (2004).

[28] Hirst, J. Mitochondrial complex I. *Annual Review of Biochemistry* **82**, 551–575 (2013).

[29] Hedderich, R. & Forzi, L. Energy-converting [NiFe] hydrogenases: more than just H_2 activation. *Journal of Molecular Microbiology and Biotechnology* **10**, 92–104 (2005).

[30] Redwood, M. D., Mikheenko, I. P., Sargent, F. & Macaskie, L. E. Dissecting the roles of *Escherichia coli* hydrogenases in biohydrogen production. *FEMS Microbiology Letters* **278**, 48–55 (2008).

[31] Sauter, M., Böhm, R. & Böck, A. Mutational analysis of the operon (hyc) determining hydrogenase 3 formation in *Escherichia coli*. *Molecular Microbiology* **6**, 1523–1532 (1992).

[32] Siegbahn, P. E., Tye, J. W. & Hall, M. B. Computational studies of [NiFe] and [FeFe] hydrogenases. *Chemical Reviews-Columbus* **107**, 4414 (2007).

[33] Surerus, K. K. *et al.* Further characterization of the spin coupling observed in oxidized hydrogenase from *Chromatium vinosum*. A moessbauer and multifrequency EPR study. *Biochemistry* **33**, 4980–4993 (1994).

[34] Dole, F. *et al.* Nature and electronic structure of the Ni-X dinuclear center of *Desulfovibrio gigas* hydrogenase. Implications for the enzymatic mechanism. *Biochemistry* **36**, 7847–7854 (1997).

[35] Huyett, J. E. *et al.* 57Fe Q-band pulsed ENDOR of the hetero-dinuclear site of nickel hydrogenase: Comparison of the NiA, NiB, and NiC states. *Journal of the American Chemical Society* **119**, 9291–9292 (1997).

[36] Carepo, M. *et al.* ^{17}O ENDOR detection of a solvent-derived Ni-(OHx)-Fe bridge that is lost upon activation of the hydrogenase from *Desulfovibrio gigas*. *Journal of the American Chemical Society* **124**, 281–286 (2002).

[37] Lukey, M. J. *et al.* How *Escherichia coli* is equipped to oxidize hydrogen under different redox conditions. *Journal of Biological Chemistry* **285**, 3928 (2010).

[38] van der Zwaan, J. W., Coremans, J. M. C. C., Bouwens, E. C. M. & Albracht, S. P. J. Effect of $^{17}O_2$ and ^{13}CO on EPR espectra of nickel in hydrogenase from *Chromatium vinosum*. *Biochimica et Biophysica Acta - Protein Structure and Molecular Enzymology* **1041**, 101–110 (1990).

[39] Roessler, M. M., Evans, R. M., Davies, R. A., Harmer, J. & Armstrong, F. A. EPR spectroscopic studies of the Fe-S clusters in the O_2-tolerant [NiFe]-hydrogenase Hyd-1 from *Escherichia coli* and characterization of the unique [4Fe-3S] cluster by HYSCORE. *Journal of the American Chemical Society* **134**, 15581–15594 (2012).

[40] Abou Hamdan, A. *et al.* O_2-independent formation of the inactive states of [NiFe] hydrogenase. *Nature Chemical Biology* **9**, 15–17 (2013).

[41] Volbeda, A. *et al.* Structural differences between the ready and unready oxidized states of [NiFe] hydrogenases. *Journal of Biological Inorganic Chemistry* **10**, 239–249 (2005).

[42] Stripp, S. T. *et al.* How oxygen attacks [FeFe] hydrogenases from photosynthetic organisms. *Proceedings of the National Academy of Sciences* **106**, 17331–17336 (2009).

[43] Lambertz, C. *et al.* O_2 reactions at the six-iron active site (H-cluster) in [FeFe] hydrogenase. *Journal of Biological Chemistry* **286**, 40614–40623 (2011).

[44] Bruska, M. K., Stiebritz, M. T. & Reiher, M. Regioselectivity of H cluster oxidation. *Journal of the American Chemical Society* **133**, 20588–20603 (2011).

[45] Crack, J., Green, J. & Thomson, A. J. Mechanism of oxygen sensing by the bacterial transcription factor fumarate-nitrate reduction (FNR). *Journal of Biological Chemistry* **279**, 9278–9286 (2004).

[46] Bennett, B., Lemon, B. J. & Peters, J. W. Reversible carbon monoxide binding and inhibition at the active site of the Fe-only hydrogenase. *Biochemistry* **39**, 7455–7460 (2000).

[47] Vincent, K. A., Parkin, A. & Armstrong, F. A. Investigating and exploiting the electrocatalytic properties of hydrogenases. *Chemical Reviews* **107**, 4366–4413 (2007).

[48] Foster, C. *Reactions of [FeFe] Hydrogenases with Carbon Monoxide and Formaldehyde* (University of Oxford, DPhil Thesis, 2012).

[49] Parkin, A., Goldet, G., Cavazza, C., Fontecilla-Camps, J. C. & Armstrong, F. A. The difference a Se makes? Oxygen-tolerant hydrogen production by the [NiFeSe]-hydrogenase from *Desulfomicrobium baculatum*. *Journal of the American Chemical Society* **130**, 13410–13416 (2008).

[50] Lauterbach, L. & Lenz, O. Catalytic production of hydrogen peroxide and water by oxygen-tolerant [NiFe]-hydrogenase during H_2 cycling in the presence of O_2. *Journal of the American Chemical Society* (2013).

[51] Lamle, S., Albracht, S. & Armstrong, F. Electrochemical potential-step investigations of the aerobic interconversions of [NiFe] hydrogenase from *Allochromatium vinosum*: Insights into the puzzling difference between unready and ready oxidized inactive states. *Journal of the American Chemical Society* **126**, 14899–14909 (2004).

[52] Vincent, K. *et al.* Electrochemical definitions of O_2 sensitivity and oxidative inactivation in hydrogenases. *Journal of the American Chemical Society* **127**, 18179–18189 (2005).

[53] Lauterbach, L. *et al.* The hydrogenase subcomplex of the NAD^+-reducing [NiFe] hydrogenase from *Ralstonia eutropha* - insights into catalysis and redox interconversions. *European Journal of Inorganic Chemistry* **2011**, 1067–1079 (2011).

[54] Horch, M., Lauterbach, L., Lenz, O., Hildebrandt, P. & Zebger, I. NAD(H)-coupled hydrogen cycling - structure- function relationships of bidirectional [NiFe]hydrogenases. *FEBS Letters* (2012).

[55] Fritsch, J., Lenz, O. & Friedrich, B. Structure, function and biosynthesis of O_2-tolerant hydrogenases. *Nature Reviews Microbiology* **11**, 106–114 (2013).

[56] Goris, T. *et al.* A unique iron-sulfur cluster is crucial for oxygen tolerance of a [NiFe]-hydrogenase. *Nature Chemical Biology* **7**, 648–648 (2011).

[57] Lukey, M. *et al.* Oxygen tolerant [NiFe]-hydrogenases: the individual and collective importance of supernumerary cysteines at the proximal FeS cluster. *Journal of the American Chemical Society* (2011).

[58] Cracknell, J., Wait, A., Lenz, O., Friedrich, B. & Armstrong, F. A kinetic and thermodynamic understanding of O_2-tolerance in [NiFe]-hydrogenases. *Proceedings of the National Academy of Sciences* **106**, 20681 (2009).

[59] Ludwig, M., Cracknell, J., Vincent, K., Armstrong, F. & Lenz, O. Oxygen-tolerant H_2 oxidation by membrane-bound [NiFe] hydrogenases of *Ralstonia* species. *Journal of Biological Chemistry* **284**, 465 (2009).

[60] Duché, O., Elsen, S., Cournac, L. & Colbeau, A. Enlarging the gas access channel to the active site renders the regulatory hydrogenase HupUV of *Rhodobacter capsulatus* O_2-sensitive without affecting its transductory activity. *FEBS Journal* **272**, 3899–3908 (2005).

[61] Murphy, B. J. *The Importance of Electron Transfer in Determining Properties of [NiFe] Hydrogenases* (University of Oxford, DPhil Thesis, 2013).

[62] Fourmond, V., Infossi, P., Giudici-Orticoni, M.-T., Bertrand, P. & Léger, C. 'Two-step' chronoamperometric method for studying the anaerobic inactivation of an oxygen-tolerant [NiFe] hydrogenase. *Journal of the American Chemical Society* **132**, 4848–4857 (2010).

[63] Abou Hamdan, A. *et al.* Relation between anaerobic inactivation and oxygen tolerance in a large series of [NiFe] hydrogenase mutants. *Proceedings of the National Academy of Sciences* **109**, 19916–19921 (2012).

[64] Volbeda, A. *et al.* X-ray crystallographic and computational studies of the O_2-tolerant [NiFe]-hydrogenase 1 from *Escherichia coli*. *Proceedings of the National Academy of Sciences* **109**, 5305–5310 (2012).

[65] Shomura, Y., Yoon, K.-S., Nishihara, H. & Higuchi, Y. Structural basis for a [4Fe-3S] cluster in the oxygen-tolerant membrane-bound [NiFe]-hydrogenase. *Nature* **479**, 253–256 (2011).

[66] Fritsch, J. *et al.* The crystal structure of an oxygen-tolerant hydrogenase uncovers a novel iron-sulphur centre. *Nature* **479**, 249–252 (2011).

[67] Wulff, P., Day, C. C., Sargent, F. & Armstrong, F. A. How oxygen reacts with oxygen-tolerant respiratory [NiFe]-hydrogenases. *Proceedings of the National Academy of Sciences* **111**, 6606–6611 (2014).

[68] Teixeira, M. *et al.* Redox intermediates of *Desulfovibrio gigas* [NiFe] hydrogenase generated under hydrogen. Mössbauer and EPR characterization of the metal centers. *Journal of Biological Chemistry* **264**, 16435–16450 (1989).

[69] Beinert, H., Holm, R. H. & Münck, E. Iron-sulfur clusters: Nature's modular, multipurpose

structures. *Science* **277**, 653–659 (1997).

[70] Rousset, M. *et al.* [3Fe-4S] to [4Fe-4S] cluster conversion in *Desulfovibrio fructosovorans* [NiFe] hydrogenase by site-directed mutagenesis. *Proceedings of the National Academy of Sciences* **95**, 11625 (1998).

[71] Evans, R. M. *et al.* Principles of sustained enzymatic hydrogen oxidation in the presence of oxygen - the crucial influence of high potential Fe-S clusters in the electron relay of [NiFe] hydrogenases. *Journal of the American Chemical Society* **135**, 2694–2707 (2013).

[72] Sawers, R. Formate and its role in hydrogen production in *Escherichia coli*. *Biochemical Society Transactions* **33**, 42–46 (2005).

[73] Forzi, L. & Sawers, R. Maturation of [NiFe] hydrogenases in *Escherichia coli*. *BioMetals* **20**, 565–578 (2007).

[74] Skibinski, D. A. G. *et al.* Regulation of the hydrogenase-4 operon of escherichia coli by the σ 54-dependent transcriptional activators FhlA and HyfR. *Journal of Bacteriology* **184**, 6642–6653 (2002).

[75] Ballantine, S. P. & Boxer, D. H. Nickel-containing hydrogenase isoenzymes from anaerobically grown *Escherichia coli* K-12. *Journal of Bacteriology* **163**, 454–459 (1985).

[76] Sawers, R. G., Ballantine, S. P. & Boxer, D. H. Differential expression of hydrogenase isoenzymes in *Escherichia coli* K-12: evidence for a third isoenzyme. *Journal of Bacteriology* **164**, 1324 (1985).

[77] Richard, D. J., Sawers, G., Sargent, F., McWalter, L. & Boxer, D. H. Transcriptional regulation in response to oxygen and nitrate of the operons encoding the [NiFe] hydrogenases 1 and 2 of *Escherichia coli*. *Microbiology* **145**, 2903–2912 (1999).

[78] Menon, N. K. *et al.* Cloning, sequencing, and mutational analysis of the hyb operon encoding *Escherichia coli* hydrogenase 2. *Journal of Bacteriology* **176**, 4416–4423 (1994).

[79] Sawers, R. G. & Boxer, D. H. Purification and properties of membrane-bound hydrogenase isoenzyme 1 from anaerobically grown *Escherichia coli* K12. *European Journal of Biochemistry* **156**, 265–275 (1986).

[80] Brøndsted, L. & Atlung, T. Anaerobic regulation of the hydrogenase 1 (hya) operon of *Escherichia coli*. *Journal of Bacteriology* **176**, 5423–5428 (1994).

[81] Nesbit, A. D., Fleischhacker, A. S., Teter, S. J. & Kiley, P. J. ArcA and AppY antagonize IscR repression of hydrogenase-1 expression under anaerobic conditions, revealing a novel mode of O_2 regulation of gene expression in *Escherichia coli*. *Journal of Bacteriology* **194**, 6892–6899 (2012).

[82] Partridge, J. D. *et al.* Transition of *Escherichia coli* from aerobic to micro-aerobic conditions involves fast and slow reacting regulatory components. *Journal of Biological Chemistry* **282**, 11230–11237 (2007).

[83] Atlung, T., Knudsen, K., Heerfordt, L. & Brøndsted, L. Effects of sigmaS and the transcriptional activator AppY on induction of the *Escherichia coli* hya and cbdAB-appA operons in response to carbon and phosphate starvation. *Journal of Bacteriology* **179**, 2141–2146 (1997).

[84] Theodoratou, E. *et al.* Nickel serves as a substrate recognition motif for the endopeptidase involved in hydrogenase maturation. *European Journal of Biochemistry* **267**, 1995–1999 (2000).

[85] Palmer, T., Sargent, F. & Berks, B. C. Export of complex cofactor-containing proteins by the bacterial Tat pathway. *Trends in Microbiology* **13**, 175–180 (2005).

[86] Dubini, A. & Sargent, F. Assembly of Tat-dependent [NiFe] hydrogenases: identification of precursor-binding accessory proteins. *FEBS Letters* **549**, 141–146 (2003).

[87] Jack, R. L. *et al.* Coordinating assembly and export of complex bacterial proteins. *EMBO Journal* **23**, 3962–3972 (2004).

[88] Richardson, D. J. Bacterial respiration: a flexible process for a changing environment. *Microbiology* **146**, 551–571 (2000).

[89] Unden, G. & Bongaerts, J. Alternative respiratory pathways of *Escherichia coli*: energetics and transcriptional regulation in response to electron acceptors. *Biochimica et Biophysica Acta - Bioenergetics* **1320**, 217–234 (1997).

[90] Sharma, P., Teixeira de Mattos, M. J., Hellingwerf, K. J. & Bekker, M. On the function of the various quinone species in *Escherichia coli*. *FEBS Journal* **279**, 3364–3373 (2012).

[91] Georgellis, D., Kwon, O. & Lin, E. C. C. Quinones as the redox signal for the arc two-component system of bacteria. *Science* **292**, 2314–2316 (2001).

[92] Bekker, M. *et al.* The ArcBA two-component system of *Escherichia coli* is regulated by the redox state of both the ubiquinone and the menaquinone pool. *Journal of Bacteriology* **192**, 746–754 (2010).

[93] Wikström, M. Cytochrome c oxidase: 25 years of the elusive proton pump. *Biochimica et Biophysica Acta - Bioenergetics* **1655**, 241–247 (2004).

[94] Simon, J., van Spanning, R. J. M. & Richardson, D. J. The organisation of proton motive and non-proton motive redox loops in prokaryotic respiratory systems. *Biochimica et Biophysica Acta - Bioenergetics* **1777**, 1480–1490 (2008).

[95] Hirst, J. Towards the molecular mechanism of respiratory complex I. *Biochemical Journal* **425**, 327–339 (2010).

[96] Efremov, R. G. & Sazanov, L. A. Structure of the membrane domain of respiratory complex I. *Nature* **476**, 414–420 (2011).

[97] Kussmaul, L. & Hirst, J. The mechanism of superoxide production by NADH:ubiquinone oxidoreductase (complex I) from bovine heart mitochondria. *Proceedings of the National Academy of Sciences* **103**, 7607–7612 (2006).

[98] Pryde, K. R. & Hirst, J. Superoxide is produced by the reduced flavin in mitochondrial complex

I: A single, unified mechanism that applies during both forward and reverse electron transfer. *Journal of Biological Chemistry* **286**, 18056–18065 (2011).

[99] Puustinen, A., Finel, M., Haltia, T., Gennis, R. B. & Wikstrom, M. Properties of the two terminal oxidases of *Escherichia coli*. *Biochemistry* **30**, 3936–3942 (1991).

[100] Poole, R. Oxygen reactions with bacterial oxidases and globins: binding, reduction and regulation. *Antonie Van Leeuwenhoek* **65**, 289–310 (1994).

[101] D'mello, R., Hill, S. & Poole, R. K. The cytochrome bd quinol oxidase in *Escherichia coli* has an extremely high oxygen affinity and two oxygen-binding haems: implications for regulation of activity in vivo by oxygen inhibition. *Microbiology* **142**, 755–763 (1996).

[102] Borisov, V. B. *et al.* Aerobic respiratory chain of *Escherichia coli* is not allowed to work in fully uncoupled mode. *Proceedings of the National Academy of Sciences* **108**, 17320–17324 (2011).

[103] Morris, R. L. & Schmidt, T. M. Shallow breathing: bacterial life at low O_2. *Nature Reviews Microbiology* **11**, 205–212 (2013).

[104] Charrier, M. & Brune, A. The gut microenvironment of helicid snails (gastropoda: Pulmonata): in-situ profiles of pH, oxygen, and hydrogen determined by microsensors. *Canadian Journal of Zoology* **81**, 928–935 (2003).

[105] Marteyn, B. *et al.* Modulation of shigella virulence in response to available oxygen in vivo. *Nature* **465**, 355–358 (2010).

[106] Eddowes, M. J. & Hill, H. A. O. Novel method for the investigation of the electrochemistry of metalloproteins: cytochrome c. *Journal of the Chemical Society, Chemical Communications* 771b–772 (1977).

[107] Yeh, P. & Kuwana, T. Reversible electrode reaction of cytochrome c. *Chemistry Letters* **6**, 1145–1148 (1977).

[108] Leger, C. *et al.* Enzyme electrokinetics: Using protein film voltammetry to investigate redox enzymes and their mechanisms. *Biochemistry* **42**, 8653–8662 (2003).

[109] Sucheta, A., Cammack, R., Weiner, J. & Armstrong, F. A. Reversible electrochemistry of fumarate reductase immobilized on an electrode surface. direct voltammetric observations of redox centers and their participation in rapid catalytic electron transport. *Biochemistry* **32**, 5455–5465 (1993).

[110] Bard, A. J. & Faulkner, L. R. *Electrochemical methods: fundamentals and applications* (Wiley and Sons, 2001), 2nd edn.

[111] Murphy, B. J., Sargent, F. & Armstrong, F. A. Transforming an oxygen-tolerant [NiFe] uptake hydrogenase into a proficient, reversible hydrogen producer. *Energy and Environmental Science* **7**, 1426–1433 (2014).

[112] Cracknell, J. A. *et al.* Enzymatic oxidation of H_2 in atmospheric O_2: The electrochemistry of energy generation from trace H_2 by aerobic microorganisms. *Journal of the American Chemical*

Society **130**, 424–425 (2008).

[113] Pandelia, M.-E. *et al.* Membrane-bound hydrogenase I from the hyperthermophilic bacterium *Aquifex aeolicus*: Enzyme activation, redox intermediates and oxygen tolerance. *Journal of the American Chemical Society* **132**, 6991–7004 (2010).

[114] Hexter, S. V., Grey, F., Happe, T., Climent, V. & Armstrong, F. A. Electrocatalytic mechanism of reversible hydrogen cycling by enzymes and distinctions between the major classes of hydrogenases. *Proceedings of the National Academy of Sciences* **109**, 11516–11521 (2012).

[115] Solomon, E. I., Sundaram, U. M. & Machonkin, T. E. Multicopper oxidases and oxygenases. *Chemical Reviews* **96**, 2563–2606 (1996).

[116] Moore, A. L. *et al.* Unraveling the heater: New insights into the structure of the alternative oxidase. *Annual Review of Plant Biology* **64**, 637–663 (2013).

[117] Rich, P. R. & Moore, A. L. The involvement of the protonmotive ubiquinone cycle in the respiratory chain of higher plants and its relation to the branchpoint of the alternate pathway. *FEBS Letters* **65**, 339–344 (1976).

[118] Shiba, T. *et al.* Structure of the trypanosome cyanide-insensitive alternative oxidase. *Proceedings of the National Academy of Sciences* **110**, 4580–4585 (2013).

[119] Moore, A. L., Bonner Jr, W. D. & Rich, P. R. The determination of the proton-motive force during cyanide-insensitive respiration in plant mitochondria. *Archives of Biochemistry and Biophysics* **186**, 298–306 (1978).

[120] Nelson, S. T. A simple, practical methodology for routine VSMOW/SLAP normalization of water samples analyzed by continuous flow methods. *Rapid Communications in Mass Spectrometry* **14**, 1044–1046 (2000).

[121] Balvers, W. G., Boersma, M. G., Vervoort, J. & Rietjens, I. M. C. M. Experimental and theoretical study on the redox cycling of resorufin by solubilized and membrane-bound nadph-cytochrome reductase. *Chemical Research in Toxicology* **5**, 268–273 (1992).

[122] Elstner, E. F. & Heupel, A. Inhibition of nitrite formation from hydroxylammoniumchloride: A simple assay for superoxide dismutase. *Analytical Biochemistry* **70**, 616–620 (1976).

[123] Schneider, K. & Schlegel, H. Production of superoxide radicals by soluble hydrogenase from *Alcaligenes eutrophus* H16. *Biochemical Journal* **193**, 99–107 (1981).

[124] Elstner, E. F., Heupel, A. & Vaklinov.S. Inhibition of photosynthetic electron transport in isolated chloroplasts by hydroxylamine. *Zeitschrift Für Pflanzenphysiologie* **62**, 173 (1970).

[125] Elstner, E., Heupel, A. & Vaklinova, S. On the oxidation of hydroxylamine in isolated chloroplasts and the possible role of a peroxidase from spinach leaves in the oxidation of ascorbate and glycolate. *Zeitschrift Für Pflanzenphysiologie* **62**, 184–200 (1970).

[126] Denisov, E. T. & Afanasev, I. B. *Oxidation and antioxidants in organic chemistry and biology* (CRC press, 2010).

[127] Kono, Y. Generation of superoxide radical during autoxidation of hydroxylamine and an assay for superoxide dismutase. *Archives of Biochemistry and Biophysics* **186**, 189–195 (1978).

[128] Yankovskaya, V. *et al.* Architecture of succinate dehydrogenase and reactive oxygen species generation. *Science* **299**, 700–704 (2003).

[129] Bielski, B. H., Cabelli, D. E., Arudi, R. L. & Ross, A. B. Reactivity of HO/O radicals in aqueous solution. *Journal of Physical and Chemical Reference Data* **14**, 1041 (1985).

[130] Feder, N. A heme-peptide as an ultrastructural tracer. *Journal of Histochemistry and Cytochemistry* **18**, 911–913 (1970).

[131] Volbeda, A. *et al.* Crystal structure of the O_2-tolerant membrane-bound hydrogenase 1 from *Escherichia coli* in complex with its cognate cytochrome b. *Structure* **21**, 184–190 (2013).

[132] Lauterbach, L., Idris, Z., Vincent, K. A. & Lenz, O. Catalytic properties of the isolated diaphorase fragment of the NAD^+-reducing [NiFe]-hydrogenase from *Ralstonia eutropha*. *PLoS ONE* **6**, e25939 (2011).

[133] Menon, N. K., Robbins, J., Wendt, J. C., Shanmugam, K. T. & Przybyla, A. E. Mutational analysis and characterization of the *Escherichia coli* hya operon, which encodes [NiFe] hydrogenase 1. *Journal of Bacteriology* **173**, 4851 (1991).

[134] Søballe, B. & Poole, R. K. Microbial ubiquinones: multiple roles in respiration, gene regulation and oxidative stress management. *Microbiology* **145**, 1817–1830 (1999).

[135] Fukai, Y. *et al.* Functional expression of the ascofuranone-sensitive *Trypanosoma brucei* alternative oxidase in the cytoplasmic membrane of *Escherichia coli*. *Comparative Biochemistry and Physiology Part C: Pharmacology, Toxicology and Endocrinology* **124**, 141–148 (1999).

[136] Chandel, N. S., Budinger, G. S. & Schumacker, P. T. Molecular oxygen modulates cytochrome c oxidase function. *Journal of Biological Chemistry* **271**, 18672–18677 (1996).

[137] Kulys, J., Krikstopaitis, K. & Ziemys, A. Kinetics and thermodynamics of peroxidase- and laccase-catalyzed oxidation of n-substituted phenothiazines and phenoxazines. *Journal of Biological Inorganic Chemistry* **5**, 333–340 (2000).

[138] Xu, F. *et al.* Redox chemistry in laccase-catalyzed oxidation of n-hydroxy compounds. *Applied and Environmental Microbiology* **66**, 2052–2056 (2000).

[139] Xiuyin, X., Zhiyong, W., Dingquan, W., Songsheng, Q. & Cunxin, W. Microcalorimetric studies of *Rhus vernicifera* laccase catalytic oxidation reactions. *Journal of Thermal Analysis and Calorimetry* **70**, 889–896 (2002).

[140] Nitschke, W. & Russell, M. Hydrothermal focusing of chemical and chemiosmotic energy, supported by delivery of catalytic Fe, Ni, Mo/W, Co, S and Se, forced life to emerge. *Journal of Molecular Evolution* **69**, 481–496 (2009).

[141] Sleep, N. & Bird, D. Evolutionary ecology during the rise of dioxygen in the earth's atmosphere. *Philosophical Transactions of the Royal Society B: Biological Sciences* **363**, 2651–2664 (2008).

[142] Vignais, P. M., Billoud, B. & Meyer, J. Classification and phylogeny of hydrogenases. *FEMS Microbiology Reviews* **25**, 455–501 (2001).

[143] Lisa, B. *et al.* How the structure of the large subunit controls function in an oxygen-tolerant [NiFe] hydrogenase. *Biochemical Journal* (2014).

[144] Page, C., Moser, C., Chen, X. & Dutton, P. Natural engineering principles of electron tunnelling in biological oxidation-reduction. *Nature* **402**, 47–52 (1999).

[145] Krissinel, E. & Henrick, K. Inference of macromolecular assemblies from crystalline state. *Journal of Molecular Biology* **372**, 774–797 (2007).

[146] Frielingsdorf, S., Schubert, T., Pohlmann, A., Lenz, O. & Friedrich, B. A trimeric supercomplex of the oxygen-tolerant membrane-bound [NiFe] hydrogenase from *Ralstonia eutropha* H16. *Biochemistry* **50**, 10836–10843 (2011).

[147] Wait, A. F., Parkin, A., Morley, G. M., dos Santos, L. & Armstrong, F. A. Characteristics of enzyme-based hydrogen fuel cells using an oxygen-tolerant hydrogenase as the anodic catalyst. *The Journal of Physical Chemistry C* **114**, 12003–12009 (2010).

[148] Marianayagam, N. J., Sunde, M. & Matthews, J. M. The power of two: protein dimerization in biology. *Trends in Biochemical Sciences* **29**, 618–625 (2004).

[149] Tina, P. *et al.* The emergence of protein complexes: quaternary structure, dynamics and allostery. *Biochemical Society Transactions* **40**, 475–491 (2012).

[150] Navia, M. A. *et al.* Three-dimensional structure of aspartyl protease from human immunodeficiency virus HIV-1. *Nature* **337**, 615–620 (1989).

[151] Berg, J., Tymoczko, J. & Stryer, L. *Biochemie, 5. Auflage* (Spektrum Akademischer Verlag Heidelberg, Berlin, Deutschland, 2003).

[152] Cansu, S. & Doruker, P. Dimerization affects collective dynamics of triosephosphate isomerase. *Biochemistry* **47**, 1358–1368 (2008).

[153] Rios, C., Jordan, B., Gomes, I. & Devi, L. G-protein-coupled receptor dimerization: modulation of receptor function. *Pharmacology and Therapeutics* **92**, 71–87 (2001).

[154] Breitwieser, G. E. G protein-coupled receptor oligomerization implications for g protein activation and cell signaling. *Circulation Research* **94**, 17–27 (2004).

[155] Beckett, D. Regulated assembly of transcription factors and control of transcription initiation. *Journal of Molecular Biology* **314**, 335–352 (2001).

[156] Frese, R. N. *et al.* Protein shape and crowding drive domain formation and curvature in biological membranes. *Biophysical Journal* **94**, 640–647 (2008).

[157] Agre, P. *et al.* Aquaporin water channels - from atomic structure to clinical medicine. *The Journal of Physiology* **542**, 3–16 (2002).

[158] MacKinnon, R. Potassium channels. *FEBS Letters* **555**, 62–65 (2003).

[159] Robinson-Rechavi, M., Alibés, A. & Godzik, A. Contribution of electrostatic interactions,

compactness and quaternary structure to protein thermostability: Lessons from structural genomics of *Thermotoga maritima*. *Journal of Molecular Biology* **356**, 547–557 (2006).

[160] Drennan, C. L., Heo, J., Sintchak, M. D., Schreiter, E. & Ludden, P. W. Life on carbon monoxide: X-ray structure of *Rhodospirillum rubrum* Ni-Fe-S carbon monoxide dehydrogenase. *Proceedings of the National Academy of Sciences* **98**, 11973–11978 (2001).

[161] Lottspeich, F. & Engels, J. W. *Bioanalytik* (Spektrum Akademischer Verlag, Elsevier, Munich, 2006), 2nd edn.

[162] Léger, C., Jones, A. K., Albracht, S. P. J. & Armstrong, F. A. Effect of a dispersion of interfacial electron transfer rates on steady state catalytic electron transport in [NiFe] hydrogenase and other enzymes. *Journal of Physical Chemistry B* **106**, 13058–13063 (2002).

[163] Rath, A., Glibowicka, M., Nadeau, V. G., Chen, G. & Deber, C. M. Detergent binding explains anomalous SDS-PAGE migration of membrane proteins. *Proceedings of the National Academy of Sciences* **106**, 1760–1765 (2009).

[164] Sezer, M. *et al.* Role of the HoxZ subunit in the electron transfer pathway of the membrane-bound [NiFe] hydrogenase from *Ralstonia Eutropha* immobilized on electrodes. *The Journal of Physical Chemistry B* (2011).

[165] Lamle, S. E., Albracht, S. P. J. & Armstrong, F. A. The mechanism of activation of a [NiFe] hydrogenase by electrons, hydrogen, and carbon monoxide. *Journal of the American Chemical Society* **127**, 6595–6604 (2005).

[166] Radu, V., Frielingsdorf, S., Evans, S. D., Lenz, O. & Jeuken, L. J. C. Enhanced oxygen-tolerance of the full heterotrimeric membrane-bound [NiFe] hydrogenase of *Ralstonia eutropha*. *Journal of the American Chemical Society* (2014).

[167] Jones, A. K. *et al.* Enzyme electrokinetics: Electrochemical studies of the anaerobic interconversions between active and inactive states of *Allochromatium vinosum* [NiFe] hydrogenase. *Journal of the American Chemical Society* **125**, 8505–8514 (2003).

[168] Dincturk, H. B., Demir, V. & Aykanat, T. Bd oxidase homologue of photosynthetic purple sulfur bacterium *Allochromatium vinosum* is co-transcribed with a nitrogen fixation related gene. *Antonie Van Leeuwenhoek* **99**, 211–220 (2011).

[169] Summerer, D. *et al.* A genetically encoded fluorescent amino acid. *Proceedings of the National Academy of Sciences* **103**, 9785 (2006).

[170] Chin, J. W., Martin, A. B., King, D. S., Wang, L. & Schultz, P. G. Addition of a photocrosslinking amino acid to the genetic code of *Escherichia coli*. *Proceedings of the National Academy of Sciences* **99**, 11020 (2002).

[171] Lee, H. S., Spraggon, G., Schultz, P. G. & Wang, F. Genetic incorporation of a metal-ion chelating amino acid into proteins as a biophysical probe. *Journal of the American Chemical Society* **131**, 2481 (2009).

[172] Brustad, E. *et al.* A genetically encoded boronate-containing amino acid. *Angewandte Chemie International Edition* **120**, 8344–8347 (2008).

[173] Wang, L., Brock, A., Herberich, B. & Schultz, P. G. Expanding the genetic code of *Escherichia coli*. *Science* **292**, 498 (2001).

[174] Chin, J., Cropp, T. A., Jc, A., Zw, M. M. Z. & Pg, S. An expanded eukaryotic genetic code. *Science* **301**, 5635 (2003).

[175] Sakamoto, K. *et al.* Site-specific incorporation of an unnatural amino acid into proteins in mammalian cells. *Nucleic Acids Research* **30**, 4692 (2002).

[176] Young, T. S., Ahmad, I., Yin, J. A. & Schultz, P. G. An enhanced system for unnatural amino acid mutagenesis in *E. coli*. *Journal of Molecular Biology* **395**, 361–374 (2010).

[177] Englesberg, E. *et al.* L-Arabinose-sensitive, L-ribulose 5-phosphate 4-epimerase-deficient mutants of *Escherichia coli*. *Journal of Bacteriology* **84**, 137 (1962).

[178] Chin, J. *et al.* Addition of p-azido-L-phenylalanine to the genetic code of *Escherichia coli*. *Journal of the American Chemical Society* **124**, 9026–9027 (2002).

[179] Neumann, H., Wang, K., Davis, L., Garcia-Alai, M. & Chin, J. Encoding multiple unnatural amino acids via evolution of a quadruplet-decoding ribosome. *Nature* **464**, 441–444 (2010).

[180] Isaacs, F. J. *et al.* Precise manipulation of chromosomes in vivo enables genome-wide codon replacement. *Science* **333**, 348–353 (2011).

[181] Huisgen, R. Kinetics and mechanism of 1,3-dipolar cycloadditions. *Angewandte Chemie International Edition* **2**, 633–645 (1963).

[182] Tornoe, C. W., Christensen, C. & Meldal, M. Peptidotriazoles on solid phase: [1,2,3]-triazoles by regiospecific copper(I)-catalyzed 1,3-dipolar cycloadditions of terminal alkynes to azides. *The Journal of Organic Chemistry* **67**, 3057–3064 (2002).

[183] Hein, J. E. & Fokin, V. V. Copper-catalyzed azide-alkyne cycloaddition (CuAAC) and beyond: new reactivity of copper(I) acetylides. *Chemical Society Reviews* **39**, 1302–1315 (2010).

[184] Chan, T. R., Hilgraf, R., Sharpless, K. B. & Fokin, V. V. Polytriazoles as copper(I)-stabilizing ligands in catalysis. *Organic Letters* **6**, 2853–2855 (2004).

[185] Shea, K. J. & Kim, J. S. Influence of strain on chemical reactivity. Relative reactivity of torsionally strained double bonds in 1,3-dipolar cycloadditions. *Journal of the American Chemical Society* **114**, 4846–4855 (1992).

[186] Agard, N. J., Prescher, J. A. & Bertozzi, C. R. A strain-promoted [3 + 2] azide-alkyne cycloaddition for covalent modification of biomolecules in living systems. *Journal of the American Chemical Society* **126**, 15046–15047 (2004).

[187] Ning, X., Guo, J., Wolfert, M. & Boons, G.-J. Visualizing metabolically labeled glycoconjugates of living cells by copper-free and fast huisgen cycloadditions. *Angewandte Chemie International Edition* **47**, 2253–2255 (2008).

[188] Debets, M. F. *et al.* Aza-dibenzocyclooctynes for fast and efficient enzyme pegylation via copper-free (3+ 2) cycloaddition. *Chemical Communications* **46**, 97–99 (2010).

[189] Kolb, H. C., Finn, M. G. & Sharpless, K. B. Click chemistry: diverse chemical function from a few good reactions. *Angewandte Chemie International Edition* **40**, 2004–2021 (2001).

[190] Schwyzer, R. & Caviezel, M. p-Azido-L-phenylalanine: A photo affinity probe related to tyrosine. *Helvetica Chimica Acta* **54**, 1395–1400 (1971).

[191] Liu, Q. & Tor, Y. Simple conversion of aromatic amines into azides. *Organic Letters* **5**, 2571–2572 (2003).

[192] Gottlieb, H., Kotlyar, V. & Nudelman, A. NMR chemical shifts of common laboratory solvents as trace impurities. *Journal of Organic Chemistry* **62**, 7512–7515 (1997).

[193] Deiters, A. Site-specific PEGylation of proteins containing unnatural amino acids. *Bioorganic and Medicinal Chemistry Letters* **14**, 5743 (2004).

[194] Johnson, K. A., Verhagen, M. F. J. M., Brereton, P. S., Adams, M. W. W. & Amster, I. J. Probing the stoichiometry and oxidation states of metal centers in iron-sulfur proteins using electrospray FTICR mass spectrometry. *Analytical Chemistry* **72**, 1410–1418 (2000).

[195] L'Abbe, G. Decomposition and addition reactions of organic azides. *Chemical Reviews* **69**, 345–363 (1969).

[196] Schrock, A. K. & Schuster, G. B. Photochemistry of phenyl azide: chemical properties of the transient intermediates. *Journal of the American Chemical Society* **106**, 5228–5234 (1984).

[197] Leyva, E., Platz, M. S., Persy, G. & Wirz, J. Photochemistry of phenyl azide: the role of singlet and triplet phenylnitrene as transient intermediates. *Journal of the American Chemical Society* **108**, 3783–3790 (1986).

[198] van Dongen, S. F. M. *et al.* Single-step azide introduction in proteins via an aqueous diazo transfer. *Bioconjugate Chemistry* **20**, 20–23 (2009).

[199] Krishnan, S. & Armstrong, F. Order-of-magnitude enhancement of an enzymatic hydrogen-air fuel cell based on pyrenyl carbon nanostructures. *Chemical Science* **3**, 1015–1023 (2012).

[200] Vollhardt, K., Schore, N. & Peter, K. *Organische Chemie, 4. Auflage* (Wiley-VCH, 2005).

[201] Bohlmann, F., Schönowsky, H., Inhoffen, E. & Grau, G. Polyacetylenverbindungen, LII. über den mechanismus der oxydativen dimerisierung von acetylenverbindungen. *Chemische Berichte* **97**, 794–800 (1964).

[202] Reymond, S. & Cossy, J. Copper-catalyzed Diels-Alder reactions. *Chemical Reviews* **108**, 5359–5406 (2008).

[203] Gay, C., Collins, J. & Gebicki, J. M. Hydroperoxide assay with the ferric-xylenol orange complex. *Analytical Biochemistry* **273**, 149–155 (1999).

[204] Chance, B. Techniques for the assay of the respiratory enzymes. In *Methods in Enzymology*, vol. Volume 4, 273–329 (Academic Press, 1957).